



Adam Mickiewicz University, Poznań
Faculty of Physics
Institute of Spintronics and Quantum Information

DOCTORAL THESIS

**Impact of interactions between
ferromagnetic layers on spin-wave
dynamics**

Krzysztof Szulc

under the supervision of **prof. dr hab. Maciej Krawczyk**

June 2024

Abstract

Magnetic materials have been known for thousands of years. They play an important role in today's world, thanks to their widespread use in devices such as motors, sensors, and computers, as well as regular fridge magnets. Great hopes are given to the application of waves in the ferromagnetic materials, i.e., spin waves. Nowadays, the majority of computing units are based on electronic devices. However, further miniaturization of integrated circuits may soon be impossible due to the limitations associated with the use of high power densities and high voltages. The big advantage of the spin waves is their very low energy, which, combined with the wavelengths of several hundreds or even tens of nanometers in microwave frequencies, gives the possibility to design nanoscale devices with significantly lower energy consumption than electronic devices. In the last two decades, the scientists have put special emphasis on the design of basic magnonic devices such as directional couplers, diodes, transistors, or logic gates, which can find the application in the magnonic integrated circuits. In these systems, the control of the interaction between the elements is crucial to take a full advantage of the spin-wave properties.

In this Thesis, I study the ferromagnetic multilayers which can find application in the magnonic systems. I start the Thesis with the introduction of magnetism. This is followed by the explanation of micromagnetism, the interactions governing the magnetic systems, the magnetization textures, and the spin waves, concluding with the currently intensively studied topics of magnonic crystals and spin-wave computing. Then, I explain the numerical methods used in the Thesis with a detailed presentation of the problem implementation. In the first part of the research, I show how the non-reciprocal interactions can be used to design non-reciprocal devices. The Dzyaloshinskii–Moriya interaction was used to induce the asymmetry of the dispersion relation, which was further used to design a spin-wave diode and circulator. In the second study, the surface character of the Damon–Eshbach mode resulting from the dipolar interaction was used to design a four-port device that can have different functionalities—circulator, directional coupler, or reflector—for different excitation frequencies. The next study shows how the Dzyaloshinskii–Moriya interaction together with the perpendicular magnetic anisotropy can lead to the neglect of the interaction between layers at the distance of 1 nm, which can be further used to design systems of densely packed non-interacting waveguides. In the third part, I will focus on using the interaction between the layers to couple the material with magnetization texture and the material with good spin-wave propagation properties to make a magnonic crystal. The first system is a layer with weak perpendicular magnetic anisotropy in which the stripe domains are induced, which interact with the permalloy layer. Due to the

interaction, the stripe-domain structure is imprinted on the permalloy layer, giving the system the character of a magnonic crystal with a non-reciprocal dispersion relation. Moreover, we show how the dispersion relation of the system can be controlled by changing the magnetization direction. The second system was a permalloy waveguide over which the chain of dots with the Dzyaloshinskii–Moriya interaction is placed. In the dots, it is possible to stabilize the single-domain state and the skyrmion state. I show that the dispersion relation changes with the change of the configuration of the dot. Due to different character of excitation of the single-domain state and the skyrmion, the system with skyrmions in dots can interact at lower frequencies. Furthermore, I show that one part of the skyrmion modes hybridize with the waveguide modes, sometimes inducing additional band gaps in the spectrum, while the second part does not interact, forming bound states.

Streszczenie

Materiały magnetyczne są znane od tysiącleci. Dzięki ich szerokiemu zastosowaniu w urządzeniach takich jak silniki, sensory, komputery czy też nawet jako zwykłe magnesy na lodówkę, pełnią one istotną rolę w dzisiejszym świecie. Duże nadzieje aplikacyjne wiązane są z falami w ferromagnetykach, tj. falami spinowymi. Obecnie wykorzystywane jednostki obliczeniowe bazują głównie na urządzeniach elektronicznych, jednakże dalsza miniaturyzacja układów scalonych może być wkrótce niemożliwa ze względu na ograniczenia dotyczące wysokich gęstości mocy i napięć. Ogromną zaletą fal spinowych jest ich niska energia, która w połączeniu z długościami fal rzędu setek, a nawet dziesiątek nanometrów w zakresie częstotliwości mikrofalowych daje możliwość stworzenia urządzeń w nanoskali o dużo mniejszym zużyciu energii od urządzeń elektronicznych. W ostatnich dwóch dekadach naukowcy kładą duży nacisk na projektowanie podstawowych magnonicznych urządzeń logicznych takich jak sprzęgacz, dioda, tranzystor czy bramki logiczne, które mogłyby znaleźć zastosowanie w magnonicznych układach scalonych. W takich układach ważna jest kontrola oddziaływania pomiędzy elementami, aby następnie mieć możliwość wykorzystania pełnego potencjału fal spinowych.

W tej rozprawie doktorskiej badam ferromagnetyczne układy wielowarstwowe, które mogłyby znaleźć zastosowanie w układach magnonicznych. Rozprawę rozpoczynam od wprowadzenia do magnetyzmu. Dalej zostają wyjaśnione pojęcie mikromagnetyzmu, oddziaływania rządzące układami magnetycznymi, tekstury magnetyczne oraz fale spinowe, kończąc na obecnie intensywnie badanych kryształach magnonicznych i obliczeniach z wykorzystaniem fal spinowych. Następnie wyjaśniam metody numeryczne wykorzystane w pracy doktorskiej wraz ze szczegółowym przedstawieniem implementacji problemów. W pierwszej części badań pokazuję jak oddziaływania o nieodwracalnym charakterze mogą być wykorzystane do zaprojektowania urządzeń o asymetrycznym działaniu. Oddziaływanie Działoszynskiego-Moriyi zostało wykorzystane do wyindukowania asymetrii w relacji dyspersji fal spinowych, co następnie posłużyło do zaprojektowania diody oraz cyrkulatora dla fal spinowych. W drugim badaniu, powierzchniowy charakter modów Damona-Eshbacha pochodzący od oddziaływań dipolowych został wykorzystany do stworzenia czteroportowego urządzenia, które w zależności od częstotliwości pełni różne funkcje takie jak cyrkulator, sprzęgacz czy reflektor. Kolejne badanie pokazuje jak oddziaływanie Działoszynskiego-Moriyi wraz z prostopadłą anizotropią magnetyczną może przyczynić się do zaniku oddziaływania pomiędzy warstwami na dystansie zaledwie jednego nanometra, co może być wykorzystane do stworzenia układów nieoddziałujących falowodów. W trzeciej części skupiam się na wykorzystaniu oddziaływania pomiędzy warstwami do sprzężenia

materiałów z teksturą magnetyzacji z materiałami o niskim tłumieniu fal spinowych w celu stworzenia kryształów magnonicznych. Pierwszym układem jest warstwa ze słabą prostopadłą anizotropią magnetyczną, w której indukują się domeny paskowe, które oddziałują z warstwą permaloju. Dzięki oddziaływaniu, tekstura domen paskowych nadrukowuje się na permaloju, dzięki czemu układ ma charakter kryształu magnonicznego, którego relacja ma charakter nieodwracalny i którą można kontrolować poprzez zmianę kierunku magnetyzacji permaloju. Drugim układem był falowód z permaloju, nad którym umieszczony został łańcuch dysków z oddziaływaniem Dzialoszynskiego-Moriya. W dyskach może być ustabilizowana konfiguracja jednodomenowa oraz skyrmion. Pokazuję, że relacja dyspersji zmienia się wraz ze zmianą konfiguracji w dysku. Ze względu na inny charakter wzbudzeń konfiguracji jednodomenowej oraz skyrmionu, układ ze skyrmionami może oddziaływać na niższych częstotliwościach. Ponadto pokazuję, że jedna część modów skyrmionowych hybrydyzuje z modami falowodowymi, czasem indukując dodatkowe przerwy pasmowe, zaś druga część nie oddziałuje, tworząc stany związane.

Table of contents

Acknowledgments	vii
Preface	ix
List of publications included in the Thesis	xiii
1 Introduction to magnetism	1
1.1 Magnetic states	1
1.2 Ferromagnetism	2
2 Micromagnetism	5
2.1 Magnetic energy and equation of motion	5
2.1.1 Exchange interaction	6
2.1.2 Dipolar interaction	7
2.1.3 Zeeman interaction	9
2.1.4 Anisotropy	9
2.1.5 Dzyaloshinskii–Moriya interaction	10
2.1.6 Landau–Lifshitz–Gilbert equation	11
2.1.7 Boundary conditions	13
2.1.8 Ruderman–Kittel–Kasuya–Yosida interaction	13
2.2 Magnetization textures	14
2.2.1 Magnetic domain and domain wall	14
2.2.2 Regular stripe-domain pattern	16
2.2.3 Skyrmion	16
2.3 Spin waves	18
2.3.1 Magnetostatic waves	18
2.3.2 Dipole–exchange regime	21
2.3.3 Multilayer systems	24
2.3.4 Magnonic crystals	25
2.4 Spin-wave computing	27
2.4.1 Computational methods	27
2.4.2 Spin-wave devices	28

3	Micromagnetic simulations	31
3.1	Numerical methods	31
3.2	Implementation in COMSOL Multiphysics	33
4	Research	43
4.1	[P1] Spin-wave diode and circulator based on unidirectional coupling	43
4.2	[P2] Multifunctional operation of the double-layer ferromagnetic structure coupled by a rectangular nanoresonator	57
4.3	[P3] Nonreciprocal spin-wave dynamics in Pt/Co/W/Co/Pt multilayers	66
4.4	[P4] Reconfigurable magnonic crystals based on imprinted magnetization textures in hard and soft dipolar-coupled bilayers	77
4.5	[P5] Reconfigurable spin-wave platform based on interplay between nanodots and waveguide in hybrid magnonic crystal	92
4.6	Outlook	106
4.7	Other research	106
5	Summary	109
	Bibliography	111
	About the Author	121

Acknowledgments

Out of more than 28 years of my life, I have spent the last 8 years doing science. It has been a fantastic journey during which I have met many people who have contributed significantly to the fact that these acknowledgments could be written.

First of all, I would like to thank my supervisor, Maciej Krawczyk, who has guided me during these 8 years. It would be hard to find a better supervisor who is always ready for discussion and whose head is always full of ideas. I have learned a lot as your student and I'm sure it will pay off in my research career.

I would also like to thank all my colleagues from the Department of Physics of Nanostructures and the Institute of Spintronics and Quantum Information, with whom I drank hectoliters of coffee. In particular, I would like to thank Mateusz Zelent, who convinced me to join the group and makes the work of the whole department much easier (at the cost of his work); Piotr Graczyk who is my COMSOL master and always finds a way to make the program work (just not his program); Paweł Gruszecki, Jarosław Kłos, and Andriy Serebryannikov for the opportunity to be involved in your research projects; people with whom I had the opportunity to work: Grzegorz Centała, Mateusz Gołębiewski, Julia Kharlan, Sara Memarzadeh, Mathieu Moalic, Michał Mruczkiewicz, Krzysztof Sobucki, Olena Tartakivska, and those mentioned earlier – thank you all for the fruitful scientific discussions and the nice work which we did together.

The work also wouldn't be the same without the collaboration with the scientists from different research centers all around the world. I would like to thank you all for your great ideas and fruitful collaboration.

They say that money does not bring happiness, but it allows you to buy the workstations and programs you work with and to go to the conferences on the other side of the world. I would like to thank the National Science Center, Poland and the Foundation for Polish Science for recognizing my research and awarding me the PRELUDIUM project and the START scholarship. This work would be much harder to do without the financial support from the NCN grants no. 2021/41/N/ST3/04478, 2020/39/I/ST3/02413, 2018/30/Q/ST3/00416, 2015/17/B/ST3/00118, and 2021/43/I/ST3/00550, and the European Union program Horizon 2020 grant ID 644348.

Preface

For decades, the electronics is on the leading edge in the field of computing devices. The invention of the complementary metal–oxide–semiconductor (CMOS) technology, which led to the design and further development of the semiconductor-based transistor, was responsible for the rapid progress in this field. The current "3 nm" manufacturing process is associated with the gate pitch of about 48 nm [1]. The size of the gate is no longer decreasing at the rate of the last decades, and further decrease may soon be impossible due to the limitations associated with the use of high power densities and high voltages. Despite that, the International Roadmap for Devices and Systems predicts that the semiconductor technology will still maintain the rate of progress in the next decade [1]. Since a significant slowdown in the development of the electronic-based computing seems to be ultimately inevitable, scientists all over the world are searching for a technology that can surpass or at least significantly complement CMOS technology, making the further development of computing possible.

Magnonics is believed to be a strong contender in this field. A major advantage of spin waves is that their propagation does not require the motion of electrons, but only the precession of spins, hence the energy consumption can be significantly reduced in comparison to electronics. Another important aspect is the very high frequency of spin waves, which is usually in the GHz range, but can be even extended to the THz range. In addition, this spin-wave frequency range is associated with the wavelengths in the nm range, which opens the possibility of fast high-frequency operations in the nanoscale. Moreover, spin waves can be easily controlled by magnetic and electric fields. It should be noted that the spin wave, as a wave phenomenon, is governed by different physics than electronics, therefore, the existing computing schemes may not be the best for spin waves. However, it does not have to be seen as a disadvantage, since it opens the way for the use of non-Boolean logic schemes, analog computing, or even unconventional computing paradigms such as quantum computing or neural networks, where magnonics seems to have great potential. To be able to compete with such a developed field as electronics, the physical mechanisms governing the spin-wave dynamics must be thoroughly studied, the logic devices proposed, and the spin-wave circuits designed. I believe that magnonics has a big chance to become an important element of the computing units in the near future.

The main goal of the Thesis is to study the spin-wave dynamics in the systems of interacting layers with their possible use in the device applications. I would like to focus on the systems that have not been thoroughly studied yet, i.e., the systems with nonreciprocal couplers, systems

with strong Dzyaloshinskii–Moriya interaction, and magnonic crystals based on non-collinear magnetization texture.

In this Thesis, I would like to verify the following research hypotheses:

- Dzyaloshinskii–Moriya interaction in the bilayer system can lead to the presence of the effect of unidirectional coupling of spin waves;
- rotating modes in the resonator can couple asymmetrically with spin waves in the film;
- unidirectional coupling and rotating modes can form a basis for the design of magnonic devices such as diode or circulator;
- two thin magnetic layers with different perpendicular magnetic anisotropies can form a system of non-interacting spin-wave conduits;
- the layer with perpendicular magnetic anisotropy interacting with a thin magnetic layer forms a stable regular stripe-domain pattern;
- magnonic crystal can be based on the magnetic stripe-domain structure and it has rich dispersion relation;
- waveguide and skyrmion in the dot can interact statically and dynamically;
- waveguide with a periodic chain of dots with skyrmions inside can form a magnonic crystal with a complex band structure.

I believe that these hypotheses are proven by my Thesis containing a series of 5 research articles of which I am the main co-author. Four of these articles have been published in the peer-reviewed physics journals, and one has been published as a preprint and is currently under review.

The Thesis contains an English and a Polish abstract, acknowledgments, a preface, five chapters, and a note about the Author. **Chapter 1** introduces the phenomenon of magnetism with particular reference to ferromagnetism. **Chapter 2** explains in detail the micromagnetic approach, presenting the most fundamental interactions governing the motion of spins and the equation of motion itself. It continues with the definition of the magnetic domain and the domain wall, focusing on two systems considered in the research articles: the stripe-domain pattern and skyrmions. In the next section, the spin waves are introduced and their dynamics are pictured first in bulk materials and thin films in the magnetostatic approximation and then in the dipole–exchange regime, extending the description by the multilayer systems and magnonic crystals. At the end, the state-of-the-art in the spin-wave computing is presented. **Chapter 3** deals with the numerical simulations. First, the approaches used in magnonics are presented. Next, all the implementations used by the Author are explained in detail. **Chapter 4** presents the research articles containing the main results of the Thesis. The first two papers, *Spin-wave diode and circulator based on unidirectional coupling* and *Multifunctional operation of the double-layer ferromagnetic structure coupled by a rectangular nanoresonator*, show the designs of the spin-wave diode, the spin-wave circulator, and the multifunctional device, which can find the application in the future spin-wave circuits. The next paper, *Nonreciprocal spin-wave dynamics in Pt/Co/W/Co/Pt multilayers*, presents the system of two non-interacting spin-wave

conduits separated by only 1 nm, showing the promise for application in nanoscale devices. The last two publications, *Reconfigurable magnonic crystals based on imprinted magnetization textures in hard and soft dipolar-coupled bilayers* and *Reconfigurable spin-wave platform based on interplay between nanodots and waveguide in hybrid magnonic crystal*, show two different designs of magnonic crystals with non-collinear magnetization textures, with the possibility of using them to control the spin-wave propagation. The last chapter, **Chapter 5**, summarizes the results.

List of publications included in the Thesis

- [P1] **K. Szulc**, P. Graczyk, M. Mruczkiewicz, G. Gubbiotti, M. Krawczyk
Spin-wave diode and circulator based on unidirectional coupling
Physical Review Applied 14, 034063 (2020)
- [P2] P. Roberjot, **K. Szulc**, J. W. Kłos, M. Krawczyk
Multifunctional operation of the double-layer ferromagnetic structure coupled by a rectangular nanoresonator
Applied Physics Letters 118, 182406 (2021)
- [P3] **K. Szulc**, S. Mendisch, M. Mruczkiewicz, F. Casoli, M. Becherer, G. Gubbiotti
Nonreciprocal spin-wave dynamics in Pt/Co/W/Co/Pt multilayers
Physical Review B 103, 134404 (2021)
- [P4] **K. Szulc**, S. Tacchi, A. Hierro-Rodríguez, J. Díaz, P. Gruszecki, P. Graczyk, C. Quirós, D. Markó, J. I. Martín, M. Vélez, D. S. Schmool, G. Carlotti, M. Krawczyk, L. M. Álvarez-Prado
Reconfigurable magnonic crystals based on imprinted magnetization textures in hard and soft dipolar-coupled bilayers
ACS Nano 16, 14168-14177 (2022)
- [P5] **K. Szulc**, M. Zelent, M. Krawczyk
Reconfigurable spin-wave platform based on interplay between nanodots and waveguide in hybrid magnonic crystal
arXiv:2404.10493 [cond-mat.mes-hall] (2024)

Chapter 1

Introduction to magnetism

Magnetism has a very long history. The existence of the permanent magnets in nature could not be ignored by the curiosity of the human kind. The possibility of two separate objects to interact with each other at a distance had to be seen as something remarkable by the ancient people. The first to take advantage of magnetism were the Chinese, who found that if you carved a piece of lodestone into the shape of a spoon, it would point south. In the 11th century, they found that iron could become a permanent magnet after heating, which was later used to design the first compass. The importance of this device is beyond doubt. The exploration of the Earth would not have been so easy without a compass that could point north day and night in any weather conditions. Since then, magnetic materials have found numerous applications in many fields. The phenomenon of magnetism, which has pronounced effects at the macroscale, has its roots at the nanoscale.¹

1.1 Magnetic states

Magnetism emerges as an intrinsic property of all matter. All the particles from which the atoms are made—protons, neutrons, and electrons—have a property called magnetic moment which is an elementary quantity describing the strength of magnetism of an object. Among them, the electrons have the largest magnetic moment, by many orders of magnitude, making the contribution of protons and neutrons negligible. In fact, crucial for the magnetic effects are the electrons placed in the last orbital according to Hund's rules. As a consequence of the Pauli principle, all electrons in the inner shells must compensate their magnetic moment, resulting in a zero net magnetic moment. In the outer shell, the electrons do not have to compensate and an atom can have a non-zero magnetic moment.

The primary magnetic phenomena in materials are categorized basing on their response to an external magnetic field. The first effect, diamagnetism, is present in all materials. It manifests itself as the repulsion of the magnetic field from the material. This results in a net magnetic moment of the material that is opposite to the external field. This is the weakest magnetic effect

¹This chapter was based on the book *Magnetism and magnetic materials* by J.M.D. Coey [2].

and it is the only one that occurs in the materials with compensated electrons in the atoms or molecules. These materials are called diamagnets or diamagnetic materials.

In the materials where the electrons are unpaired, the effect of the magnetic field is opposite. The magnetic moments of the unpaired electrons try to align with the magnetic field, resulting in a net magnetic moment of the whole material in the direction of the magnetic field. This effect, called paramagnetism, is almost always stronger than diamagnetism. When the external magnetic field disappears, the net magnetic moment disappears with it. The reason for this is the thermal motion. The magnetic moment of the electron is constantly changing direction due to thermal fluctuations, so the material reacts almost instantaneously to any change in the external field. Also, due to thermal energy being much stronger than the magnetic energy, the response of the paramagnetic material is very weak—the magnetic field produced by the net magnetic moment of the material is orders of magnitude smaller than the external field.

There is a class of materials, in which the magnetic forces can be stronger than thermal fluctuations in a certain temperature range. In this case, the magnetic moments of the electrons can be ordered even in the absence of the external magnetic field. We can distinguish 3 fundamental types of ordering, depending on the strength and mutual orientation of the magnetic moments:

- ferromagnetism, where all magnetic moments point in the same direction,
- antiferromagnetism, where the magnetic moments are equal and point in the opposite direction to their neighbors,
- ferrimagnetism, where the magnetic moments are not equal and point in the opposite direction to their neighbors.

This classification is related to the crystalline materials. For the amorphous materials, their counterparts are called asperomagnetism, speromagnetism, and sperimagnetism, respectively, but usually the original names for the crystalline materials are also used in this case.

Due to different characteristics, these materials have different properties. Antiferromagnets have a zero magnetic moment in the absence of the external magnetic field, while ferro- and ferrimagnets have a non-zero magnetic moment (generally much stronger for ferromagnets). Ferrimagnets always consist of different atoms (or at least different ions), because identical atoms always have the same magnetic moment. On the other hand, ferromagnets and antiferromagnets can be made of identical atoms, but does not have to be.

This Thesis will deal with the materials with non-zero net magnetic moment, focusing mainly on ferromagnetic materials.

1.2 Ferromagnetism

The magnetic moment \mathcal{M} is an extensive quantity, i.e., it depends on the volume of the material. It will be useful to derive an intensive quantity based on the magnetic moment. This quantity, the

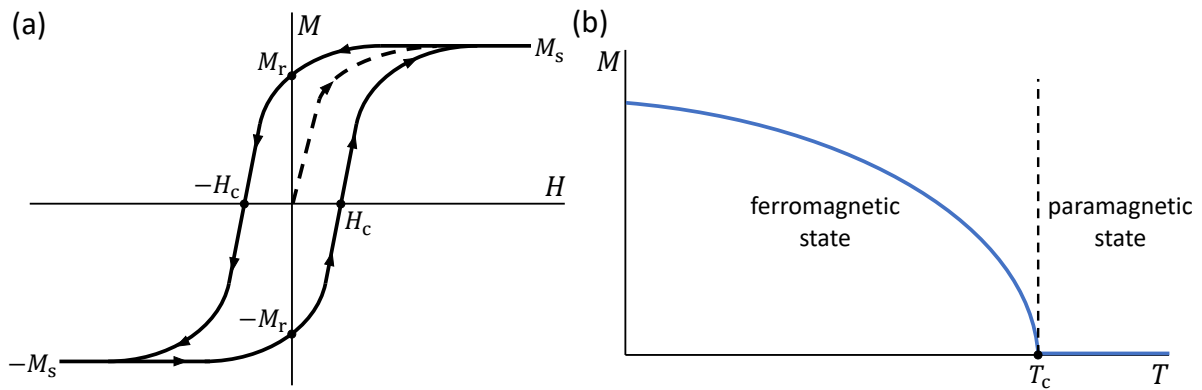


Figure 1.1 The dependence of the magnetization (a) over the external magnetic field in the ferromagnetic material and (b) over the temperature in the absence of the external magnetic field.

magnetization \mathbf{M} , is defined as the time-averaged magnetic moment $\langle \mathcal{M} \rangle$ over a small volume δV

$$\mathbf{M} = \langle \mathcal{M} \rangle / \delta V. \quad (1.1)$$

The unit of the magnetization is A/m, the same as the magnetic H -field.

The presence of the net magnetic moment in the absence of the external magnetic field results in an interesting dependence of the magnetization on the magnetic field, which is shown in Figure 1.1a. Starting from zero field, the magnetic material can have zero magnetic moment. It is because even the magnetic moments are aligned parallel in the short range, the magnetic domains are usually present in the magnetic material. After the magnetic field is applied, the magnetization increases, and for the large magnetic field it will reach the maximum magnetization value for a given material, which is called the *saturation magnetization* M_s . From this point on, the decrease of the magnetic field will cause a slow decrease of the magnetization, usually through the formation of magnetic domains. At the zero magnetic field, the magnetization usually has a non-zero value, which is called the *remanent magnetization* M_r . The magnetic field can then be further reduced to negative values. For a certain value of the magnetic field, called the *coercive field* H_c (or simply the coercivity), the magnetization will reach zero. The coercivity depends mainly on the anisotropy of the magnetic material. If the field is further decreased, the material will reach a negative saturation. When the magnetic field is increased back to large positive values, the magnetization of the material will take another path, which is usually symmetric to the previous path with respect to the center of the coordinate system. Therefore, the information of the magnetic field value will not give the information of the magnetization value – the knowledge of history of the magnetic field evolution is required. This effect is called *hysteresis* and the characteristic plot of magnetization as a function of magnetic field – *hysteresis loop*. Such an effect is not present in paramagnets, where the magnetization is a linear function of the magnetic field.

Based on coercivity, ferromagnetic materials can be divided into two main groups: hard and soft magnets. Hard magnets have a very high coercivity, reaching values as high as 10^7 A/m. On the other hand, soft magnets have very low coercivity, reaching values as low as 10^{-1} A/m. This

division is also the most fundamental division of magnetic materials based on the application. Hard magnets are used as permanent magnets in many devices such as sensors, motors, actuators, etc., as well as in regular fridge magnets. Soft magnets are used as magnetic cores in transformers, microwave devices, and spintronic devices such as sensors [3, 4] and magnetoresistive random access memory (MRAM) [5]. Their properties are also favorable for the computing devices. There is also a group of materials used in magnetic recording devices whose effective anisotropy field is much smaller than the magnetization.

As mentioned above, the ferromagnets are characterized by their magnetic forces being stronger than thermal fluctuations, which results in the magnetic ordering. However, the thermal energy can always overcome the magnetic energy of the material. The magnetization as a function of temperature is shown in Figure 1.1b. The maximum value of the magnetization is at 0 K and with increasing temperature, the magnetization decreases. Above a well-defined critical temperature T_c , the magnetic materials lose the ordering of the magnetic moments and undergo a phase transition, becoming paramagnetic. For ferro- and ferrimagnets, this temperature is called the Curie temperature while for antiferromagnets – the Néel temperature. According to the Ehrenfest classification of the phase transitions, this is a second-order transition – since the magnetization is an order parameter, this means that it gradually decreases to zero when the critical temperature is reached, without any abrupt change in its value. The dependence of the magnetization on the temperature is given by the Bloch law:

$$M_s(T) = M_s(0)(1 - (T/T_c)^{3/2}), \quad (1.2)$$

where $M_s(0)$ is the saturation magnetization at absolute zero. This law gives an approximation of the magnetization changes at temperatures much lower than T_c . Close to the phase transition, this dependence changes to

$$M_s(T) = M_s(0)(1 - (T/T_c)^\alpha)^\beta, \quad (1.3)$$

where α and β are the critical exponents of the phase transition which depends on the material.

In the next Chapter, the intrinsic properties of ferromagnetic materials will be presented. It will be explained which magnetic interaction is responsible for the ferromagnetism, how other magnetic interactions affect the magnetization ordering in the ferromagnetic materials, what is the physics of the spin precession, how it can lead to the collective motion of spin—the spin wave, and what is the current state-of-the-art in spin-wave computing.

Chapter 2

Micromagnetism

The theory of magnetism is based on a quantum phenomenon such as spin, therefore, the dynamics of the magnetization are described by quantum theory. A variety of magnetic interactions makes even small systems exhibit complex behavior, making them very difficult to rigorously describe. However, many effects, even at the nanoscale, can be described classically or approximated using classical theories when the length scales governing the effects are much larger than the distance between the atoms. In this case, the magnetic moments on the atomic lattice can be described as a continuous magnetic medium using the continuum approximation. This approach, called *micromagnetism*, is a very useful tool for solving many problems related to magnetic materials. In this Chapter, the theory of micromagnetism will be explained with the description of the most important problems from the magnetization statics and dynamics.

2.1 Magnetic energy and equation of motion

The total energy of a magnetic system E_{total} is a sum of energies coming from many different interactions:

$$E_{\text{total}} = E_{\text{ex}} + E_{\text{d}} + E_{\text{Z}} + E_{\text{anis}} + E_{\text{DMI}} + (\dots), \quad (2.1)$$

the most fundamental of which are the exchange energy E_{ex} , the dipolar energy E_{d} , and the Zeeman energy E_{Z} . In the studies described in the Thesis, there is also an important contribution of the anisotropy energy E_{anis} , the Dzyaloshinskii–Moriya energy E_{DMI} , and the Ruderman–Kittel–Kasuya–Yosida interaction, which gives the contribution to the boundary conditions in the multilayer systems. The other interactions such as magnetoelastic [6, 7] and electromagnetic [8] coupling, or spin-transfer torque [9, 10] do not contribute to the effects presented in the Thesis and, therefore, are not described here. However, it is worth mentioning their existence as it shows the complexity of the interactions governing the magnetic systems.

From the energy, it is possible to calculate the effective magnetic field \mathbf{H}_{eff} by calculating the functional derivative of the energy over the magnetization:

$$\mathbf{H}_{\text{eff}} = -\frac{1}{\mu_0} \frac{\delta E}{\delta \mathbf{M}}, \quad (2.2)$$

where μ_0 is the vacuum permeability. As will be shown later, the use of \mathbf{H}_{eff} is advantageous for describing the motion of the magnetic moment.

2.1.1 Exchange interaction

The exchange interaction is a strong short-range interaction responsible for ordering the magnetic moments of neighboring atoms in the lattice, giving rise to ferromagnetism, as described in Chapter 1. It has its source in the interplay between the Pauli exclusion principle and the Coulomb repulsion of electrons. If the spins are antiparallel, the electrons can occupy the same orbital. This is not the case for the parallel spins, since it is forbidden by the Pauli principle, and, as a result, the Coulomb force between the electrons is reduced. therefore, these two configurations have different energies [11].

In the semi-quantum representation, where the spin is treated in the classical way as a vector, the energy of the exchange interaction is represented by the following Hamiltonian:

$$\hat{\mathcal{H}}_{\text{ex}} = -2 \sum_{i,j} J_{ij} \mathbf{S}_i \cdot \mathbf{S}_j, \quad (2.3)$$

where the $\mathbf{S}_{i(j)}$ represents the i th (j th) magnetic moment and J_{ij} is the exchange interaction strength between the i th and j th magnetic moment. This interaction decreases very fast with the distance, therefore, it is sufficient in most cases to take into account only the nearest neighbors (n.n.) to the calculation of the energy. Moreover, in the crystal structure, the interaction between the nearest neighbors often has the same strength, e.g., in the cubic crystals, so we can assume that the exchange constant does not depend on the electron index, $J_{ij} = J$. After these assumptions, the Hamiltonian can be written as

$$\hat{\mathcal{H}}_{\text{ex}} = -2J \mathbf{S}_i \cdot \sum_{j=n.n.} \mathbf{S}_j. \quad (2.4)$$

The sign of the exchange constant J determines the type of ordering. For a positive value of the constant, the magnetic moments are parallel to each other and the material is ferromagnetic. For a negative value, the magnetic moments are aligned antiparallel to each other and the material is antiferromagnetic or ferrimagnetic.

In the continuum approximation, the Hamiltonian is changed to the form of energy. Assuming the arbitrary magnetization configuration, after expanding the Hamiltonian into the Taylor series and truncating it after the first position-dependent term, the final form of the exchange energy

E_{ex} in the continuum approximation is

$$E_{\text{ex}} = \frac{A_{\text{ex}}}{M_s^2} \int_V (\nabla \mathbf{M})^2 d^3r, \quad (2.5)$$

where $A_{\text{ex}} = M_s JSZa^2/6g\mu_B$ ¹ is the exchange constant [12], S is the spin quantum number, Z is the number of nearest neighbors, a is the distance between the nearest neighbors, g is the g -factor, and μ_B is the Bohr magneton. Finally, from the energy it is possible to derive the exchange field using Eq. 2.2

$$\mathbf{H}_{\text{ex}} = \frac{2A_{\text{ex}}}{\mu_0 M_s^2} \nabla^2 \mathbf{M}. \quad (2.6)$$

It is useful to define a characteristic distance associated with the exchange interaction, called the *exchange length* l_{ex} , which is defined as [13]

$$l_{\text{ex}} = \sqrt{\frac{2A_{\text{ex}}}{\mu_0 M_s^2}}. \quad (2.7)$$

For the monoatomic magnetic materials, its value is in the range of several nanometers, but in ferrimagnetic garnets it can reach values as high as 82 nm [14].

2.1.2 Dipolar interaction

The dipolar interaction results from the interaction of a magnetic moment with the magnetic field produced by other magnetic moment(s). The dipolar field \mathbf{H}_d generated by a magnetic moment is

$$\mathbf{H}_d = -\frac{1}{4\pi} \left(\frac{\mathcal{M}}{|\mathbf{r}|^3} - \frac{(\mathcal{M} \cdot \mathbf{r})\mathbf{r}}{|\mathbf{r}|^5} \right). \quad (2.8)$$

If we consider the interaction between two magnetic moments, the dipolar energy of their interaction can be calculated as $E_d = -\mu_0 \mathbf{H}_{d,1} \cdot \mathcal{M}_2 = -\mu_0 \mathbf{H}_{d,2} \cdot \mathcal{M}_1$. After substituting Eq. 2.8 into this formula, we get the dipolar energy of two interacting dipoles

$$E_d = \frac{\mu_0}{4\pi} \left(\frac{\mathcal{M}_1 \cdot \mathcal{M}_2}{|\mathbf{r}|^3} - \frac{3(\mathcal{M}_1 \cdot \mathbf{r})(\mathcal{M}_2 \cdot \mathbf{r})}{|\mathbf{r}|^5} \right). \quad (2.9)$$

In contrast to the exchange interaction, the dipolar interaction is weaker, but the field goes as the inverse cube of the distance, making it to work over long distances. The change of the direction of a single magnetic moment will significantly affect not only the nearest neighbors but also distant magnetic moments, making this interaction highly non-local and complicating the calculation of the total field distribution, which requires the summation of the contribution of all magnetic moments everywhere.

¹This formula is true only for cubic crystals.

In the continuum approximation, this field can be calculated from the Maxwell's equations. Assuming the magnetostatic approximation (the absence of free currents and time-dependent electric fields), the Maxwell's equations take the form

$$\nabla \cdot \mathbf{B} = 0, \quad (2.10)$$

$$\nabla \times \mathbf{H} = 0. \quad (2.11)$$

Knowing that for any arbitrary scalar function f , $\nabla \times \nabla f = 0$, it is possible to define the magnetic scalar potential φ from Eq. 2.11 as $\mathbf{H} = -\nabla\varphi$. Further, knowing that $\mathbf{B} = \mu_0(\mathbf{H} + \mathbf{M}) = \mu_0(-\nabla\varphi + \mathbf{M})$, we get from Eq. 2.10 the equation for the magnetic scalar potential

$$\nabla^2 \varphi = \nabla \cdot \mathbf{M}. \quad (2.12)$$

The right side of Eq. 2.12, $\nabla \cdot \mathbf{M} = -\rho_v$ gives the volume magnetic charge density. From the boundary condition $\mathbf{M} \cdot \mathbf{n} = \rho_s$, we get the surface magnetic charge density. Finally, the magnetic scalar potential can be calculated as [13]

$$\varphi(\mathbf{r}) = \frac{1}{4\pi} \left(\int_V \frac{\rho_v(\mathbf{r}')}{|\mathbf{r} - \mathbf{r}'|} d^3 r' + \oint_S \frac{\rho_s(\mathbf{r}')}{|\mathbf{r} - \mathbf{r}'|} d^2 r' \right), \quad (2.13)$$

where V is the volume of the magnetic material and S is the surface of the magnetic material. The dipolar field \mathbf{H}_d can then be calculated directly from $-\nabla\varphi$.

The dipolar energy in a continuum approximation can be calculated in two ways—if the dipolar field is known in all space, or if the dipolar field and magnetization are known in the magnetic material:

$$E_d = -\frac{\mu_0}{2} \int_V \mathbf{M} \cdot \mathbf{H}_d d^3 r = \frac{\mu_0}{2} \int_{V_{\text{all space}}} \mathbf{H}_d^2 d^3 r. \quad (2.14)$$

For ellipsoids, in which the magnetization is uniform, it is useful to calculate the dipolar field using the approach of demagnetizing tensor $\hat{\mathbf{N}}$ [13]

$$\mathbf{H}_d = -\hat{\mathbf{N}} \cdot \mathbf{M}, \quad (2.15)$$

where

$$N_{xx} = \frac{1}{2} abc \int_0^\infty \left[(a^2 + \eta) \sqrt{(a^2 + \eta)(b^2 + \eta)(c^2 + \eta)} \right]^{-1} d\eta, \quad (2.16)$$

and a, b, c are the dimensions of the ellipsoid in the x -, y -, and z -direction, respectively. Analogous formulas exist for N_{yy} and N_{zz} . In general, the demagnetizing tensor has a form of a symmetric matrix with the property $\text{Tr}(\hat{\mathbf{N}}) = 1$ [15, 16]. Only for ellipsoids, only the diagonal components have a non-zero value and are position-independent. The following list shows the diagonal components of the demagnetizing tensor for the simple geometries:

- infinite film with thickness along z -axis

$$N_{xx} = N_{yy} = 0, N_{zz} = 1,$$

- infinitely long round cylinder along z -axis

$$N_{xx} = N_{yy} = 1/2, N_{zz} = 0,$$

- finite sphere

$$N_{xx} = N_{yy} = N_{zz} = 1/3.$$

Note that these values can be calculated from Eq. 2.16—the infinite film is a limiting case of an ellipsoid with $a, b \rightarrow \infty$ and the infinitely long cylinder for an ellipsoid with $c \rightarrow \infty$.

2.1.3 Zeeman interaction

The Zeeman interaction represents the interaction of the magnetic system with the external magnetic field. The Zeeman energy is simply represented by a scalar product of magnetization and external magnetic field:

$$E_Z = -\mu_0 \int_V \mathbf{H}_0 \cdot \mathbf{M} d^3r. \quad (2.17)$$

The external magnetic field \mathbf{H}_0 contributes directly to the effective magnetic field.

2.1.4 Anisotropy

The anisotropic character of the magnetic field can be found already in the dipolar interaction which was described in Section 2.1.2. Not without reason the effect connected to the inhomogeneity of the dipolar field inside the magnetic material due to its shape is called the shape anisotropy. However, there are other sources of the anisotropy of magnetic materials. The most fundamental is related to the crystal lattice and comes from the fact that the orbitals of the electrons in the crystal may not be spherically symmetric. Other anisotropies can be induced by lattice defects, strains, or at the surfaces or interfaces [13]. Two fundamental types of anisotropy are uniaxial and cubic anisotropy.

Uniaxial anisotropy

The anisotropy of uniaxial character is present in the hexagonal, tetragonal, and orthorhombic crystals. Moreover, the uniaxial anisotropy can usually describe the contribution of surface and interface anisotropies [17]. The energy density for the uniaxial anisotropy can be written as

$$\begin{aligned} W_{\text{anis}} &= K_{u1} \sin^2 \theta + K_{u2} \sin^4 \theta + \dots \\ &= \frac{K_{u1}}{M_s^2} (1 - (\mathbf{u} \cdot \mathbf{M})^2) + \frac{K_{u2}}{M_s^4} (1 - (\mathbf{u} \cdot \mathbf{M})^4) + \dots \end{aligned} \quad (2.18)$$

where K_{u1} and K_{u2} are the first- and second-order uniaxial anisotropy constants and θ is the angle between the magnetization and the anisotropy vector \mathbf{u} which has length of 1 ($|\mathbf{u}|^2 = 1$). For the surface and interface anisotropies, only the first term with K_{u1} should be taken into account [13]. In the case where only the first-order anisotropy constant is considered, it is usually simply

referred to as K_u . Since the uniaxial anisotropy is uniform throughout the magnetic material, the energy can be calculated by simply multiplying the energy density by the volume $E_{\text{anis}} = W_{\text{anis}}V$.

From the energy and Eq. 2.2, the uniaxial anisotropy field can be derived as

$$\mathbf{H}_{\text{anis}} = \frac{2K_{u1}}{\mu_0 M_s^2} (\mathbf{u} \cdot \mathbf{M}) \mathbf{u} + \frac{4K_{u2}}{\mu_0 M_s^4} (\mathbf{u} \cdot \mathbf{M})^3 \mathbf{u}. \quad (2.19)$$

There is an important parameter related to the uniaxial perpendicular magnetic anisotropy in thin films and it is called the *quality factor* Q . It is defined as the ratio of the intrinsic anisotropy energy and the shape anisotropy energy

$$Q = \frac{E_{\text{anis}}}{E_d} = \frac{2K_u}{\mu_0 M_s^2}, \quad (2.20)$$

where E_d is calculated by applying Eq. 2.15 for a thin film to Eq. 2.14. For the value $Q < 1$, the thin film has an in-plane easy axis, while for the value $Q > 1$, the easy axis is in the out-of-plane direction. The situation where $Q = 1$ describes the situation where the dipolar and anisotropy energies are equal and there is no highlighted axis in the system.

Cubic anisotropy

In the cubic crystals, the anisotropy has a more complex form. The energy density can be written as

$$W_{\text{anis}} = \frac{K_{c1}}{M_s^4} (M_i^2 M_j^2 + M_j^2 M_k^2 + M_k^2 M_i^2) + \frac{K_{c2}}{M_s^6} M_i^2 M_j^2 M_k^2 + \dots \quad (2.21)$$

where K_{c1} and K_{c2} are the first- and second-order cubic anisotropy constants and i, j, k mark the anisotropy easy axes. The cubic anisotropy field for the first term with K_{c1} can be written as

$$\mathbf{H}_{\text{anis}} = -\frac{K_{c1}}{\mu_0 M_s^4} \frac{\partial}{\partial \mathbf{M}} (M_i^2 M_j^2 + M_j^2 M_k^2 + M_k^2 M_i^2). \quad (2.22)$$

2.1.5 Dzyaloshinskii–Moriya interaction

In 1958, Igor Dzyaloshinskii proved that the weak "ferromagnetism" in the antiferromagnetic oxides is caused by the relativistic spin–lattice and magnetic dipole interactions [18]. Two years later, Toru Moriya showed that this effect is a result of the exchange interaction of antisymmetric character [19], later called the Dzyaloshinskii–Moriya interaction (DMI). The Hamiltonian of the DMI has the form

$$\hat{\mathcal{H}}_{\text{DMI}} = \sum_{i,j} \mathbf{D}_{ij} \cdot (\mathbf{S}_i \times \mathbf{S}_j), \quad (2.23)$$

where \mathbf{D}_{ij} is the Dzyaloshinskii vector. This form is similar to the Hamiltonian of the ordinary exchange interaction shown in Eq. 2.3 with the scalar product being replaced with the vector product of magnetic moments. From the analysis of Eq. 2.23, the lowest energy configuration is the one in which the spins are perpendicular to each other. It is important to notice that

this form favors certain chirality of spins. The DMI in bulk materials can be present in non-centrosymmetric B20 crystals [20, 21], but it was found to be much weaker than the ordinary exchange.

In 1990, Albert Fert suggested that the DMI can also be induced by asymmetry of the spin-orbit coupling at the interface [22], which was later proven theoretically by Crepieux and Lacroix [23]. The first evidence of the interfacial DMI has emerged when the spin spiral with very short period has been found in Fe/W multilayer [24]. The interfacial DMI can be stronger than its bulk counterpart, being the strongest in the ferromagnetic layers of thickness of about 1 nm (a few monolayers). The studies in this Thesis are focusing on the interfacial DMI and it will be described in the following part.

In the continuum approximation, the Dzyaloshinskii vector \mathbf{D}_{ij} can be simplified to the DMI constant D , assuming that the DMI is isotropic over the entire interface. If the normal to the interface $\mathbf{n} \parallel \hat{z}$, the interfacial DMI energy density takes the form [25]

$$W_{\text{DMI}} = \frac{D}{M_s^2} [M_z(\nabla \cdot \mathbf{M}) - (\mathbf{M} \cdot \nabla)M_z]. \quad (2.24)$$

From Eqs. 2.2 and 2.24, it is possible to derive DMI field

$$\mathbf{H}_{\text{DMI}} = \frac{2D}{\mu_0 M_s^2} \left[\frac{\partial M_z}{\partial x} \hat{\mathbf{x}} + \frac{\partial M_z}{\partial y} \hat{\mathbf{y}} - \left(\frac{\partial M_x}{\partial x} + \frac{\partial M_y}{\partial y} \right) \hat{\mathbf{z}} \right]. \quad (2.25)$$

2.1.6 Landau–Lifshitz–Gilbert equation

The magnetic moment is in the stable configuration when it is aligned parallel to the magnetic field ($\mathcal{M} \parallel \mathbf{B}$). If the magnetic moment (or the magnetic field) changes direction, as a result, the torque

$$\mathbf{T} = \mathcal{M} \times \mathbf{B} \quad (2.26)$$

will appear. The torque $\mathbf{T} = d\mathbf{J}/dt$ describes the time evolution of the total angular momentum $\mathbf{J} = \mathbf{L} + \mathbf{S}$ (where \mathbf{L} is the orbital angular momentum), which is connected to the magnetic moment by the constant called the gyromagnetic ratio γ , so that $\mathcal{M} = -\gamma\mathbf{J}$. The gyromagnetic ratio also connects the frequency of the magnetic moment precession with the magnetic field, $\omega = -\gamma B$, which is called the Larmor frequency. For the free electrons where $\mathbf{L} = 0$, its value can be calculated as $\gamma = \frac{q_e}{2m_e} g_e \approx 28.025 \text{ GHz/T}$, where q_e is the electron charge, m_e is the electron mass, and $g_e \approx 2$ is the electron g -factor. In most of the ferromagnetic materials, the gyromagnetic ratio is slightly larger due to the contribution from the orbital angular momentum \mathbf{L} . For example, for Co the effective g -factor is $g = 2.22$ [12].

Putting all the dependencies in Eq. 2.26, we get

$$\frac{\partial \mathcal{M}}{\partial t} = -\gamma \mathcal{M} \times \mathbf{B}. \quad (2.27)$$

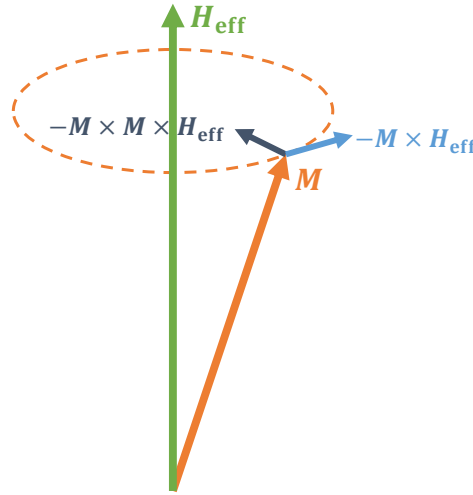


Figure 2.1 The schematic of the spin precession. The magnetization \mathbf{M} is evolving around the effective magnetic field \mathbf{H}_{eff} due to the precession torque $\mathbf{T} = -\mathbf{M} \times \mathbf{H}_{\text{eff}}$, but it is also constantly approaching \mathbf{H}_{eff} due to the damping torque $\mathbf{T}_d = -\mathbf{M} \times \mathbf{M} \times \mathbf{H}_{\text{eff}}$.

In terms of the magnetization and effective magnetic field, Eq. 2.27 takes the form

$$\frac{\partial \mathbf{M}}{\partial t} = -\gamma \mu_0 \mathbf{M} \times \mathbf{H}_{\text{eff}}. \quad (2.28)$$

This equation is known as the *Landau–Lifshitz equation*. In this form, the equation has no dissipative mechanism. Once the non-zero angle between the magnetization and the magnetic field is present, it is conserved, but the magnetization will constantly precess around the magnetic field vector in the direction given by the vector product. However, losses are always present in the magnetic systems and they cause the magnetization to slowly align with the effective magnetic field direction. Dissipation occurs by several mechanisms. These include spin–spin relaxation, in which the magnon is exchanged for another magnon by interaction with the crystal lattice or defects, and the generation of phonons, which ultimately leads to dissipation as heat. Landau and Lifshitz have taken losses into account by adding a phenomenological damping torque to Eq. 2.28 [26]

$$\frac{\partial \mathbf{M}}{\partial t} = -\gamma_L \mu_0 \mathbf{M} \times \mathbf{H}_{\text{eff}} + \frac{\gamma_L \mu_0}{M_s^2} \lambda \mathbf{M} \times \mathbf{M} \times \mathbf{H}_{\text{eff}}, \quad (2.29)$$

where λ is the Landau–Lifshitz damping constant. The magnetization precession is shown schematically in Figure 2.1. While the precession torque $-\mathbf{M} \times \mathbf{H}_{\text{eff}}$ forces the magnetization to revolve around the effective magnetic field \mathbf{H}_{eff} , the damping torque $-\mathbf{M} \times \mathbf{M} \times \mathbf{H}_{\text{eff}}$ pushes it towards \mathbf{H}_{eff} , causing the spin to asymptotically reach the equilibrium state for which $\mathbf{T} = 0$.

In 1956, Thomas L. Gilbert modified the damping term to include a time derivative of the magnetization [27]. This form is called the *Landau–Lifshitz–Gilbert equation*:

$$\frac{\partial \mathbf{M}}{\partial t} = -\gamma_G \mu_0 \mathbf{M} \times \mathbf{H}_{\text{eff}} + \frac{\alpha}{M_s} \mathbf{M} \times \frac{\partial \mathbf{M}}{\partial t}, \quad (2.30)$$

where α is a dimensionless damping constant. These equations are connected by the relations $\gamma_L = \frac{\gamma_G}{1+\alpha^2}$ and $\lambda = \frac{\alpha M_s}{1+\alpha^2}$.

Both equations are equivalent and the choice of the formulation depends on the user. In all the calculations presented in this Thesis where damping was taken into account, the Landau–Lifshitz–Gilbert equation (Eq. 2.30) was chosen.

2.1.7 Boundary conditions

The presence of the second space derivative in the exchange field in Eq. 2.6 requires the definition of a boundary condition for Eq. 2.30 for bounded systems as, e.g., thin films. The boundary condition can be derived from the Landau–Lifshitz equation by applying the Green’s theorem [28].

The most commonly used condition is the *free boundary condition* [29], which states

$$\frac{\partial \mathbf{M}}{\partial n} = 0, \quad (2.31)$$

where n is the direction normal to the boundary. This condition is true if there are no surface or interface anisotropies in the system.

The general boundary condition, which takes into account the possible presence of the surface or interface anisotropy at the boundary, was first derived by Rado and Weertman [28] and it says

$$\frac{2A_{\text{ex}}}{M_s^2} \mathbf{M} \times \frac{\partial \mathbf{M}}{\partial n} + \mathbf{T}_{\text{surf}} = 0, \quad (2.32)$$

where \mathbf{T}_{surf} is the total surface torque density.

2.1.8 Ruderman–Kittel–Kasuya–Yosida interaction

In the 1960s it was found that the ferromagnetic films are coupled when in contact [30, 31]. It was shown that this coupling is of exchange character [32]. Hoffmann *et al.* proposed the theoretical model to describe the interlayer exchange coupling between the ferromagnetic layers in contact [33, 34]. In the 1980s it was shown that such a coupling of the exchange character can also exist when the layers are separated by a thin non-magnetic metallic layer [35, 36]. Later, it was proposed that this coupling has the character of the Ruderman–Kittel–Kasuya–Yosida (RKKY) interaction [37, 38], which originally explained the broadening of the nuclear spin resonance lines by the indirect exchange coupling of the magnetic moments of the nuclei through conduction electrons [39–41]. Eventually, the theoretical formulation given by Hoffmann was also used to

describe the interlayer exchange coupling of the separated layers in a micromagnetic approach [42]. The RKKY interaction is implemented by extending the general boundary conditions to include the interlayer exchange constant A_{12} [42]

$$\frac{2A_{\text{ex}}^{(1)}}{(M_s^{(1)})^2} \mathbf{M}^{(1)} \times \frac{\partial \mathbf{M}^{(1)}}{\partial n^{(1)}} + \mathbf{T}_{\text{surf}}^{(1)} \Big|_{z=z_1} + \frac{2A_{12}}{M_s^{(1)} M_s^{(2)}} \mathbf{M}^{(1)} \times \mathbf{M}^{(2)} \Big|_{z=z_2} = 0, \quad (2.33)$$

$$\frac{2A_{\text{ex}}^{(2)}}{(M_s^{(2)})^2} \mathbf{M}^{(2)} \times \frac{\partial \mathbf{M}^{(2)}}{\partial n^{(2)}} + \mathbf{T}_{\text{surf}}^{(2)} \Big|_{z=z_2} + \frac{2A_{12}}{M_s^{(1)} M_s^{(2)}} \mathbf{M}^{(2)} \times \mathbf{M}^{(1)} \Big|_{z=z_1} = 0, \quad (2.34)$$

where (1) and (2) indicate the parameter of the first and second layer, respectively, and z_1 and z_2 are the interface positions of the first and second layer from the side of the second and first layer, respectively.

2.2 Magnetization textures

In the magnetic materials, different interactions compete with each other, wanting to force the magnetization to reach different equilibrium states. The exchange interaction wants the magnetic moments to align parallel or antiparallel to their neighbors. The Dzyaloshinskii–Moriya interaction prefers perpendicular alignment. The Zeeman and uniaxial anisotropy try to force the magnetic moments to align in the direction of their magnetic fields. Last but not least, there is dipolar interaction with its long-range, highly anisotropic character and susceptibility to the shape of the object. The mixture of these components leads to the equilibrium states with complex magnetization configurations. Here I would like to put special emphasis on two systems considered in the papers included in the Thesis—a regular stripe-domain pattern [P4] and a skyrmion [P5]. Before that, it is worth describing two fundamental elements of the magnetization textures: the domain and the domain wall.

2.2.1 Magnetic domain and domain wall

A *magnetic domain* is a uniformly magnetized region in a ferromagnetic material, which borders with other domains of different orientation of magnetization. Domains are separated from each other by a non-uniform magnetization textures called *domain walls*.

The whole gamut of magnetic domain types can exist in the magnetic objects. They can differ depending on the material characteristics with particular reference to the type of anisotropy, the anisotropy strength defined by the quality factor Q , and the shape and size of the object. However, the classification of the magnetic domain structures is beyond the scope of this Thesis. It is splendidly described with the support of great pictures in Chapter 5 of the book *Magnetic domains* by Alex Hubert and Rudolf Schäfer [13].

The domains exist due to the competition between anisotropy, dipolar, and exchange interactions. It is easy to understand the presence of magnetic domains for an example of a thin

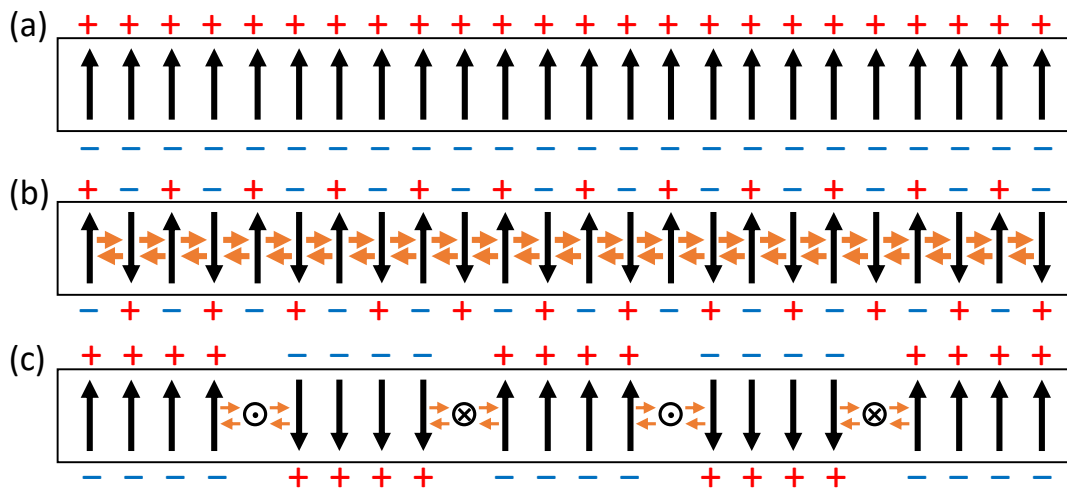


Figure 2.2 Thin magnetic film with out-of-plane anisotropy in (a) the uniformly out-of-plane magnetized state, (b) the antiparallel state, and (c) the domain state. Black arrows denote the magnetic moments, red pluses and blue minuses – the positive and negative magnetic charges, and orange arrows – the exchange interaction.

film with strong uniaxial out-of-plane anisotropy, as shown in Fig. 2.2. If the film is saturated out of plane (Fig. 2.2a), the magnetic moments will produce inside the film a strong dipolar field opposite to direction of the magnetic moments, or in other words, the magnetic charges of opposite polarity will gather on opposite film surfaces, creating a high-energy state. On the other hand, if the magnetic moments are aligned antiparallel to their nearest neighbors (Fig. 2.2b), the dipolar energy is minimized, but the exchange energy is maximized. Since the exchange interaction works only in a short range and the dipolar interaction works in a long range, the minimum energy state contains domains separated by domain walls (Fig. 2.2c).

Two fundamental types of domain walls can be distinguished, as shown in Fig. 2.3. In the Bloch domain wall (Fig. 2.3a), the magnetic moments rotate in a plane perpendicular to the plane on which the magnetic moments are lying. In the Néel domain wall (Fig. 2.3b), the rotation is in the same plane as the one produced by the rotating magnetic moments. Bloch domain walls are usually present in bulk materials and thick films while Néel domain walls – in very thin films with thickness less than the exchange length l_{ex} [11]. It is worth noting that the systems with DMI also favor the Néel domain wall, however, DMI prefers a certain domain wall chirality, while in the systems without DMI both chiralities have the same energy.

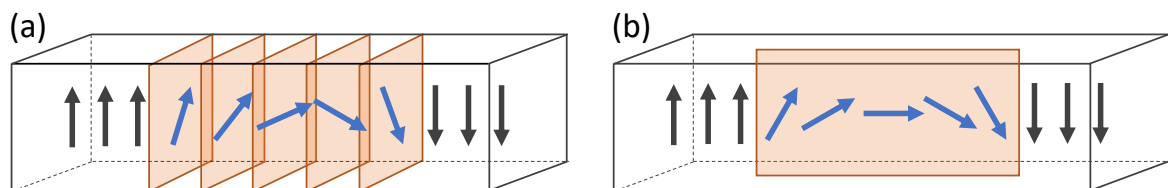


Figure 2.3 The schematic representation of (a) the Bloch domain wall and (b) the Néel domain wall. Orange rectangles denote the planes in which the magnetic moments rotate.

The domain wall width is mainly determined by the competition between the exchange interaction and anisotropy. The domain wall consisting of two antiparallel magnetic moments minimizes the anisotropy energy while the exchange energy is maximal. On the other hand, a very wide domain wall is beneficial for exchange but not for anisotropy. The minimum of the sum of exchange and anisotropy energies is given for the domain wall described by the equation $x = \sqrt{A_{\text{ex}}/K_{\text{u}}} \ln \tan(\theta/2)$ where θ is the angle of magnetization. This formula gives the approximate width of the domain wall $\Delta = \pi \sqrt{A_{\text{ex}}/K_{\text{u}}}$ [2].

2.2.2 Regular stripe-domain pattern

Stripe domains are a type of magnetic domains that occur in thin films in the form of long, narrow channels which can be magnetized in an arbitrary direction depending on the external field and the character of a magnetic material. They were first predicted theoretically [43, 44], and soon later observed experimentally [45–47]. Stripe domains usually form a well-ordered texture of parallel domains. However, these textures are often far from regular patterns because the domains can have different widths and the density of defects is high.

It was found that the thin films with quality factor $Q \ll 1$ can retain stripe-domain textures of high regularity [48–56]. Such a stripe-domain pattern is shown in Figure 1(b) in [P4] (Section 4.4). The critical parameters for the stripe-domain pattern [57] are the critical film thickness

$$d_{\text{c}} = \frac{2\pi}{1-h} \sqrt{\frac{A_{\text{ex}}}{K_{\text{u}}}} \quad (2.35)$$

and the critical stripe-domain width

$$w_{\text{c}} = d_{\text{c}} \sqrt{\frac{1-h}{1+h}}, \quad (2.36)$$

where $h = H_0 \mu_0 M_{\text{s}} / 2K_{\text{u}}$. These values give a good approximation in the limit $Q < 0.1$. The critical thickness d_{c} gives the minimum value of the thickness for which the film can hold stripe domains. The critical width w_{c} is the width of a single stripe domain at a critical thickness. For $h = 0$, these parameters simplify to $d_{\text{c}} = 2\pi \sqrt{A_{\text{ex}}/K_{\text{u}}}$ and $w_{\text{c}} = d_{\text{c}}$. For the films thicker than d_{c} , the stripe-domain width becomes smaller than w_{c} . On the other hand, for $Q > 0.1$, the stripe-domain width increases with the increase of Q .

2.2.3 Skyrmion

Skyrmion is a topologically protected field configuration, which was first described in particle theory by Tony Skyrme [58], who used it as a model of nucleon. It was later implemented in many fields of physics including magnetism.

The magnetic skyrmion represents the configuration of the magnetization field [59]. It is a topological soliton having a form of a very small domain, usually stabilized by the DMI (in

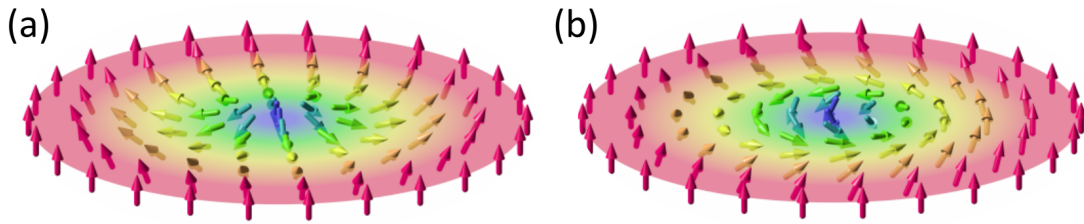


Figure 2.4 The schematic representation of (a) the Néel-type skyrmion with $Q_c = -1$, $Q_h = 1$, and $Q_v = 0$ and (b) the Bloch-type skyrmion with $Q_c = -1$, $Q_h = 1$, and $Q_v = \pi/2$. Licensed under CC BY-SA 3.0. Authors: Karin Everschor-Sitte and Matthias Sitte. Original figure was rearranged.

contrast to the so-called bubble domains, which are large and stabilized by dipolar interactions). The topological protection of the skyrmion is important for its stability. The creation or annihilation of a skyrmion requires passing through a Bloch point, where the neighboring spins are antiparallel, which is connected with a very large exchange energy [60]. It is worth noting that such a transition is possible thanks to the discrete nature of matter—in the continuous model, the creation/annihilation of a Bloch point requires infinite energy and is therefore not possible.

Magnetic skyrmions were first proposed by Pokrovsky [61]. Later, the possibility of their stabilization in systems with DMI was confirmed in the works of Bogdanov *et al.* [62–65]. The presence of the DMI is very important as, due to the competition with symmetric exchange interaction, the spin rotation becomes beneficial for the energy minimization. Skyrmions can be stabilized with bulk DMI in B20 crystals, where they can form skyrmion lattices at very low temperatures [66–68] or with interfacial DMI, where they can exist even at the room temperature [69–72]. It has also been shown that in the confined geometries, such as nanodisk, it is possible to create a skyrmion without DMI [73].

Two types of 2D skyrmions can be distinguished: the Néel-type skyrmion (Figure 2.4a) and the Bloch-type skyrmion (Figure 2.4b). The connection of their names with domain walls is not accidental—if a cross-section of the skyrmion is taken along its radius, that of the Néel-type skyrmion has a Néel domain wall, and the one of the Bloch-type skyrmion—a Bloch domain wall. The formation of Néel-type skyrmion is preferred in the systems with interfacial DMI, while Bloch-type skyrmion is preferred in the systems with bulk DMI and confined systems without DMI. Skyrmions are just one element of a class of topological solitons, which includes other magnetic textures such as vortex, meron, antiskyrmion, biskyrmion, skyrmionium, chiral bobber [74, 75], and hopfion [76].

There are three characteristic values which describe two-dimensional topological solitons—topological charge, vorticity, and helicity [75]. The first one, the topological charge, is defined as

$$Q_c = \frac{1}{4\pi|\mathbf{M}|^3} \int \mathbf{M} \cdot \left(\frac{\partial \mathbf{M}}{\partial x} \times \frac{\partial \mathbf{M}}{\partial y} \right) dx dy. \quad (2.37)$$

Skyrmions have a topological charge $Q_c = \pm 1$. The positive or negative value depends on the polarity p , which defines the direction of the core: $p = 1$ if the core has spins pointing up and $p = -1$ for spins pointing down (as in Figure 2.4). For skyrmions, $Q_c = p$. Other systems

can also be described with a topological charge, e.g., antiskyrmion has $Q_c = \pm 1$, vortex and meron— $Q_c = \pm 1/2$, skyrmionium— $Q_c = 0$, biskyrmion— $Q_c = \pm 2$, and also non-topological textures such as single-domain state and onion state which has $Q_c = 0$. In contrast to skyrmions, for antiskyrmions the connection between topological charge and polarity yields $Q_c = -p$.

Another parameter, vorticity, describes the in-plane spin texture and is defined as

$$Q_v = \frac{1}{2\pi} \oint_C d\phi, \quad (2.38)$$

where ϕ is the in-plane angle of the magnetization and the integration goes over the contour C determined by the line of in-plane spins. This is another parameter that separates skyrmions (for which $Q_v = 1$) from antiskyrmions ($Q_v = -1$).

The last parameter, helicity Q_h , defines the phase of the magnetic texture. This parameter is different for Néel-type skyrmion ($Q_h = 0$ or π) and Bloch-type skyrmion ($Q_h = \pi/2$ or $3\pi/2$).

2.3 Spin waves

When the magnetic moment is pushed out of the equilibrium, it will begin to precess around the effective magnetic field. However, this will also cause a change in the magnetic field, which will push other spins further out of equilibrium. This disturbance can form a collective excitation of spins propagating through the magnetic material, which is called a *spin wave*. The spin-wave dynamics is governed by the Landau–Lifshitz–Gilbert equation (Eq. 2.30). In many cases, the angle of the precession of magnetic moments is very small, so that assuming the magnetization along the z -direction, $M_x, M_y \ll M_z \approx M_s$. In such a case, Eq. 2.30 can be linearized and solved only for M_x and M_y , which reduces the problem significantly. Due to anisotropic character of the dipolar interaction and its competition with exchange interaction and other phenomena, the spin-wave dynamics show much more complicated dispersion relation than electromagnetic waves, which are usually described by a linear dependence of the frequency on the wavevector. In this Section, the dispersion relations of spin waves for different systems and geometries are presented.

2.3.1 Magnetostatic waves

In the first approximation, it is sufficient to limit the interactions to dipolar and Zeeman interactions only. In this case, the total energy from Eq. 2.1 simplifies to the form $E_{\text{total}} = E_Z + E_d$. For the case where the exchange interaction is neglected, the spin waves are usually called *magnetostatic waves*. This approximation gives realistic results for long waves, much longer than the exchange length, $\lambda \gg l_{\text{ex}}$.

Bulk magnetic material

In the bulk ferromagnetic materials, where the dimensions are much larger than the wavelength of the magnetostatic wave, the dispersion relation is represented as [77]

$$f = \frac{\gamma\mu_0}{2\pi} \sqrt{H_0 (H_0 + M_s \sin^2 \theta_k)}, \quad (2.39)$$

where θ_k is the angle between the magnetization and wavevector. As you can see, the frequency depends only on the direction of propagation, but not on the wavevector itself. The frequency is the highest for the propagation perpendicular to the magnetization and the lowest for the parallel propagation.

The situation changes in thin films, where the dispersion relation becomes dependent on the wavevector. This is due to the presence of the surface and volume magnetic charges coming from the dynamic magnetic field. We can distinguish three main geometries of the magnetostatic waves in the uniformly magnetized thin film.

In-plane magnetized thin film: propagation parallel to magnetization

For the case when the film is magnetized in the plane and we consider the propagation in the direction parallel to the magnetization, the dispersion relation can be written as [78]

$$f = \frac{\gamma\mu_0}{2\pi} \sqrt{H_0 \left(H_0 + M_s \frac{1 - e^{-kd}}{kd} \right)}. \quad (2.40)$$

It is shown with the blue lines in Figure 2.5. The frequency in the limit of zero wavevector goes to the ferromagnetic resonance (FMR) frequency $f_{k \rightarrow 0} = f_{\text{FMR}} = \frac{\gamma\mu_0}{2\pi} \sqrt{H_0 (H_0 + M_s)}$, while in the limit of infinite wavevector, $f_{k \rightarrow \infty} = f_0 = \frac{\gamma\mu_0}{2\pi} H_0$. The frequency decreases with the increase of the wavevector, which means that while the phase velocity $v_{\text{ph}} = \omega/k$ is positive, the group velocity $v_{\text{gr}} = d\omega/dk$ is negative. These dependencies give the wave a backward character, as the phase is propagating in the opposite direction to the wavefront. Regarding the spin-wave amplitude, it has a volume character. The mode is delocalized at $k \approx 0$ and with the increase of the wavevector, its amplitude in the center increases [79]. Because of this character, this geometry is called the *backward volume geometry*.

In-plane magnetized thin film: propagation perpendicular to magnetization

The situation changes when the magnetostatic wave propagates in the direction perpendicular to the magnetization. In this case, the dispersion relation is given by the formula [80]

$$f = \frac{\gamma\mu_0}{2\pi} \sqrt{H_0 (H_0 + M_s) + \frac{M_s^2}{4} (1 - e^{-2kd})}. \quad (2.41)$$

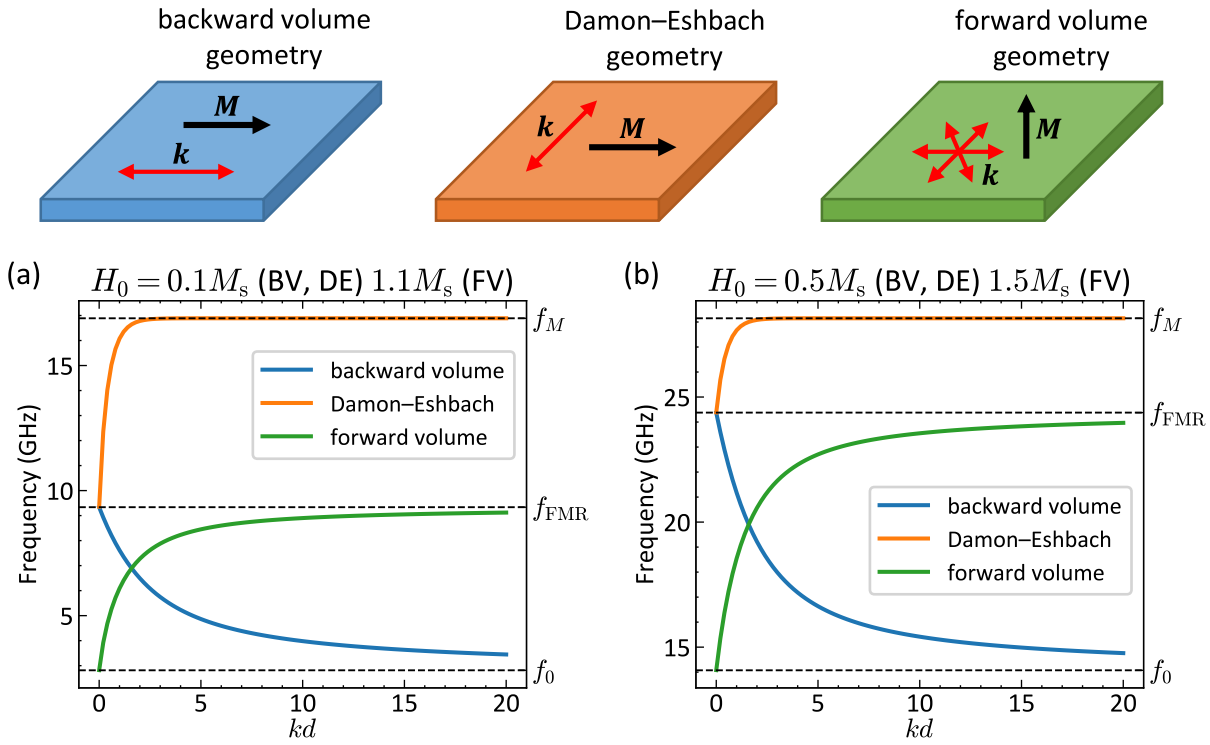


Figure 2.5 The dispersion relation of magnetostatic waves in the backward volume (blue lines), Damon–Eshbach (orange lines), and forward volume (green lines) geometries for the permalloy layer with $M_s = 800 \text{ kA/m}$. The value of the external magnetic field H_0 is (a) $0.1M_s$ and (b) $0.5M_s$ for the backward volume and the Damon–Eshbach geometries and (a) $1.1M_s$ and (b) $1.5M_s$ for the forward volume geometry. On top, the sketches of the magnetostatic wave geometries with the directions of magnetization and wavevector marked.

It is shown with the orange lines in Figure 2.5. In contrast to the propagation parallel to the magnetization, here the magnetostatic wave is a forward wave. The zero- k frequency is the same as for the backward volume geometry while for the limit of very large wavevectors, $f_{k \rightarrow \infty} = f_M = \frac{\gamma \mu_0}{2\pi} (H_0 + M_s/2)$. This wave also differs in the case of amplitude localization. This mode is localized on the surface, hence the name of the geometry – the surface geometry or, from the names of the authors of the paper describing this effect [80], the *Damon–Eshbach geometry*.

The propagation of the spin wave for the in-plane magnetized film can be considered in any direction, but the solution is more complex since it is the mixture of the surface wave and the volume wave. It is described in more detail in Ref. [79].

Out-of-plane magnetized thin film

Due to the shape anisotropy, the thin film is magnetized in-plane in the absence of the external magnetic field. To magnetize it out of the plane, it is necessary to overcome the demagnetizing field $H_d = -N_{zz}M_s = -M_s$, so the external field $H_0 \geq M_s$ has to be applied. It also affects the

frequency of the spin wave. The dispersion relation is described by the formula [78]

$$f = \frac{\gamma\mu_0}{2\pi} \sqrt{(H_0 - M_s) \left(H_0 - M_s \frac{1 - e^{-kd}}{kd} \right)}. \quad (2.42)$$

It is shown with the green lines in Figure 2.5. Similar to the Damon–Eshbach geometry, the frequency increases with the wavevector. The frequency for very small wavevectors is $f_{k \rightarrow 0} = \frac{\gamma\mu_0}{2\pi} (H_0 - M_s)$ while for very large wavevectors, $f_{k \rightarrow \infty} = \frac{\gamma\mu_0}{2\pi} \sqrt{H_0(H_0 - M_s)}$. The spin-wave amplitude of this mode is distributed over the volume of the film. Because of the character, this geometry is called the *forward volume geometry*.

2.3.2 Dipole–exchange regime

Adding the exchange interaction to the magnetostatic dispersion relation is generally not a trivial task. In the case of the bulk materials, the solution still has a simple form, but already for thin films there is no strict formula and the solution requires solving complex matrices.

Spin waves in bulk

For bulk materials, the inclusion of the exchange interaction can be done by making a simple transformation $H_0 \rightarrow H_0 + M_s l_{\text{ex}}^2 k^2$ [77]. Eq. 2.39 changes to

$$f = \frac{\gamma\mu_0}{2\pi} \sqrt{(H_0 + M_s l_{\text{ex}}^2 k^2) (H_0 + M_s l_{\text{ex}}^2 k^2 + M_s \sin^2 \theta_k)}. \quad (2.43)$$

The effect of the exchange interaction is that the dispersion relation gains a parabolic character. This will also be the most pronounced effect in other systems.

Spin waves in thin film

As mentioned earlier, the derivation of the dispersion relation of a thin film in the dipole–exchange regime is a complex task. All explicit formulas available in the literature are only approximations. Two methods have been proposed to obtain strict solutions to the problem.

The first is the partial-wave approach proposed by De Wames and Wolfram [81, 82]. In this method, the magnetization and the magnetic scalar potential are represented by a set of plane-wave solutions, which are then substituted into the Landau–Lifshitz equation and the equation for the scalar potential. The final solution is based on zeroing of the determinant of a 6x6-matrix. This method has been also used to solve the dispersion relation of cylindrical nanowires [83, 84]. Its strength is that it provides a complete solution directly. However, this method is rarely used due to its limitations as it can only be solved in systems with unbroken symmetry.

This gave an advantage to a second method proposed by Kalinikos and Slavin [85, 86] – the spin-wave mode approach. Here, the demagnetizing field is represented in the integral

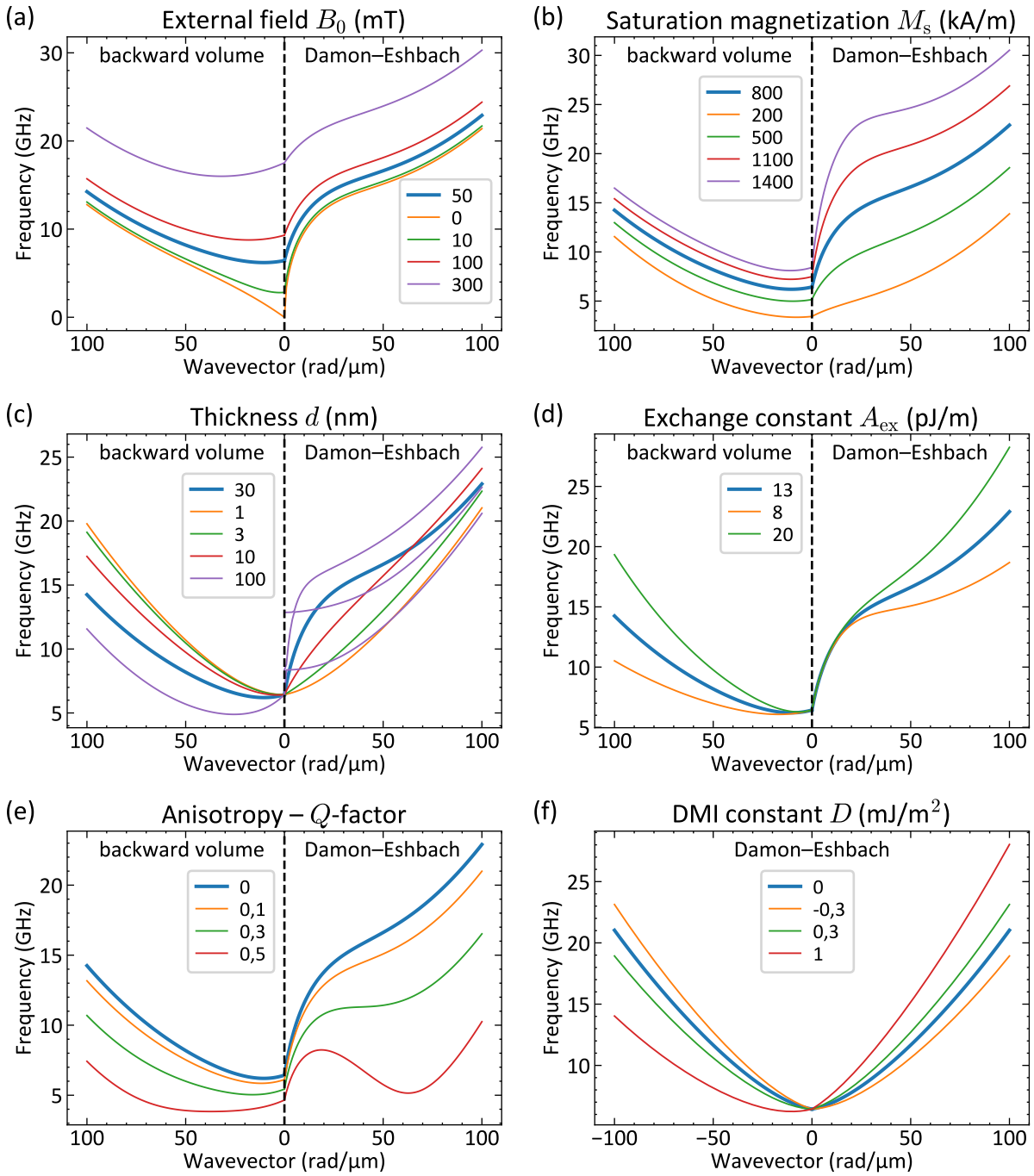


Figure 2.6 Analysis of the impact of different parameters on the spin-wave dispersion relation—(a) external magnetic field B_0 , (b) saturation magnetization M_s (keeping constant l_{ex}^2), (c) film thickness d , (d) exchange constant A_{ex} , (e) perpendicular magnetic anisotropy in terms of quality factor Q , and (f) DMI constant D . The reference film (plotted with a thick blue line) is a 30 nm-thick permalloy film with $M_s = 800$ kA/m, $A_{ex} = 13$ pJ/m, $Q = 0$, and $D = 0$ in the external field $B_0 = 50$ mT. In (a)-(e), the left side of the plot presents the dispersion in the backward volume geometry and on the right side in the Damon–Eshbach geometry. In (f), the dispersion relation is shown only for the Damon–Eshbach geometry but for positive and negative wavevectors. Also, the dispersion is shown for the layer thickness of 1 nm. The results shown in this figure were calculated using COMSOL.

form and, applied to the Landau–Lifshitz equation, it is transformed into an integro-differential equation. This method is versatile as it can be applied to many more systems than the partial-wave approach, making this method much more commonly used. However, even if the solution using the spin-wave mode approach is strict, it is not really possible to obtain. The magnetization is represented by an infinite series, which is followed by the solution of the determinant of an infinite matrix. In reality, it is necessary to truncate the series to make it finite and then solve a finite matrix, which already makes the solution only an approximation. However, this method can provide simple formulas that give a good approximation of the complete solution. This is done using the diagonal approximation in which the interaction between modes is neglected. However, this approximation has to be used carefully as it can lead to significant discrepancies with the complete solution, especially in the Damon–Eshbach geometry [87]. Due to the complexity of the analytical solution, an alternative approach can be to use the numerical simulations to solve the problem. This approach is described in detail in Chapter 3.

It is worth analyzing how different parameters can affect the spin-wave dispersion relation. In Figure 2.6 such an analysis is provided for 6 parameters—external magnetic field $B_0 = \mu_0 H_0$, saturation magnetization M_s , film thickness d , exchange constant A_{ex} , perpendicular magnetic anisotropy in terms of quality factor Q , and DMI constant D . The 30 nm-thick permalloy film with $M_s = 800 \text{ kA/m}$, $A_{\text{ex}} = 13 \text{ pJ/m}$, $Q = 0$, and $D = 0$ in the external field $B_0 = 50 \text{ mT}$ was chosen as a reference. With the increase of the external magnetic field (Figure 2.6a), the dispersion relation shifts up. In the backward volume geometry, the backward wave character is present only in higher fields, with the dispersion well becoming deeper. In the Damon–Eshbach geometry, the dispersion relation with the external field flattens significantly for small wavevectors. With the increase of the saturation magnetization M_s (Figure 2.6b), the dispersion curve shifts up. For Damon–Eshbach geometry, it also leads to a significantly larger slope at small wavevectors. The dispersion evolution with the layer thickness is complex (Figure 2.6c). The frequency at $k = 0$ does not change. In the backward volume geometry, the dispersion shifts down with thickness, causing the deepening of the dispersion well. In the Damon–Eshbach geometry, the dispersion slope increases with thickness at small wavevectors, but then flattens out so that the slope for larger wavevectors is larger for smaller thicknesses. Interestingly, for 100 nm thickness (purple curves), the fundamental mode crosses with two higher-order modes that are quantized over the thickness. With the increase of the exchange constant A_{ex} (Figure 2.6d), the dispersion slope increases more with the increase of wavevector. It does not affect the frequency at $k = 0$. With the increase of the quality factor Q (Figure 2.6e), the dispersion shifts down. The most significant shift is present at large wavevectors. Interestingly, in the Damon–Eshbach geometry, it leads to the backward wave behavior for $Q = 0.5$ (red line), with the local frequency minimum at about $60 \text{ rad}/\mu\text{m}$. The presence of the DMI (Figure 2.6f) causes the dispersion relation in the Damon–Eshbach configuration to "twist" with respect to $k = 0$. The twist amplitude depends on the absolute value of D but the twist direction depends on the sign of D —positive sign increases the frequency at the positive wavevectors and decreases at negative wavevectors; the opposite is

true for negative sign of D . The DMI has no effect on the dispersion relation in the backward volume geometry (not shown here).

As shown in Figure 2.6, the spin waves offer a complex dispersion relation that can be controlled by many parameters, with each parameter having a unique influence on the spin-wave propagation. This gives the possibility to control the dispersion relation in a way not seen in other wave phenomena such as electromagnetic or acoustic waves.

2.3.3 Multilayer systems

Despite the fact that the spin waves can propagate only in the magnetic materials, they can interact and transfer between the separated elements through the non-magnetic media (which includes not only solids, but also liquids and gases) by the magnetic field as it can exist in any material. The primary way is the coupling through the dipolar field [88]. The dipolar interaction is a long-range interaction and it allows coupling between the magnetic materials at a distance approximately equal to the spin-wave wavelength. The second option is the RKKY interaction [42]. However, the range of this interaction does not exceed a few nanometers, while it has significant strength up to only about 1 nm of separation between ferromagnetic materials [89].

The spin-wave mode interaction in the ferromagnetic multilayer systems has been studied since the 1970s [82, 90]. The investigations intensified in the 1980s with the work of Peter Grünberg on the interaction between dipolar modes in double-layer systems [88, 91], and continued by in-plane magnetized multilayers [92–94], out-of-plane magnetized multilayers [95], also the exchange modes' interaction in multilayers [96–98], and RKKY-coupled double layers [99], finishing with the work of Burkard Hillebrands for multilayers in the dipole–exchange regime from 1990 [42]. This comprehensive study combines not only the effect of dipolar and exchange interactions, but it also adds the contribution of surface and interface anisotropies and interlayer exchange coupling. Recently, the study of the spin-wave interaction between magnetic multilayers has been extended to the presence of the interfacial DMI [100].

To present the effect of the dipolar coupling between the ferromagnetic layers, the dispersion relation is shown in Figure 2.7 for two systems: two identical 10 nm-thick Py layers and two different layers—10 nm-thick Co layer and 20 nm-thick CoFeB layer. For the case of identical layers (Figure 2.7a), the fundamental branch separates into two branches. The distance between the branches decreases with the increase of the separation between the layers since the dipolar field produced by the spin wave decreases. For 300 nm-thick spacer (purple lines), there is only a small splitting for very small wavevectors. For 30 nm-thick spacer (red lines), the splitting is large for small wavevectors, but decreases to almost zero for large wavevectors. For 3 nm-thick spacer (green lines), the splitting is large in entire investigated range of wavevectors. As mentioned above, the range of coupling between the layers is of about one spin-wave wavelength. For the spacer thickness of 300 nm, this is associated with the wavevector $k = 21 \text{ rad}/\mu\text{m}$. In this case, the frequency difference between the branches at $k = 21 \text{ rad}/\mu\text{m}$ is only 9 MHz, very small in comparison to the maximum calculated value of 625 MHz at $k = 2 \text{ rad}/\mu\text{m}$, but much larger than at $k = 42 \text{ rad}/\mu\text{m}$, where the frequency difference is only 17 kHz. The situation is slightly

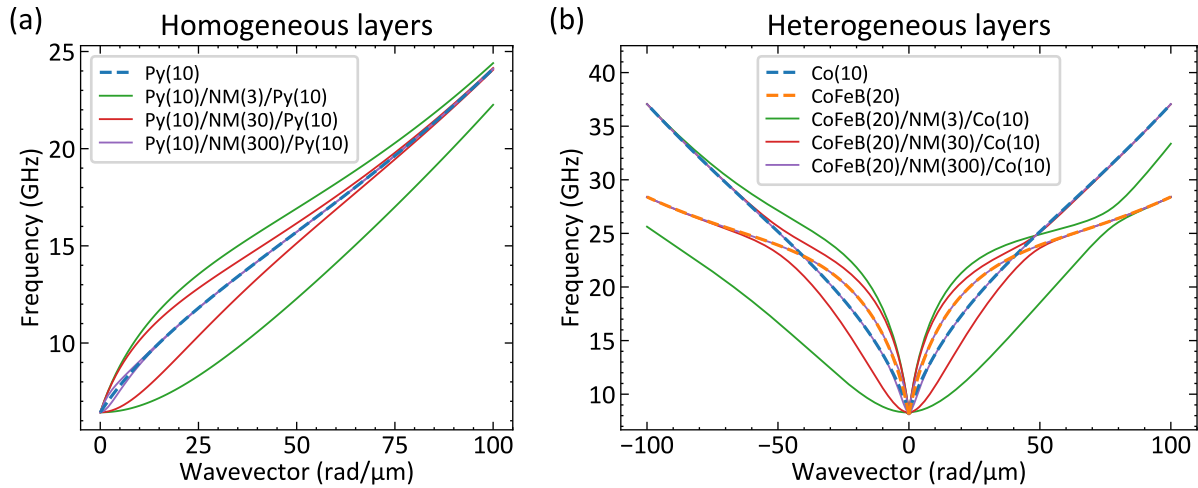


Figure 2.7 Dispersion relation of a double-layer system in the Damon–Eshbach geometry with (a) homogeneous layers of 10 nm-thick permalloy and (b) heterogeneous system with 20 nm-thick CoFeB layer and 10 nm-thick Co layer. The dispersions for double layer are shown with solid lines for three different separations: 3 nm, 30 nm, and 300 nm, assuming the separation by a nono-magnetic (NM) spacer. The reference dispersions for isolated single layers are shown as dashed lines. Material parameters—Py: $M_s = 800$ kA/m and $A_{ex} = 13$ pJ/m; CoFeB: $M_s = 1300$ kA/m and $A_{ex} = 15$ pJ/m; Co: $M_s = 1400$ kA/m and $A_{ex} = 30$ pJ/m. The external field $B_0 = 50$ mT. The results shown in this figure were calculated using COMSOL.

different for the system of heterogeneous ferromagnetic layers (Figure 2.7b). The dispersion relation is asymmetric with respect to $k = 0$ due to the asymmetry of the surface waves. The coupling is stronger for negative wavevectors, which has reflection in a stronger splitting of the branches. Also, since the dispersion relations of the isolated single layers are different, the relatively strongest interaction is present at the point of dispersion crossing at $k = \pm 40$ rad/μm. This is especially visible for the 30 nm-thick spacer (red lines).

2.3.4 Magnonic crystals

Systems with periodic modulation of the material found interest in physics due to their ability to manipulate wave propagation, including the appearance of forbidden frequency bands [101]. These systems to some extent mimic the behavior of the atomic crystal lattices and, therefore, they borrowed the name *crystal*. Despite the fact that periodic systems were studied analytically before, the first experimental evidence of their ability to form band gaps came for electromagnetic waves with works of Yablonovitch [102] and John [103] in 1987, the year that marks the invention of photonic crystals.

Periodic modulation of magnetic material, i.e., *magnonic crystal* [104], was already studied in the 1970s [105, 106]. Józef Barnaś developed the transfer-matrix approach for one-dimensional periodic systems [107, 108]. The analytical studies intensified in the 2000s [109–114]. They were followed by the experimental studies which showed the presence of band gaps in the spin-wave spectrum [115–117], proving the existence of magnonic crystals. Besides the before-mentioned

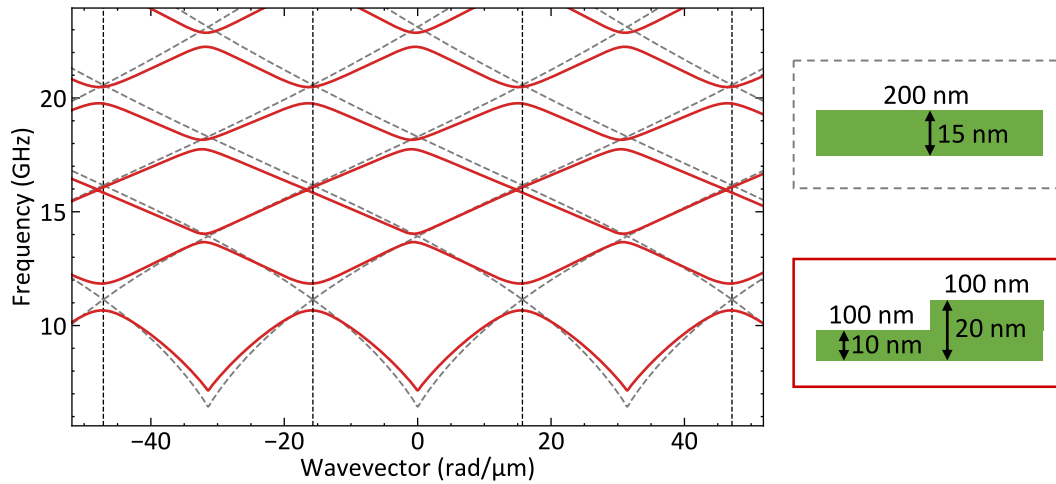


Figure 2.8 Dispersion relation of a magnonic crystal based on a corrugated permalloy layer (solid red lines) in the Damon–Eshbach configuration. The long grooves with the width of 100 nm and depth of 10 nm were made in the 20 nm-thick layer with the periodicity 200 nm. As a reference, the dispersion relation for uniform 15 nm-thick permalloy layer is shown with dashed gray lines. Parameters of Py: $M_s = 800 \text{ kA/m}$ and $A_{\text{ex}} = 13 \text{ pJ/m}$. The external magnetic field B_0 has been set to 50 mT. The results shown in this figure were calculated using COMSOL.

works of thin-film systems with a periodic pattern present along one direction, the magnonic crystal behavior has also been shown for two-dimensional thin-film systems [118, 119], including artificial spin ices [120, 121].

Interestingly, in contrast to atomic crystal lattices, the artificial crystals can be designed to have a reconfigurable structure and thus reconfigurable wave spectra. This property is particularly easy to implement in magnetic materials, where the magnetization can be controlled by the external stimuli, e.g., bias magnetic field, electric and spin current, or laser pulse. The reconfigurable magnonic crystal has been demonstrated for the first time with a system of long nanowires with possible parallel and antiparallel ordering of magnetic moments [122, 123].

Recently, the periodically arranged systems have been studied from a different point of view. The magnonic crystal behavior was shown in the systems without the artificial patterning, where the only source of periodicity came from the regular stripe-domain structure, which additionally has the property of reconfigurability [P4] or from the external magnetic field periodically modified by the Abrikosov vortices in the superconductor [124]. Also, the magnonic quasicrystals [125] and space–time crystals [126] have been demonstrated.

The exemplary dispersion relation of a magnonic crystal is shown in Figure 2.8. It is constructed by making long grooves of the 100 nm width and 10 nm depth periodically every 200 nm in the 20 nm-thick Py layer. The dispersion of this system is shown by solid red lines. As a reference, the dispersion of a uniform 15 nm-thick Py layer is shown with dashed gray lines assuming the artificial lattice constant of 200 nm. In the magnonic crystal, the band gaps appear in the dispersion relation. They are slightly shifted to the left from the edges (odd gaps) and centers (even gaps) of the Brillouin zone. Moreover, the dispersion relation is asymmetric. This is because of the asymmetry between the top and the bottom surface which induces an

asymmetry in the spin-wave propagation in the Damon–Eshbach configuration. The band gaps vary greatly in size. Interestingly, the third band gap is very small, not visible at this scale. In the crystal band structure, some of the gaps can close for the certain values of the periodic parameter, in this case, the groove width. The dispersion relation of a reference layer is similar, but there are significant differences besides the presence of band gaps. The discrepancy will be much smaller for smaller modulation of the material, e.g., if the layer will be 16 nm thick and the grooves will be 2 nm deep. However, smaller modulation of the layer will lead to significantly smaller band gaps.

2.4 Spin-wave computing

The dominance of electronics in the computing market is gigantic. The continuous development of complementary metal–oxide–semiconductor (CMOS) technology has led to tremendous progress in computing. However, electronics faces many difficulties. Further miniaturization of electronic devices is hampered by the inevitable approach to the dimensions where the quantum effects will play a significant role. Moreover, large amounts of heat are generated during operation, which raises the problem of cooling of computing systems.

For these reasons, a great emphasis is put on the development of the computing devices and methods based on other physical phenomena. In recent years, magnonics has found an increasing attention of scientists [127–129]. Spin waves have many advantages that make them a promising carrier for the future computing devices. As listed by Chumak *et al.* [129], "among the key advantages offered by magnons for data processing are the scalability down to atomic dimensions, the compatibility with existing CMOS and spintronic technologies, the operations in the frequency range from several GHz to hundreds of THz, the possibility to process data in the wide temperature range from ultra-low temperatures to room temperature, and the access to pronounced nonlinear phenomena". One should not forget another advantage, which is the very low energy consumption of spin waves, since only the rotation of the spin is required comparing to the movement of electrons in electronic systems, which requires significantly more energy.

2.4.1 Computational methods

The question has to be asked about how to perform computations on the spin waves. The information can be carried in the spin-wave amplitude, phase, wavelength, frequency, or a few of these options combined, with the first two being the most commonly used in the design of devices. The most common mode of operation follows the widely used approach of von Neumann architecture, where the central processing unit (CPU) and the memory unit function as individual systems which are connected by a data bus. While the research on the CPU elements is very active (and will be described later), the literature on spin-wave-based memory and interconnects is limited [130–136]. Spin waves also show the possibility of interconnection with current CMOS devices. Another way is to take advantage of the wave properties for the realization

of analog computing, which has been used for tasks like data processing, prime factorization, or Fourier transform [135, 137, 138]. Intensive studies are underway in quantum magnonics, with work already done in single-magnon detection [139], Bose–Einstein condensation [140], polarons [141], entangled magnons [142], photon-to-magnon coupling [143], and the coupling with superconducting qubits [144]. Recently, the neural networks have received attention with the increasing interest in the artificial intelligence all around the world. Here, the spin waves seem to show potential for applications in neuromorphic computing [145–149] and reservoir computing [150–152].

2.4.2 Spin-wave devices

The basis of any spin-wave device is a wave conduit. Low damping is essential in such systems to be able to process the spin wave at a sufficiently long distance, therefore, the fabrication of waveguides involves the materials like yttrium iron garnet (YIG) [153], Heusler alloys [154], and magnetic atoms (Fe, Co, Ni) and their alloys such as permalloy ($\text{Ni}_{80}\text{Fe}_{20}$) [155], CoFeB, and CoFe. They are usually magnetized in plane, but also the systems with out-of-plane magnetization have been studied [156]. However, the main disadvantage of such systems is their relatively higher damping. Another interesting proposal involves the use of domain walls as spin-wave conduits [157, 158].

One of the key challenges is to be able to change the direction of spin-wave propagation. This is usually done using curved waveguides [159, 160], also in three-dimensional systems [161]. However, the curvature contributes to additional energy losses. They can be overcome by different methods like graded index [162–164] or using spin textures [165]. The control of spin-wave propagation can also be achieved by manipulating the dispersion relation, for example, by using magnonic crystals (described in Section 2.3.4). Another important point is to gain the possibility of the spin-wave amplification. This can be done by spin-transfer or spin-orbit torque [166], spin-wave pumping by antenna [167], voltage-controlled magnetic anisotropy [168], or magnetoelectric effect [169]. An alternative way to increase the spin-wave amplitude is to use the spin-wave repeater [134, 170].

The circuits of the computing systems usually contain many different devices. The basic device characteristic for the von Neumann architecture is the transistor, which acts both as a switch and an amplifier. It was experimentally demonstrated for spin waves by Chumak *et al.* [171, 172] in a macroscale YIG sample. Other typical devices are logic gates, which, for the waves, seem to be more convenient than transistors. For the amplitude-based calculations, the logic is based on Boolean logic, in particular, it can be reduced to only the NAND and NOR gates, which are sufficient to design any logic operation. There are several demonstrations of these gates for spin waves [168, 173–175], as well as other gates including NOT [173, 176], XOR [176], XNOR [174–176], AND and OR [130]. Most of these devices are based on the Mach–Zehnder interferometer which is controlled by the current [173, 174, 176], but there are also proposals that rely on the voltage-controlled magnetic anisotropy [168, 175]. The phase-based computations require a different type of logic gate, in particular the majority gate,

which consists of three or more inputs and the result at its output depends on the phase of the majority of the inputs, hence the name. After first theoretical proposals [170, 177], the spin-wave majority gate has been experimentally demonstrated [178–180].

Important complementary devices to logic gates are phase shifters [181, 182], which provide the possibility to manipulate the phase of the propagating wave. Another important device is an adder, which makes it possible to perform a summation of numbers. There is an experimental demonstration of a spin-wave half adder [183], as well as a design of a more complex ripple-carry adder [184]. They are based on directional couplers, which give the ability to couple the waveguides at a distance thanks to the dipolar interactions. The first spin-wave directional couplers were proposed in the macroscale [185, 186], with later demonstration also in the nanoscale [183, 187]. The other devices include diodes [P1] [188–191] and circulators [P1,P2] [192], which increase the control of the spin-wave propagation, and multiplexers [193] and demultiplexers [194], which enable frequency- and wavelength-based computations.

The next step in the spin-wave computing is to combine the devices into a spin-wave circuit. Several proposals have been advanced [130, 132, 170, 195], however, we are still waiting for the experimental demonstration. There are several challenges associated with the implementation of the circuits. The design of a circuit requires the possibility to use the output as an input of another device or even several devices, the output should not affect its original input, and the signal should not degrade during the whole process [127]. Ensuring all these properties is a challenging task for spin waves. On the one hand, the generally high damping of spin waves considerably hampers the possibility of transmitting a signal of considerable amplitude through the whole circuit without amplification. Moreover, the spin wave is several orders of magnitude slower than the electrically-transmitted information. The isolation from the reverse signal between inputs and output can be done using diodes, but they must have high transmission in the forward direction to minimize losses. Another problem is the signal transfer from a single output to multiple inputs. This can be done by converting to an electrical signal and then back to a spin wave, but this requires significant signal amplitude at the input and can be effectively energy-consuming.

Chapter 3

Micromagnetic simulations

With the development of magnetism, the magnetic systems studied experimentally become more and more complex in terms of the geometry and the magnetization configuration. Analytical methods can usually provide only an approximate solution to the problem. As mentioned in Chapter 2, even a problem as fundamental as spin-wave dynamics in the uniformly magnetized thin ferromagnetic film requires solving a 6x6 matrix to obtain an exact solution, to say nothing of verifying the performance of a spin-wave device. The use of numerical simulations offers the possibility to study systems of considerable complexity and on a large scale. As the implementation is based on the general differential equations, such a model is a universal tool to calculate different problems requiring only the change of system geometry and parameters. Thanks to the rapid growth of the speed of computational units and algorithms, the numerical methods find the continuously increasing attention not only in magnetism, but also in other fields of physics, as well as in other areas of science and engineering. This Chapter presents the numerical simulation tools that have found the attention of researchers in magnetism, especially those working in the nano- and microscale, with a focus on the method and implementation used by the Author.

3.1 Numerical methods

Two different numerical methods, which found the implementation in the micromagnetism, can be distinguished. The first is the finite-difference method. It is based on the approximation of the differential equations to a system of linear equations. The continuous system is discretized with a regular grid, representing the infinitesimal evolution by finite differences. The main advantage of this method is its relative simplicity of implementation compared to other numerical methods. However, one of the problems is the inaccurate discretization of curved geometries, as the system can only be represented by cuboid elements. Moreover, the system with many bodies scattered in the large area faces the calculation of large amount of unnecessary elements, as the whole volume of the system must be calculated with a constant difference, so there is no possibility to reduce the difference in the most important areas. In the micromagnetism, the most used numerical tools taking advantage of the finite-difference method are MuMax3 [196] and OOMMF [197].

The second method, which is also the method used in the Thesis, is the finite-element method. In this case, the system is divided into irregularly shaped elements of different sizes. In two-dimensional systems, these are usually triangles and quadrangles, while in three-dimensional systems they are tetrahedrons and cuboids, which can be mixed together. Each element has defined material parameters and physical properties.

The generation of the elements starts with the positioning of their nodes. The density of the nodes is defined by the user. The objects that need to be calculated with high precision can be meshed finer. On the other hand, areas of lesser importance can be meshed coarsely. In this way, the computing power is allocated more effectively. This method shows its advantages in systems with curved geometries, as the curvature can be reconstructed with good efficiency. Moreover, the creation of the mesh with different sizes of elements allows of the proper discretization of scattered systems and the capture of local effects.

In order to solve the problem, the system of partial differential equations is simplified to algebraic equations (for the steady-state problems) or ordinary differential equations (for time-evolving systems) which are then solved by numerical integration using techniques such as the Runge–Kutta method. Another advantage is the possibility to solve the problem using the weak formulation, in which the differential equations are transformed into integral equations. In this way, the order of the equation can be reduced which allows the problem to be solved faster.

Among the finite-element method solvers dedicated for magnetism one can find *tetmag2* [198], *FinMag* [199], *Tetrax* [200, 201], *FastMag* [202], or *magnum.fe* [203]. In addition, a *Micromagnetics* module has been added to *COMSOL Multiphysics* [204].

In the studies presented in the Thesis, the implementation in *COMSOL Multiphysics* was used. *COMSOL Multiphysics* is a commercial program made by *COMSOL AB* – a company founded in 1986 in Stockholm, Sweden [205]. The first version of the program was released in 1998 under the name *FEMLAB*. It is a multipurpose software with the implementation of numerous problems of physics, chemistry, and engineering. In addition to the basic *Multiphysics* module, the current version has more than 30 additional modules covering the problems of mechanics, electrodynamics, thermodynamics, hydrodynamics, wave physics, and chemical engineering. The software covers the entire simulation process, from the preparation of the system (including the generation of geometry and mesh, and the definition of materials, parameters, and physics), through the solution of the problem, to the post-processing of the obtained results. All these functionalities are available through a simple graphical user interface. A major advantage of *COMSOL* is the ability to couple different physics modules and solve them together, allowing the user to solve complex multi-physics problems. It also allows the user to define their own system of equations.

In the following section, the implementations used in the studies of the Thesis are described in detail.

3.2 Implementation in COMSOL Multiphysics

The implementation was developed by scientists from the Department of Physics of Nanostructures, Faculty of Physics, Adam Mickiewicz University, Poznań, to which the Author belongs. The authors of the current implementations are Piotr Graczyk, Grzegorz Centała, and the Author himself. The authors of the previous versions—Michał Mruczkiewicz and Justyna Rychły-Gruszecka—should also be mentioned, as their work significantly contributed to the development of the currently used models. The implementation consists of many different models for different geometries and has been improved over the years to include new physical phenomena. Parts of the implementations have been presented in Refs. [84, 206–209].

Three different models have been used in the studies presented in the Thesis. In publications [P1], [P2], and [P3], the linearized Landau–Lifshitz–Gilbert equation adapted to the Damon–Eshbach geometry of spin waves is implemented in the two-dimensional model (Implementation 1). In publication [P4], the full Landau–Lifshitz–Gilbert equation is implemented in the two-dimensional model (Implementation 2). In publications [P5], the full Landau–Lifshitz–Gilbert equation is implemented in the three-dimensional model (Implementation 3).

The basis of each implementation described in this Thesis is the basic version of COMSOL. No additional modules are needed. The implementation starts with the Landau–Lifshitz–Gilbert equation (Eq. 2.30) and the dipolar field in the form of a magnetic scalar potential (Eq. 2.12). Both are implemented using the Coefficient Form PDE¹ interface.

Firstly, let's focus on the COMSOL interface. The Coefficient Form PDE is an interface that provides the possibility to implement the partial differential equations based on coefficients. The implementation is based on the equation

$$e_a \frac{\partial^2 \mathbf{u}}{\partial t^2} + d_a \frac{\partial \mathbf{u}}{\partial t} + \nabla \cdot (-c \nabla \mathbf{u} - \alpha \mathbf{u} + \gamma) + \beta \cdot \nabla \mathbf{u} + a \mathbf{u} = f \quad (3.1)$$

where $e_a, d_a, c, \alpha, \gamma, \beta, a, f$ are the coefficients. Since the symbols of some of the coefficients are the same as the parameters used in the Thesis, they are enclosed in square brackets for clarity, e.g., $[e_a]$. The form of the coefficients and other parameters depends on the implementation. All three implementations are described in detail below.

Implementation 1 (publications P1, P2, and P3)

In Implementation 1, the Landau–Lifshitz–Gilbert equation is solved with the effective magnetic field in the form:

$$\mathbf{H}_{\text{eff}} = H_0 \hat{\mathbf{z}} + \frac{2A_{\text{ex}}}{\mu_0 M_s^2} \nabla^2 \mathbf{M} + \frac{2D}{\mu_0 M_s^2} \hat{\mathbf{z}} \times \frac{\partial \mathbf{M}}{\partial x} + \frac{2K_u}{\mu_0 M_s^2} M_y \hat{\mathbf{y}} - \nabla \phi, \quad (3.2)$$

¹For clarity, the COMSOL functions have been written in sans-serif font and the expressions in monospace font.

with $\nabla = (\partial_x, \partial_y)$, while the equation for the magnetic scalar potential in the form

$$\frac{\partial^2 \varphi}{\partial x^2} + \frac{\partial^2 \varphi}{\partial y^2} = -\frac{\partial m_x}{\partial x} - \frac{\partial m_y}{\partial y} \quad (3.3)$$

inside the magnetic material and

$$\frac{\partial^2 \varphi}{\partial x^2} + \frac{\partial^2 \varphi}{\partial y^2} = 0 \quad (3.4)$$

outside the magnetic material.

The coefficients in the Coefficient Form PDE for the Landau–Lifshitz–Gilbert equation are defined as follows

$$[c] = \begin{array}{|c|c|} \hline 0 & P \cdot A_{\text{ex}} \\ \hline -P \cdot A_{\text{ex}} & 0 \\ \hline \end{array}$$

$$[a] = \begin{array}{|c|c|} \hline 0 & \gamma \mu_0 H_0 - P \cdot K_{\text{oop}} + P \cdot K_{\text{ip}} \\ \hline -\gamma \mu_0 H_0 - P \cdot K_{\text{ip}} & 0 \\ \hline \end{array}$$

$$[f] = \begin{array}{|c|} \hline \gamma \mu_0 M_s \cdot \text{phiy} \\ \hline -\gamma \mu_0 M_s \cdot \text{phix} \\ \hline \end{array}$$

$$[d_a] = \begin{array}{|c|c|} \hline 1 & \alpha \\ \hline -\alpha & 1 \\ \hline \end{array}$$

$$[\beta] = \begin{array}{|c|c|} \hline P \cdot D & 0 \\ \hline 0 & 0 \\ \hline 0 & P \cdot D \\ \hline 0 & 0 \\ \hline \end{array}$$

where $[\mathbf{u}] = (M_x, M_y)^T \rightarrow (m_1, m_2)^T$ and $[\nabla] = (\partial_x, \partial_y)$, M_s is the saturation magnetization M_s , A_{ex} is the exchange constant A_{ex} , γ is the gyromagnetic ratio γ , μ_0 is the vacuum permeability μ_0 , α is the damping constant α , K_{oop} is the out-of-plane anisotropy K_{OOP} , K_{ip} is the in-plane anisotropy K_{IP} (the last two are defined as uniaxial anisotropies K_u in different directions), D is the DMI constant D , and P is the proportionality constant $2\gamma/M_s$. All other coefficients are set to zero. In the main node, the unit of the dependent variable is defined as A m^{-1} , while the unit of source as $\text{A m}^{-1} \text{ s}^{-1}$.

Note that the dependent variables sometimes appear with an additional letter at the end, e.g., m_1y or phix . This is COMSOL abbreviated notation of the derivative, e.g., m_1y is $\partial m_x / \partial y$ and phix is $\partial \varphi / \partial x$.

In the Coefficient Form PDE node for the magnetic scalar potential, there must be two internal Coefficient Form PDE nodes. In the first one, only the ferromagnetic materials should be selected in the geometry. Here, the coefficients have the form

$$[c] = \boxed{1}$$

$$[\gamma] = \begin{matrix} \boxed{m1} \\ \boxed{m2} \end{matrix}$$

In the second Coefficient Form PDE node, only the non-magnetic materials in the geometry should be selected and

$$[c] = \boxed{1}$$

All other coefficients are set to zero. In this case, $[u] = \varphi \rightarrow \text{phi}$. In the main node, the unit of the dependent variable is defined as A, while the unit of the source is defined as A m^{-2} .

The free boundary conditions at the magnetic material boundaries are automatically satisfied by the Zero Flux node.

Additionally, in the Coefficient Form PDE interface for the magnetic scalar potential, a Dirichlet Boundary Condition with $\varphi = 0$ is added to the top and the bottom boundary of the computational cell. This is done by checking the box Prescribed value of phi and writing 0 in the field of the parameter $[r]$. This condition guarantees that the magnetic field far from the magnetic material is equal to zero.

Eigenfrequency study

The geometry in these studies consists of Rectangle nodes. Due to the implementation of the Bloch boundary conditions, the width of all rectangles is constant. It is set to 5π nm. Thus, the reciprocal-space vector is integer and is equal to $k = 400 \text{ rad}/\mu\text{m}$. Apart from the Rectangle nodes for the ferromagnetic layers, the Rectangle representing the non-magnetic surrounding (which includes the non-magnetic layers and the air around) is required for the correct distribution of the dipolar field. The height of the non-magnetic region should be at least two wavelengths of the longest calculated wave (excluding the ferromagnetic resonance of $\lambda \rightarrow \infty$), for example, if the minimum calculated wavevector is $1 \text{ rad}/\mu\text{m}$, then the cell should have the height $h \geq 2\lambda_{\text{max}} = 4\pi/k_{\text{min}} \approx 12.5 \mu\text{m}$. The ferromagnetic layers should be placed in the center of the non-magnetic area.

The simulations of the eigenproblem require the implementation of the Bloch boundary conditions. They are implemented using the Pointwise Constraint boundary node in the Coefficient Form PDE interface and the Linear Extrusion coupling operator in Definitions. The function implemented in the Pointwise Constraint node is, for the example of m_x component, $\text{linext1}(m1) - m1 * \exp(i * k * a)$ in the Constraint expression field and $\text{test}(\text{linext1}(m1) * \exp(i * k * a) - m1)$ in the Constraint force expression field, where linext1 is the automatic name of the first Linear Extrusion operator created in the program, k is the wavevector, a is the width of the calculation cell, and test is the test function in the weak form formulation. The implementation of the Linear Extrusion operator is shown in Figure 3.1a for an example from publication [P1]. The image shows the geometry of the system, which consists of 5 gray rectangles. The two rectangles with the dot in the middle represent the ferromagnetic layers. The implementation is shown for the Co layer. In the Linear Extrusion, the orange boundary is selected. The Source Vertices are marked in purple while the Destination Vertices are marked in

orange. The order of the vertices is important. If the Source vertex 1 is the top purple vertex, then Destination vertex 1 must be the top orange vertex. Next, in the Pointwise Constraint node, the boundary placed between the orange vertices is selected. The Linear Extrusion operators and Pointwise Constraint nodes must be applied to each ferromagnetic layer touching the left and right sides of the geometry, separately for the m_1 and m_2 variables, in the Coefficient Form PDE interface for the Landau–Lifshitz–Gilbert equation and for the whole geometry for the variable ϕ_i in the Coefficient Form PDE interface for the magnetic scalar potential.

To study of the dispersion relation, the Study node contains the Eigenfrequency study with Search for eigenfrequencies around taken to value of 1 Hz and Eigenfrequency search method around shift is set to Larger real part. This will filter out the possible numerical errors. The Parametric Sweep with the sweep over the wavevector k is added to the study. In the Parameter value list, the function range $(-\pi/a, 0.01*\pi/a, \pi/a)$ (which is 101 steps between the edges of the Brillouin zone) is set, where the following values give the start, step, and stop of the range function. Predefined settings in the Solver Configurations are used.

In the publication [P3], the RKKY interaction is also added. The first step, the Linear Extrusion coupling operator, is similar to the Bloch boundary conditions, but instead of being used at the left and right boundaries, it is used at the inner boundaries of the double-layer system. Let the Linear Extrusion operator be named `linextTop` for the top layer and `linextBottom` for the bottom layer. For the RKKY interaction, the Flux/Source boundary node is used instead of the Pointwise Constraint node. The coefficient in the Flux/Source for the bottom boundary of the top layer has the form

$$[g] = \frac{P/2*J*(\text{linextBottom}(m_2) - m_2)}{-P/2*J*(\text{linextBottom}(m_1) - m_1)}$$

where J is the RKKY constant A_{12} . The coefficient $[g]$ is set to zero. A similar Flux/Source node should be applied to the top boundary of the bottom layer, only by replacing `linextBottom` with `linextTop`.

Time-domain study

Similar to the eigenfrequency study, the geometry in the time-domain study consists of Rectangle nodes. The rules for height are the same. In the case of the width, it must be enough to cover all the required elements such as the resonator in [P2], the antenna (tens of nanometers), the area to measure the spin-wave intensity (a few spin-wave wavelengths), and the area with increased damping to suppress the spin wave and prevent the reflection from both edges (at least one spin-wave wavelength from both sides). Also, the antenna must be added as an additional Rectangle. Its width should not be larger than half of the wavelength.

Damping near the boundary is implemented using Ramp functions in Definitions. In the Slope field, the value should be equal to at most $1/\lambda$, but can be smaller for better spin-wave attenuation. Let the Ramp functions be named `leftRamp` and `rightRamp`, with the Location field marking the left and right sides of the geometry. To implement the damping boundary conditions

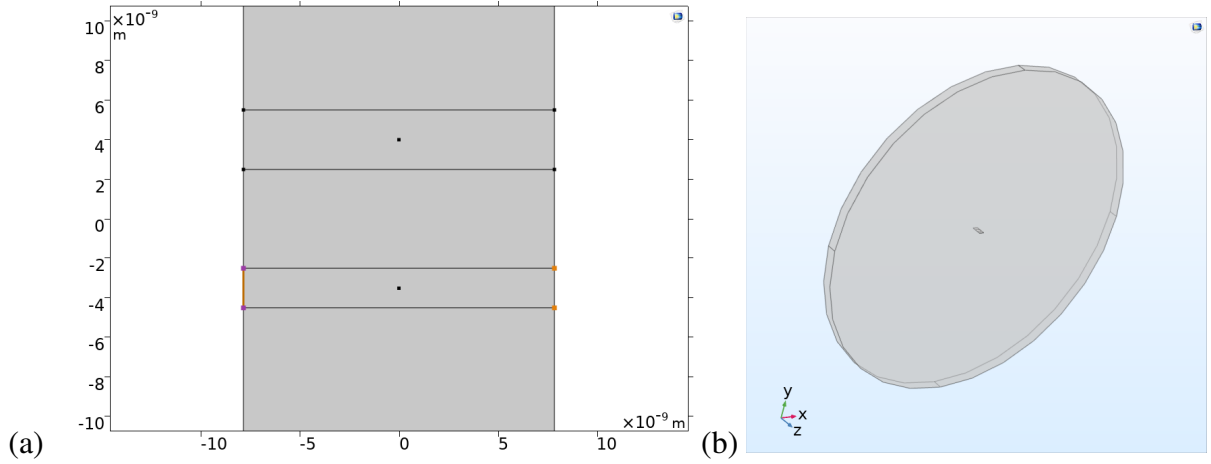


Figure 3.1 (a) Screen from the COMSOL program for the Eigenfrequency study in publication [P1]. It shows the geometry as viewed from the Linear Extrusion operator. (b) Screen from the COMSOL program showing the geometry of the system investigated in publication [P5].

for the equations in the Coefficient Form PDE for the Landau–Lifshitz–Gilbert equation, they are added to the Source node. It says

$$[f] = \frac{\text{rightRamp}(x) * m2t + (1 - \text{leftRamp}(x)) * m2t}{-\text{rightRamp}(x) * m1t - (1 - \text{leftRamp}(x)) * m1t}$$

The antenna is also added as another Source node to the Coefficient Form PDE for the Landau–Lifshitz–Gilbert equation. Assuming that the excitation antenna generates the ac external magnetic field of the amplitude $\mathbf{h}_{ac} = (h_x, h_y) \rightarrow (h1, h2)$, it is implemented as

$$[f] = \frac{-\text{gamma} * \mu_0 * M_s * h2 * \sin(2 * \pi * \text{fr} * t)}{\text{gamma} * \mu_0 * M_s * h1 * \sin(2 * \pi * \text{fr} * t)}$$

where fr is the excitation frequency which should be defined in Global Definitions>Parameters.

The Study node contains the Time Dependent study. The Times field should be set to cover the spin-wave propagation through whole system with a constant step. For this purpose, it is good to use the range function. For example, in publication [P1] the Times field is set to range(0, 0.01, 3) with Time unit set to ns. Predefined Solver Configurations are used.

Implementation 2 (publication P4)

In Implementation 2, the Landau–Lifshitz–Gilbert equation is solved with the effective magnetic field in the form:

$$\mathbf{H}_{\text{eff}} = H_0 \hat{\mathbf{x}} + \frac{2A_{\text{ex}}}{\mu_0 M_s^2} \nabla^2 \mathbf{M} + \frac{2K_{\text{PMA}}}{\mu_0 M_s^2} M_z \hat{\mathbf{z}} + \frac{2K_{\text{IMA}}}{\mu_0 M_s^2} M_x \hat{\mathbf{x}} - \nabla \varphi, \quad (3.5)$$

while the equation for the magnetic scalar potential in the form

$$\frac{\partial^2 \phi}{\partial x^2} + \frac{\partial^2 \phi}{\partial y^2} = -\frac{\partial m_x}{\partial x} - \frac{\partial m_y}{\partial y} \quad (3.6)$$

inside the magnetic material and

$$\frac{\partial^2 \phi}{\partial x^2} + \frac{\partial^2 \phi}{\partial y^2} = 0 \quad (3.7)$$

outside the magnetic material.

The coefficients in the Coefficient Form PDE for the Landau–Lifshitz–Gilbert equation are defined as follows

$$[c] = \begin{array}{|c|c|c|} \hline 0 & P \cdot A_{ex} \cdot m_3 & -P \cdot A_{ex} \cdot m_2 \\ \hline -P \cdot A_{ex} \cdot m_3 & 0 & P \cdot A_{ex} \cdot m_1 \\ \hline P \cdot A_{ex} \cdot m_2 & -P \cdot A_{ex} \cdot m_1 & 0 \\ \hline \end{array}$$

$$[a] = \begin{array}{|c|c|c|} \hline 0 & \gamma \cdot \mu_0 \cdot H_z 0 & -\gamma \cdot \mu_0 \cdot H_y 0 \\ \hline -\gamma \cdot \mu_0 \cdot H_z 0 & 0 & \gamma \cdot \mu_0 \cdot H_x 0 \\ \hline \gamma \cdot \mu_0 \cdot H_y 0 & -\gamma \cdot \mu_0 \cdot H_x 0 & 0 \\ \hline \end{array}$$

$$[f] = \begin{array}{|c|} \hline \gamma \cdot \mu_0 \cdot m_3 \cdot \phi_{iy} \\ \hline -\gamma \cdot \mu_0 \cdot m_3 \cdot \phi_{ix} \\ \hline \gamma \cdot \mu_0 \cdot (m_1 \cdot \phi_{iy} - m_2 \cdot \phi_{ix}) \\ \hline \end{array}$$

$$[d_a] = \begin{array}{|c|c|c|} \hline 1 & \alpha \cdot m_3 / M_s & -\alpha \cdot m_2 / M_s \\ \hline -\alpha \cdot m_3 / M_s & 1 & \alpha \cdot m_1 / M_s \\ \hline \alpha \cdot m_2 / M_s & -\alpha \cdot m_1 / M_s & 1 \\ \hline \end{array}$$

where $[\mathbf{u}] = (M_x, M_y, M_z)^T$ and $[\nabla] = (\partial_x, \partial_y, \partial_z)$, $H_x 0, H_y 0, H_z 0$ are the x -, y -, and z -components of the external field, and P is the proportionality constant, which in this case is different from the Implementation 1 and is equal to $2\gamma/M_s^2$.

Magnetic anisotropy is implemented separately using a Source node, which is implemented on the magnetic domain where the anisotropy is present. It is added as an extra term to $[f]$ as

$$[f] = \begin{array}{|c|} \hline P \cdot K_u \cdot (n_{K1} \cdot m_1 + n_{K2} \cdot m_2 \cdot n_{K3} \cdot m_3) \cdot (n_{K2} \cdot m_3 - n_{K3} \cdot m_2) \\ \hline P \cdot K_u \cdot (n_{K1} \cdot m_1 + n_{K2} \cdot m_2 \cdot n_{K3} \cdot m_3) \cdot (n_{K3} \cdot m_1 - n_{K1} \cdot m_3) \\ \hline P \cdot K_u \cdot (n_{K1} \cdot m_1 + n_{K2} \cdot m_2 \cdot n_{K3} \cdot m_3) \cdot (n_{K1} \cdot m_2 - n_{K2} \cdot m_1) \\ \hline \end{array}$$

where n_{K1}, n_{K2}, n_{K3} are the x -, y -, and z -components of the anisotropy vector \mathbf{u} as defined in Section 2.1.4.

In Implementation 2, the implementation of the magnetic scalar potential is identical to Implementation 1.

The geometry of the system is created in the same way as the eigenfrequency study in Implementation 1. The same applies to the implementation of the free boundary conditions,

Dirichlet boundary conditions, and Bloch boundary conditions. In the case of the Bloch boundary conditions, one must not forget about the implementation for the variable m_3 , which is analogous to m_1 and m_2 .

Relaxation of magnetic state

For the relaxation of the magnetic state, the Study node contains the Time Dependent study. In all cases, the Times field is set to 1000 ns. This value is sufficient to completely relax the system. The Relative tolerance is set to 0.0001. In the Solver Configurations > Solution > Time-Dependent Solver > Direct node, the PARDISO solver is used.

An important element of the Time Dependent study of the relaxation is the choice of the parameter coupling. This can be set in Solver Configurations > Solution > Time-Dependent Solver node. One option is the Fully Coupled node, where all variables are solved together. The other is the Segregated node, where the calculation of a step can be divided into substeps for certain groups of variables. The optimal method of simulating the relaxation is to start with the Segregated node enabled, with the first step calculating m_1 , m_2 , and m_3 , and the second step calculating only ϕ_i , and then switching to finish with the Fully Coupled node enabled. The change of the nodes should happen at the moment when the magnetic state is about to reach the final state. It is because the simulation with the Segregated node is faster but at some point, the simulation time step often can't increase beyond a certain value, which is not the case for the Fully Coupled node.

For the study of the relaxation, the damping parameter α must be set to a high value between 0.5 and 1.

In the Coefficient Form PDE for the Landau–Lifshitz–Gilbert equation, it is useful to define the initial state in the Initial Values node.

Eigenfrequency study

For the study of the dispersion relation, the Study node contains the Eigenfrequency study and the implementation is analogous to Implementation 1. However, there is an important difference as the final magnetic state from the relaxation has to be used. To do this, in the Values of the linearization point, the Settings field should be set to User controlled, the Method field to Solution, from the Study field, the study with the magnetic state relaxation should be selected, and the Time field should be set to Last.

Implementation 3 (publication P5)

In Implementation 3, the Landau–Lifshitz–Gilbert equation is solved with the effective magnetic field in the form:

$$\mathbf{H}_{\text{eff}} = \mathbf{H}_0 + \frac{2A_{\text{ex}}}{\mu_0 M_s^2} \nabla^2 \mathbf{M} + \frac{2K_{\text{PMA}}}{\mu_0 M_s^2} M_z \hat{\mathbf{z}} - \nabla \varphi + \frac{2D}{\mu_0 M_s^2} \left(\frac{\partial M_z}{\partial x} \hat{\mathbf{x}} + \frac{\partial M_z}{\partial y} \hat{\mathbf{y}} - \left(\frac{\partial M_x}{\partial x} + \frac{\partial M_y}{\partial y} \right) \hat{\mathbf{z}} \right), \quad (3.8)$$

while the equation for the magnetic scalar potential in the form

$$\frac{\partial^2 \varphi}{\partial x^2} + \frac{\partial^2 \varphi}{\partial y^2} = -\frac{\partial m_x}{\partial x} - \frac{\partial m_y}{\partial y} \quad (3.9)$$

inside the magnetic material and

$$\frac{\partial^2 \varphi}{\partial x^2} + \frac{\partial^2 \varphi}{\partial y^2} = 0 \quad (3.10)$$

outside the magnetic material.

The coefficients in the Coefficient Form PDE for the Landau–Lifshitz–Gilbert equation are defined as follows

$$[f] = \begin{array}{|l} \hline \text{gamma*mu0*(m2*phiz-m3*phiy)} \\ \hline \text{gamma*mu0*(m3*phix-m1*phiz)} \\ \hline \text{gamma*mu0*(m1*phiy-m2*phix)} \\ \hline \end{array}$$

$$[\alpha] = \begin{array}{|c|c|c|} \hline -P/2*D*m3 & 0 & 0 \\ \hline 0 & 0 & 0 \\ \hline 0 & -P/2*D*m2 & -P/2*D*m3 \\ \hline 0 & -P/2*D*m3 & 0 \\ \hline 0 & 0 & 0 \\ \hline 0 & 0 & 0 \\ \hline P/2*D*m1 & P/2*D*m2 & 0 \\ \hline 0 & 0 & 0 \\ \hline 0 & 0 & P/2*D*m3 \\ \hline \end{array}$$

$$[\beta] = \begin{array}{|c|c|c|} \hline P/2*D*m3 & 0 & -P/2*D*m1 \\ \hline 0 & 0 & 0 \\ \hline 0 & 0 & 0 \\ \hline 0 & P/2*D*m3 & -P/2*D*m2 \\ \hline 0 & 0 & 0 \\ \hline P/2*D*m2 & -P/2*D*m1 & 0 \\ \hline 0 & 0 & 0 \\ \hline 0 & 0 & 0 \\ \hline P/2*D*m3 & 0 & -P/2*D*m1 \\ \hline \end{array}$$

where $[\mathbf{u}] = (M_x, M_y, M_z)^T$ and $[\nabla] = (\partial_x, \partial_y, \partial_z)$, and $P = 2\gamma/M_s^2$ is a proportionality constant. The implementation of the coefficients $[c]$, $[a]$, and $[d_a]$, as well as the implementation of the magnetic anisotropy as an additional Source node, is identical to Implementation 2.

In the Coefficient Form PDE node for the magnetic scalar potential, there must be two internal Coefficient Form PDE nodes. In the first one, only the ferromagnetic materials should be selected from the geometry. Here, the coefficients have the form

$$[c] = \boxed{1}$$

$$[\gamma] = \begin{array}{|c|} \hline m1 \\ \hline m2 \\ \hline m3 \\ \hline \end{array}$$

In the second Coefficient Form PDE node, only the non-magnetic materials in the geometry should be selected and

$$[c] = \boxed{1}$$

All other coefficients are set to zero.

The geometry of the system follows the rules analogous to Implementations 1 and 2, but for the three-dimensional system. The Rectangle elements are replaced by the Block elements. Additionally, in the study presented in publication [P5], as shown in Figure 3.1b, two Cylinder elements are used. One, barely visible at this scale, is used to create a nanodot. The second Cylinder element replaces the Rectangle node for the non-magnetic area. The bases of the Cylinder are where the Bloch boundary conditions are applied. The Dirichlet boundary condition is applied on the side of the Cylinder.

The implementation of the free boundary conditions, Dirichlet boundary conditions, and Bloch boundary conditions is created in the same way as in the eigenfrequency study in Implementation 1.

All studies in Implementation 3 are identical to Implementation 2 and the rules presented in the subsections *Relaxation of magnetic state* and *Eigenfrequency study* should be followed.

Chapter 4

Research

In this Chapter, I present the results of my studies on the impact of the interactions between ferromagnetic layers on the spin-wave dynamics in the form of five research articles. Four of these articles have been published in peer-reviewed journals, while the last one has been published as a preprint and is currently under review. Each research article is preceded by an introduction describing the main results of the article and the contribution of the Author. The Chapter ends with the presentation of the outlook and other studies carried out during the doctoral studies.

4.1 [P1] Spin-wave diode and circulator based on unidirectional coupling

The Dzyaloshinskii–Moriya interaction leads to the non-reciprocity of the dispersion relation of a thin film in the Damon–Eshbach configuration as shown in Figure 2.6f, while the other interactions do not. The idea of this paper was to study a double-layer system where one layer is in contact with a heavy metal layer inducing DMI while the other layer is not. In such a case, the dispersion relation of the first layer is asymmetric, while the second is symmetric. The main point was to select the layers so that on one side of the dispersion relation, the branches of isolated layers are far apart, while on the opposite side of the dispersion, the branches cross or even overlap in the wide frequency range. As shown in Figure 2.7b, the interaction between the spin waves in a heterogeneous double-layer system is the strongest at the crossing of the dispersions of isolated layers, or at least when they are close to each other. Therefore, in this system, the layers should interact strongly with each other for the spin waves propagating in one direction, while they will interact weakly in the opposite direction. We called this effect the *unidirectional coupling*. It was successfully obtained in the multilayer system Py(3)/NM(5)/Co(2)/Pt¹, where it was observed in a very wide frequency range of about 10 GHz. The asymmetric character of the effect suggested its possible use in the design of non-reciprocal devices, which task was

¹NM is the non-magnetic layer, numbers in brackets are thicknesses of layers in nanometers

performed as well. The designs of a spin-wave diode and a spin-wave circulator of nm size were demonstrated. The design of the diode was possible thanks to the high damping usually present in the Co/Pt systems. In the diode forward direction, the spin wave was not coupled between the layers and passed through the system. In the reverse direction, the spin wave was transmitted from Py to Co and strongly attenuated there, so that the transmission was very low. For the spin-wave circulator, the four-port circulator was demonstrated and the design of the three-port circulator was proposed. It was also shown that these devices can work efficiently in a wide range of frequencies.

Contribution of the Author

In this publication, I have participated in all steps, starting from the idea, the problem definition (together with M. Krawczyk and G. Gubbiotti), the execution of all numerical simulations, their interpretation and discussion (together with all co-authors), the preparation of the whole manuscript, the submission of the manuscript and the correspondence with the journal.

Spin-Wave Diode and Circulator Based on Unidirectional Coupling

Krzysztof Szulc^{1,*}, Piotr Graczyk², Michał Mruczkiewicz^{3,4}, Gianluca Gubbiotti⁵, and Maciej Krawczyk^{1,†}


¹*Faculty of Physics, Adam Mickiewicz University, Poznań, Uniwersytetu Poznańskiego 2, Poznań 61-614, Poland*

²*Institute of Molecular Physics, Polish Academy of Sciences, M. Smoluchowskiego 17, Poznań 60-179, Poland*

³*Institute of Electrical Engineering, SAS, Bratislava 841 04, Slovakia*

⁴*Centre for Advanced Materials Application CEMEA, Slovak Academy of Sciences, Dúbravská cesta 5807/9, Bratislava 845 11, Slovakia*

⁵*Istituto Officina dei Materiali del CNR (CNR-IOM), Sede Secondaria di Perugia, c/o Dipartimento di Fisica e Geologia, Università di Perugia, Perugia I-06123, Italy*

 (Received 20 November 2019; revised 20 June 2020; accepted 18 August 2020; published 25 September 2020)

In magnonics, a fast-growing branch of wave physics characterized by low energy consumption, it is highly desirable to create circuit elements useful for wave computing. However, it is crucial to reach the nanoscale so as to be competitive with the electronics, which vastly dominates in computing devices. Here, based on numerical simulations, we demonstrate the functionality of the spin-wave diode and the circulator to steer and manipulate spin waves over a wide range of frequency in the GHz regime. They take advantage of the unidirectional magnetostatic coupling induced by the interfacial Dzyaloshinskii-Moriya interaction, allowing the transfer of the spin wave between thin ferromagnetic layers in only one direction of propagation. Using the multilayered structure consisting of Py and Co in direct contact with heavy metal, we obtain submicrometer-size nonreciprocal devices of high efficiency. Thus, our work contributes to the emerging branch of energy-efficient magnonic logic devices, giving rise to the possibility of application as a signal-processing unit in the digital and analog nanoscaled spin-wave circuits.

DOI: [10.1103/PhysRevApplied.14.034063](https://doi.org/10.1103/PhysRevApplied.14.034063)

I. INTRODUCTION

A diode and a circulator are electronic and microwave components, which have found wide applications in many devices for signal processing. A diode allows the flow of signal in only one direction, and for microwaves, it is also known as an isolator. It already has equivalents in optics [1], heat transfer [2,3], acoustics [4,5], and spin Seebeck effect [6]. Diodes for spin waves (SWs) relying on the dipolar [7–9] or interfacial Dzyaloshinskii-Moriya interaction (IDMI) [10] were recently proposed. In circulators, the signal going from one port is always directed only to the nearest port, according to the same sense of rotation. It usually consists of three or four ports. Apart from microwaves and photonics, where the circulators have found applications [11–14], they have been recently demonstrated also for acoustic waves [15], while a demonstration for SWs is still missing. Circulators used in industry are mostly macroscopic devices. Their miniaturization with the possibility of implementation to real-life systems is a crucial point of the present studies.

Antisymmetric exchange interaction was described by Dzyaloshinsky [16] and Moriya [17] about 60 years ago. Recently, it has found interest due to induced chirality of the magnetization configuration [18,19] and nonreciprocity in the SW propagation [20–25]. The DMI can exist in bulk noncentrosymmetric crystals [26] or at the interface between ferromagnetic and heavy-metal layers (IDMI). The IDMI is of high interest due to a larger DMI constant value [27,28], flexibility in shaping its strength, and the possibility of working at the nanoscale.

In this paper, we propose a layered sequence of ultrathin ferromagnetic films where the presence of IDMI over one layer leads to asymmetric or even unidirectional coupling of SWs between the layers. Interestingly, the multilayer composition can work as a SW diode or a three- or four-port SW circulator, in dependence on the particular structuration. The proposed SW diode, based on Py ($\text{Ni}_{80}\text{Fe}_{20}$) and Co ultrathin films, offers isolation of SW signal in the reverse direction reaching 22 dB with respect to the transmission in the forward direction. From the application point of view, the functionality of the device is preserved for a broad GHz-frequency range. We investigate the coupling between SWs in a heterogeneous ultrathin bilayer by numerical frequency-domain and time-dependent simulations. Then we discuss the coupling strength and the

*krzysztof.szulc@amu.edu.pl

†krawczyk@amu.edu.pl

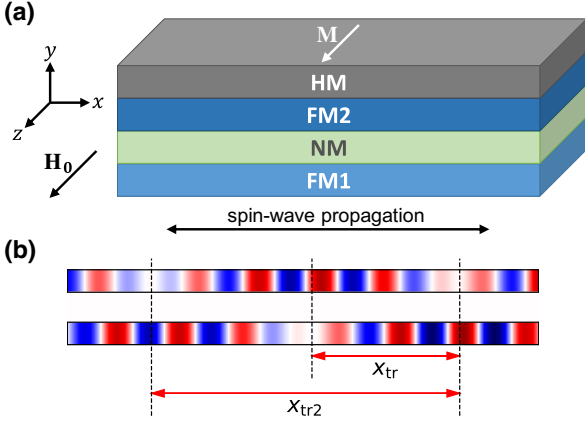


FIG. 1. (a) Schematic representation of the multilayer stack and the geometry considered. The layer sequence consists of two ferromagnetic films, FM1 and FM2, separated by the nonmagnetic layer (NM). In FM2, the IDMI is induced by the proximity with the heavy metal (HM). Generally, this structure underlies the unidirectional coupling in a wide range of frequency. (b) Definition of the transmission lengths x_{tr} and x_{tr2} on the basis of the SW in the coupled FM bilayer system.

SW transmission between the layers in the framework of the coupled-mode theory. Finally, we present possible realizations of the SW devices—the SW diode and the four-port circulator, with in-depth analysis of their efficiency.

The considered multilayer stack consists of two ferromagnetic (FM) layers separated by a nonmagnetic spacer, and heavy-metal layer in contact with one of the FM layers [Fig. 1(a)]. We consider SW propagation in the Damon-Eshbach geometry, where the magnetization \mathbf{M} and the external magnetic field H_0 are aligned in plane of the films and perpendicular to SW propagation defined by the wavevector \mathbf{k} .

II. THEORETICAL MODEL

Magnetization dynamics in the systems under investigation are described by the Landau-Lifshitz-Gilbert equation:

$$\frac{\partial \mathbf{M}}{\partial t} = -\gamma \mu_0 \mathbf{M} \times \mathbf{H}_{\text{eff}} + \frac{\alpha}{M_S} \mathbf{M} \times \frac{\partial \mathbf{M}}{\partial t}, \quad (1)$$

where $\mathbf{M} = (m_x, m_y, m_z)$ is the magnetization vector, γ is the gyromagnetic ratio, μ_0 is the magnetic permeability of vacuum, and H_{eff} is the effective magnetic field, which is given as follows:

$$\mathbf{H}_{\text{eff}} = H_0 \hat{z} + \frac{2A_{\text{ex}}}{\mu_0 M_S^2} \nabla^2 \mathbf{M} + \frac{2D}{\mu_0 M_S^2} \left(\hat{z} \times \frac{\partial \mathbf{M}}{\partial x} \right) - \nabla \varphi, \quad (2)$$

where A_{ex} is the exchange stiffness constant, D is the IDMI constant, and φ is the magnetic scalar potential fulfilling

Maxwell equations in a magnetostatic approximation:

$$\nabla^2 \varphi = \nabla \cdot \mathbf{M}. \quad (3)$$

Equations (1) and (3) are solved numerically in the linear approximation, i.e., assuming $m_x, m_y \ll m_z \approx M_S$, where M_S is saturation magnetization, using the finite-element method in COMSOL Multiphysics environment [29]. Frequency-domain simulations are carried out to calculate the SW dispersion relation in the system of coupled FM layers. Time-domain simulations are performed to demonstrate the functionality of the designed devices. A dynamic magnetic field is used to excite the system sinusoidally at the desired frequency. We use triangular mesh with a maximum element size of 1 nm inside the FM layers and a growth rate of 1.15 outside of the FM layers. We assume that the NM spacer is made from a dielectric material. The metallic layer, such as Cu or Au, can screen the dipolar microwave field [30], causing the reduction of the dipolar interaction between the layers and changing the dispersion relation. However, the effect is negligible for the thin spacer.

In the first step of calculations, we consider a multilayer of the Py(3 nm)/NM(5 nm)/Co(2 nm)/Pt composition. For the Co layer we assume $M_S = 956$ kA/m, exchange stiffness constant $A_{\text{ex}} = 21$ pJ/m [31], Gilbert damping constant $\alpha = 0.05$, IDMI constant $D = -0.7$ mJ/m² [32], and for Py layer $M_S = 800$ kA/m, $A_{\text{ex}} = 13$ pJ/m, $\alpha = 0.005$, $D = 0$. External static magnetic field H_0 is fixed to 50 mT.

A. Coupled-mode theory with damping

The SWs propagating in the system composed of two FM layers separated by a NM layer are magnetostatically coupled. We can describe this phenomenon using general coupled-mode theory [33,34] based only on the wave properties. To describe the interaction between propagating modes, we use coupling-in-space formalism. The differential equation describing the scalar wave ψ_l propagating in a single layer l is

$$\frac{d\psi_l}{dx} = -i\beta_l \psi_l, \quad (4)$$

with

$$\beta_l = k_l' - i\alpha_l k_l'' \quad (5)$$

denoting the complex wavevector, where the real part corresponds to the propagation, and the imaginary part to the attenuation of the wave. For the waves propagating in two coupled layers, we get the mutually dependent differential equations:

$$\frac{d\psi_1}{dx} = -i\beta_1 \psi_1 + \kappa_{12} \psi_2, \quad (6)$$

$$\frac{d\psi_2}{dx} = -i\beta_2\psi_2 + \kappa_{21}\psi_1, \quad (7)$$

where for the codirectional coupling, i.e., coupling of the waves propagating in the same direction

$$\kappa_{12} = -\kappa_{21} = \frac{1}{2} (|k_P - k_{CP}| - |k_1 - k_2|) \quad (8)$$

are the coupling coefficients. k_P and k_{CP} are wavevectors of the in-phase and in-counterphase modes of the coupled bilayered system, respectively. Generally, the waves can be described by the complex numbers with the coupling magnitude described with the right side of Eq. (8). In our case, we are only interested in the magnitude of coupling, and not the phase of the wave, which derives from the argument of κ_{12} .

The system of differential equations [Eqs. (6) and (7)] can be reduced to the homogeneous linear equations. Assuming that the solutions are in the form of $e^{-i\beta x}$, the solvability condition requires that

$$\beta^2 - (\beta_1 - \beta_2)\beta + (\beta_1\beta_2 + \kappa_{12}\kappa_{21}) = 0. \quad (9)$$

The solutions of this equation are

$$\beta_{\pm} = \bar{\beta} \pm B, \quad (10)$$

where

$$\bar{\beta} = \frac{\beta_1 + \beta_2}{2}, \quad B = \sqrt{\Delta\beta^2 + |\kappa_{12}|^2}, \quad \text{and}$$

$$\Delta\beta = \frac{\beta_1 - \beta_2}{2}.$$

Substituting the solutions of Eq. (10) to Eqs. (6) and (7) and assuming the initial conditions as $\psi_1(0) = A$ and $\psi_2(0) = 0$, we end with the general solutions for the coupled wave functions

$$\psi_1(x) = A \left(\cos Bx - i \frac{\Delta\beta}{B} \sin Bx \right) e^{-i\bar{\beta}x}, \quad (11)$$

$$\psi_2(x) = A \frac{\kappa_{21}}{B} \sin Bx e^{-i\bar{\beta}x}. \quad (12)$$

In the synchronous state $k'_1 = k'_2 = k'$, so we can determine transmission length x_{tr} of the wave from layer 1 to layer 2 [see Fig. 1(b)] from zeroing of the term in the brackets in Eq. (11):

$$x_{tr} = \frac{1}{B} \left(\frac{\pi}{2} - \arctan \frac{i\Delta\beta}{B} \right). \quad (13)$$

In the synchronous state, $\Delta\beta = -i(\alpha_1 k'_1 - \alpha_2 k'_2)$, so the term in the arctangent is real. In the case when the wave is transferred from the layer with lower damping to the layer with higher damping, the transmission length becomes larger, while in the opposite case, it becomes smaller. If $-\Delta\beta^2 > |\kappa_{12}|^2$, then the parameter B becomes imaginary, and if $\alpha_1 k'_1 < \alpha_2 k'_2$ then $x_{tr} < 0$ and complete transmission cannot be achieved (the structure behaves like an over-damped harmonic oscillator), while if $\alpha_1 k'_1 > \alpha_2 k'_2$ then $x_{tr} > 0$ and complete transmission can be achieved but only once.

We can also extract “there and back transmission” length x_{tr2} considering the length at which the wave transfers from layer 1 to layer 2 and then transfers back from layer 2 to layer 1 [see Fig. 1(b)]. The solution comes from zeroing of the sine term in Eq. (12). The lowest positive solution is

$$x_{tr2} = \frac{\pi}{B}. \quad (14)$$

At this point, we have to introduce the SW parameters to the coupled-mode theory. Knowing that $\omega' = v_{ph}k'$ and $\omega'' = v_{gr}k''$ [35], where v_{ph} is the phase velocity and v_{gr} – the group velocity of the SW, Eq. (5) is transformed into

$$\beta_l = \frac{1}{v_{ph,l}} \omega'_l - \frac{i\alpha_l}{v_{gr,l}} \omega''_l, \quad (15)$$

where the real ω' and imaginary ω'' parts of the frequency of a single layer in the Damon-Eshbach geometry are defined as [21,35]

$$\omega' = \gamma\mu_0 \left(\sqrt{\left(H_0 + \frac{M_S}{4} + \frac{2A_{ex}}{\mu_0 M_S} k^2 \right) \left(H_0 + \frac{3M_S}{4} + \frac{2A_{ex}}{\mu_0 M_S} k^2 \right) - \frac{e^{-4|k|d} M_S^2}{16} (1 + 2e^{2|k|d}) + \frac{2D}{\mu_0 M_S} k} \right), \quad (16)$$

$$\omega'' = \gamma\mu_0 \left(H_0 + \frac{M_S}{2} + \frac{2A_{ex}}{\mu_0 M_S} k^2 + \frac{2D}{\mu_0 M_S} k \right). \quad (17)$$

The value of the κ_{12} is determined from the dispersion relation of the coupled bilayer system obtained in the numerical simulations. The parameters in Eq. (8) are calculated for the given frequency ω' .

B. Coupling parameters

To describe the coupling between the SWs propagating in a bilayered structure, we define the two coupling parameters between the FM layers. The first is the power-transfer factor F_P , which relies upon the dispersion relation. From the coupled-mode theory, we get that the power-transfer factor is [34]

$$F_P = \frac{f_{\text{coup}}^2}{f_{\text{coup}}^2 + \Delta f^2}, \quad (18)$$

where

$$\Delta f = |f_1 - f_2|, \quad \text{and} \quad (19)$$

$$f_{\text{coup}} = f_P - f_{\text{CP}} - \Delta f, \quad (20)$$

$f_1 = \omega_1/2\pi$, $f_2 = \omega_2/2\pi$ are frequencies of the SWs in the single layers, f_P and f_{CP} are frequencies of SWs, related to the in-phase and in-counterphase oscillations of the amplitude in the coupled layers, respectively, discussed later in more details.

The second parameter is the energy-distribution factor F_E . We assume that the mode energy of fully coupled SWs is shared equally between both FM layers. The mode energy for uncoupled SWs is accumulated only in one of the layers. The total energy density in the i th layer is

$$E_i = E_{i,\text{dip}} + E_{i,\text{ex}}, \quad (21)$$

where the dipolar-energy density E_{dip} is defined as

$$E_{i,\text{dip}} = \frac{1}{L_i} \frac{1}{2\mu_0} \iint_{S_i} \mathbf{m} \cdot \nabla \varphi \, dy \, dx, \quad (22)$$

and the exchange-energy density E_{ex}

$$E_{i,\text{ex}} = \frac{1}{L_i} \frac{A_{\text{ex}}}{M_S^2} \iint_{S_i} (\nabla \mathbf{m})^2 \, dy \, dx, \quad (23)$$

where L_i is the length of the FM layer in the simulations, $S_i = d_i L_i$, where d_i is the thickness of FM layer, and $\mathbf{m} = (m_x, m_y)$ is a dynamical component of the magnetization.

The energy-distribution factor is defined as follows:

$$F_E = 1 - \frac{1}{2} \left| \frac{E_1^P - E_2^P}{E_1^P + E_2^P} \right| - \frac{1}{2} \left| \frac{E_1^{\text{CP}} - E_2^{\text{CP}}}{E_1^{\text{CP}} + E_2^{\text{CP}}} \right|. \quad (24)$$

Values of F_P and F_E are in the range $[0,1]$, where we interpret 0 as no coupling and 1 as a full coupling between SWs propagating in the FM layers.

III. RESULTS

A. Unidirectional coupling in the wide range of frequency

The first step of the investigation of the SW dynamics is the calculation of a dispersion relation. In Fig. 2, we plot the dispersion relations of the Py(3)/NM(5)/Co(2)/Pt multilayer (solid lines) and uncoupled Co(2)/Pt (dashed lines) and Py(3) (dotted lines) layers for two different values of IDMI constant. For $D = 0$ [Fig. 2(a)] all dispersion relations are almost symmetric with respect to $k = 0$ with only small asymmetry related to dipolar interaction. A small change of the dispersion relation for the multilayer, in comparison to the uncoupled layers, is the effect of weak coupling between the FM layers. Taking the nonzero IDMI constant, we introduce strong nonreciprocity to the SW dispersion of the mode related to the Co layer. Interestingly, for $D = -0.7 \text{ mJ/m}^2$ [see Fig. 2(b)] the dispersion relation for the Co layer almost overlaps with the dispersion relation for Py in the broad range of positive wavevector. Since both modes have almost the same frequency (resonance) and wavevector (phase matching), one can expect strong interaction between them in the multilayer system [34]. Two interacting modes are hybridized forming collective excitations, with in-phase (at frequency f_P) [see inset 3 in Fig. 2(b)] and in-counterphase (at frequency f_{CP}) [see inset 4 in Fig. 2(b)] SW modes at a higher and lower frequency, respectively [29,36]. Indeed, we can see the repulsion of the dispersion branches related to the in-phase and in-counterphase modes for positive k in the multilayer [see the red and blue curves in Fig. 2(b)], being the effect of strong dipolar coupling between modes in Py and Co. For the negative wavevectors, the dispersions for the uncoupled FM layers are well separated, and in the multilayer, they follow the same lines pointing at the weak coupling between FM layers [see insets 1 and 2 in Fig. 2(b)]. Comparing both dispersions in Figs. 2(a) and 2(b), we conclude that adding IDMI to the Co layer can lead to strong SW coupling between FM layers for the waves propagating in one ($+k$) direction, while in the structure without IDMI, the coupling is weak and symmetrical. The general procedure for achieving unidirectional coupling is described in the Appendix.

At this point, we can look at the SW propagation in the Py(3)/NM(5)/Co(2)/Pt multilayer. The model of the investigated structure is shown in Fig. 2(c). The antenna located in the Py layer excites the SW at 15.2-GHz frequency. Over the antenna, we made the indent in the Co/Pt layer to avoid the excitation coming from the dipolar field. It comes from the dispersion relation in Fig. 2(b) that a SW propagating in $+x$ direction should be influenced by the strong coupling between Co and Py layer while propagating in $-x$ direction should go through the Py layer only weakly interacting with the Co layer. Indeed, on the right side

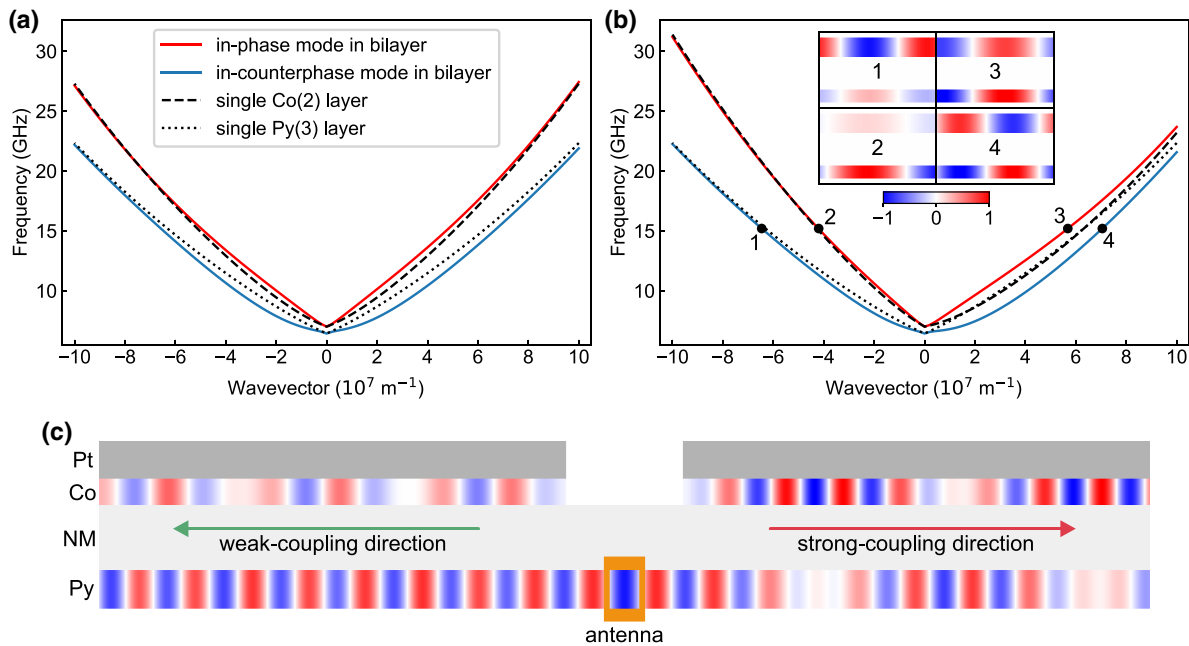


FIG. 2. (a),(b) Dispersion relation of SWs as a function of wavevector k in the Py(3)/NM(5)/Co(2)/Pt multilayer for the IDMI constant in the Co layer (a) $D = 0$ and (b) $D = -0.7 \text{ mJ/m}^2$. For reference, we show the dispersion relation of SWs in the uncoupled Pt/Co and Py layers with dashed and dotted lines, respectively. In the insets in (b), we show the m_x amplitude of the SWs propagating in both directions at 15.2 GHz. For $D = 0$, the dispersion relation is almost symmetrical with respect to $k = 0$. For $D = -0.7 \text{ mJ/m}^2$, the IDMI breaks the symmetry leading to strongly coupled modes in the $+k$ range (insets 3 and 4) and single-layer excitation in the $-k$ range (insets 1 and 2). The highest coupling occurs in the region of overlapping of the dispersion relation of the uncoupled layers. (c) Propagation of the SW at 15.2-GHz frequency in the Py(3)/NM(5)/Co(2)/Pt multilayer. The antenna is located in the Py layer, below the indent in the Co/Pt layer. SW propagating in the $+x$ direction transfers back and forth between Py and Co layer. The transmission to the Co layer in the $-x$ direction is weak, and most of the SW intensity remains in the Py layer.

of Fig. 2(c) a SW appears alternately in Co and Py layer being the effect of the interference between in-phase and in-counterphase modes. On the left side, most of the SW intensity remains in the Py layer, with only weak transfer to the Co layer being the effect of weak dynamic coupling. We term this effect as a unidirectional coupling.

For further investigations, the determination of the SW coupling in a broad spectrum is the crucial point. For this purpose, we use the coupling parameters defined in Eqs. (18) and (24). In Fig. 3, we plot F_P (vertical axis) and F_E (color of the points) in the Pt/Co(2)/NM/Py(3) multilayer with $D = -0.7 \text{ mJ/m}^2$ for different thicknesses of NM layer in dependence on the wavevector of the SW. On the positive k side, both coupling parameters are very close to the maximum value in the range between two dispersion crossing points (1.6×10^7 and $6.3 \times 10^7 \text{ m}^{-1}$). That means the SWs are nearly fully coupled in a wide range of wavevector and frequency. On the negative k side, the coupling is significant only in the long-wavelength range, reaching its maximum for $k \approx -2 \times 10^7 \text{ m}^{-1}$. The increase of the thickness of the NM spacer leads to a decrease of coupling parameters, except the range of strong coupling between the dispersion crossing points. It is

ascribed to the weaker dipolar interaction between the layers.

Another important parameters associated with the coupling between the two layers are the transmission lengths defined in Eqs. (13) and (14). Many parameters affect these physical quantities. We focus on two of them, which are important in our study—the damping constant and the NM-layer thickness. In Fig. 4(a), we show the transmission length in the Py(3)/NM(5)/Co(2)/Pt multilayer depending on the damping constant in the Co layer. In the simulations, the SW source emitting the SW at frequency $\omega'/2\pi = 15.2 \text{ GHz}$ is located in the Py layer. From Eq. (17), we get $\omega''/2\pi = 20.6 \text{ GHz}$ for the Co layer and 19.2 GHz for the Py layer. Results from the numerical simulations are compared with Eqs. (13) and (14) derived from the coupled-mode theory. We get a satisfying agreement between these approaches. Both x_{tr} and x_{tr2} are increasing with the increase of the damping constant. However, x_{tr} is growing faster than x_{tr2} leading to the conclusion that the transmission length from the layer with higher damping (Co layer) to the layer with lower damping (Py layer) is decreasing with the increase of the damping constant. In Fig. 4(b), we show the transmission

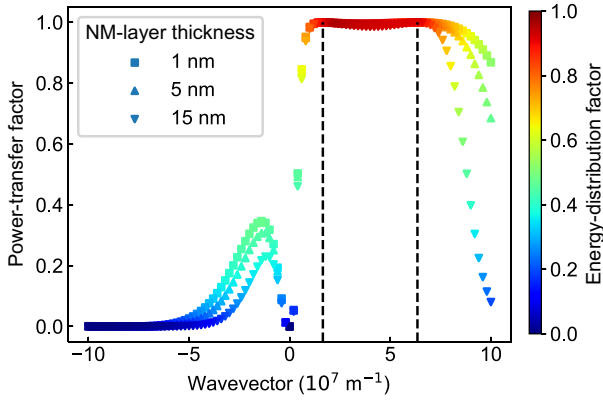


FIG. 3. Power-transfer factor F_P (the vertical axis) and energy-distribution factor F_E (color scale) as a function of the wavevector in the Py(3)/NM(t)/Co(2)/Pt multilayer with the IDMI constant in the Co layer $D = -0.7 \text{ mJ/m}^2$ for three different thicknesses of the NM layer. We reach coupling parameters close to a maximum value of 1 in the range between 1.6×10^7 and $6.3 \times 10^7 \text{ m}^{-1}$ (marked with dashed lines). In the negative k range, the coupling is weak and reduces with the increase of the NM-layer thickness.

length in the Py(3)/NM(t)/Co(2)/Pt multilayer depending on the NM-layer thickness t . We assume $\alpha_{\text{Co}} = \alpha_{\text{Py}} = 0$. The transmission length is increasing with the exponential character of growth. When $\Delta\beta = 0$, Eq. (13) reduces to the form $x_{\text{tr}} = \pi/(2|\kappa_{12}|)$. Thus, the coupling coefficient is decreasing exponentially with the increase of the separation between the layers [37].

B. Spin-wave diode

Taking into account the unidirectional coupling discussed above, we can design the SW diode. The proposed structure is shown in Fig. 5. It consists of continuous Py film, which is the medium where the SWs propagate from the input to the output and Co/Pt stripe, which is a functional element of a diode where IDMI introduces non-reciprocal interaction. They are separated by a 5-nm-thick NM spacer, which is sufficient to neglect Ruderman-Kittel-Kasuya-Yosida interaction. We chose the frequency of the SW from the crossing point of the dispersion relation of uncoupled layers shown in Fig. 2(b) to get the full coupling between FM layers. The width of the Co/Pt stripe is matched to the transmission length x_{tr} , which is related to the coupling strength and the damping in the layers. To determine the efficiency of the device, we calculate the power loss $d_P = 10 \log(E_{\text{in}}/E_{\text{out}})$, where E_{in} is the energy measured in the steady state in front of the device and E_{out} behind the device, calculated according to Eq. (21).

The operation of the diode is depicted in Figs. 5(a) and 5(b), which shows results from the time-domain simulations of SW continuously excited at the 15.2-GHz frequency in Py at the antenna (A). We fix the width of the

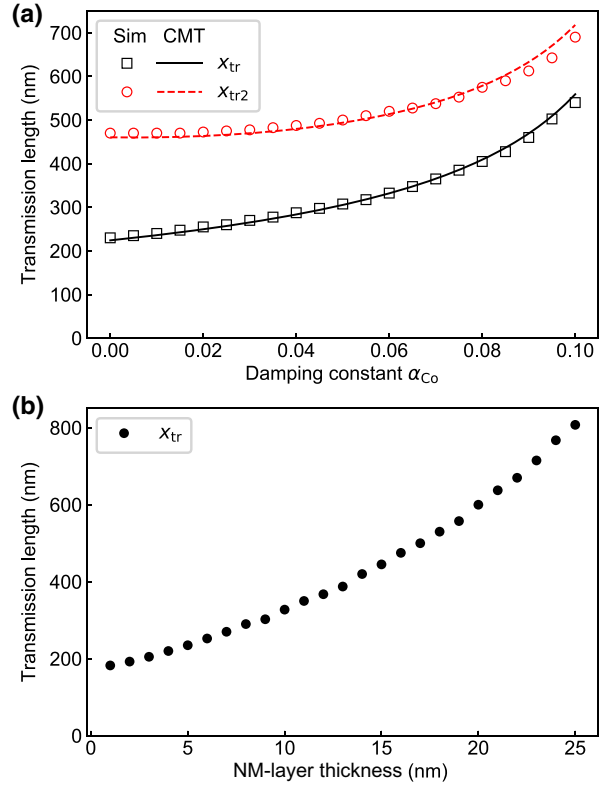


FIG. 4. Transmission-length dependence on (a) the damping constant in the Co layer in the Py(3)/NM(5)/Co(2)/Pt multilayer with the damping in the Py $\alpha_{\text{Py}} = 0.005$ and (b) the thickness of NM layer in the Py(3)/NM(t)/Co(2)/Pt multilayer. The source of the SW of 15.2 GHz is located in the Py layer. In (a), the simulations (Sim) results are compared with Eqs. (13) and (14) from the coupled-mode theory (CMT). In (b), we present only the simulation results for x_{tr} .

Co/Pt stripe to 320 nm. The signal for efficiency analysis is collected from the areas marked as input and output ports, which are located at a distance of 20 nm from the Co/Pt stripe edges. Due to weak coupling between the SWs propagating in the $-x$ direction [Fig. 5(a), see also the animation, Movie S1, within the Supplemental Material [38]], the transmission to the Co stripe is small, and the SW passes the diode retaining its intensity. The total power loss in this direction reaches 3.3 dB, and it is mainly due to the Gilbert damping in Py (2.2 dB). On the other hand, the SW propagating in the $+x$ direction [Fig. 5(b), see also the animation, Movie S2, within the Supplemental Material [38]] transfers almost entirely to the Co stripe where it is strongly attenuated due to the high damping. Some residual intensity at the output is the effect of incomplete transfer to Co and return transfer from Co after reflections from the boundaries of the stripe. In fact, along the reverse direction, the total power loss increases to 25 dB. To sum up, the difference in the SW energy in the forward and reverse

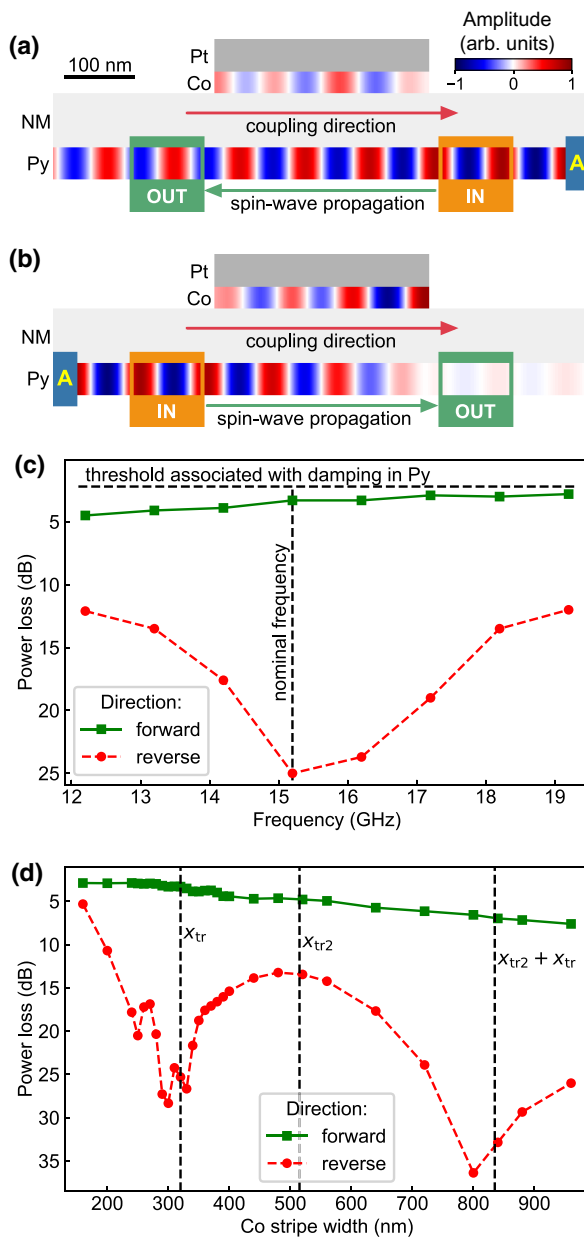


FIG. 5. (a),(b) Propagation of the SW (m_x component) in a diode at 15.2-GHz frequency in Py(3)/NM(5)/Co(2)/Pt in (a) forward and (b) reverse direction for the width of the Co/Pt stripe 320 nm. In (a), the SW propagation direction is opposite to the coupling direction, so that the SW transfers weakly to the Co stripe, and we get a signal of high intensity in the output. In (b), the SW propagation direction is the same as the coupling direction, so that the SW transfers to the Co stripe, where is strongly damped, leading to the low intensity of the signal at the output. (c) The power loss in the forward and reverse direction in dependence on the frequency. In a broad frequency range of 7 GHz, the SW diode preserves its strong isolating properties. (d) The power loss in the forward and reverse direction in dependence on Co stripe width.

direction equals 21.7 dB. The change of the position of the ports impacts the power loss only by the damping in the Py layer, thus it is not changing the difference between the forward and reverse direction.

We investigate the efficiency of the Py(3)/NM(5)/Co(2)/Pt SW diode in the wide range of frequency. Obtained results of the power loss in both directions of propagation are collected in Fig. 5(c). Although SW transmission length varies in dependence on the frequency, the structure preserves strongly asymmetric transmission in a broad range of frequency. In the forward direction, the diode works as well as in nominal frequency. The power loss is decreasing with the frequency due to the decrease of the coupling for negative wavevectors as shown in Fig. 3. The power loss in the reverse direction is reduced but remains significantly higher than in the forward direction. Estimated relative frequency range in which the device works is $\Delta\omega'/\omega'_0 \approx 0.5$ (at $\omega'_0/2\pi = 15.2$ GHz).

Additional simulations are made to check the efficiency of the diode for different widths of the Co stripe at 15.2 GHz. The results are presented in Fig. 5(d). The power loss in the forward direction is mainly associated with the damping in the Py layer. A small negative slope reflects the increasing distance between the input and output. In the reverse direction, the most substantial effect on the results come from the SW transmission between the Py and Co layers. The curve reaches the first minimum for 300 nm, being close to $x_{tr} = 320$ nm, then increases up to $x_{tr2} = 515$ nm, and decreases again, reaching the second minimum near $x_{tr2} + x_{tr} = 835$ nm. The power loss in the reverse direction at x_{tr2} is significantly higher than in the forward direction because the SW intensity strongly decreases during the propagation through the Co stripe. Moreover, we perform detailed investigations in the vicinity of x_{tr} in Fig. 5(d) to check if the resonance effect in Co stripe plays any role in the coupling. Indeed, the local maxima and minima in both forward and reverse directions are present with an approximate period of $\lambda/2 = 50$ nm, confirming the influence of the resonance on the power-loss value. However, its impact is small in comparison with the interlayer SW transmission. In conclusion, we show that the SW diode is efficient in a wide range of the Co stripe width.

Moreover, we investigate the SW diode working with SWs of longer (390 nm) wavelength, which should simplify the detection of the effect experimentally. We select another crossing point from Fig. 2(b), located at 8.2-GHz frequency. The width of the Co stripe is set to 190 nm. We obtain a power loss of 6.7 dB in the forward direction and 14.6 dB in the reverse direction. In this case, we distinguish three mechanisms responsible for the smaller efficiency of the diode. First, SWs of longer wavelength are coupled stronger than SWs of shorter wavelength. This effect is shown in Fig. 3. The SW at 8.2 GHz corresponds

to $k = 1.6 \times 10^7 \text{ m}^{-1}$. The coupling for negative k reaches its maximum in the vicinity of this point. This effect leads to an additional decrease in the signal in the forward direction. Second, the width of the Co stripe is too small to attenuate the SWs in reverse direction effectively. Third, the SW tends to reflect partially inside the Py layer in the points where the Co layer has its boundaries, which leads to additional losses. Besides these limitations, which can be further optimized, the structure is still efficient enough to be considered as a diode.

C. Four-port spin-wave circulator

Next, we exploit the unidirectional coupling further to design a SW circulator. The schematic structure of the four-port circulator is shown in Fig. 6. As compared with the structure of the diode, an additional FM layer is present on the opposite side of the stripe, playing the role of two additional ports. To get the functionality of the circulator, we need the stripe, which is unidirectionally coupled with both top and bottom layers but in opposite directions of SW propagation. We achieve this condition by taking identical outer layers having opposite IDMI constant and the inner stripe lacking IDMI. In our case, we propose to use Py as an IDMI-free coupling stripe and Co/Pt as guiding layers with swapped order in the bottom and top layers. The separation between the stripe and the layer is increased to 15 nm to reduce the dipolar coupling between the Co layers. We keep the width of the Py stripe sufficient to transfer the SW fully from one layer to another, thus for 15.2 GHz, we assume 440 nm. The SW is excited by antenna A, and the SW energy is measured by the ports located 20 nm from the device. Moreover, we perform simulations with assuming no damping to check the efficiency in the ideal case, while the effect of the damping constant is presented further. The structure has a center of symmetry, therefore, the ports on the same diagonal, i.e., P1 and P3 as well as P2 and P4, work identically, and it is sufficient to investigate only two cases—propagation in the coupling and the noncoupling direction.

In the noncoupling case, antenna A is located in the upper-right corner and emits the SWs at 15.2 GHz propagating to the left, as shown in Fig. 6(a) [see also the animation, Movie S3, within the Supplemental Material [38]]. We observe very weak transfer of energy to the Py stripe, so the SW propagates mainly in the top Co layer. The SWs of low intensity in the bottom Co layer result from direct magnetostatic coupling between Co layers. In the lossless structure, the power loss in port P2 reaches 0.2 dB, port P3—12.8 dB, and port P4—19.4 dB. The coupling direction is shown in Fig. 6(b) [see also the animation, Movie S4, within the Supplemental Material [38]]. Here, antenna A is located in the upper-left corner. The SW is transferred to the Py stripe, and it reflects from the right edge of the stripe. After the reflection, the SW

is coupled with the bottom Co layer, and, as a result, is transferred to it. In the lossless structure, the power loss in port P3 reaches 0.1 dB, port P4—24.9 dB, and port P1—16.1 dB.

The SW circulator can also be used as a SW diode. However, it benefits the mechanism of the redirection rather than the attenuation of a SW. Considering port P1 and P2 as the input-output ports, the transmission from port P1 to port P2 works as a forward direction and the transmission from port P2 to port P1 as a reverse direction. In that case, the difference in the SW energy in the forward and reverse direction equals 15.9 dB.

Figures 6(c) and 6(d) show the power loss in the circulator as the function of NM-layer thickness for the input port P1 and P2, respectively. We assume $\alpha_{\text{Co}} = \alpha_{\text{Py}} = 0$ to focus on the principle transmission properties of the system. The width of the Py stripe is set to the transmission length, which is plotted in Fig. 4(b). In the noncoupling case [Fig. 6(c)], the power loss in the target port P2 is decreasing, reaching almost no loss for about 10 nm, while in port P3 and P4, we see the oscillations. This is the result of the resonance in the Py stripe. This behavior is even more relevant in Fig. 6(d) representing the coupling case. The power loss in the target port P3 is oscillating in counterphase with respect to port P1. The points with large power loss in port P3 correspond to the width w of the Py stripe fulfilling the resonance condition $w = N\lambda/2$, where $\lambda = 100$ nm. In the resonance, the SW is reflecting from the left side of the Py stripe, and it is coupled with the top Co layer. As a result, we observe the increase of the intensity of the SW in port P1 and, simultaneously, decrease of the intensity in port P3. Interestingly, the effect of negative power loss occurs in Fig. 6(d). It comes from the unwanted effect of the weak direct coupling between Co layers. For the thin NM layer, the coupling is significant enough to reach weak SW transmission from the top to bottom Co layer. In that case, we measure the SW energy in the range where we get the maximum value of the transmission. Moreover, the method of calculating the SW energy does not distinguish between the SW propagating in the left and right direction, which can fix this misleading effect. Moreover, because of the weak direct transmission between Co layers, the power loss can vary depending on the position of the antenna, as well as the position of the ports. However, the effect is relatively small for assumed separation between the outer layers, and the circulator preserves its properties even for ports located far away from the Py stripe edges.

The effect of the damping in the Co layers on the SW circulator functionality is shown in Figs. 6(e) and 6(f). The damping constant in the Py layer is set to 0.005. In the noncoupling direction [Fig. 6(e)], the power loss in port P4 is almost constant, ultimately reaching the value of power loss in target port P2 for $\alpha_{\text{Co}} \approx 0.035$. The mechanism is identical to the one described in Fig. 6(d). The Co layers

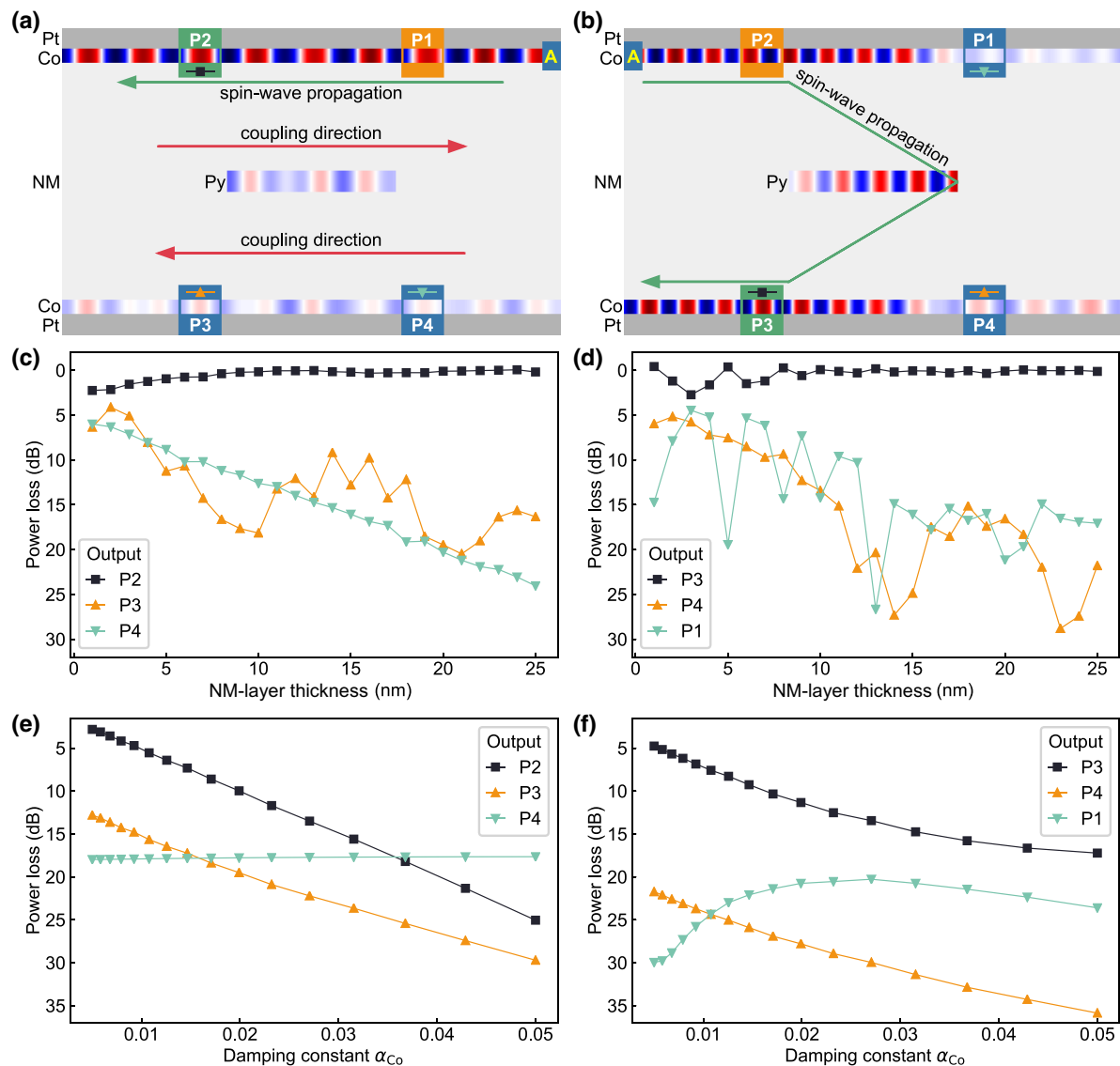


FIG. 6. (a),(b) Model of the four-port SW circulator based on the multilayered structure with unidirectional coupling. Propagation of the SW (m_x component) of 15.2-GHz frequency in the lossless Pt/Co(2)/NM(15)/Py(3)/NM(15)/Co(2)/Pt circulator in the (a) noncoupling direction and (b) coupling direction. In (a), the antenna A is located in the upper-right corner. The SW transfers weakly to the Py layer, so it goes mainly to port P2. In (b), the antenna A is located in the upper-left corner. The SW transfers from the upper Co layer to Py, and after the reflection from the right side of Py, it transfers to the lower Co layer, reaching port P3 in the end. A small-amplitude signal visible at isolated ports is a result of weak direct magnetostatic coupling between Co layers. (c),(d) The power loss measured in the output ports in regard to the input port in dependence on the NM-layer thickness for the input located in (c) port P1 and (d) port P2. In (c), the power loss in the target port P2 is increasing and in the rest of the ports is decreasing with the increase of NM-layer thickness. In (d), the power loss in the target port P3 and port P1 is fluctuating due to the resonance in the Py stripe. The minima of the power loss are corresponding to the Py stripe width fulfilling the resonance condition. (e),(f) The power loss measured in dependence on the damping constant in the Co layer for the input located in (e) port P1 and (f) port P2. In (e), the power loss in port P4 is almost constant, ultimately reaching the value in the target port P2. In (f), the power loss in the target port P2 is significantly larger than in the other ports. The SW circulator is not working properly for $\alpha_{Co} > 0.025$.

are coupled, which leads to the additional SW energy in port P4 coming from the SW going into the circulator. The power loss in port P4 exceeds 35 dB when the SW going into the circulator is excluded from the calculations

of the power loss using the reference simulations without the Py stripe. In the coupling direction [Fig. 6(f)], the power loss in port P1 is decreasing with increasing α_{Co} and approaches the value of the power loss in target port P3.

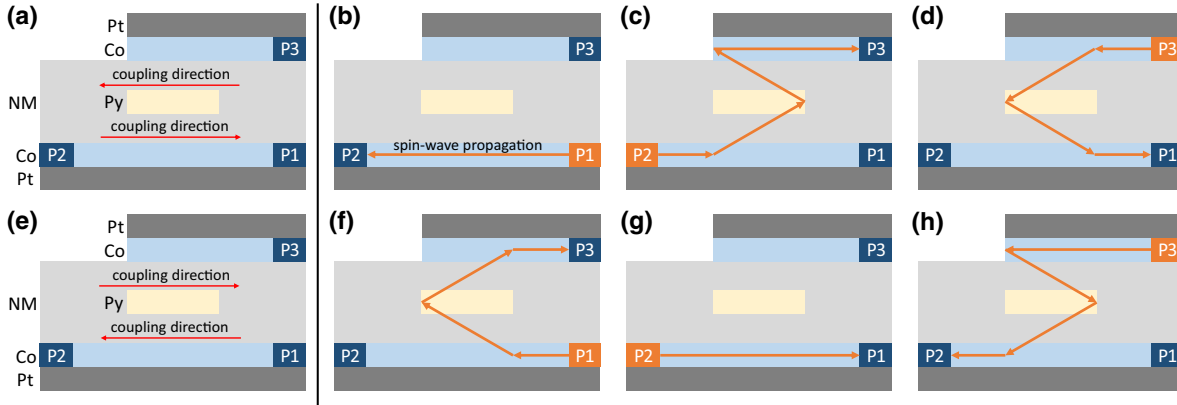


FIG. 7. Three-port SW circulator in (a)–(d) easy-input and (e)–(h) easy-output port P3 configurations. We present the models (a),(e) and the way of acting when the input of SWs is localized in (b),(f) port P1, (c),(g) port P2, and (d),(h) port P3. The coupling direction determines the direction in which the SW will be transmitted from one layer to another. The orange arrows directing from one layer to another denote the SW transmission.

This effect comes from the fact that the SW has to be transmitted from Co to Py as well as from Py to Co. The sign of $\Delta\beta$ in Eq. (13) is opposite for these two cases, and with increasing the difference between the transmission lengths in both directions, the circulator becomes less efficient. In comparison with the SW diode, the damping is, in general, an adverse effect in the SW circulator, so the materials with strong IDMI and low damping are highly desirable. A recent paper indicates Co/Ru as a possible low-damping alternative of Co/Pt bilayers [28,32]. The SW circulator remains efficient for the damping constant $\alpha_{Co} = 0.017$ reported in Ref. [32].

D. Three-port spin-wave circulator

Along with the four-port circulator, we can propose the three-port circulator with a slightly modified structure, as shown in Fig. 7. As compared to the structure of the four-port circulator, here the upper Co/Pt layer length is reduced and consists now from one port. Furthermore, this layer has to fully cover the Py stripe to preserve the possibility of complete transfer of the SW between the layers. The three-port device does not have any symmetries, therefore, we have to take three cases into account independently. Moreover, the number of cases is doubled due to the reversal of the coupling directions. We can distinguish them by considering the efficiency of port P3 localized in the upper Co layer. If the coupling direction between the upper Co layer and Py stripe is directed onto the port P3, we can consider it as an easy-output port because the SW coming from the Py stripe will be directed straight into port P3 [Fig. 7(f)]. On the other hand, with the opposite coupling direction, the SW coming from port P3 will be transmitted directly to the Py stripe [Fig. 7(d)], and port P3 becomes an easy-input port. Figure 7 shows that the wave propagating from port P2 or P3 in the easy-input or easy-output configuration,

respectively, have to reflect two times before reaching the output port [Figs. 7(c) and 7(h)]. On the other hand, in the four-port circulator, only one reflection is needed. It means that the phenomenon in the three-port circulator requires very efficient reflections of SWs from the edges of the stripe. Further investigations are required to optimize its functionality.

IV. CONCLUSIONS

To sum up, we show the effect of unidirectional magnetostatic coupling between the SW modes, which arises due to the IDMI-induced nonreciprocity in the ultrathin multilayer system. The modes related to each layer are strongly coupled in only one direction of the SW propagation in a broad GHz range of frequency. In the opposite direction, within the same range of frequency, the SW modes propagate in only one layer. We propose to exploit this effect for the realization of the magnonic devices in the submicrometer scale. In the Py/NM/Co/Pt structure, limiting the Co/Pt stripe width to the length required to transfer the SW from the Py layer to the stripe, the possibility to get the diode effect is arising. In the forward direction, the SW propagates through the stripe area with small losses associated mainly with the Gilbert damping in Py, while in the reverse direction, the SW transmits to the Co stripe, in which the strong damping significantly reduces the SW intensity in the output. The device works efficiently in a broad range of microwave frequencies, as well as a broad range of Co stripe width. The SW diode can be further improved by opening the possibility to control the magnetization direction in the Co layer and thus becoming the SW transistor [39–45]. The main advantage of the transistor based on the unidirectional coupling is that it will work immediately, so that the time of operation is limited only by the SW velocity and the time needed to reach the steady state.

Another proposed type of the magnonic device, which bases on the same effect, is the SW circulator. It uses the two extended Co layers with Pt inducing IDMI as the waveguides with the input and output ports and the Py stripe in between as a coupler. In each possible case, we get efficient SW transfer to the target port with the strongly suppressed signal at the other ports. The high damping in the Co/Pt films suppresses transmission to the required port of the circulator. To preserve the functionality, the damping constant in the layer shall be smaller than 0.025 and as close as possible to the damping of the Py stripe. In the circulator, the isolation effect in the selected output ports is achieved without involving losses. Moreover, the SW circulator can also work as a diode. A diode and a circulator take a place among the signal processing devices, thus demonstrating unidirectional coupling and proposing magnonic devices open the possibility for further development of energy-efficient, miniaturized beyond-CMOS, magnonic logic components [46–49].

ACKNOWLEDGMENTS

The study has received financial support from the National Science Center of Poland, Projects Nos. UMO-2018/30/Q/ST3/00416 and UMO-2018/28/C/ST3/00052. M.M. acknowledges funding from the Slovak Grant Agency APVV, No. APVV-16-0068 (NanoSky) and APVV-19-0311 (RSWFA). G.G. acknowledges the financial support by the European Metrology Programme for Innovation and Research (EMPIR), under the Grant Agreement 17FUN08 TOPS.

APPENDIX: PROCEDURE FOR ACHIEVING THE UNIDIRECTIONAL COUPLING IN A WIDE FREQUENCY RANGE

The effect of unidirectional coupling of SWs in a wide frequency range can be obtained according to the following procedure. We limit our approach to the Landau-Lifshitz equation consisting of the Zeeman, exchange, magneto-static, and Dzyaloshinskii-Moriya terms [Eq. (1)].

At first, we assume that the external magnetic field is uniform. Next, one should fulfill a condition, that

$$\begin{aligned} &\text{if } M_{S,FM1} > (<) M_{S,FM2}, \\ &\text{then } A_{ex,FM1}/M_{S,FM1} > (<) A_{ex,FM2}/M_{S,FM2}. \end{aligned}$$

It yields the noncrossing of the dispersion relation between noninteracting bilayers. If this condition is not fulfilled, we always will get crossing of the dispersion relations, and the coupling can be only asymmetric rather than unidirectional. Moreover, it is difficult to obtain the effect of coupling in a wide frequency range without fulfilling this condition. In the last step, the DMI parameter has to be fitted to get proper matching of dispersion relations for noninteracting layers.

- [1] M. D. Tocci, M. J. Bloemer, M. Scalora, J. P. Dowling, and C. M. Bowden, Thin-film nonlinear optical diode, *Appl. Phys. Lett.* **66**, 2324 (1995).
- [2] B. Li, L. Wang, and G. Casati, Thermal Diode: Rectification of Heat Flux, *Phys. Rev. Lett.* **93**, 184301 (2004).
- [3] C. W. Chang, D. Okawa, A. Majumdar, and A. Zettl, Solid-state thermal rectifier, *Science* **314**, 1121 (2006).
- [4] B. Liang, B. Yuan, and J.-C. Cheng, Acoustic Diode: Rectification of Acoustic Energy Flux in One-Dimensional Systems, *Phys. Rev. Lett.* **103**, 104301 (2009).
- [5] B. Liang, X. S. Guo, J. Tu, D. Zhang, and J. C. Cheng, An acoustic rectifier, *Nat. Mater.* **9**, 989 (2010).
- [6] S. Borlenghi, W. Wang, H. Fangohr, L. Bergqvist, and A. Delin, Designing a Spin-Seebeck Diode, *Phys. Rev. Lett.* **112**, 047203 (2014).
- [7] J. Wu, X. Yang, S. Beguhn, J. Lou, and N. X. Sun, Nonreciprocal tunable low-loss bandpass filters with ultra-wideband isolation based on magnetostatic surface wave, *IEEE Trans. Microw. Theory Techn.* **60**, 3959 (2012).
- [8] S. Shichi, N. Kanazawa, K. Matsuda, S. Okajima, T. Hasegawa, T. Okada, T. Goto, H. Takagi, and M. Inoue, Spin wave isolator based on frequency displacement nonreciprocity in ferromagnetic bilayer, *J. Appl. Phys.* **117**, 17D125 (2015).
- [9] M. Grassi, M. Geilen, D. Louis, M. Mohseni, T. Brächer, M. Hehn, D. Stoeffler, M. Bailleul, P. Pirro, and Y. Henry, Slow-Wave-Based Nanomagnonic Diode, *Phys. Rev. Appl.* **14**, 024047 (2020).
- [10] J. Lan, W. Yu, R. Wu, and J. Xiao, Spin-Wave Diode, *Phys. Rev. X* **5**, 041049 (2015).
- [11] E. F. Schloemann, Circulators for microwave and millimeter-wave integrated circuits, *Proc. IEEE* **76**, 188 (1988).
- [12] H. Dötsch, N. Bahlmann, O. Zhuromskyy, M. Hammer, L. Wilkens, R. Gerhardt, P. Hertel, and A. F. Popkov, Applications of magneto-optical waveguides in integrated optics: Review, *J. Opt. Soc. Am. B* **22**, 240 (2005).
- [13] V. G. Harris, A. Geiler, Y. Chen, S. D. Yoon, M. Wu, A. Yang, Z. Chen, P. He, P. V. Parimi, X. Zuo, C. E. Patton, M. Abe, O. Acher, and C. Vittoria, Recent advances in processing and applications of microwave ferrites, *J. Magn. Magn. Mater.* **321**, 2035 (2009).
- [14] W. Śmigaj, J. Romero-Vivas, B. Gralak, L. Magdenko, B. Dagens, and M. Vanwolleghem, Magneto-optical circulator designed for operation in a uniform external magnetic field, *Opt. Lett.* **35**, 568 (2010).
- [15] R. Fleury, D. L. Sounas, C. F. Sieck, M. R. Haberman, and A. Alù, Sound isolation and giant linear nonreciprocity in a compact acoustic circulator, *Science* **343**, 516 (2014).
- [16] I. Dzyaloshinsky, A thermodynamic theory of “weak” ferromagnetism of antiferromagnetics, *J. Phys. Chem. Solids* **4**, 241 (1958).
- [17] T. Moriya, Anisotropic superexchange interaction and weak ferromagnetism, *Phys. Rev.* **120**, 91 (1960).
- [18] X. Yu, Y. Onose, N. Kanazawa, J. Park, J. Han, Y. Matsui, N. Nagaosa, and Y. Tokura, Real-space observation of a two-dimensional skyrmion crystal, *Nature* **465**, 901 (2010).
- [19] G. Chen, J. Zhu, A. Quesada, J. Li, A. T. N’Diaye, Y. Huo, T. P. Ma, Y. Chen, H. Y. Kwon, C. Won, Z. Q. Qiu, A. K. Schmid, and Y. Z. Wu, Novel Chiral Magnetic

- Domain Wall Structure in Fe/Ni/Cu(001) Films, *Phys. Rev. Lett.* **110**, 177204 (2013).
- [20] L. Udvardi and L. Szunyogh, Chiral Asymmetry of the Spin-Wave Spectra in Ultrathin Magnetic Films, *Phys. Rev. Lett.* **102**, 207204 (2009).
- [21] J.-H. Moon, S.-M. Seo, K.-J. Lee, K.-W. Kim, J. Ryu, H.-W. Lee, R. D. McMichael, and M. D. Stiles, Spin-wave propagation in the presence of interfacial Dzyaloshinskii-Moriya interaction, *Phys. Rev. B* **88**, 184404 (2013).
- [22] D. Cortés-Ortuño and P. Landeros, Influence of the Dzyaloshinskii-Moriya interaction on the spin-wave spectra of thin films, *J. Phys.: Condens. Matter* **25**, 156001 (2013).
- [23] A. A. Stashkevich, M. Belmeguenai, Y. Roussigné, S. M. Cherif, M. Kostylev, M. Gabor, D. Lacour, C. Tiusan, and M. Hehn, Experimental study of spin-wave dispersion in Py/Pt film structures in the presence of an interface Dzyaloshinskii-Moriya interaction, *Phys. Rev. B* **91**, 214409 (2015).
- [24] J. Cho, N.-H. Kim, S. Lee, J.-S. Kim, R. Lavrijsen, A. Solignac, Y. Yin, D.-S. Han, N. J. van Hoof, H. J. Swagten, B. Koopmans, and C.-Y. You, Thickness dependence of the interfacial Dzyaloshinskii-Moriya interaction in inversion symmetry broken systems, *Nat. Commun.* **6**, 7635 (2015).
- [25] M. Garst, J. Waizner, and D. Grundler, Collective spin excitations of helices and magnetic skyrmions: Review and perspectives of magnonics in non-centrosymmetric magnets, *J. Phys. D: Appl. Phys.* **50**, 293002 (2017).
- [26] S. Mühlbauer, B. Binz, F. Jonietz, C. Pfleiderer, A. Rosch, A. Neubauer, R. Georgii, and P. Böni, Skyrmion lattice in a chiral magnet, *Science* **323**, 915 (2009).
- [27] S. Tacchi, R. E. Troncoso, M. Ahlberg, G. Gubbiotti, M. Madami, J. Åkerman, and P. Landeros, Interfacial Dzyaloshinskii-Moriya Interaction in Pt/CoFeB Films: Effect of the Heavy-Metal Thickness, *Phys. Rev. Lett.* **118**, 147201 (2017).
- [28] A. Samardak, A. Kolesnikov, M. Stebliy, L. Chebotkevich, A. Sadovnikov, S. Nikitov, A. Talapatra, J. Mohanty, and A. Ognev, Enhanced interfacial Dzyaloshinskii-Moriya interaction and isolated skyrmions in the inversion-symmetry-broken Ru/Co/W/Ru films, *Appl. Phys. Lett.* **112**, 192406 (2018).
- [29] P. Graczyk, M. Zelent, and M. Krawczyk, Co- and contra-directional vertical coupling between ferromagnetic layers with grating for short-wavelength spin wave generation, *New J. Phys.* **20**, 053021 (2018).
- [30] S. Seshadri, Surface magnetostatic modes of a ferrite slab, *Proc. IEEE* **58**, 506 (1970).
- [31] C. Moreau-Luchaire, C. Moutafis, N. Reyren, J. Sampaio, C. Vaz, N. Van Horne, K. Bouzehouane, K. Garcia, C. Deranlot, P. Warnicke, P. Wohlhüter, J.-M. George, M. Weigand, J. Raabe, V. Cros, and A. Fert, Additive interfacial chiral interaction in multilayers for stabilization of small individual skyrmions at room temperature, *Nat. Nanotechnol.* **11**, 444 (2016).
- [32] T. Štěpka, P. Neilinger, A. Samardak, A. Kolesnikov, A. Ognev, A. Sadovnikov, V. Gubanov, S. Nikitov, K. Palotás, E. Simon, L. Szunyogh, J. Dérer, V. Campbell, and M. Mrućkiewicz, Damping in Ru/Co-based multilayer films with large Dzyaloshinskii-Moriya interaction, arXiv:1911.02467 (2019).
- [33] A. Yariv, Coupled-mode theory for guided-wave optics, *IEEE J. Quantum Electron.* **9**, 919 (1973).
- [34] K. Zhang and D. Li, *Electromagnetic Theory for Microwaves and Optoelectronics* (Springer-Verlag, Heidelberg, 2008), 2nd ed.
- [35] A. G. Gurevich and G. A. Melkov, *Magnetization Oscillations and Waves* (CRC press, New York, 1996).
- [36] M. Mrućkiewicz, M. Krawczyk, V. K. Sakharov, Y. V. Khivintsev, Y. A. Filimonov, and S. A. Nikitov, Standing spin waves in magnonic crystals, *J. Appl. Phys.* **113**, 093908 (2013).
- [37] P. Grünberg, Magnetostatic spin-wave modes of a heterogeneous ferromagnetic double layer, *J. Appl. Phys.* **52**, 6824 (1981).
- [38] See Supplemental Material at <http://link.aps.org/supplemental/10.1103/PhysRevApplied.14.034063> for the animations of the SW transmission through the diode and the circulator.
- [39] P. Graczyk and M. Krawczyk, Nonresonant amplification of coherent spin waves through voltage-induced interface magnetoelectric effect and spin-transfer torque, arXiv:2001.07474 (2020).
- [40] A. I. Nikitchenko and N. A. Pertsev, Spin injection and pumping generated by a direct current flowing through a magnetic tunnel junction, *Phys. Rev. B* **99**, 224426 (2019).
- [41] Z. Duan, C. T. Boone, X. Cheng, I. N. Krivorotov, N. Reckers, S. Stienen, M. Farle, and J. Lindner, Spin-wave modes in permalloy/platinum wires and tuning of the mode damping by spin Hall current, *Phys. Rev. B* **90**, 024427 (2014).
- [42] E. Padrón-Hernández, A. Azevedo, and S. M. Rezende, Amplification of spin waves in yttrium iron garnet films through the spin Hall effect, *Appl. Phys. Lett.* **99**, 192511 (2011).
- [43] A. Khitun, D. E. Nikonov, and K. L. Wang, Magnetoelectric spin wave amplifier for spin wave logic circuits, *J. Appl. Phys.* **106**, 123909 (2009).
- [44] M. Balinskiy, A. C. Chavez, A. Barra, H. Chiang, G. P. Carman, and A. Khitun, Magnetoelectric spin wave modulator based on synthetic multiferroic structure, *Sci. Rep.* **8**, 10867 (2018).
- [45] K. An, D. R. Birt, C.-F. Pai, K. Olsson, D. C. Ralph, R. A. Buhrman, and X. Li, Control of propagating spin waves via spin transfer torque in a metallic bilayer waveguide, *Phys. Rev. B* **89**, 140405(R) (2014).
- [46] Y. Au, M. Dvornik, O. Dmytriiev, and V. Kruglyak, Nanoscale spin wave valve and phase shifter, *Appl. Phys. Lett.* **100**, 172408 (2012).
- [47] A. V. Chumak, A. A. Serga, and B. Hillebrands, Magnon transistor for all-magnon data processing, *Nat. Commun.* **5**, 4700 (2014).
- [48] R. Cheng, M. W. Daniels, J.-G. Zhu, and D. Xiao, Antiferromagnetic spin wave field-effect transistor, *Sci. Rep.* **6**, 24223 (2016).
- [49] J. Cramer, F. Fuhrmann, U. Ritzmann, V. Gall, T. Niizeki, R. Ramos, Z. Qiu, D. Hou, T. Kikkawa, J. Sinova, U. Nowak, E. Saitoh, and M. Kläui, Magnon detection using a ferroc collinear multilayer spin valve, *Nat. Commun.* **9**, 1089 (2018).

4.2 [P2] Multifunctional operation of the double-layer ferromagnetic structure coupled by a rectangular nanoresonator

This study was done together with Pierre Roberjot, who came from University Rennes 1 in France for one semester as part of the double-diploma program. For this time, he joined our group and I was his research co-supervisor. This work is the continuation of the research presented in the article [P1]. The effect presented there was based on the non-reciprocity of the dispersion relation in the system with Dzyaloshinskii–Moriya interaction. As shown in Figure 2.7, the asymmetry can also be induced by only the dipolar coupling of two different layers in the Damon–Eshbach geometry. This was also the case for the system in [P1], but thicknesses of the layers were very small and the asymmetry resulting from the dipolar interaction alone was not pronounced. In this study, we decided to use thicker layers to obtain stronger coupling. We also decided to start with the system that could work as a device. This was achieved by taking the system with two Co layers acting as spin-wave conduits, separated by a thick non-magnetic layer in which the resonator in the form of a long Py strip was placed. Such a system forms a four-port device. The numerical simulations in the time domain showed that, depending on the frequency of the spin wave, this system can act as a circulator, a directional coupler, or a reflector. We attributed this character to the behavior of the resonator. We found that in the Damon–Eshbach configuration, the resonator has only one standing mode and the other modes are rotating modes. In such a case, the excitation of a rotating mode can lead to the redirection of a spin wave to the particular output.

Contribution of the Author

In this publication, I defined the problem together with M. Krawczyk, performed the numerical simulations in COMSOL of the eigenfrequency problem, supervised the simulations performed by P. Roberjot, participated in the interpretation and discussion of results, prepared Figures 2 and 3, wrote part of the description of the results, prepared the Supplementary Material, and made corrections to the manuscript.

Multifunctional operation of the double-layer ferromagnetic structure coupled by a rectangular nanoresonator

Cite as: Appl. Phys. Lett. **118**, 182406 (2021); doi: [10.1063/5.0046001](https://doi.org/10.1063/5.0046001)

Submitted: 31 January 2021 · Accepted: 9 April 2021 ·

Published Online: 5 May 2021



View Online



Export Citation



CrossMark

Pierre Roberjot, Krzysztof Szulc,^{a)} Jarosław W. Kłos,^{a)} and Maciej Krawczyk^{a)}

AFFILIATIONS

Institute of Spintronics and Quantum Information, Faculty of Physics, Adam Mickiewicz University, Poznań, Uniwersytetu Poznańskiego 2, 61-614 Poznań, Poland

Note: This paper is part of the APL Special Collection on Mesoscopic Magnetic Systems: From Fundamental Properties to Devices.

^{a)}Authors to whom correspondence should be addressed: krzysztof.szulc@amu.edu.pl and krawczyk@amu.edu.pl

ABSTRACT

The use of spin waves as a signal carrier requires developing the functional elements allowing for multiplexing and demultiplexing information coded at different wavelengths. For this purpose, we propose a system of thin ferromagnetic layers dynamically coupled by a rectangular ferromagnetic resonator. We show that single and double, clockwise and counterclockwise, circulating modes of the resonator offer a wide possibility of control of propagating waves. Particularly, at frequency related to the double-clockwise circulating spin-wave mode of the resonator, the spin wave excited in one layer is transferred to the second one where it propagates in the backward direction. Interestingly, the wave excited in the second layer propagates in the forward direction only in that layer. This demonstrates add-drop filtering and circulator functionality. Thus, the proposed system can become an important part of future magnonic technology for signal routing.

Published under license by AIP Publishing. <https://doi.org/10.1063/5.0046001>

A modern society is experiencing a rapidly growing demand for interconnected wireless facilities, known as Internet of Things (IoT),^{1,2} which requires the development of faster ways to communicate and lower energy consumption to satisfy the environmental sustainability.³ IoTs are devices receiving and sending back information using microwaves, and thus, the spin waves (SWs) are perfect candidates to be used in these developments.⁴ This is due to the same range of frequencies as microwaves and a few orders shorter wavelengths, enabling miniaturization down to the nanoscale. The SWs allow processing both the analog and digital signals at low energy cost, being inductively coupled to microwaves and compatible with CMOS technology.^{5–7}

A possibility of frequency-dependent SW routing in a multiport device is essential to build any complex magnonic system.⁸ Therefore, implementation of the magnonic counterpart of the channel add-drop filter, which was demonstrated in photonics,^{9,10} is highly desirable. The crucial element of the add-drop filter is the resonator, e.g., a dot, a stripe, or a ring, where the resonant modes mediate the coupling between the waves in unconstrained conduits. The resonance related to the fundamental mode of the stripe is widely explored to control the SW propagation, and the interesting effects related to the chirality of

the magnetostatic-stray-field coupling have already been demonstrated.^{11–13} On the other hand, the ring-shaped resonators, extensively investigated in photonics, have been tested as a coupler between two SW waveguides, only recently.¹⁴ However, a single solid element with the circulating modes for SW routing remains unexplored.

In our paper, we investigate theoretically a system composed of two Co ferromagnetic films coupled through a multimode resonant element—a stripe of the rectangular cross section made from Py (Ni₈₀Fe₂₀). We observe various kinds of SW eigenmodes in the stripe. In particular, we found resonance modes in the form of single and double, clockwise (CW) and counterclockwise (CCW), circulating waves. Our study goes along the exploitation of these modes for various functionalities, including add-drop filtering and a circulator. Our study is in line with recent activities in magnonics aiming in prototyping functional magnonic devices, like diodes,¹⁵ circulators,¹⁶ couplers,^{17,18} multiplexers,¹⁹ and logic gates.^{20–24}

This paper is organized as follows. First, we present the geometry of the structure. Then, we describe the dispersion relations of the subsystems and analyze the eigenmode spectra. Finally, we demonstrate the operation of the system at different frequencies and present a summary.

We consider a system composed of two parallel, infinitely extended in the xy -plane, 5 nm-thick Co films and a resonant element in the form of a Py stripe of thickness 50 nm and width 100 nm placed between the films and oriented along the z -axis, as presented in Fig. 1(a). The stripe is separated from the films by the 10 nm-thick nonmagnetic spacers. The system is magnetized by a uniform in-plane bias magnetic field of magnitude $\mu_0 H_0 = 0.05$ T directed along the stripe and perpendicular to the direction of SW propagation. We assume the magnetization saturation and the exchange constant of Co to be $M_S = 1100$ kA/m and $A = 20$ pJ/m, respectively, and for Py $M_S = 850$ kA/m and $A = 13$ pJ/m. The gyromagnetic ratio for the whole structure is $\gamma = 175.95 \times 10^9$ rad/(sT). We consider the Damon–Eshbach geometry, where the SW group velocity and the magnetostatic coupling are significant.⁵

We consider the system shown in Fig. 1(a) as a four-terminal magnonic device, from which one is selected as an input (I1 or I3) and the others as outputs (O1, O2, O3, and O4), as shown in Fig. 1(b). We want to guide the signal between pairs of selected terminals through the stripe element by properly tuning the frequency of the excited SW.

To describe the propagation in the system, we solve numerically the Landau–Lifshitz–Gilbert equation,

$$\frac{\partial \mathbf{M}}{\partial t} = -\gamma \mu_0 \mathbf{M} \times \mathbf{H}_{\text{eff}} + \frac{\alpha}{M_S} \mathbf{M} \times \frac{\partial \mathbf{M}}{\partial t}, \quad (1)$$

where $\mathbf{M} = (m_x, m_y, m_z)$ is the magnetization vector, μ_0 is the magnetic permeability of vacuum, α is the dimensionless damping parameter, and \mathbf{H}_{eff} is the effective magnetic field,

$$\mathbf{H}_{\text{eff}} = \mathbf{H}_0 + \mathbf{H}_m + \mathbf{H}_{\text{ex}}, \quad (2)$$

which is a sum of the external magnetic field $\mathbf{H}_0 = H_0 \hat{z}$, the magnetostatic field $\mathbf{H}_m = -\nabla \varphi$, and the exchange field $\mathbf{H}_{\text{ex}} = \frac{2A}{\mu_0 M_S^2} \nabla^2 \mathbf{M}$. φ is the scalar magnetic potential that fulfills Maxwell equations in the magnetostatic approximation,

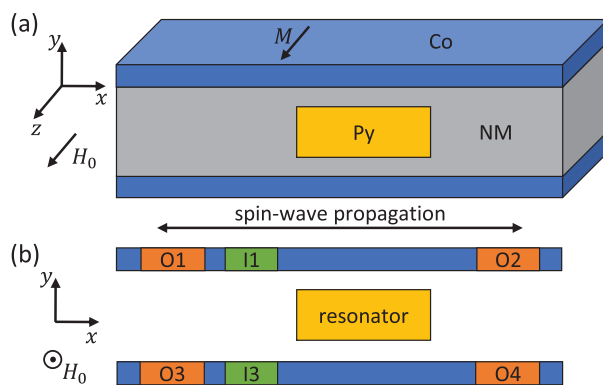


FIG. 1. (a) The geometry of the bilayer structure under investigation. The system consists of two Co layers and a Py stripe separated by a nonmagnetic material. The separation between the layers and the stripe is 10 nm, the thickness and the width of the stripe are 50 nm and 100 nm, respectively, and the thickness of the layers is 5 nm. (b) Schematic representation of the four-terminal device. The possible positions for the inputs, i.e., the sources of SWs, are marked in green, while the four outputs in gray.

$$\nabla^2 \varphi = \nabla \cdot \mathbf{M}. \quad (3)$$

We linearized Eq. (1), assuming the harmonic time dependence $\exp(-i\omega t)$ and H_0 saturating the sample. We split the magnetization and the magnetostatic field into the static components parallel to the z -axis, $m_z = M_S$, $H_{m,z} = 0$, and the dynamic components lying in the xy -plane, $\mathbf{m} = [m_x, m_y, 0]$, $\mathbf{H}_m = [-\partial_x \varphi, -\partial_y \varphi, 0]$. With these approximations, we have performed the finite-element method (FEM) simulations of the magnetization dynamics using COMSOL Multiphysics.

First, we solve the eigenproblem based on linearized Eq. (1) using the frequency-domain solver in order to obtain the dispersion relation of SWs. In these simulations, the Floquet–Bloch boundary conditions are applied along the x -direction at the edges of the unit cell, which reproduce the effect of infinite layers. We neglect damping in these studies.

In the second approach, we solve linearized Eq. (1) in the time domain and for the finite structure. We used this approach to demonstrate functionality of the proposed devices. We excite the SWs in the input port with an antenna positioned 20 nm from the stripe edge. The antenna generates a dynamic magnetic sinusoidal signal of small amplitude,

$$S_{\text{ant}}(t) = 10^{-7} \gamma \mu_0 M_S^2 \sin(2\pi f_0 t), \quad (4)$$

where f_0 is the frequency of excitation and the antenna's width $w_{\text{ant}} = \pi/k_{z0}$, with k_{z0} being a wavenumber at the excitation frequency determined numerically from the dispersion relation obtained in frequency-domain simulations. In order to avoid reflection of the SWs from the system edges, we assume a linearly increasing damping at the edges of the Co layers. The excitation lasts 3 ns, which is sufficient to observe the SW propagation and a resonant behavior, if present.

In order to understand the impact of the stripe on the propagation of the SWs in the bilayered structure, we calculate the dispersion relations and the eigenmode spectra for two additional systems. The first one is made of two 5 nm-thick Co layers, separated by 70 nm-thick nonmagnetic material. The second one is a single Py stripe of width 100 nm and thickness 50 nm, i.e., the system in Fig. 1(a) without the Co layers.

The dispersion relation of the Co bilayer without a resonator is shown in Fig. 2. There are two bands with the frequency difference proportional to the dynamical coupling between the SWs in the layers.^{16,25,26} The low- (blue) and high-frequency (red) modes can be assigned to antisymmetric and symmetric oscillations in the top and the bottom Co layer, respectively. We notice that these branches are getting closer with the increase in the frequency (and the wavevector), which means that the coupling between the two layers is getting weaker with the decreasing wavelength of the propagating waves. This magnetostatic coupling between layers means that the SW excited in one layer will transfer between the layers periodically during the propagation. The distance on which the SW migrates between the layers is defined by the coupling strength. This effect was exploited in the directional couplers.^{17,18,26–28}

The spectrum of the eigenmodes of the second subsystem is presented in Fig. 2 with dashed black lines and indicates SW resonant modes of the infinitely long Py stripe with the magnetization saturated along the z -axis. In the investigated frequency range, the six modes are

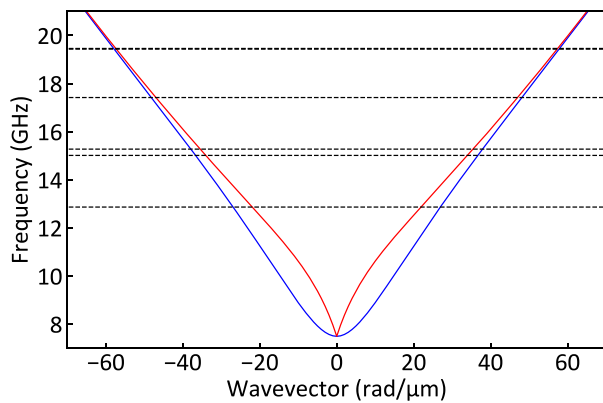


FIG. 2. Dispersion relation of SWs in the subsystem composed of two Co layers separated by 70-nm-thick nonmagnetic material (red and blue solid lines) and the eigenfrequencies of the Py stripe of width 100 nm and thickness 50 nm (horizontal dashed black lines).

present with two pairs of the modes very close in frequency, at about 15 and 19 GHz. To analyze the types of resonant excitations, we plot in Fig. 3 the amplitude and phase of the y -component of the magnetization, $\text{Abs}(m_y)$ and $\text{Arg}(m_y)$, respectively. We can see a fundamental mode with the in-phase oscillations in the stripe cross section at 15.28 GHz. Interestingly, all other modes are CW or CCW circulating SWs, as indicated by the continuous change of the SW phase in Fig. 3(b) and marked with the white arrows. We also found the modes composed of the two CCW (at 15.01 GHz) or two CW (19.43 GHz) circulated oscillations, and we will call them double-CCW and

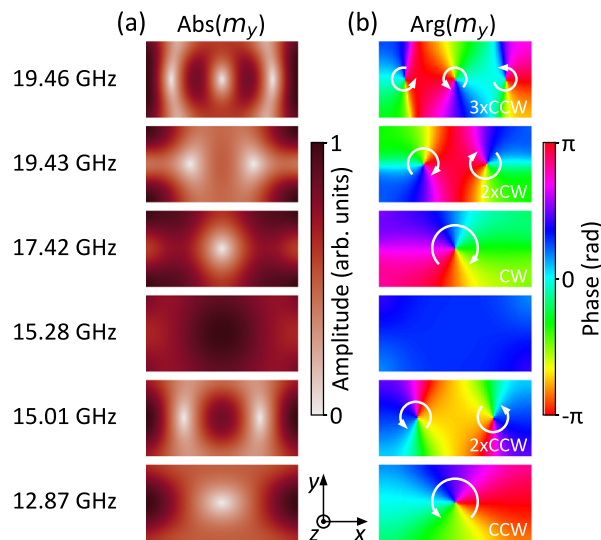


FIG. 3. Amplitude (a) and phase (b) of the m_y component of the magnetization in the isolated Py stripe for the modes shown by dashed black lines in Fig. 2. The CW and CCW modes are indicated in (b) with the continuous phase change. The two zeros of the amplitude at 15.01 and 19.43 GHz indicate double CCW and CW circulating modes, respectively.

double-CW circulating modes, respectively. All considered CCW modes have lower frequency, than the corresponding CW modes, which points at the presence of a nonreciprocity in this system. As shown in Fig. 3(b), the double circulating modes present circulations possessing a relative phase shift by 180° at the top and the bottom edges of the stripe. These two properties shall cause different coupling of the circulating resonant modes to the modes propagating in the same direction in the upper and lower ferromagnetic layers or, alternatively, a different coupling between the modes propagating in the same layer, but in the opposite directions. Indeed, this feature is used to control waves in the waveguides coupled with the ring resonators and whispering gallery modes in photonics^{29–31} and magnonics.^{14,32} We will use this property for demonstration of the SW circulator.

The gradient of the phase on the sides of the resonator depends on the number of circulation areas, which is one for single CW/CCW and two for double-CW/double-CCW modes [see Fig. 3(b)]. We expect that if the gradient of the phase at the top and bottom edge of the resonator matches the wavenumber and the phase change of the SW propagating in the ferromagnetic layer, there will be an enhanced transmission of the SW in one and suppressed in the opposite direction of propagation.

Before studying the transfer of SWs between Co layers at frequencies close to the circulating resonances of the Py stripe, we also analyzed the dispersion relation of the base system, i.e., bilayered structure with the Py stripe in-between, with periodic boundary conditions along the x -axis. The spectra (shown in the supplementary material, Sec. 1) have many bandgaps between more or less dispersive bands, and it is significantly different from the spectra of the two Co layers shown in Fig. 2. This indicates a strong and complex coupling between the propagating modes in the bilayer and the resonant modes of the Py stripe.

To demonstrate how different resonances in the Py stripe influence the coupling and transfer of SWs between the Co layers, we perform time-domain simulations for the four cases. For case 1 at 15 GHz, it is around the resonance of the fundamental and the double-CCW mode. For case 2, we selected the frequency 19 GHz, which is close to the double-CW circular mode of the stripe (mode at 19.43 GHz in Fig. 3). Case 3, 13 GHz, was chosen to be close to the single-CCW circulating mode of the stripe (12.87 GHz in Fig. 3), and case 4, at 17 GHz, was the frequency close to the single-CW circulating mode (mode 17.42 GHz).

Case 1 at 15 GHz is shown in Figs. 4(a) and 4(b) for the SW source placed in the top and the bottom layer, respectively. The SW is transferred to the Py resonator but then transfers back to the Co layer, propagating in the same direction. We can observe two phenomena. First, the SW changes its phase upon the movement through the resonator. Second, the transfer between Co layers is delayed. During propagation, the SW transfers between the layers coupled by the stray dynamic magnetic field, similar to the directional couplers.^{17,26,27,33} Such behavior is also present at low frequencies, i.e., below the fundamental mode of the resonator, where the dynamical magnetostatic coupling between Co layers is strongest, and thus, the period of the transfer between the layers is shortest.

Case 2 is add-drop filtering and circulator. In this case, we found a functionality analogous to the circulator, as demonstrated in Figs. 4(c) and 4(d). In this device, the wave excited in one terminal has to be transferred only to one of the remaining terminals according to

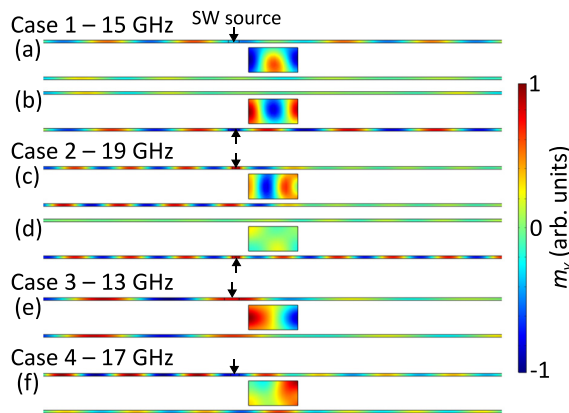


FIG. 4. Dynamic out-of-plane magnetization component m_y plots showing propagation in the investigated structure at selected excitation frequencies after reaching the steady state to demonstrate different functionalities. The wave excited in the top (a) or bottom (b) layer at 15 GHz weakly couples with the resonator. The observed transfer of the wave from the top to the bottom layer is an effect of the direct coupling between the Co layers. This is case 1. (c) The excitation at 19 GHz in the top-left part of the layer is transferred via the resonator to the bottom layer and propagates to the left. (d) The excitation is located in the bottom layer on the left, and the wave propagates straight to the right without coupling. This is operation of the magnonic add-drop filter and circulator, case 2. (e) The wave excited at 13 GHz is transferred through the resonator to the bottom layer and propagates in both directions, case 3. (f) The wave excited in the top layer at 17 GHz is reflected back from the resonator, case 4.

the assumed clockwise or counterclockwise circulation rule.¹⁶ We found the 19 GHz frequency optimal for such a functionality, close to the double-CW circulating mode resonance of the Py stripe (Fig. 3, mode at 19.43 GHz). At this frequency, the wave propagating from the antenna can excite the resonant mode of the stripe, which will act as an energy harvester due to the magnetization circulating mode. Indeed, when the wave is excited on the left side of the top layer (input port I1) [Fig. 4(c)], the Py resonator redirects it to the bottom layer as a wave propagating to the left, to the output port O3. Importantly, an isolation of ports O2 and O4, exceeding 5 times of the signal directed to O3, exists over the 600 MHz range. When the input port is placed in the bottom layer on the left (I3) from the resonator [Fig. 4(d)], the wave propagates directly to port O4 in the same layer. For the wave excited in I4, the resonator redirects to O2, while excited in I2 will propagate to O1. We also observe similar functionality at 13 GHz but with larger leakage of the energy to the other ports. The presented operation can be used for a design of a magnonic circulator or add-drop filtering.

Case 3 at 13 GHz is shown in Fig. 4(e). The wave introduced in port I1 couples with the single-CCW circulating mode in the Py stripe, which allows us to make transfer to the bottom layer and forms waves propagating to the both ports located there, O3 and O4. Although the intensity of the waves reaching ports O3 and O4 differs, the clear splitting of the wave propagating in the top layer has been demonstrated.

In case 4, we introduce the wave at 17 GHz in port I1. As can be seen from Fig. 4(f), the excited wave is transferred to the Py stripe and the circulating mode passes it to different ports but mostly go back to top-left output O1. The Py resonance involved in this operation is related to a single-CW circulating mode, and thus, the functionality

can be expected to be similar to the coupling with the ring resonators¹⁴ or of the circulator shown in case 2. However, the mismatch between the wavelength of the propagating SW and the resonance length results in a weak coupling and unclear operation.

Interestingly, the coupling of SWs excited in the left part of the bottom Co layer (I3 port) with the Py stripe is suppressed at all considered frequencies. We attribute this to the unidirectional magnetization precession and the chirality of the magnetostatic stray field coupling.^{11,12}

The investigations presented above were made without damping in order to have clear visualization of the coupling processes. We also performed the same simulations, but with a damping, we assume in Co layers $\alpha_{Co} = 0.01$ and in Py stripe $\alpha_{Py} = 0.005$. We observed the presence of the same phenomena only with an attenuation. The results are presented in the [supplementary material](#), Fig. S2.

Using a stripe of width 100 nm and thickness 50 nm, we have demonstrated some of the possibilities to control the propagation of the SWs in thin ferromagnetic films at different frequencies. The energy-density plots shown in the [supplementary material](#) (Sec. 3) additionally support these demonstrations. However, the demonstrations were done for selected materials, the one with relative magnetization orientation and at the fixed geometrical parameters. The functionality of the resonance element depends on the wavelength of the propagating wave and its relation to the size of the stripe and chirality of the magnetization precession, and thus, further investigations and model developing are necessary to optimize the operation of the proposed solutions.

In conclusion, we explored numerically the SW behavior in a structure composed of two 5 nm-thick Co layers separated by a rectangular Py stripe, all homogeneously magnetized parallel to the stripe axis. We show that its dispersion relation is significantly different as compared to a bilayer structure due to dynamical coupling of propagating SWs in Co layers with the resonant modes of the Py stripe. Interestingly, the low-frequency part of the isolated-stripe spectra consists of the fundamental mode and a number of single and double, non-degenerated CW and CCW circulating modes. The interaction between propagating SWs in layers and modes circulating in the resonator allows for design add-drop filters and circulators for SWs.

In particular, we show that depending on the direction of the SW propagation and on the excitation frequency, the SWs can transmit in four possible routes: direct propagation between the two Co layers, circulation (SWs are propagating from one layer to the other keeping the direction of propagation), reflection (forth and back to the excitation point), and uncoupled propagation (SWs are propagating in the one layer only). Specifically effective is the use of double-CW circulating mode of the stripe, allowing us to demonstrate the functionality of the magnonic circulator. This shows that the circulating modes in the ferromagnetic stripe are promising for design of signal-processing magnonic devices—especially multiplexers and demultiplexers.

See the [supplementary material](#) for the analysis of the spin-wave band structure of the considered system (Sec. 1), the demonstration of the system functionality with the damping (Sec. 2), and the analysis of the spin-wave energy density distribution in the system (Sec. 3).

The research leading to these results received funding from the Polish National Science Centre, Project No. UMO-2018/30/Q/ST3/00416.

DATA AVAILABILITY

The data that support the findings of this study are available from the corresponding author upon reasonable request.

REFERENCES

- ¹F. Mattern and C. Floerkemeier, "From the internet of computers to the internet of things," in *From Active Data Management to Event-Based Systems and More: Papers in Honor of Alejandro Buchmann on the Occasion of His 60th Birthday*, edited by K. Sachs, I. Petrov, and P. Guerrero (Springer Berlin Heidelberg, Berlin, Heidelberg, 2010), pp. 242–259.
- ²J. Lin, W. Yu, N. Zhang, X. Yang, H. Zhang, and W. Zhao, "A survey on internet of things: Architecture, enabling technologies, security and privacy, and applications," *IEEE Internet Things J.* **4**, 1125–1142 (2017).
- ³L. Roselli, C. Mariotti, P. Mezzanotte, F. Alimenti, G. Orecchini, M. Virili, and N. B. Carvalho, "Review of the present technologies concurrently contributing to the implementation of the internet of things (IoT) paradigm: RFID, green electronics, WPT and energy harvesting," in *IEEE Topical Conference on Wireless Sensors and Sensor Networks (WiSNet)* (2015), pp. 1–3.
- ⁴A. Mahmoud, F. Ciubotaru, F. Vanderveken, A. V. Chumak, S. Hamdioui, C. Adelman, and S. Cotofana, "Introduction to spin wave computing," *J. Appl. Phys.* **128**, 161101 (2020).
- ⁵A. Chumak, V. Vasyuchka, A. Serga, and B. Hillebrands, "Magnon spintronics," *Nat. Phys.* **11**, 453–461 (2015).
- ⁶V. Kruglyak, S. Demokritov, and D. Grundler, "Magnonics," *J. Phys. D: Appl. Phys.* **43**, 264001 (2010).
- ⁷*Magnonics. From Fundamentals to Applications Preface*, edited by S. O. Demokritov and A. N. Slavin (Springer-Verlag, Berlin, Germany, 2013).
- ⁸A. Khitun, M. Bao, and K. L. Wang, "Magnonic logic circuits," *J. Phys. D: Appl. Phys.* **43**, 264005 (2010).
- ⁹S. Fan, P. R. Villeneuve, J. D. Joannopoulos, and H. A. Haus, "Channel drop filters in photonic crystals," *Opt. Express* **3**, 4–11 (1998).
- ¹⁰C. Manolatu, M. J. Khan, S. Fan, P. R. Villeneuve, H. A. Haus, and J. D. Joannopoulos, "Coupling of modes analysis of resonant channel add-drop filters," *IEEE J. Quantum Electron.* **35**, 1322–1331 (1999).
- ¹¹Y. Au, E. Ahmad, O. Dmytriiev, M. Dvornik, T. Davison, and V. V. Kruglyak, "Resonant microwave-to-spin-wave transducer," *Appl. Phys. Lett.* **100**, 182404 (2012).
- ¹²T. Yu, Y. M. Blanter, and G. E. W. Bauer, "Chiral pumping of spin waves," *Phys. Rev. Lett.* **123**, 247202 (2019).
- ¹³J. Chen, T. Yu, C. Liu, T. Liu, M. Madami, K. Shen, J. Zhang, S. Tu, M. S. Alam, K. Xia, M. Wu, G. Gubbiotti, Y. M. Blanter, G. E. W. Bauer, and H. Yu, "Excitation of unidirectional exchange spin waves by a nanoscale magnetic grating," *Phys. Rev. B* **100**, 104427 (2019).
- ¹⁴Q. Wang, A. Hamadeh, R. Verba, V. Lomakin, M. Mohseni, B. Hillebrands, A. V. Chumak, and P. Pirro, "A nonlinear magnonic nano-ring resonator," *npj Comput. Mater.* **6**, 192 (2020).
- ¹⁵M. Grassi, M. Geilen, D. Louis, M. Mohseni, T. Brächer, M. Hehn, D. Stoeffler, M. Bailleul, P. Pirro, and Y. Henry, "Slow-wave-based nanomagnonic diode," *Phys. Rev. Appl.* **14**, 024047 (2020).
- ¹⁶K. Szulc, P. Graczyk, M. Mruczkiewicz, G. Gubbiotti, and M. Krawczyk, "Spin-wave diode and circulator based on unidirectional coupling," *Phys. Rev. Appl.* **14**, 034063 (2020).
- ¹⁷Q. Wang, P. Pirro, R. Verba, A. Slavin, B. Hillebrands, and A. V. Chumak, "Reconfigurable nanoscale spin-wave directional coupler," *Sci. Adv.* **4**, e1701517 (2018).
- ¹⁸Q. Wang, M. Kewenig, M. Schneider, R. Verba, F. Kohl, B. Heinz, M. Geilen, M. Mohseni, B. Lägél, F. Ciubotaru, C. Adelman, C. Dubs, S. D. Cotofana, O. V. Dobrovolskiy, T. Brächer, P. Pirro, and A. V. Chumak, "A magnonic directional coupler for integrated magnonic half-adders," *Nat. Electron.* **3**, 765 (2020).
- ¹⁹F. Heussner, G. Talmelli, M. Geilen, B. Heinz, T. Brächer, T. Meyer, F. Ciubotaru, C. Adelman, K. Yamamoto, A. Sega, B. Hillebrands, and P. Pirro, "Experimental realization of a passive gigahertz frequency-division demultiplexer for magnonic logic networks," *Phys. Status Solidi RRL* **14**, 1900695 (2020).
- ²⁰S. Klingler, P. Pirro, T. Brächer, B. Leven, B. Hillebrands, and A. V. Chumak, "Design of a spin-wave majority gate employing mode selection," *Appl. Phys. Lett.* **105**, 152410 (2014).
- ²¹O. Zografos, S. Dutta, M. Manfrini, A. Vaysset, B. Sorée, A. Naeemi, P. Raghavan, R. Lauwereins, and I. P. Radu, "Non-volatile spin wave majority gate at the nanoscale," *AIP Adv.* **7**, 056020 (2017).
- ²²B. Rana and Y. Otani, "Voltage-controlled reconfigurable spin-wave nanochannels and logic devices," *Phys. Rev. Appl.* **9**, 014033 (2018).
- ²³A. B. Ustinov, E. Lähderanta, M. Inoue, and B. A. Kalinikos, "Nonlinear spin-wave logic gates," *IEEE Magn. Lett.* **10**, 1–4 (2019).
- ²⁴A. Mahmoud, F. Vanderveken, C. Adelman, F. Ciubotaru, S. Hamdioui, and S. Cotofana, "Fan-out enabled spin wave majority gate," *AIP Adv.* **10**, 035119 (2020).
- ²⁵P. Grünberg, "Magnetostatic spin-wave modes of a heterogeneous ferromagnetic double layer," *J. Appl. Phys.* **52**, 6824–6829 (1981).
- ²⁶P. Graczyk, M. Zelent, and M. Krawczyk, "Co- and contra-directional vertical coupling between ferromagnetic layers with grating for short-wavelength spin wave generation," *New J. Phys.* **20**, 053021 (2018).
- ²⁷A. V. Sadovnikov, E. N. Beginin, S. E. Sheshukova, D. V. Romanenko, Y. P. Sharaevskii, and S. A. Nikitov, "Directional multimode coupler for planar magnonics: Side-coupled magnetic stripes," *Appl. Phys. Lett.* **107**, 202405 (2015).
- ²⁸A. V. Sadovnikov, V. A. Gubanov, S. E. Sheshukova, Y. P. Sharaevskii, and S. A. Nikitov, "Spin-wave drop filter based on asymmetric side-coupled magnonic crystals," *Phys. Rev. Appl.* **9**, 051002 (2018).
- ²⁹D. Rowland and J. Love, "Evanescent wave coupling of whispering gallery modes of a dielectric cylinder," *IEEE Proc. J. Optoelectron.* **140**, 177 (1993).
- ³⁰B. E. Little, S. T. Chu, H. A. Haus, J. Foresi, and J. Laine, "Microring resonator channel dropping filters," *J. Light. Technol.* **15**, 998 (1997).
- ³¹W. Bogaerts, P. De Heyn, T. Van Vaerenbergh, K. De Vos, S. Kumar Selvaraja, T. Claes, P. Dumon, P. Bienstman, D. Van Thourhout, and R. Baets, "Silicon microring resonators," *Laser Photonics Rev.* **6**, 47 (2012).
- ³²S. A. Odintsov, E. N. Beginin, S. Sheshukova, and A. V. Sadovnikov, "Reconfigurable lateral spin-wave transport in a ring magnonic micro-waveguide," *IETP Lett.* **110**, 430 (2019).
- ³³A. V. Sadovnikov, A. A. Grachev, E. N. Beginin, S. E. Sheshukova, Y. P. Sharaevskii, and S. A. Nikitov, "Voltage-controlled spin-wave coupling in adjacent ferromagnetic-ferroelectric heterostructures," *Phys. Rev. Appl.* **7**, 014013 (2017).

Supplementary Material

Multifunctional operation of the double-layer ferromagnetic structure coupled by a rectangular nanoresonator

Pierre Roberjot,¹ Krzysztof Szulc,^{1, a)} Jarosław W. Kłos,¹ and Maciej Krawczyk^{1, b)}
*Institute of Spintronics and Quantum Information, Faculty of Physics, Adam Mickiewicz University, Poznań,
 Uniwersytetu Poznańskiego 2, 61-614 Poznań, Poland*

(Dated: April 5, 2021)

I. ANALYSIS OF THE DISPERSION RELATIONS FOR THE SYSTEMS UNDER INVESTIGATIONS WITH PERIODIC BOUNDARY CONDITION

In order to understand the impact of the stripe on the propagation of the spin waves (SWs) in the bilayered structure under investigation, we calculate the dispersion relations for three systems with the same periodic boundary conditions (PBC) along the propagation direction, i.e., the x -axis: (i) the first one consists of the two Co layers with thickness 5 nm and separated by 70 nm nonmagnetic material, (ii) the second one is a single Py stripe of width 100 nm and thickness 50 nm, i.e., the system in Fig. 1 (main text) without the Co layers, and (iii) for the bilayered structure with the Py resonator in between. The assumed period in all simulations is 250 nm and the structures are schematically shown at the top insets of Fig. S1.

For the Co bilayer without resonator, we obtain the dispersion relation shown in Fig. S1(a). This is the same structure and the dispersion relation as one shown in Fig. 2 of the main text, i.e., there are two bands with the frequency difference proportional to the dynamical coupling between the SWs in the layers.¹⁻³ Due to the PBC, the folding effect is observed at the Brillouin zone borders $k = \pm\pi/a$ ($a = 250$ nm), thus the crossing points in the dispersion relation are artificial. We notice that these branches are getting closer with the increase of the frequency which means the coupling between the two layers is getting weaker with increasing frequency, which corresponds to the increase of the wavevector in extended Brillouin zone scheme. This means that the SW excited in one layer will transfer between the layers periodically during the propagation. The distance on which the SW migrate between the layers is defined by the coupling strength. This effect is exploited in directional couplers.^{2,4-6}

As expected, the dispersion relation of the second subsystem presented in Fig. S1(c) is very close to the energy spectra of the isolated Py stripe shown in Fig. 2 of the main text, and consists of the flat bands being indicative for the SWs confined to the Py stripes and a lack of the coupling between the mode in successive copies of the system. The only mode, marked as 3c, shows a small dispersion near the Brillouin zone center,

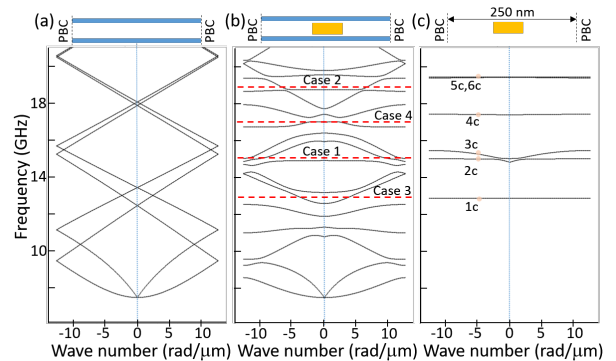


Figure S1: Dispersion relation of SWs for three systems as indicated by the insets at the top of the figure; (a) The subsystem composed of two Co layers separated by 70 nm of nonmagnetic material; (b) The main structure, the two Co layers with the Py stripe in between. The horizontal red-dashed lines indicate the frequencies used in time-domain simulations; (c) The Py stripe of 100-nm width and 50-nm thickness. In simulations, we assume the Floquet-Bloch periodic boundary conditions (PBC) along the direction of the SW propagation (the x -axis), with lattice constant of 250 nm.

$k = 0$. Thus, the bands and their frequencies can be directly related to the SW resonant modes of the infinitely-long Py stripe saturated along its axis. Looking at the amplitude of the SWs shown in Fig. 3 of the main text, we can see that the only dispersive mode, 3c in Fig. S1(c), is a fundamental mode creating sufficiently strong stray field to couple magnetization oscillations between the stripes in the successive unit cells.

The dispersion relation of the base system, i.e., bilayered structure with the Py stripe in-between, with PBCs is shown in Fig. S1(b). The spectra has many band gaps between more or less dispersive bands and it is significantly different from the spectra of the two Co layers shown in Fig. S1(a). Nevertheless, we can distinguish the dispersion lines originating from the coupled modes of the two Co layers and also from the resonant modes of the Py stripe, both modified by the hybridization between them. Due to PBCs the presence of hybridizations is coming from the interaction of resonant Py modes and the propagating modes in Co layers from the neighboring Brillouin zones, folded back to the first Brillouin zone in Fig. S1(b).

^{a)} Author to whom correspondence should be addressed: Krzysztof Szulc, krzysztof.szulc@amu.edu.pl

^{b)} Author to whom correspondence should be addressed: Maciej Krawczyk, krawczyk@amu.edu.pl

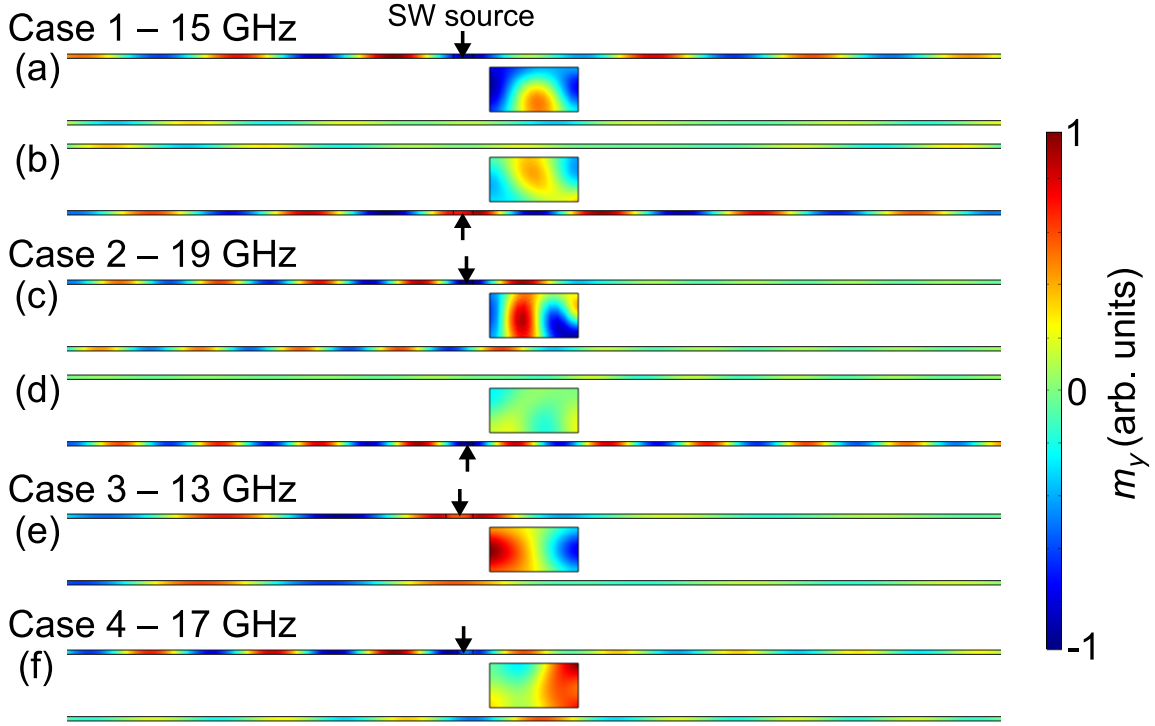


Figure S2: SW amplitude plots showing propagation in the investigated structure at selected excitation frequencies.

Reproduction of Fig. 4 in the main text with the non-zero damping. The damping constant in Co $\alpha_{Co} = 0.01$ and in Py $\alpha_{Py} = 0.005$. (a,b) Excitation of the SW of the 15-GHz frequency with the antenna located in the top (a) and bottom (b) Co layer. (c,d) Excitation of the SW of the 19-GHz frequency with the antenna located in the top (c) and bottom (d) Co layer. (e) Excitation of the SW of the 13-GHz frequency with the antenna located in the top Co layer. (f) Excitation of the SW of the 17-GHz frequency with the antenna located in the top Co layer.

II. INFLUENCE OF THE DAMPING ON DISPERSION RELATION

Figure 4 presented in the main text was reproduced with the non-zero damping taken into account. The results are present in Fig. S2. It is clear that the assumed damping ($\alpha_{Co} = 0.01$, $\alpha_{Py} = 0.005$) does not influence the coupling between the Co layers and Py resonator. All functionalities are reproduced with satisfactory agreement, the only observed result of the damping is the SW attenuation.

III. SPIN-WAVE ENERGY DENSITY

SW amplitude is not a perfect way to show the SW propagation, as the value changes in time and for the complicated structures (as the Py resonator) a frame of one of the magnetic components is not sufficient to fully describe the SW propagation. Therefore, we calculated the energy density of the SWs. The total energy density can be calculated as

$$E = E_{\text{dip}} + E_{\text{ex}}, \quad (\text{S1})$$

where the dipolar energy density E_{dip} is defined as

$$E_{\text{dip}} = \frac{1}{2\mu_0} \mathbf{m} \cdot \nabla \varphi \quad (\text{S2})$$

and the exchange energy density E_{ex} as

$$E_{\text{ex}} = \frac{A_{\text{ex}}}{M_S^2} (\nabla \mathbf{m})^2. \quad (\text{S3})$$

Results are presented in Fig. S3. In all of the investigated cases, the functionality is confirmed. In the case 1 [Fig. S3(a, b)], the energy is transferred forward through the resonator. Interestingly, the SW excited on the top-left side [Fig. S3(a)] is absorbed to the resonator and then pumped back, while the SW excited in the bottom-left side [Fig. S3(b)] is locally amplified by the resonator. In the case 2 [Fig. S3(c, d)], the SW circulator is showed. The circulation of the wave excited in the top-left side [Fig. S3(c)] is clearly connected to the SW resonance in the Py stripe. The energy is concentrated at the top- and bottom-right corners. The SW energy is transferred partially to the stray-field energy in the process. For the SW excited in the bottom-left side [Fig. S3(d)], the resonance in the Py stripe is not excited. In the case 3 [Fig. S3(e)], the circulating mode in the resonator is also present. However, it is

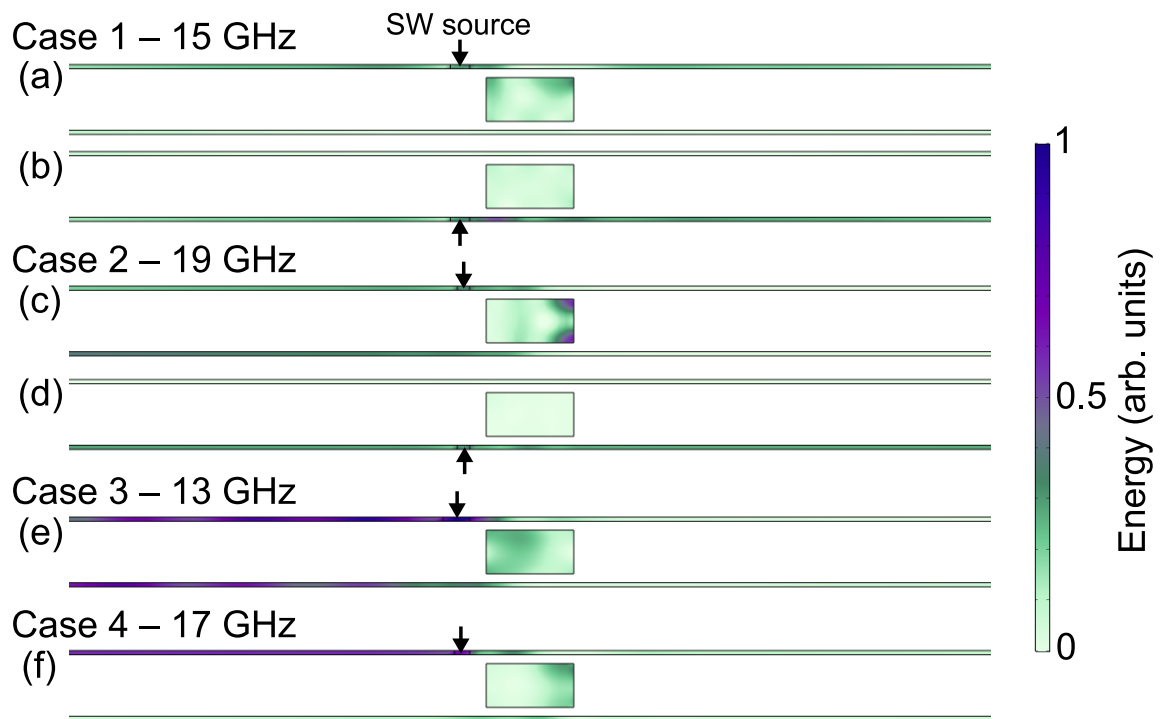


Figure S3: SW energy density plots at selected excitation frequencies taken from the average over 200 timesteps between 2 and 3 ns. Results corresponding to the one presented in Fig. 4 in the main text. (a,b) Excitation of the SW of the 15-GHz frequency with the antenna located in the top (a) and bottom (b) Co layer. (c,d) Excitation of the SW of the 19-GHz frequency with the antenna located in the top (c) and bottom (d) Co layer. (e) Excitation of the SW of the 13-GHz frequency with the antenna located in the top Co layer. (f) Excitation of the SW of the 17-GHz frequency with the antenna located in the top Co layer.

concentrated at the front of the stripe instead of the end as in the case 2. In the case 4 [Fig. S3(f)], the energy is concentrated mostly in the top-left side as the resonance in the Py stripe reverses back the SW.

REFERENCES

- ¹P. Grünberg, "Magnetostatic spin-wave modes of a heterogeneous ferromagnetic double layer," *J. Appl. Phys.* **52**, 6824–6829 (1981).
- ²P. Graczyk, M. Zelent, and M. Krawczyk, "Co- and contra-directional vertical coupling between ferromagnetic layers with grating for short-wavelength spin wave generation," *New J. Phys.* **20**, 053021 (2018).
- ³K. Szulc, P. Graczyk, M. Mruczkiewicz, G. Gubbiotti, and M. Krawczyk, "Spin-wave diode and circulator based on unidirectional coupling," *Phys. Rev. Appl.* **14**, 034063 (2020).
- ⁴A. V. Sadovnikov, E. N. Beginin, S. E. Sheshukova, D. V. Romanenko, Y. P. Sharaevskii, and S. A. Nikitov, "Directional multimode coupler for planar magnonics: Side-coupled magnetic stripes," *Appl. Phys. Lett.* **107**, 202405 (2015).
- ⁵Q. Wang, P. Pirro, R. Verba, A. Slavin, B. Hillebrands, and A. V. Chumak, "Reconfigurable nanoscale spin-wave directional coupler," *Sci. Adv.* **4**, e1701517 (2018).
- ⁶A. V. Sadovnikov, V. A. Gubanov, S. E. Sheshukova, Y. P. Sharaevskii, and S. A. Nikitov, "Spin-wave drop filter based on asymmetric side-coupled magnonic crystals," *Phys. Rev. Appl.* **9**, 051002 (2018).

4.3 [P3] Nonreciprocal spin-wave dynamics in Pt/Co/W/Co/Pt multilayers

This study started in 2018 with the proposal of collaboration with G. Gubbiotti from CNR in Perugia, Italy. He performed the Brillouin light scattering (BLS) spectroscopy measurements on the set of Pt/Co/W and Pt/Co/W/Co/Pt samples provided by the group of M. Becherer at the Technical University of Munich. The characteristic feature of the double-layer sample was that the thicknesses of the Co layers were chosen so that they are both close to $Q = 1$, but one has an in-plane effective anisotropy ($Q < 1$) and the other an out-of-plane effective anisotropy ($Q > 1$). Moreover, due to the interface with the Pt layer from different sides, both Co layers should be characterized by DMI constants of opposite sign. Surprisingly, the frequency difference between the two lowest spin-wave modes was massive – about 15 GHz. We expected the difference to be no more than a few GHz. Our initial hypothesis that interlayer exchange coupling was responsible for such a strong frequency split was rejected. My numerical simulations showed that the RKKY interaction must be very strong to split the frequencies so far apart. Moreover, the RKKY-coupled layers should have significantly modified the dispersion relation; it was not the case for these samples, whose dispersion curves were characteristic of uncoupled layers. To confirm the results of the numerical simulations, the alternating gradient force magnetometer (AGFM) measurements were performed. They showed that the layers are indeed not exchange coupled, confirming the second hypothesis that the order of deposition of the layers is crucial for the strength of the anisotropy. The reference layers had only the Pt/Co/W stack, while the double layers had both Pt/Co/W and W/Co/Pt stacks. The combined results of BLS and AGFM measurements confirmed that despite the same thickness of the Co layer and the same interfaces, the Co layer in the W/Co/Pt stack has significantly lower anisotropy than in the Pt/Co/W stack. Moreover, the results showed that despite the ultrathin W spacer of 0.95 nm thickness, the Co layers were almost completely uncoupled; the effect of coupling was not pronounced in either the BLS or the AGFM measurements. Only from the numerical simulations could it be concluded that the layers are very weakly coupled. The results showed that this system can be used as densely packed spin-wave conduits.

Contribution of the Author

In this publication, I performed the numerical simulations in COMSOL, extended the numerical model to include the RKKY interaction, participated in the interpretation and discussion of the experimental and numerical results, wrote the Theoretical and Numerical Methods and Results sections, prepared Figures 2, 3e-h, and 4e-l, corrected the manuscript, was responsible for the manuscript submission and the correspondence with the journal.

Nonreciprocal spin-wave dynamics in Pt/Co/W/Co/Pt multilayers

Krzysztof Szulc^{1,*}, Simon Mendisch,² Michał Mruczkiewicz,^{3,4} Francesca Casoli⁵,
Markus Becherer,² and Gianluca Gubbiotti⁶

¹*Institute of Spintronics and Quantum Information, Faculty of Physics, Adam Mickiewicz University, Poznań, Uniwersytetu Poznańskiego 2, 61-614 Poznań, Poland*

²*Department of Electrical and Computer Engineering, Technical University of Munich (TUM), Arcisstrasse 21, 80333 Munich, Germany*

³*Institute of Electrical Engineering, Slovak Academy of Sciences, 841 04 Bratislava, Slovakia*

⁴*Centre for Advanced Materials Application (CEMEA), Slovak Academy of Sciences, Dúbravská cesta 5807/9, 845 11 Bratislava, Slovakia*

⁵*Istituto dei Materiali per l'Elettronica ed il Magnetismo (IMEM-CNR), I-43124 Parma, Italy*

⁶*Istituto Officina dei Materiali del CNR (CNR-IOM), Sede Secondaria di Perugia, c/o Dipartimento di Fisica e Geologia, Università di Perugia, I-06123 Perugia, Italy*

 (Received 15 November 2020; revised 9 February 2021; accepted 16 March 2021; published 5 April 2021)

We present a detailed study of the spin-wave dynamics in single Pt/Co/W and double Pt/Co/W/Co/Pt ferromagnetic layer systems. The dispersion of spin waves was measured by wave-vector-resolved Brillouin light scattering spectroscopy while the in-plane and out-of-plane magnetization curves were measured by alternating gradient field magnetometry. The interfacial Dzyaloshinskii-Moriya interaction induced nonreciprocal dispersion relation was demonstrated for both single and double ferromagnetic layers and explicated by numerical simulations and theoretical formulas. The results indicate the crucial role of the order of layers deposition on the magnetic parameters. A significant difference between the perpendicular magnetic anisotropy constant in double ferromagnetic layer systems conduces to the decline of the interlayer interactions and different dispersion relations for the spin-wave modes. Our study provides a significant contribution to the realization of the multifunctional nonreciprocal magnonic devices based on ultrathin ferromagnetic/heavy-metal layer systems.

DOI: [10.1103/PhysRevB.103.134404](https://doi.org/10.1103/PhysRevB.103.134404)

I. INTRODUCTION

High demand for improvement in storage and computing devices and decrease of their power consumption leads to continued interest in spintronic phenomena. Recently, the interfacial Dzyaloshinskii-Moriya interaction (iDMI) [1] brought the attention of the researchers as it permits us to stabilize topological magnetic solitons, e.g., skyrmions and radial vortices [2]. The iDMI is an asymmetric exchange interaction and can be induced in ultrathin multilayer systems where the inversion symmetry is broken between both interfaces of the ferromagnetic layer. It is induced by large spin-orbit coupling between a ferromagnet and heavy-metal atoms at one of the interfaces of an ultrathin ferromagnet. The energy contribution of iDMI is minimized when spins are aligned perpendicularly in a specific direction, described by the equation $E_{\text{DMI}} = -\sum_{i,j} \mathbf{D}_{ij} \cdot (\mathbf{S}_i \times \mathbf{S}_j)$, where \mathbf{D}_{ij} is the Dzyaloshinskii-Moriya vector. Therefore, the orientation of the \mathbf{D}_{ij} determines whether right-handed or left-handed rotation sense between neighboring spins is the configuration of lower energy. Even if the iDMI favors noncollinear alignment of spins when it is strong, the single-domain state can be achieved at high magnetic fields. Then, the chiral property of the iDMI is exhibited in nonreciprocal spin-wave dynamics [3–6] and can be used to tailor the magnon dispersion relation,

and thus used to extend the functionality of the magnonic devices [7].

The iDMI value is one of the highest in Pt/Co systems, which are also characterized by strong perpendicular magnetic anisotropy (PMA). Thus, many of the iDMI systems are based on Pt/Co ultrathin films with broken inversion symmetry, e.g., Pt/Co/AlO_x [8,9], Pt/Co/MgO [10] Pt/Co/Ta [11], Pt/Co/(W,Ta,Pd) [12], Pt/Co-Ni/Ta [13], Ir/Fe/Co/Pt [14], Pt/Co/Cu/AlO_x [15], Pt/Co/Os/Pt [16], Pt/Cu/Co/Pt [17]. In Ref. [18] the implications of asymmetric multilayers [Pt/Co/Ir]₅ with broken inversion symmetry on domain wall chirality, skyrmion stability, and its dynamics were reported. Interestingly, weak iDMI was also present in symmetric Pt/Co/Pt multilayers [19] due to different quality of the Co interfaces. The influence of the surface quality can also have a significant impact on the anisotropy of the sample [20].

Most of the studies, also cited above, considered structures with sandwich multilayers, where the unit Pt/Co/X was repeated n times, and magnetic parameters of Co layers had negligible differences. Nevertheless, the stack of layers with deliberately different magnetic properties of magnetic materials across the thickness might also have interesting properties especially related to the magnetization and spin-wave dynamics, useful for applications in spintronics and magnonics as indicated by recent studies. For example, in the antiferromagnetic-exchange-coupled symmetric bilayer CoFeB/Ru/CoFeB, the measured Ru thickness-dependent nonreciprocity was related to the difference between

*krzysztof.szulc@amu.edu.pl

TABLE I. Magnetic parameters of the SFL and DFL samples.

Abbrev.	Sample	M_S (kA/m) [48]	M_{eff} (kA/m)	K_u (kJ/m ³)	D (mJ/m ²)
SFL1	Co(1.95)/W(0.95)	1100	28	741	0.74
SFL2	Co(1.6)/W(0.95)	1050	-235	848	0.84
DFL1	Co(1.6)/W(0.95)/Co(1.95)	1100	774	225	-0.64
		1050	-194	821	0.72
DFL2	Co(1.6)/W(0.95)/Co(1.6)	1050	626	280	-0.49
		1050	-246	855	0.84

perpendicular interface anisotropy of the bottom and top CoFeB layer [21]. Thus, in this paper, we will investigate the spin-wave properties in systems composed of two ferromagnetic layers, i.e., double ferromagnetic layer (DFL) systems.

DFL systems with opposite sign of iDMI in the limit of noninteracting layers shall exhibit two nonreciprocal dispersion-relation branches that are mirror images at wave vector $k = 0$. Therefore, having a dispersion resembling the electronic Rashba splitting is expected [22–24]. Additionally, the coupling strength between the layers can be tuned by Ruderman-Kittel-Kasuya-Yosida (RKKY) interaction or dipolar interaction [25,26]. Also, interlayer DMI interaction in the DFL system, competing with RKKY interaction, was recently shown [27]. These works point out that magnonic dispersion can be tailored in many ways in the DFLs and multilayers with varied iDMI, magnetic properties of the sublayers, and the coupling strength between them.

The strength of iDMI can be quantified by several methods, such as domain-wall velocity [28,29], asymmetric hysteresis loop method [30], and magnetic force microscopy [31]. A detailed review of the different techniques used to measure iDMI in ultrathin films has been recently published by Kuepferling *et al.* [32]. Among them, Brillouin light scattering (BLS) spectroscopy has demonstrated to be a powerful and reliable technique since it combines the high sensitivity to detect signals from spin waves in magnetic monolayers [33–40], and the possibility to explore a wide range of wave vectors (0–25 rad/ μm) and frequencies (1–500 GHz). The estimation of iDMI constant from experimental measurements was studied also for complex multilayers [41].

In this work we study Pt/Co/W/Co/Pt DFL systems and, as the reference samples, the Pt/Co/W single ferromagnetic layer (SFL) systems. Hysteresis loops were measured using the alternating gradient force magnetometer (AGFM). BLS is used to measure the dispersion relation of spin waves and to extract the iDMI constant by measuring the frequency asymmetry (Δf) between the spin waves propagating in opposite directions. The numerical simulation in the time and frequency domain provides an interpretation of the experimental results and allows us to extract effective magnetization and anisotropy constant of the Co layers. In particular, we found that in DFL samples, the Co layers have an opposite sign of iDMI due to the inversion of interfaces and significantly different anisotropies due to a different order of the layers deposition. With these properties we aim to demonstrate systems with two, almost independent spin-wave dispersion relations possessing nonreciprocal properties.

II. EXPERIMENTAL METHODS

The characterized thin films were deposited at room temperature via confocal rf-magnetron sputtering (base pressure $< 2 \times 10^{-7}$ mbar) onto n^- doped silicon (100) substrates with an in-house grown thermal oxide (thickness ≈ 20 nm). Before the deposition, residual water was removed from the samples using a 300 eV Ar^+ ion beam. All materials were deposited at a constant argon pressure 4 μbar (≈ 3 mTorr) except for the Ta adhesive, which was deposited at 2 μbar (≈ 1.5 mTorr). The rf power applied to the 2-in. targets was identical for all materials (40 W). To reduce contaminants the dead times between elements during the automated deposition were generally kept below 1s. All multilayer stacks feature a standard adhesive (1.5 nm Ta), seed (6 nm Pt), and capping (3 nm Pt) layer. The stacks are, therefore, solely addressed by their magnetic layer compositions with thicknesses given in nanometers [e.g., Co(1.6)/W(0.95)/Co(1.95)]. Single ferromagnetic Co layers having a thickness of 1.6 and 1.95 nm have also been grown on Pt films and used as reference samples. The set of four fabricated samples is listed in Table I.

Hysteresis loops were measured by the AGFM, applying a magnetic field up to 15 kOe in the directions parallel and perpendicular to the film plane.

BLS spectra were recorded at room temperature in the backscattering configuration using a (3+3)-tandem Sandercock-type interferometer [42]. About 200-mW p -polarized monochromatic light from a solid-state laser $\lambda = 532$ nm was focused onto the sample surface. An in-plane magnetic field H was applied parallel to the sample surface and perpendicular to the plane of incidence of light in the so-called Damon-Eshbach configuration. A schematic representation of the scattering geometry is represented in Fig. 1. Due to in-plane momentum conservation, the wave vector k of spin waves entering into the scattering process is given by $k = (4\pi/\lambda) \sin \theta$. Spin waves traveling in the $-x$ and $+x$ directions appear as peaks in the Stokes and anti-Stokes side of the spectra, respectively. BLS measurements were performed in two different configurations: (1) by changing the magnitude of the external magnetic field applied in the sample plane at normal incidence of light upon the sample surface ($\theta = 0^\circ$), i.e., $k = 0$; and (2) by sweeping the wave vector k in the range from 0 to 20 rad/ μm at fixed applied field $H = \pm 5.5$ kOe [43]. Reversing the direction of the external magnetic field from +5.5 to -5.5 kOe is equivalent to reverse the direction of the propagating spin waves. The frequency asymmetry induced by iDMI is proportional to the sine function of the in-plane angle ϕ between the applied field and the wave vector

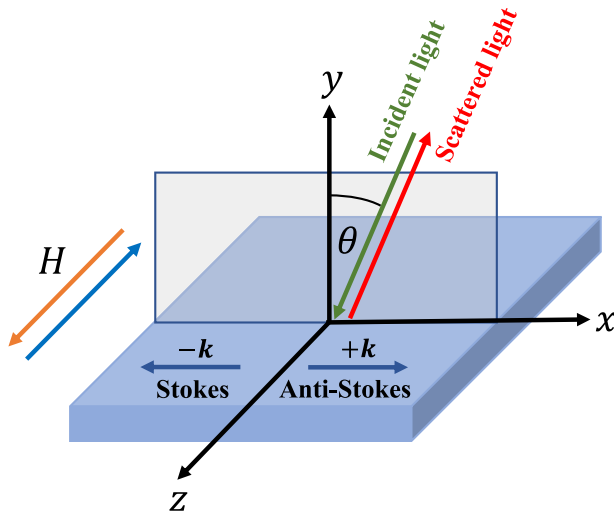


FIG. 1. Schematic drawing of the BLS scattering geometry in the Damon-Eshbach configuration. The incident light makes an angle θ with respect to the sample normal. Measurements are performed in the backscattering configuration, where the same camera objective is used to focus laser light upon the sample surface and to collect scattered light sent to the interferometer for the frequency analysis. A magnetic field H is applied in the sample plane and perpendicular to the incidence plane of light.

direction [5]. In the Damon-Eshbach configuration ($\phi = 90^\circ$), Δf is maximum.

III. THEORETICAL AND NUMERICAL METHODS

Motion of the spin is described by the Landau-Lifshitz equation:

$$\frac{\partial \mathbf{M}}{\partial t} = -\gamma \mu_0 \mathbf{M} \times \mathbf{H}_{\text{eff}}, \quad (1)$$

where $\mathbf{M} = (m_x, m_y, m_z)$ is the magnetization vector, γ is the gyromagnetic ratio, μ_0 is the magnetic permeability of vacuum, and H_{eff} is the effective magnetic field, which is given

$$f = \frac{\gamma \mu_0}{2\pi} \left\{ \sqrt{\left(H + M_S \frac{d|k|}{2} + \frac{2A_{\text{ex}}}{\mu_0 M_S} k^2 \right) \left[H + M_S \left(1 - \frac{d|k|}{2} \right) + \frac{2A_{\text{ex}}}{\mu_0 M_S} k^2 - \frac{2K_u}{\mu_0 M_S} \right] + \frac{2D}{\mu_0 M_S} k} \right\}. \quad (6)$$

The frequency difference between the Stokes and anti-Stokes peaks Δf can be derived from Eq. (6) as

$$\Delta f = f_{+k} - f_{-k} = \frac{\gamma}{2\pi} \frac{4D}{M_S} k. \quad (7)$$

The field dependence of the frequency was measured at normal-incidence angle $\theta = 0^\circ$, therefore, Eq. (6) simplifies

as follows:

$$\begin{aligned} \mathbf{H}_{\text{eff}} = & H \hat{\mathbf{z}} + \frac{2A_{\text{ex}}}{\mu_0 M_S^2} \nabla^2 \mathbf{M} + \frac{2D}{\mu_0 M_S^2} \hat{\mathbf{z}} \times \frac{\partial \mathbf{M}}{\partial x} \\ & + \frac{2K_u}{\mu_0 M_S^2} m_y \hat{\mathbf{y}} - \nabla \varphi, \end{aligned} \quad (2)$$

where H is the external magnetic field, M_S is the saturation magnetization, A_{ex} is the exchange stiffness constant, D is the iDMI constant, K_u is the PMA constant, and φ is the magnetic scalar potential fulfilling Poisson-like equation

$$\nabla^2 \varphi = \nabla \cdot \mathbf{M}. \quad (3)$$

In the DFL structures, the RKKY interaction is applied as the boundary conditions on the inner interfaces of the ferromagnetic layers [44] along with the boundary condition for the exchange interaction

$$\begin{aligned} 0 = & 2A_{\text{ex}} \hat{\mathbf{z}} \times \frac{\partial \mathbf{M}_{1(2)}(y)}{\partial y} \Big|_{y=y_{1(2)}^{\text{in}}} \\ & - J \hat{\mathbf{z}} \times [\mathbf{M}_{2(1)} - \mathbf{M}_{1(2)}(y_{1(2)}^{\text{in}})], \end{aligned} \quad (4)$$

where J is the RKKY constant and subscripts numerate bottom and top layers in DFL samples. The boundary condition on the outer interfaces consist only of the exchange interaction term

$$0 = 2A_{\text{ex}} \hat{\mathbf{z}} \times \frac{\partial \mathbf{M}_{1(2)}(y)}{\partial y} \Big|_{y=y_{1(2)}^{\text{out}}}. \quad (5)$$

Spin-wave dynamics are calculated numerically using the finite-element method in COMSOL Multiphysics [45]. The system was implemented to a two-dimensional model with Floquet boundary conditions to simulate an infinite plane with finite thickness. Time-domain simulations were used to simulate the hysteresis loops of the DFL system. Frequency-domain simulations were carried out to calculate the spin-wave dispersion relation of the DFL system. Eigenfrequency problem employs a linear approximation of Eqs. (1) and (3), i.e., assuming $m_x, m_y \ll m_z \approx M_S$. Triangular mesh with a maximum element size of 1 nm inside the ferromagnetic layers and a growth rate of 1.15 outside of the ferromagnetic layers was used.

In the SFL system, the spin-wave dispersion relation was fitted using the analytical formula [46,47]

to the following formula:

$$f = \frac{\gamma \mu_0}{2\pi} \sqrt{H \left(H + M_S - \frac{2K_u}{\mu_0 M_S} \right)}, \quad (8)$$

which describes the sample saturated in the film plane. The field dependence for the saturation out of the plane is

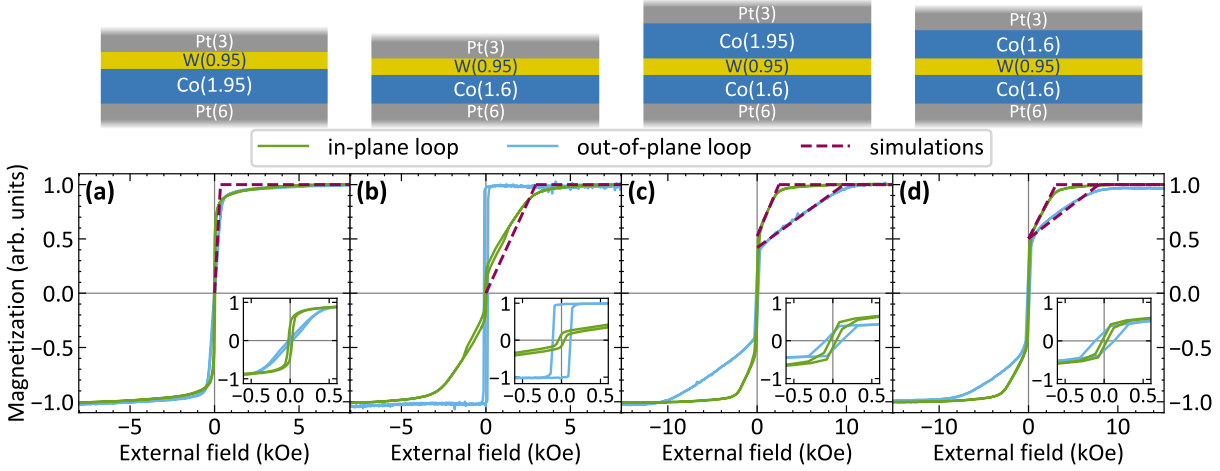


FIG. 2. AGFM hysteresis loops measured in the in-plane configuration and out-of-plane configuration. The purple dashed lines represent the fitting using the numerical simulations. In the inset plots, the zoom to low external fields is shown. On top of the figure, the schematic representation of the samples is shown.

described by the formula

$$f = \frac{\gamma \mu_0}{2\pi} \sqrt{\left(M_S - \frac{2K_u}{\mu_0 M_S}\right)^2 - H^2}. \quad (9)$$

Based on Eq. (8), the effective magnetization M_{eff} can be defined as

$$M_{\text{eff}} = M_S - \frac{2K_u}{\mu_0 M_S}. \quad (10)$$

M_S values are extracted from the out-of-plane magnetization curves obtained by Mendisch *et al.* [48]. For Co(1.6) is $M_S = 1050$ kA/m while for Co(1.95) is $M_S = 1100$ kA/m.

IV. RESULTS

A. AGFM hysteresis loops

The AGFM hysteresis loops measured in the film plane (green curves) and perpendicular to the plane (blue curves) are shown in Fig. 2. The results were used to determine M_{eff} values of the layers in all of the samples. Hard-axis hysteresis loops were fitted with the numerical simulations. The saturation field values obtained from the simulations should be consistent with the M_{eff} values. The beginning of the magnetization reversal process is sharp, so the extracted M_{eff} values are considered to be well defined. At this point, the effect of the RKKY interaction between the layers is neglected. Its effect is explained in Sec. IV C. Using the predefined M_S from Ref. [48], we also determined the PMA constant K_u using Eq. (10). They are collected in Table I.

In the Co(1.95)/W(0.95) (SFL1) sample [Fig. 2(a)] the parallel loop has a square shape while the perpendicular loop has the typical S-shape behavior characterized by an almost linear dependence on the applied field, indicating an in-plane easy axis. The magnetic saturation in the perpendicular direction is reached in a field much lower than $\mu_0 M_S$, thus indicating that a strong PMA is present in this sample, which competes with the shape anisotropy. K_u is slightly lower than the value

required to get a change from an in-plane to an out-of-plane easy magnetization axis, which is 760 kJ/m³, and the sample remains in the in-plane configuration in the remanence. In-plane and perpendicular coercivity values are low, but both loops close at higher field values, i.e., around 0.2 – 0.3 kOe.

The Co(1.6)/W(0.95) (SFL2) sample [Fig. 2(b)] shows a clear PMA contribution, which dominates over the magnetostatic in-plane contribution, giving rise to an easy magnetization direction perpendicular to the film plane. The hysteresis loop measured with the field applied in the film plane shows a transcritical shape with a saturation field around 3 kOe, low coercivity, but an open loop up to a higher field (approximately 1.2 kOe). The latter feature might depend on a secondary phase with a tilted easy magnetization axis. The hysteresis loop measured in the perpendicular direction shows a square shape with a larger coercive field compared to the in-plane direction.

In the DFL samples [Figs. 2(c) and 2(d)], the PMA contribution is evident. The hysteresis loops along the in-plane and perpendicular directions clearly show the contribution of two magnetic components: one with an easy magnetization axis in the film plane and the other with an easy magnetization axis perpendicular to the film plane. In the Co(1.6)/W(0.95)/Co(1.95) (DFL1) sample [Fig. 2(c)], the in-plane easy-axis part appears to have a larger magnetic moment, indicating that it is associated with the Co(1.95) layer, while the out-of-plane easy-axis is present in the Co(1.6) layer. In the Co(1.6)/W(0.95)/Co(1.6) (DFL2) sample [Fig. 2(d)], the in-plane and out-of-plane parts carry the same magnetic moment because of the same thicknesses of the ferromagnetic layers. Also, comparing the magnetic parameters in the DFL and SFL samples, we can ascribe a larger K_u value to the bottom Co layer and smaller K_u to the top Co layer. We associate this effect with the order of the layers deposition. Even though the Co layer has the same vicinity (Pt and W), the effect on the magnetic parameters is different if the material plays the role of the seed or capping layer [49] as well as depends on the growth conditions [50]. Moreover, in

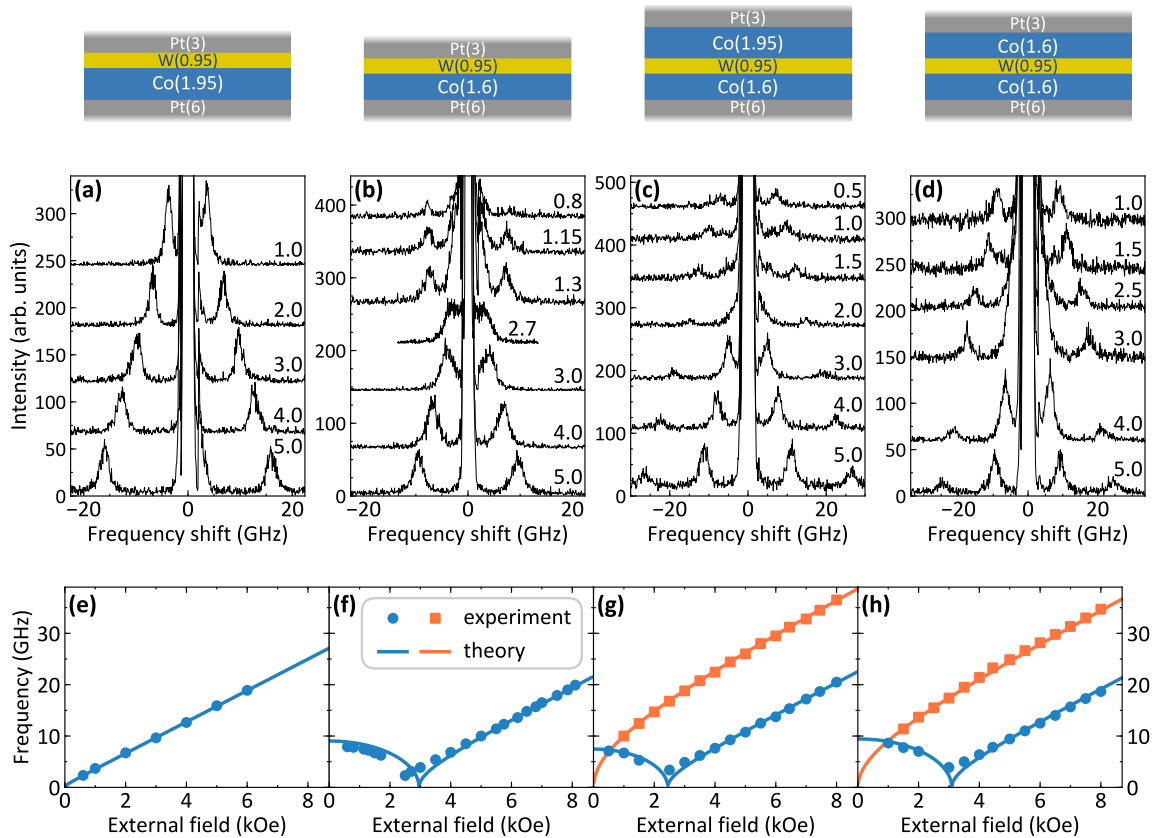


FIG. 3. (a)–(d) The sequence of BLS spectra measured at $k = 0$ ($\theta = 0^\circ$) and different magnitudes of the externally applied field for all the investigated samples. (e)–(h) The spin-wave frequency measured by BLS in the function of the external field H and fitting with the theoretical formula in Eqs. (8) and (9).

both DFL samples, the coercive-field values are larger in the perpendicular direction.

B. Field-dependent BLS measurements

Figures 3(a)–3(d) present the sequences of measured BLS spectra and Figs. 3(e)–3(h) present the frequency values plotted as a function of H at $k = 0$ for all of the investigated samples. BLS spectra were measured starting from $H = 8$ kOe and decreasing it down to zero, i.e., along the descending branches of the in-plane loops in Fig. 2. For SFL samples, only one peak is observed. For the SFL1 sample, it has a monotonic dependence on H , while for the SFL2 sample, it first decreases, reaching a minimum at 2.4 kOe, and then increases again. For DFL samples, two peaks are visible on both the Stokes and anti-Stokes sides of the spectra. Here the field dependence is more complicated since the frequency of high-frequency mode monotonously decreases with decreasing H while the low-frequency peak first decreases, reaches a minimum, and then increases. Since the spectra are measured at $k = 0$, the frequency position of the peaks are symmetric ($f_S = f_{AS}$) on both the Stokes and anti-Stokes sides of the spectra. Based on PMA constants derived from the AGFM hysteresis loops, we used Eq. (8) to determine the gyromagnetic ratio γ of the analyzed samples. We reached satisfactory fitting for $\gamma = 192$ rad/(Ts), as shown in Figs. 3(e)–3(h) with

solid lines. These results, together with the values of the saturation fields derived from the AGFM measured loops, permit us to unambiguously affirm that above 4 kOe the magnetization is saturated and aligned parallel to the sample plane. Therefore, we performed the wave-vector-dependent measurements for an externally applied field of ± 5.5 kOe.

C. Role of RKKY interaction in DFL samples

The numerical simulations were used to check the presence of the RKKY interaction in the DFL samples. First, $K_{u,1}$ and $K_{u,2}$ were fitted to the hysteresis loops from Fig. 2 in the function of the RKKY constant J . The results show that the difference between $K_{u,1}$ and $K_{u,2}$ increases with the RKKY constant. However, the hysteresis loop does not change its character. The shape is identical to the shape of the loop of the noninteracting layers. The possible cause is the large difference between M_{eff} . In the next step, the RKKY constant (along with related to it $K_{u,1}$ and $K_{u,2}$) was fitted to the field dependence of the frequency results obtained from the BLS measurements shown in Figs. 3(e)–3(h). The gyromagnetic ratio γ was used to fit the low-frequency mode, and the RKKY constant was fitted to the high-frequency mode. The value of the RKKY constant for DFL1 equals $-100 \mu\text{J}/\text{m}^2$ for $\gamma = 195$ rad/(Ts) and for DFL2 equals $20 \mu\text{J}/\text{m}^2$ for $\gamma = 190$ rad/(Ts). However, the best fit assuming the absence of the RKKY is as far as 1 GHz from the satisfactory fit.

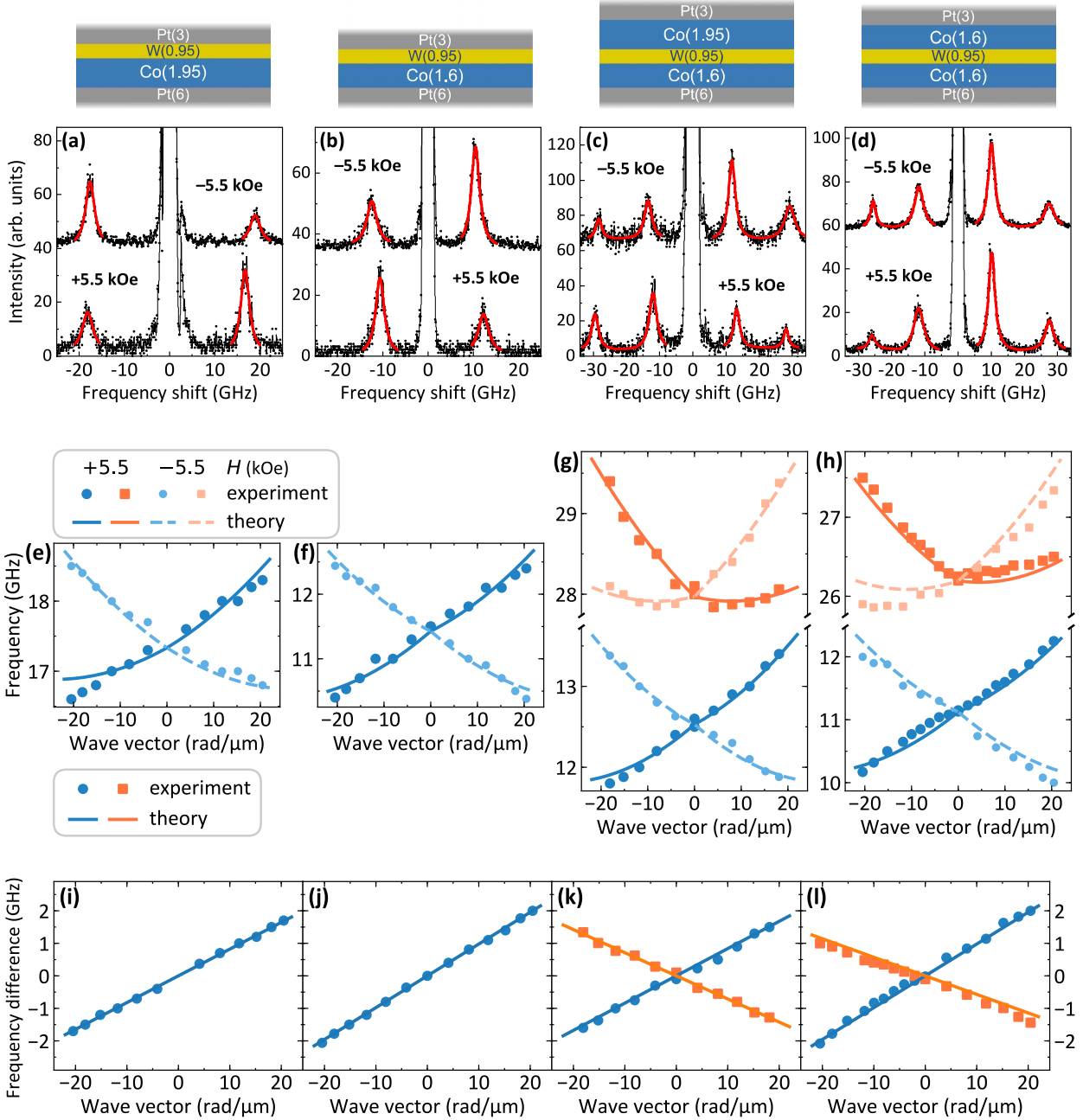


FIG. 4. (a)–(d) Measured BLS spectra at $k = 18.1 \text{ rad}/\mu\text{m}$ ($\theta = 50^\circ$) and for two different orientations of the external field: $H = +5.5$ and -5.5 kOe . Black points represent the measured spectra, while red curves are the Lorentzian fitting of the peaks. (e)–(h) Dispersion relations measured by the BLS spectroscopy in the external field of $\pm 5.5 \text{ kOe}$ and fitted using finite-element method simulations. (i)–(l) Frequency asymmetry plots measured by the BLS spectroscopy with the linear regression fitting based on Eq. (7).

It lies within the error range, which considers the reading of M_{eff} from the hysteresis loops and instrument errors. In general, the frequency shift is small even for a large value of the RKKY constant (exceeding $\pm 100 \mu\text{J}/\text{m}^2$). Moreover, the shape of the hysteresis loops and the field dependence of the frequency with RKKY are identical to the case of the noninteracting layers. Therefore, the presence of the RKKY interaction cannot be confirmed when the difference between

M_{eff} of the layers in the bilayered structure is too large, and thus its effect is neglected in the analysis of the results.

D. Wave-vector-dependent BLS measurements

In order to derive the iDMI constant, we measured the BLS spectra for different wave-vector values in the range from 0 to $20 \text{ rad}/\mu\text{m}$ for H fixed at $+5.5$ and -5.5 kOe . Typical

BLS spectra measured at these fields for $k = 18.1 \text{ rad}/\mu\text{m}$ are shown in Figs. 4(a)–4(d) for all the investigated samples. Because of the small sample thickness, both the Stokes and anti-Stokes peaks, corresponding to spin waves propagating in opposite directions, are simultaneously observed with slightly different intensity. Frequencies of the spin-wave modes were extracted by fitting the peaks in the BLS spectra [displayed in Figs. 4(a)–4(d) by the red curves] with Lorentzian functions and were plotted as a function of their respective wave vectors k in Figs. 4(e)–4(h). It is noteworthy that on reversing the direction of the applied magnetic field, the respective center frequencies and intensities of the Stokes and anti-Stokes peaks interchange due to the fact that reversing the magnetization is equivalent to a reversal operation. For that reason, the following discussion will pertain to the results in positive external magnetic field. The dispersions were calculated by the finite-element method simulations in COMSOL Multiphysics. We set the exchange stiffness $A_{\text{ex}} = 15 \text{ pJ/m}$. The values of M_S and K_u used in simulations are written in Table I. The iDMI constant D was the free parameter in the fitting procedure for each sample separately.

In the SFL samples [Figs. 4(e) and 4(f)], the frequency dependence is close to linear and has a positive slope. A more detailed analysis of Eq. (6) allows explaining the character of the dispersion relation. First, the effect of the dipolar interaction is significantly weakened by the PMA as $M_S \approx 2K_u/\mu_0 M_S$ and so $M_{\text{eff}} \approx 0$. In fact, when $M_{\text{eff}} < 0$, the surface wave propagates backward, and the dispersion relation has a negative slope even with the absence of iDMI, until the effect of the exchange interaction starts to dominate. The small thickness of the layer leads to the additional flattening of the dispersion. In the BLS range of the wave vector, the effect of the exchange interaction is small, and so the dispersion relation is close to linear. The slope of the dispersion is directly connected to the iDMI.

The dispersion relations of the DFL samples [Figs. 4(g) and 4(h)] show two branches of a different character. Comparing the dispersion relations with the systems of noninteracting layers, the frequency is changing by less than 100 MHz, indicating very weak dipolar coupling between the layers. The lowering of the dipolar-coupling influence on frequency is caused by the large difference between the PMAs of the layers. Interestingly, it allows us to use the approximation of the noninteracting layers, even for separations as small as 1 nm. The low-frequency mode is close to linear with the positive slope. Its character is identical to the single-layer dispersion confirming the connection with the bottom layer. The high-frequency mode is flat on the positive wave vectors' side and has a negative slope on the negative wave vectors' side. The flattening is the result of the compensation of dynamic dipolar interaction by the iDMI.

Figures 4(i)–4(l) show the frequency difference Δf between the Stokes and the anti-Stokes peaks measured as a function of the wave vector k . The values for positive wave vectors represents the measurements in the positive external field and negative wave vectors—in the negative external field. The frequency asymmetry exhibits a linear dependence as a function of k , agreeing with the theoretical prediction of Eq. (7). The frequency-difference plots were fitted using the linear regression method based on Eq. (7), and the values

of iDMI constant D are collected in Table I. The values are in agreement with values presented in the literature for the similar thickness of Co layer [9], where the iDMI constant is about 1 mJ/m^2 for 1.6 nm Co thickness and lower for larger thicknesses of Co.

In the DFL samples [Figs. 4(k) and 4(l)], the frequency asymmetry always has a linear dependence on k , but for the two modes, it has an opposite sign since the Co layers have Pt as a bottom or top layer. However, the iDMI constants in the layers differ. This effect can come from the different thicknesses of the Pt layers, as well as in the DFL1 sample [Fig. 4(k)], from the different thicknesses of the Co layers. The sputtering order of the layers can also affect the iDMI constant absolute value, as it is observed for the PMA constant.

V. CONCLUSIONS

We have studied the iDMI and spin-wave dynamics in Pt/Co/W/Co/Pt DFL structures with the opposite arrangement of Co and Pt layers and Pt/Co/W SFL samples. AGFM hysteresis loops show a strong PMA contribution, leading to a resultant out-of-plane easy magnetization axis in Co(1.6) layer and in-plane easy magnetization axis in Co(1.95) layer with small effective magnetization. Hysteresis loops of DFL samples indicate both in-plane and out-of-plane anisotropy contributions, also pointing at a significant difference between the PMA constants of the Co layers. Field-dependent measurements of the BLS spectra at normal incidence confirm the presence of strong PMA in the Co layers. Numerical simulations were made to check the presence of the RKKY interaction through the W spacer. We find that AGFM and BLS results can be fitted without this interaction taken into account, which does not confirm the presence of the RKKY interaction in the DFL samples.

Wave-vector-dependent BLS measurements were made in a large external field of $\pm 5.5 \text{ kOe}$ to reach the in-plane configuration of magnetization. The results show the iDMI-dominated linear dispersion in SFL samples and two-mode dispersion in DFL samples related to the two Co layers in the studied system. The strong asymmetry between the Stokes and anti-Stokes peaks is present. In the DFL samples, the slope of the two branches and thus the signs of the iDMI constant are opposite due to the opposite arrangement of Co and Pt layers. The iDMI constant values vary between 0.49 and 0.84 mJ/m^2 , being in line with the values known from the literature.

In DFL samples, the linear low-frequency mode is dominated by iDMI and resembles the dispersions measured in SFLs. The asymmetric high-frequency mode consists of a flat branch for positive wave vectors and a strongly dispersive branch for the negative wave vectors at the selected orientation of the external magnetic field. A comparison with the system of noninteracting layers points out a significant weakening of the interlayer coupling via the dynamic dipolar field. This uncoupling of spin waves between the Co layers separated by only 0.95-nm-thick nonmagnetic spacer arises from the significantly different frequencies of oscillations in both layers, with the difference equaling 15.5 GHz at $k = 0$ for both DFL1 and DFL2 samples. Such a significant difference in frequencies in nominally very similar Co films is attributed to the different PMAs originating in different deposition sequences for the bottom and top Co layers.

To sum up, we design the system based on ultrathin layers composed of the same set of materials, operating at two frequency ranges, both possessing nonreciprocal spin-wave dispersion relations but with different characteristics. We demonstrated that SWs in pair of closely-placed magnetic layers can propagate without interactions due to difference in anisotropy and opposite sign of DMI. Because of the difference in magnetic parameters, the effect of dipolar interaction is lowered and communication between the SW channels is negligible. The presented system, having two independent nonreciprocal paths for the spin waves, is important for design and miniaturization of 3D multilevel magnonic networks.

ACKNOWLEDGMENTS

The authors thank Maciej Krawczyk for a fruitful discussion. K.S. acknowledges the financial support from the

National Science Center of Poland, Project No. UMO-2018/30/Q/ST3/00416. S.M. and M.B. acknowledge the financial support by the German Research Foundation (DFG), priority program SPP2137 Project No. 403505866, as well as the TUM International Graduate School of Science and Engineering (IGSSE), Project No. GSC 81-24184165. M.M. acknowledges funding from the Slovak Grant Agency APVV, No. APVV-16-0068 (NanoSky) and APVV-19-0311 (RSWFA). This study was performed in the frame of the implementation of the project Building-up Centre for Advanced Materials Application of the Slovak Academy of Sciences, ITMS Project code 313021T081 supported by Research & Innovation Operational Programme funded by the ERDF. G.G. acknowledges the financial support by the European Metrology Programme for Innovation and Research (EMPIR) under the Grant Agreement 17FUN08 TOPS.

-
- [1] T. Moriya, Anisotropic superexchange interaction and weak ferromagnetism, *Phys. Rev.* **120**, 91 (1960).
 - [2] G. Finocchio, F. Büttner, R. Tomasello, M. Carpentieri, and M. Kläui, Magnetic skyrmions: From fundamental to applications, *J. Phys. D: Appl. Phys.* **49**, 423001 (2016).
 - [3] F. J. dos Santos, M. dos Santos Dias, and S. Lounis, Nonreciprocity of spin waves in noncollinear magnets due to the Dzyaloshinskii-Moriya interaction, *Phys. Rev. B* **102**, 104401 (2020).
 - [4] L. Udvardi and L. Szunyogh, Chiral Asymmetry of the Spin-Wave Spectra in Ultrathin Magnetic Films, *Phys. Rev. Lett.* **102**, 207204 (2009).
 - [5] D. Cortés-Ortuño and P. Landeros, Influence of the Dzyaloshinskii-Moriya interaction on the spin-wave spectra of thin films, *J. Phys. Condens. Matter* **25**, 156001 (2013).
 - [6] M. Mruczkiewicz and M. Krawczyk, Influence of the Dzyaloshinskii-Moriya interaction on the FMR spectrum of magnonic crystals and confined structures, *Phys. Rev. B* **94**, 024434 (2016).
 - [7] K. Szulc, P. Graczyk, M. Mruczkiewicz, G. Gubbiotti, and M. Krawczyk, Spin-wave diode and circulator based on unidirectional coupling, *Phys. Rev. Appl.* **14**, 034063 (2020).
 - [8] M. Belmeguenai, J.-P. Adam, Y. Roussigné, S. Eimer, T. Devolder, J.-V. Kim, S. M. Cherif, A. Stashkevich, and A. Thiaville, Interfacial Dzyaloshinskii-Moriya interaction in perpendicularly magnetized Pt/Co/AIO_x ultrathin films measured by Brillouin light spectroscopy, *Phys. Rev. B* **91**, 180405(R) (2015).
 - [9] J. Cho, N.-H. Kim, S. Lee, J.-S. Kim, R. Lavrijsen, A. Solignac, Y. Yin, D.-S. Han, N. J. J. Van Hoof, H. J. M. Swagten, B. Koopmans, and C.-Y. You, Thickness dependence of the interfacial Dzyaloshinskii-Moriya interaction in inversion symmetry broken systems, *Nat. Commun.* **6**, 7635 (2015).
 - [10] O. Boulle, J. Vogel, H. Yang, S. Pizzini, D. de Souza Chaves, A. Locatelli, T. O. Menteş, A. Sala, L. D. Buda-Prejbeanu, O. Klein, M. Belmeguenai, Y. Roussigné, A. Stashkevich, S. M. Chérif, L. Aballe, M. Foerster, M. Chshiev, S. Auffret, I. M. Miron, and G. Gaudin, Room-temperature chiral magnetic skyrmions in ultrathin magnetic nanostructures, *Nat. Nanotechnol.* **11**, 449 (2016).
 - [11] S. Woo, K. Litzius, B. Krüger, M.-Y. Im, L. Caretta, K. Richter, M. Mann, A. Krone, R. M. Reeve, M. Weigand, P. Agrawal, I. Lemesh, M.-A. Mawass, P. Fischer, M. Kläui, and G. S. D. Beach, Observation of room-temperature magnetic skyrmions and their current-driven dynamics in ultrathin metallic ferromagnets, *Nat. Mater.* **15**, 501 (2016).
 - [12] B. Zhang, A. Cao, J. Qiao, M. Tang, K. Cao, X. Zhao, S. Eimer, Z. Si, N. Lei, Z. Wang, X. Lin, Z. Zhang, M. Wu, and W. Zhao, Influence of heavy metal materials on magnetic properties of Pt/Co/heavy metal tri-layered structures, *Appl. Phys. Lett.* **110**, 012405 (2017).
 - [13] J. Yu, X. Qiu, Y. Wu, J. Yoon, P. Deorani, J. M. Besbas, A. Manchon, and H. Yang, Spin orbit torques and Dzyaloshinskii-Moriya interaction in dual-interfaced Co-Ni multilayers, *Sci. Rep.* **6**, 1 (2016).
 - [14] A. Soumyanarayanan, M. Raju, A. G. Oyarce, A. K. Tan, M.-Y. Im, A. P. Petrović, P. Ho, K. Khoo, M. Tran, C. Gan, F. Ernult, and C. Panagopoulos, Tunable room-temperature magnetic skyrmions in Ir/Fe/Co/Pt multilayers, *Nat. Mater.* **16**, 898 (2017).
 - [15] N.-H. Kim, J. Cho, J. Jung, D.-S. Han, Y. Yin, J.-S. Kim, H. J. M. Swagten, K. Lee, M.-H. Jung, and C.-Y. You, Role of top and bottom interfaces of a Pt/Co/AIO_x system in Dzyaloshinskii-Moriya interaction, interface perpendicular magnetic anisotropy, and magneto-optical Kerr effect, *AIP Adv.* **7**, 035213 (2017).
 - [16] R. Tolley, S. A. Montoya, and E. E. Fullerton, Room-temperature observation and current control of skyrmions in Pt/Co/Os/Pt thin films, *Phys. Rev. Mater.* **2**, 044404 (2018).
 - [17] V. M. Parakkat, K. R. Ganesh, and P. S. Anil Kumar, Copper dusting effects on perpendicular magnetic anisotropy in Pt/Co/Pt tri-layers, *AIP Adv.* **6**, 056122 (2016).
 - [18] W. Legrand, J.-Y. Chauleau, D. Maccariello, N. Reyren, S. Collin, K. Bouzehouane, N. Jaouen, V. Cros, and A. Fert, Hybrid chiral domain walls and skyrmions in magnetic multilayers, *Sci. Adv.* **4**, eaat0415 (2018).
 - [19] A. W. J. Wells, P. M. Shepley, C. H. Marrows, and T. A. Moore, Effect of interfacial intermixing on the Dzyaloshinskii-Moriya interaction in Pt/Co/Pt, *Phys. Rev. B* **95**, 054428 (2017).

- [20] A. P. Danilov, A. V. Scherbakov, B. A. Glavin, T. L. Linnik, A. M. Kalashnikova, L. A. Shelukhin, D. P. Pattnaik, A. W. Rushforth, C. J. Love, S. A. Cavill, D. R. Yakovlev, and M. Bayer, Optically excited spin pumping mediating collective magnetization dynamics in a spin valve structure, *Phys. Rev. B* **98**, 060406(R) (2018).
- [21] M. Belmeguenai, H. Bouloussa, Y. Roussigné, M. S. Gabor, T. Petrisor, C. Tiusan, H. Yang, A. Stashkevich, and S. M. Chérif, Interface Dzyaloshinskii-Moriya interaction in the interlayer antiferromagnetic-exchange coupled Pt/CoFeB/Ru/CoFeB systems, *Phys. Rev. B* **96**, 144402 (2017).
- [22] F. J. dos Santos, M. dos Santos Dias, and S. Lounis, Modeling spin waves in noncollinear antiferromagnets: Spin-flop states, spin spirals, skyrmions, and antiskyrmions, *Phys. Rev. B* **102**, 104436 (2020).
- [23] A. T. Costa, R. B. Muniz, S. Lounis, A. B. Klautau, and D. L. Mills, Spin-orbit coupling and spin waves in ultrathin ferromagnets: The spin-wave Rashba effect, *Phys. Rev. B* **82**, 014428 (2010).
- [24] Y. Henry, D. Stoeffler, J.-V. Kim, and M. Bailleul, Unidirectional spin-wave channeling along magnetic domain walls of Bloch type, *Phys. Rev. B* **100**, 024416 (2019).
- [25] M. Grimsditch, S. Kumar, and E. E. Fullerton, Brillouin light scattering study of Fe/Cr/Fe (211) and (100) trilayers, *Phys. Rev. B* **54**, 3385 (1996).
- [26] P. Fuchs, U. Ramsperger, A. Vaterlaus, and M. Landolt, Roughness-induced coupling between ferromagnetic films across an amorphous spacer layer, *Phys. Rev. B* **55**, 12546 (1997).
- [27] A. Fernández-Pacheco, E. Vedmedenko, F. Ummelen, R. Mansell, D. Petit, and R. P. Cowburn, Symmetry-breaking interlayer Dzyaloshinskii-Moriya interactions in synthetic antiferromagnets, *Nat. Mater.* **18**, 679 (2019).
- [28] G. V. Karnad, F. Freimuth, E. Martinez, R. Lo Conte, G. Gubbiotti, T. Schulz, S. Senz, B. Ocker, Y. Mokrousov, and M. Kläui, Modification of Dzyaloshinskii-Moriya-Interaction-Stabilized Domain Wall Chirality by Driving Currents, *Phys. Rev. Lett.* **121**, 147203 (2018).
- [29] K. Shahbazi, J.-V. Kim, H. T. Nembach, J. M. Shaw, A. Bischof, M. D. Russell, V. Jeudy, T. A. Moore, and C. H. Marrows, Domain-wall motion and interfacial Dzyaloshinskii-Moriya interactions in Pt/Co/Ir(t_{Ir})/Ta multilayers, *Phys. Rev. B* **99**, 094409 (2019).
- [30] W. Han, Perspectives for spintronics in 2D materials, *APL Mater.* **4**, 032401 (2016).
- [31] A. Samardak, A. Kolesnikov, M. Stebliy, L. Chebotkevich, A. Sadovnikov, S. Nikitov, A. Talapatra, J. Mohanty, and A. Ognev, Enhanced interfacial Dzyaloshinskii-Moriya interaction and isolated skyrmions in the inversion-symmetry-broken Ru/Co/W/Ru Films, *Appl. Phys. Lett.* **112**, 192406 (2018).
- [32] M. Kuepferling, A. Casiraghi, G. Soares, G. Durin, F. Garcia-Sanchez, L. Chen, C. H. Back, C. H. Marrows, S. Tacchi, and G. Carlotti, Measuring interfacial Dzyaloshinskii-Moriya interaction in ultra thin films, [arXiv:2009.11830](https://arxiv.org/abs/2009.11830).
- [33] P. Krams, F. Lauks, R. L. Stamps, B. Hillebrands, and G. Güntherodt, Magnetic Anisotropies of Ultrathin Co(001) Films on Cu(001), *Phys. Rev. Lett.* **69**, 3674 (1992).
- [34] M. Madami, S. Tacchi, G. Carlotti, G. Gubbiotti, and R. L. Stamps, *In situ* Brillouin scattering study of the thickness dependence of magnetic anisotropy in uncovered and Cu-covered Fe/GaAs(100) ultrathin films, *Phys. Rev. B* **69**, 144408 (2004).
- [35] H. T. Nembach, J. M. Shaw, M. Weiler, E. Jué, and T. J. Silva, Linear relation between Heisenberg exchange and interfacial Dzyaloshinskii-Moriya interaction in metal films, *Nat. Phys.* **11**, 825 (2015).
- [36] K. Di, V. L. Zhang, H. S. Lim, S. C. Ng, M. H. Kuok, J. Yu, J. Yoon, X. Qiu, and H. Yang, Direct Observation of the Dzyaloshinskii-Moriya Interaction in a Pt/Co/Ni Film, *Phys. Rev. Lett.* **114**, 047201 (2015).
- [37] S. Tacchi, R. E. Troncoso, M. Ahlberg, G. Gubbiotti, M. Madami, J. Åkerman, and P. Landeros, Interfacial Dzyaloshinskii-Moriya Interaction in Pt/CoFeB Films: Effect of the Heavy-Metal Thickness, *Phys. Rev. Lett.* **118**, 147201 (2017).
- [38] X. Ma, G. Yu, S. A. Razavi, S. S. Sasaki, X. Li, K. Hao, S. H. Tolbert, K. L. Wang, and X. Li, Dzyaloshinskii-Moriya Interaction Across an Antiferromagnet-Ferromagnet Interface, *Phys. Rev. Lett.* **119**, 027202 (2017).
- [39] X. Ma, G. Yu, C. Tang, X. Li, C. He, J. Shi, K. L. Wang, and X. Li, Interfacial Dzyaloshinskii-Moriya Interaction: Effect of $5d$ Band Filling and Correlation with Spin Mixing Conductance, *Phys. Rev. Lett.* **120**, 157204 (2018).
- [40] A. Kumar, A. K. Chaurasiya, N. Chowdhury, A. K. Mondal, R. Bansal, A. Barvat, S. P. Khanna, P. Pal, S. Chaudhary, A. Barman, and P. K. Muduli, Direct measurement of interfacial Dzyaloshinskii-Moriya interaction at the MoS₂/Ni₈₀Fe₂₀ interface, *Appl. Phys. Lett.* **116**, 232405 (2020).
- [41] H. Bouloussa, Y. Roussigné, M. Belmeguenai, A. Stashkevich, S. M. Chérif, J. Yu, and H. Yang, Spin-wave calculations for magnetic stacks with interface Dzyaloshinskii-Moriya interaction, *Phys. Rev. B* **98**, 024428 (2018).
- [42] J. R. Sandercock, *Light Scattering in Solids III* (Springer, Berlin, 1982), p. 173.
- [43] G. Carlotti and G. Gubbiotti, Magnetic properties of layered nanostructures studied by means of Brillouin light scattering and the surface magneto-optical Kerr effect, *J. Phys. Condens. Matter* **14**, 8199 (2002).
- [44] S. Klingler, V. Amin, S. Geprägs, K. Ganzhorn, H. Maier-Flaig, M. Althammer, H. Huebl, R. Gross, R. D. McMichael, M. D. Stiles, S. T. B. Goennenwein, and M. Weiler, Spin-Torque Excitation of Perpendicular Standing Spin Waves in Coupled YIG/Co Heterostructures, *Phys. Rev. Lett.* **120**, 127201 (2018).
- [45] P. Graczyk, M. Zelent, and M. Krawczyk, Co- and contra-directional vertical coupling between ferromagnetic layers with grating for short-wavelength spin wave generation, *New J. Phys.* **20**, 053021 (2018).
- [46] G. Gubbiotti, G. Carlotti, G. Socino, F. D'Orazio, F. Lucari, R. Bernardini, and M. De Crescenzi, Perpendicular and in-plane magnetic anisotropy in epitaxial Cu/Ni/Cu/Si(111) ultrathin films, *Phys. Rev. B* **56**, 11073 (1997).
- [47] J.-H. Moon, S.-M. Seo, K.-J. Lee, K.-W. Kim, J. Ryu, H.-W. Lee, R. D. McMichael, and M. D. Stiles, Spin-wave propagation in the presence of interfacial Dzyaloshinskii-Moriya interaction, *Phys. Rev. B* **88**, 184404 (2013).
- [48] S. Mendisch, G. Žiemyš, V. Ahrens, A. Papp, and M. Becherer, Pt/Co/W as a candidate for low power nanomagnetic logic, *J. Magn. Magn. Mater.* **485**, 345 (2019).

- [49] P. Chowdhury, P. D. Kulkarni, M. Krishnan, H. C. Barshilia, A. Sagdeo, S. K. Rai, G. S. Lodha, and D. V. Sridhara Rao, Effect of coherent to incoherent structural transition on magnetic anisotropy in Co/Pt multilayers, *J. Appl. Phys.* **112**, 023912 (2012).
- [50] S. Mallick, S. Mallik, B. B. Singh, N. Chowdhury, R. Gieniusz, A. Maziewski, and S. Bedanta, Tuning the anisotropy and domain structure of Co films by variable growth conditions and seed layers, *J. Phys. D: Appl. Phys.* **51**, 275003 (2018).

4.4 [P4] Reconfigurable magnonic crystals based on imprinted magnetization textures in hard and soft dipolar-coupled bilayers

This research was carried out in collaboration with the groups of S. Tacchi at CNR in Perugia, Italy, L. M. Álvarez-Prado at Universidad de Oviedo, Spain, and D. Schmool at CNRS in Versailles, France. The collaboration started in 2019. The NdCo/Al/Py samples were prepared by the Oviedo group. Thin NdCo films are characterized by a low perpendicular magnetic anisotropy, which allows the system to stabilize the stripe domains, as explained in Section 2.2.2. However, this class of materials is characterized by high damping, making them inefficient for the spin-wave transmission. The idea was to couple this layer to a layer of a soft magnetic material with low damping like permalloy. In such a case, the stripe domains from the NdCo layer have been imprinted on the Py layer, making it the spin-wave conduit with a modified magnetization configuration. Additionally, since the Py layer has a low coercivity, it was possible to change its magnetization direction without modifying the stripe-domain pattern in the NdCo layer, making the system reconfigurable. The samples were measured by BLS spectroscopy by S. Tacchi from Perugia. The results show a spin-wave mode with very strong asymmetry. The asymmetry was opposite for the systems with reversed magnetization in the Py layer. In addition, the second mode was partially visible in large wavevectors for the samples with thin Al spacer. The role of our group was to use the numerical simulations to investigate how the thickness of the Al spacer affects the magnetization configuration of the system, whether the stripe domains are responsible for the strong dispersion asymmetry, and what is the source of the second mode. Together with P. Graczyk, I extended the COMSOL model to solve the eigenfrequency problem in the systems with non-collinear magnetization. The results of the numerical simulations not only confirmed the important role of the stripe domains, but also demonstrated that the second mode comes from the interaction with a mode from the neighboring Brillouin zone, showing that this system acts as a magnonic crystal. The simulations were also crucial for understanding the role of damping on the dispersion relation; the magnonic crystal behavior was not pronounced in the system with thicker Al spacer due to high damping in the NdCo layer.

Contribution of the Author

In this publication, I performed the numerical simulations, extended the COMSOL model (together with P. Graczyk), participated in the interpretation and discussion of the experimental and numerical results, wrote the Results and Discussion, Conclusions sections, Numerical Simulations subsection in the Experimental section, prepared the Supporting Information, prepared Figures 1a, 2, 3a,c, 5, and 6, and was responsible for the manuscript submission and correspondence with the journal.

Reconfigurable Magnonic Crystals Based on Imprinted Magnetization Textures in Hard and Soft Dipolar-Coupled Bilayers

Krzysztof Szulc,^{*,△} Silvia Tacchi,^{*,△} Aurelio Hierro-Rodríguez, Javier Díaz, Paweł Gruszecki, Piotr Graczyk, Carlos Quirós, Daniel Markó, José Ignacio Martín, María Vélez, David S. Schmool, Giovanni Carlotti, Maciej Krawczyk, and Luis Manuel Álvarez-Prado



Cite This: <https://doi.org/10.1021/acsnano.2c04256>



Read Online

ACCESS |



Metrics & More



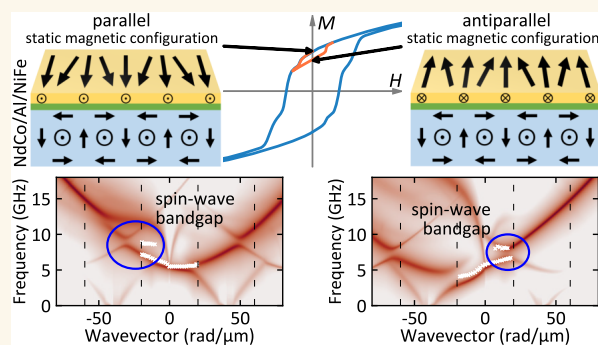
Article Recommendations



Supporting Information

ABSTRACT: Reconfigurable magnetization textures offer control of spin waves with promising properties for future low-power beyond-CMOS systems. However, materials with perpendicular magnetic anisotropy (PMA) suitable for stable magnetization-texture formation are characterized by high damping, which limits their applicability in magnonic devices. Here, we propose to overcome this limitation by using hybrid structures, i.e., a PMA layer magnetostatically coupled to a low-damping soft ferromagnetic film. We experimentally show that a periodic stripe-domain texture from a PMA layer is imprinted upon the soft layer and induces a nonreciprocal dispersion relation of the spin waves confined to the low-damping film. Moreover, an asymmetric bandgap features the spin-wave band diagram, which is a clear demonstration of collective spin-wave dynamics, a property characteristic for magnonic crystals with broken time-reversal symmetry. The composite character of the hybrid structure allows for stabilization of two magnetic states at remanence, with parallel and antiparallel orientation of net magnetization in hard and soft layers. The states can be switched using a low external magnetic field; therefore, the proposed system obtains an additional functionality of state reconfigurability. This study offers a link between reconfigurable magnetization textures and low-damping spin-wave dynamics, providing an opportunity to create miniaturized, programmable, and energy-efficient signal processing devices operating at high frequencies.

KEYWORDS: spin waves, magnonic crystal, magnetic stripe domains, perpendicular magnetic anisotropy, magnetic bilayers



INTRODUCTION

The use of nonuniform magnetic textures to control the propagation of spin waves (SWs) has attracted considerable interest in recent years.^{1,2} This approach has many advantages over conventionally used nanostructured systems at saturation. Their use reduces the negative impact of edge heterogeneity and defects, which can appear in nanofabrication processes. It has been shown that SWs can be guided along domain walls, serving as narrow graded-index waveguides.^{3–8} Domain-wall propagation also removes the limitations related to the bending of SW flow in the in-plane magnetized thin films, existing due to the strong anisotropy of SW dispersion.^{6–11} Particularly interesting in this context are systems with perpendicular magnetic anisotropy (PMA), in which naturally stable Bloch-type domain walls can be very narrow with widths of less than 10 nm, whereas nanostructuring of 50 nm-wide waveguides is

still a technological challenge.^{12,13} From an application point of view, the utilization of magnonic circuits with stable magnetic configuration in the absence of the external magnetic field is highly desirable,^{14,15} and one of the best-suited methods to achieve this is to use PMA.¹⁶ Moreover, it is often possible to achieve various stable magnetic configurations as a medium for the propagation of SWs in the same system, which provides the possibility of reprogrammability.^{6,10,17,18} For instance, in magnetic films with PMA characterized by a quality factor Q

Received: May 2, 2022

Accepted: August 26, 2022

= $2K_{\text{PMA}}/\mu_0 M_S^2$ smaller than one (where K_{PMA} is the PMA constant and M_S is the saturation magnetization), and above a certain critical thickness, it is possible to stabilize a pattern of aligned stripe domains with alternating up and down out-of-plane magnetization component, having lattice constants of 100 nm and smaller, which can be controlled by the layer thickness.^{18–27} Nevertheless, the thicker the system, the more complex the internal structure of domains and domain walls across the film thickness.^{21,28} However, for Néel- or Bloch-type walls, up and down domains are separated by flux-closure domain walls resembling vortices with cores directed along the domain wall axes.^{18,29} Domain walls in this type of system may also have different chiralities with respect to the polarity of the domain wall that can support nonreciprocal effects for SW propagation.^{18,28,29}

Analytical calculations and micromagnetic simulations have indicated that in periodic magnetization textures, the nonlocal dipole field arising from the finite film thickness leads to the formation of a band structure.³⁰ More recently, the role of the dipolar field has been also confirmed by Laliena et al.³¹ In this work, the authors have shown theoretically that Bloch domain walls, which are transparent to the SWs propagation when the dipolar interaction is neglected, are able to reflect SWs if the dipolar interaction is taken into account properly.

Periodic stripe domains has been shown to be suitable to control SW dynamics and function as magnonic crystals.^{18,28,32–35} Hitherto, the band-gap openings have only been demonstrated theoretically arising from small lattice constants causing the Brillouin-zone (BZ) edge to lie beyond the experimentally measurable range of wavevectors using conventional techniques. However, the magnonic advantages of thin ferromagnetic films with PMA are limited by the high SW damping usually present in this class of materials. There are a few exceptions to this, such as ferrimagnetic materials with very low saturation magnetization, e.g., bismuth-doped yttrium–iron garnet or thulium–iron garnet.^{36–38}

Here we propose an approach, which enables us to avoid high damping of PMA materials while still harnessing the advantages of the magnetization texture for the efficient guiding and control of the SW propagation. For this purpose, we use a hybrid system consisting of a soft ferromagnetic film, which is dipolar-coupled to a hard layer exhibiting a stripe-domain pattern.^{39–41} In previous studies, it has been shown that in this kind of hybrid system, the stripe-domain pattern from the hard magnetic layer is transferred to the soft one.^{40,42–45} Interestingly, in the bilayer system with one layer possessing an out-of-plane component of the static magnetization, the static stray field affects both static and dynamic properties of the second medium.⁴⁶ With this approach, we aim to combine the advantages of regular magnetization textures in PMA films with low-damping thin films, which can be used as an effective low-damping conduit of SWs to advance magnonics.

Moreover, in dipolar-coupled magnetic bilayers, one can achieve nonreciprocal SW propagation so that, for a given frequency, oppositely propagating SWs have different wavelengths.^{47–50} Furthermore, the alternation of the SW amplitude between the layers can be achieved, enabling one to design co- and contra-directional couplers⁵¹ or utilize the effects to design magnonic diodes and circulators.⁵²

In this work, we perform a combined experimental and theoretical study of SW dynamics in a trilayer consisting of a permalloy (Py) film coupled through an Al interlayer (of

varying thicknesses) to a NdCo_{7.5} layer with weak PMA, with a ground-state periodic stripe-domain pattern. The static properties of the system have been measured using vibrating sample magnetometry (VSM) and magnetic force microscopy (MFM), whereas SW dynamics have been measured by Brillouin light scattering (BLS) spectroscopy. The experimental results are reproduced and interpreted using finite-element method simulations, which have been further developed to treat the nonuniform magnetic textures. Two different configurations have been stabilized in remanence, and it is possible to switch between them by applying a small external magnetic field: (i) in the parallel state, the magnetization in the Py layer follows the magnetic configuration of the NdCo stripe domains, while (ii) in the antiparallel state, the in-plane magnetization component along the Py stripes axis is antiparallel to that of the NdCo stripes.

The SW dispersion in the Py film is found to be strongly affected by the periodic pattern of the stripe domains in both the parallel and the antiparallel state. In particular, the band structure is characterized by a significant frequency asymmetry induced by the dipolar coupling between the Py and NdCo layer, which becomes more marked with a reduction of the thickness of the Al layer. Moreover, in the sample with the thinnest Al spacer, the opening of a band gap, induced by the hybridization between the fundamental mode in Py from neighboring BZs, has been experimentally observed at the boundary of the first BZ. Interestingly, due to the strong frequency asymmetry of the band structure, the band gap is shifted from the edge of the BZ and occurs only on one side of the experimental dispersion, and is on opposite sides for the parallel and antiparallel state.

RESULTS AND DISCUSSION

Static Magnetic Properties. The investigated trilayer samples (Figure 1a) consist of an amorphous 64 nm-thick NdCo_{7.5} film and a 10 nm-thick Py film coupled through an Al spacer of varying thickness ($t = 2.5, 5, 10$ nm). The fabrication of the samples is described in the **Experimental Section**. The static magnetic properties of the samples have been studied by means of VSM. Figure 1c shows the hysteresis loop measured by applying a magnetic field along the in-plane easy direction (x -axis) for the sample with a 10 nm-thick Al spacer. Similar hysteresis loops have been measured for the other samples. As can be seen, coming from positive saturation, the magnetization curve exhibits the typical “transcritical shape”, characterized by the presence of a linear reversible region starting around 120 mT, corresponding to the formation of stripe domains. When the magnetic field is reversed, a small drop in magnetization, associated with the reversal of the Py magnetization component parallel to the external field, occurs at about -15 mT. Then a plateau is observed until about -25 mT, where the Py and NdCo_{7.5} net magnetizations are aligned along opposite directions, realizing an antiparallel ground state of the system. Next, a second drop can be seen and is ascribed to the reversal of the NdCo_{7.5} magnetization component parallel to the external field. Finally, negative saturation, where stripe domains disappear, is reached at about -120 mT. Furthermore, the minor hysteresis loop (orange curve) has been measured by increasing the magnitude of the applied field in the positive direction once the first plateau, due to the magnetization reversal of Py, has been reached. As can be seen, the state of antiparallel alignment between the Py and the NdCo_{7.5} magnetization remains stable when the magnetic field

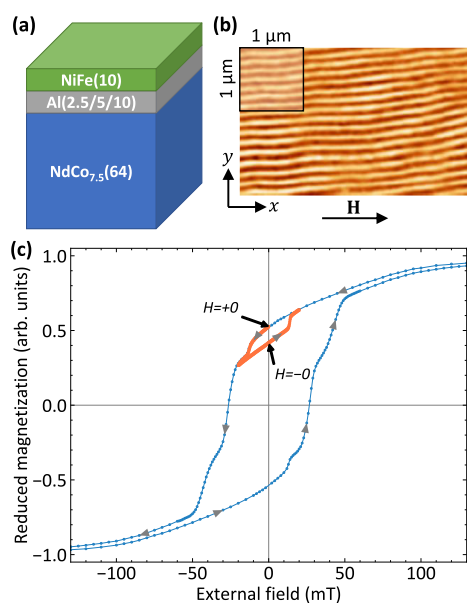


Figure 1. (a) Sketch of the investigated samples. (b) MFM image of the stripe domains taken at remanence after saturation along the x -direction for the sample with the 10 nm-thick Al layer. (c) VSM hysteresis loop measured for the sample with the 10 nm-thick Al layer (blue curve). The orange curve refers to the minor loop along which BLS measurements have been performed. The point indicated with $H = +0$ ($H = -0$) marks the remanent state with parallel (antiparallel) longitudinal component of the magnetization (m_x) in adjacent stripes.

returns to zero coming from -20 mT ($H = -0$). Moreover, it is possible to recover the parallel alignment of the magnetization in the Py and NdCo layers by applying an in-plane magnetic field $H = +20$ mT and going back to zero ($H = +0$). This shows that we can easily switch between the parallel and antiparallel state by applying a small external magnetic field. The stripe-domain structure was imaged at remanence by MFM. **Figure 1b** shows an MFM image of the sample with the 10 nm-thick Al spacer. Very regular stripe domains, aligned along the in-plane direction of the last saturating magnetic field, are observed on top surface, i.e., the Py layer, confirming the dipolar interaction between the magnetic layers. From the fast Fourier transform (FFT) of the MFM image, we obtained a stripe domains period (consisting of a couple of "up" and "down" domains) of (146 ± 10) nm. A similar stripe-domain pattern has been observed for the other samples (not shown here).

To gain a deeper insight into the magnetization configuration of stripe domains at remanence, numerical simulations (for details see **Experimental Section**) have been performed to visualize the domain structure corresponding to the parallel ($H = +0$) and antiparallel ($H = -0$) remanent states. For the parallel state (**Figure 2**, left panels), one can observe a magnetic structure in the NdCo film composed of stripe domains, which are alternately magnetized up and down (along the z -axis) with respect to the surface plane, separated by Bloch-type domain walls, with the domain-wall cores in-plane magnetized along the saturation direction ($+x$ -direction). Flux-closure domains with the in-plane magnetization along the y -axis are found at the film surfaces. Note that the flux-closure domain pattern from the top surface of NdCo is

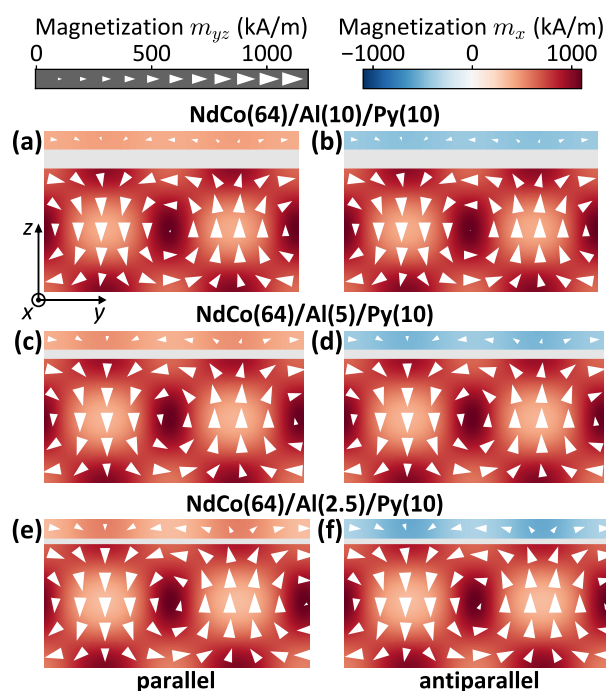


Figure 2. Equilibrium magnetization state calculated for the single unit cell of the trilayer system at remanence for the parallel (left column) and the antiparallel (right column) alignment of the x -component of magnetization in Py and NdCo. The results are shown for the samples with the Al layer thickness of (a, b) 10 nm, (c, d) 5 nm, and (e, f) 2.5 nm. The arrows represent the projection of the magnetization in the yz -plane, while the component m_x is given by a color code.

transferred to the soft Py layer whose magnetization follows the magnetic configuration of the NdCo stripe domains.

Interestingly, in the numerical simulations, the period of the stripe-domain pattern is found to only slightly increase when the Al thickness decreases, changing from 132 nm [for Al(10)] to 138 nm [for Al(2.5)] due to the increase of the dipolar interaction. Furthermore, with a reduction of the spacer layer thickness, the enhanced imprint of the domain structure in the Py film causes the domain structure itself to expand along the sample thickness and the domain-wall core to shift up toward the Py layer. This effect can be considered as an increase of the effective thickness of the NdCo layer and becomes more pronounced with an increase of the dipolar coupling between the two ferromagnetic layers. Note that the simultaneous increase of the effective thickness of the NdCo layer and of the stripe-domain period is in agreement with the fact that in low-PMA films, the single-domain width should be equal to the thickness of the layer.¹⁹

For the antiparallel state, the stripe-domain structure in the NdCo film remains stable, maintaining a period identical to that of the parallel state, while in the Py layer, the in-plane magnetization component m_x is observed to reverse along the $-x$ -direction. This magnetization configuration has an antiparallel alignment of the m_x magnetization component in Py and NdCo. As in the parallel configuration, the domain-wall core is observed to shift upward into the Py layer when the thickness of the Al spacer is reduced.

Spin-Wave Dynamics in the Saturated State. Spin-wave propagation in the trilayer samples has been investigated

by the BLS technique. First, the SW dispersion relation has been measured when both the Py and NdCo_{7.5} films are saturated with an in-plane magnetic field $H = +200$ mT along the in-plane easy direction (x -axis). BLS measurements (see the Experimental Section for details) have been performed in the Damon-Eshbach configuration, sweeping the in-plane transferred wavevector k along the perpendicular direction (y -axis). Figure 3a shows the measured frequencies (points) of

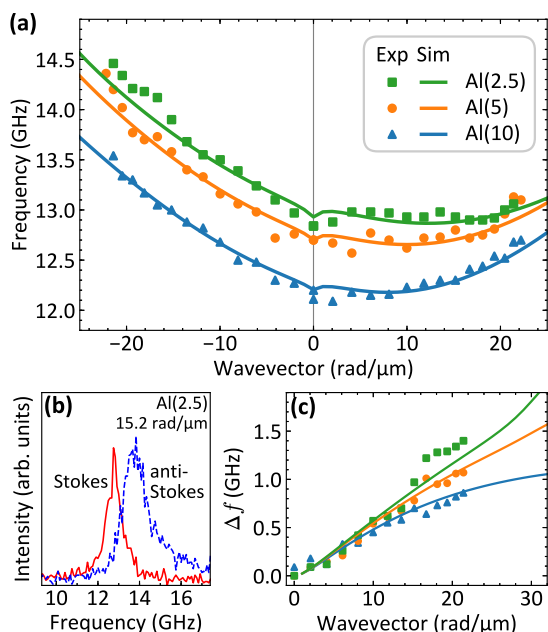


Figure 3. (a) Measured (points) and calculated (lines) SW dispersion relations in the Damon-Eshbach configuration for three samples with different thicknesses of the Al spacer, saturated by an external field $H = 200$ mT. Points at positive (negative) wavevectors are the frequencies collected from the Stokes (anti-Stokes) peaks in the BLS spectra. (b) Absolute frequency of the Stokes and anti-Stokes peaks in BLS spectra measured at $k = 15.2$ rad/μm for the Al(2.5) sample. (c) Frequency difference Δf between anti-Stokes and Stokes peaks as a function of wavevector k .

the Stokes peaks (which arise from SWs propagating with positive k) and the anti-Stokes peaks (which arise from SWs propagating with negative k) as a function of the SW wavevector. As can be seen, the two peaks exhibit different dispersion relations, and the mode propagating with $-k$ is characterized by a larger gradient. This is clearly visible in the BLS spectra shown in Figure 3b, where we observe a significant frequency asymmetry between the Stokes and the anti-Stokes peaks. Such a frequency difference between Damon-Eshbach modes propagating in opposite directions is well reproduced by theoretical calculations (lines) and can be ascribed to the dipolar interaction between the Py and NdCo layers produced by the dynamic components of the magnetization.⁴⁹ A similar frequency difference is present in the calculated dispersion of the modes localized in the NdCo layer. The absence of these modes in the experimental BLS spectra can be explained taking into account that the signal from NdCo layer is much weaker than from Py due to both the finite penetration depth of the laser light in the BLS measurements and the high damping constant of NdCo that leads to a broadening of the BLS peaks.

Figure 3c shows the measured (points) and the calculated (lines) frequency difference Δf between the Stokes and the anti-Stokes peak as a function of the wavevector. When the Al thickness is reduced, the increase of the dipolar coupling causes an increase of the frequency asymmetry. For the sample with a 2.5 nm-thick Al spacer, Δf increases almost linearly as a function of wavevector, reaching a value of about 1.4 GHz at $k = 21.4$ rad/μm. Increasing the thickness of the Al spacer, Δf assumes lower values and its slope is reduced for large wavevectors. This effect stems from the decreasing range of the dynamic stray field for large wavevectors, resulting from a weaker dynamic dipolar interaction,⁴⁹ and thus in reaching the maximum value of the nonreciprocity at relatively short wavelengths.

Interestingly, a significant increase of the measured SW frequencies with decreasing the Al spacer thickness can be observed. However, for saturated Py and NdCo layers, interacting only via dipolar coupling, the SW frequency at $k = 0$ is not expected to be affected by the thickness of the Al spacer.⁴⁹ Therefore, the above-mentioned behavior can be ascribed to a reduction of the effective magnetization of the Py film due to the increase of the surface roughness when the thickness of the Al spacer increases. This is confirmed by X-ray reflectivity measurements of Si/Al/Py samples with different thickness of the Al layer. A progressive deterioration of the Al/Py interface with increasing the Al thickness, due to the increase of the roughness of the Al layer, is observed.

Spin-Wave Dynamics at Remanence. As a second step of our BLS investigation, the SW dispersion has been measured at remanence, when the stripe domains are aligned along the in-plane easy direction (x -axis). Also, in this case, the in-plane wavevector has been swept along the y -axis, i.e., in the direction perpendicular to the axis of the stripe domains. Figure 4 shows typical BLS spectra recorded in the parallel state (top row) and the antiparallel state (bottom row). For the samples with the 10 nm-thick and 5 nm-thick Al spacer, only one peak, characterized by a sizable frequency asymmetry between the Stokes and the anti-Stokes side, is observed in the BLS spectra. For the sample with the 2.5 nm-thick Al spacer, a second peak is present at higher frequencies in the anti-Stokes (Stokes) part of the BLS spectra for parallel (antiparallel) state for wavevectors larger than about 15 rad/μm.

The comparison between the calculated (color map) and the measured (white crosses) SW dispersion at remanence is reported in Figure 5 for all of the investigated samples. Since the dynamic magnetization component perpendicular to the film surface gives the main contribution to the BLS cross-section, only the magnetization component m_z was taken into account for the SW intensity calculated using eq 5 (see Experimental Section) and presented with a color map in logarithmic scale. The calculated band structures are very feature-rich and characterized by a marked influence of the periodic pattern of the stripe domains in both the parallel and the antiparallel states. In particular, the band diagram is characterized by a significant frequency asymmetry induced by the dipolar coupling, and this is confirmed by the measured BLS data that correspond to the most intense peak in the calculated dispersion relation. Note that only the first BZ is accessible by BLS, because the maximum wavevector value achievable by this technique is limited to about 22 rad/μm. Interestingly, the bands are present only every second BZ (e.g., the parabolic highest-intensity mode marked with cyan and green lines in Figure 5c,f) as if the period of the domain

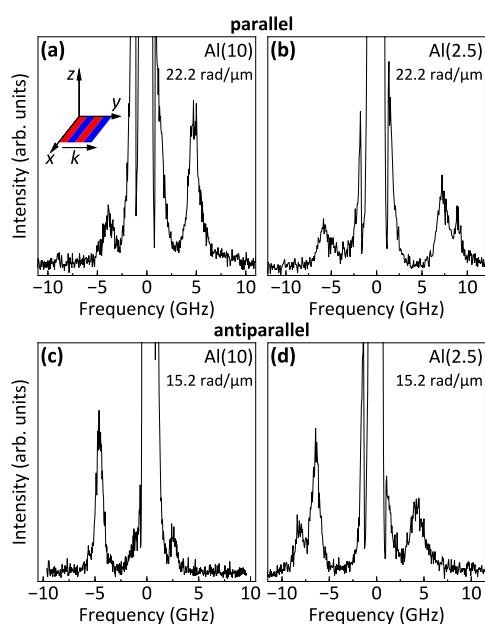


Figure 4. BLS spectra measured at $k = 22.2 \text{ rad}/\mu\text{m}$ and $k = 15.2 \text{ rad}/\mu\text{m}$ for parallel state (top row) and antiparallel state (bottom row), respectively, for the samples with a (a, c) 10 nm-thick and (b, d) 2.5 nm-thick Al spacer. The numbers in parentheses denote the thickness of the Al spacer in nm.

structure is two times smaller. Indeed, if one considers a period being a single-domain width, the m_x component is periodic while m_y and m_z components are antiperiodic. We have calculated the dispersion relation considering the contribution to the intensity from other dynamic magnetization components. Interestingly, the antiperiodic m_y and m_z components give similar results while the dispersion relation for the periodic m_x component is shifted by the reciprocal space vector

along the wavevector axis. We found that this effect is indeed the result of periodicity of magnetization components combined with the conservation of the spin precession direction in the stripe-domain structure. A detailed analysis of each magnetization components is presented in the [Supporting Information](#).

In [Figure 6](#), we present a more-detailed comparison between the calculated band structure (this time in linear scale) and the experimental points, in a restricted range of wavevector values. It can be seen that for the sample with a 2.5 nm-thick Al spacer, the formation of two stationary modes with a band gap having a width of about 1.6 GHz has been experimentally observed near the boundary of the first BZ. Moreover, it is important to note that the opening of the band gap occurs only on one side of the BZ, depending on the magnetic configuration of the system. Specifically, it appears at negative wavevectors for the parallel state and at positive wavevectors for the antiparallel one. This behavior can be explained by taking into account that the band-gap formation is caused by the hybridization of the highest-intensity mode (marked with a dashed cyan line in [Figure 5c,f](#)) and the folded branches (marked with a dashed green lines) induced by the stripe-domain periodicity. Due to the strong frequency asymmetry of the band structure, in the parallel (antiparallel) state, the mode hybridization is shifted from the edge of the BZ and occurs only for negative (positive) wavevectors, resulting in an asymmetrical opening of the frequency gap. One can see that in the antiparallel state, the numerical simulations reproduce very well the opening of the experimentally observed band gap, while a small discrepancy between the experimental results and the calculated band diagram is found for the parallel state. The lack of quantitative agreement can be ascribed to the fact that the numerical simulations have been performed using the same values of the NdCo magnetic parameters for all of the investigated samples.

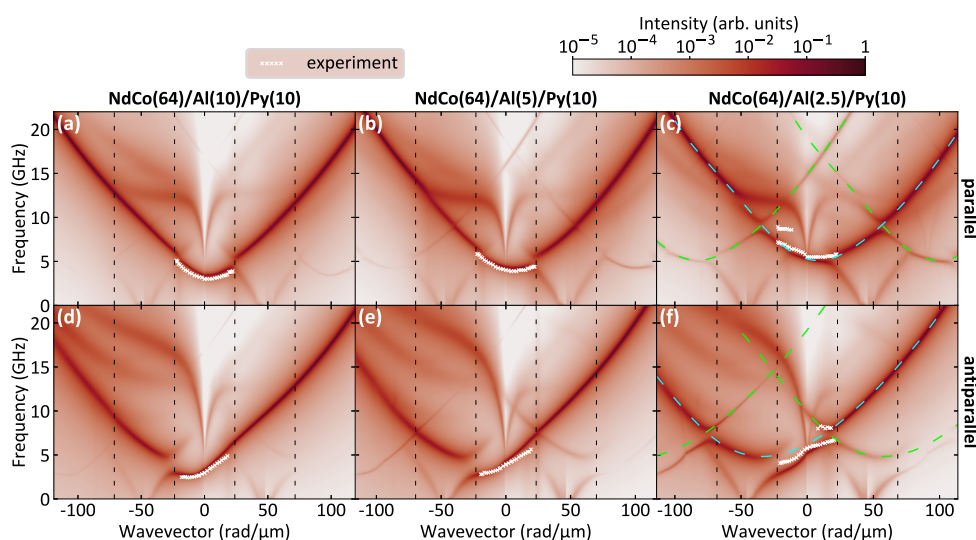


Figure 5. Measured (white crosses) and calculated (color map) dispersion relations for the three investigated samples in two magnetic configurations: (a–c) parallel and (d–f) antiparallel. The color map represents the intensity of the SWs in the Py layer in logarithmic scale obtained from numerical simulations taking into account only the perpendicular dynamic magnetization component (m_z). Vertical dashed black lines mark the Brillouin-zone boundaries. Dashed cyan and green lines depict the approximate shape of a parabolic fundamental mode in Py.

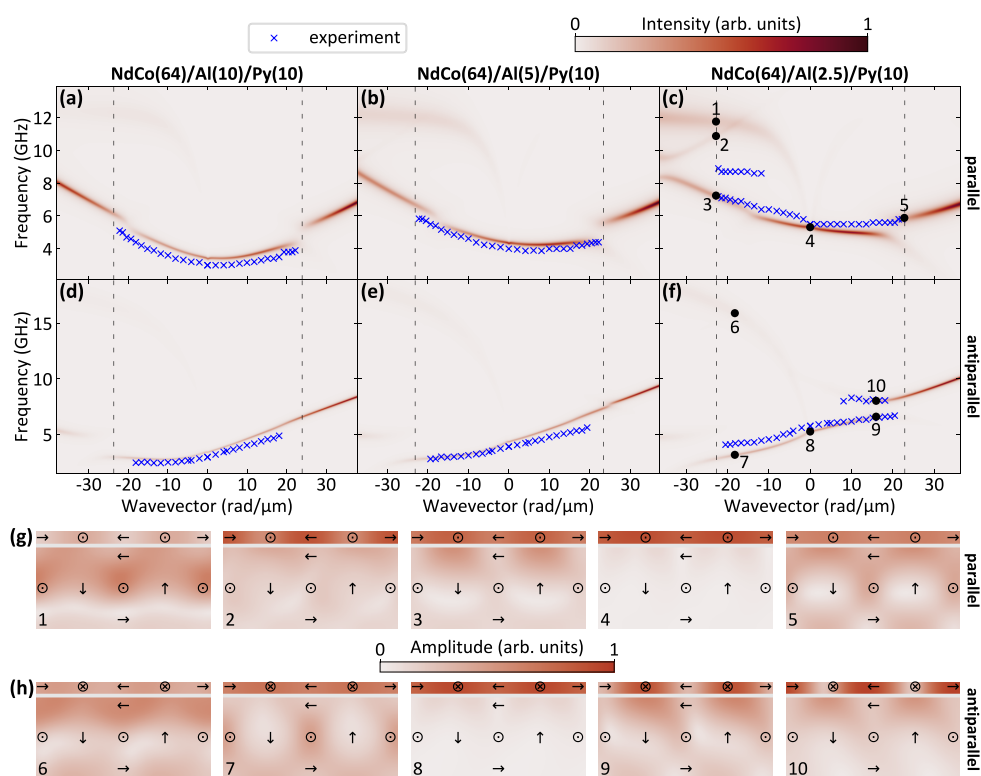


Figure 6. Top panels: dispersion relations of the three investigated samples in two magnetic configurations: (a–c) parallel and (d–f) antiparallel. The color map represents the intensity of the SWs in the Py layer in linear scale obtained with numerical simulations and blue crosses indicate the experimental results. Bottom panels: amplitude of the selected SW modes of the structure with 2.5 nm-thick Al layer in (g) parallel and (h) antiparallel state. Modes are marked with black circles on the dispersion relation plots (c) and (f). The numbers near black circles correspond to the numbers in the bottom-left corners of the sketches. The arrows in the mode amplitude pictures represent the static configuration of the magnetization.

We further note that the highest-intensity mode hybridizes only with a few modes, despite crossing many other modes. This behavior can be ascribed to the high damping of the NdCo layer that does not only affect the intensity of modes localized in the NdCo layer but also causes the hybridizations to diminish⁵² (see [Supporting Information](#)).

We further illustrate the characteristics of the calculated modes, see [Figure 6g](#) and [h](#), where the spatial distribution of the SW amplitude of selected modes, for both parallel and antiparallel states, is presented for the sample with the 2.5 nm-thick Al spacer. At $k = 0$, the mode having the largest intensity is mainly localized in the Py layer and exhibits an almost uniform spatial distribution for both the parallel (point 4) and the antiparallel (point 8) states. However, with increasing wavevector, this mode couples more strongly to the NdCo layer, and it exhibits a positive dispersion for both positive and negative wavevectors. Moreover, it is characterized by a sizable frequency asymmetry, with a larger slope in the negative wavevectors range, due to dynamic dipolar coupling between the Py and NdCo layers. On the other hand, in the antiparallel state, this mode shows a positive (negative) dispersion in the positive (negative) wavevector range, due to the reversal of the magnetization component m_x in the Py layer, where the mode is mainly localized. We further note that upon reducing the thickness of the Al layer, this mode shows a frequency increase in both the parallel and antiparallel state, caused by the stronger influence of the stray field produced by the NdCo film on the Py layer. Furthermore, we analyze the character of the

modes involved in the band-gap formation at the boundary of the first BZ. In both the parallel and the antiparallel state, the two stationary modes have different spatial localizations in the Py layer: the mode at higher frequency has its maximum amplitude in the area where the local magnetization is directed along the y -axis (points 2 and 10), while the mode at lower frequency is mainly localized in the region magnetized along the x -axis (points 3 and 9). On the opposite side of the BZ with respect to the band gap (points 5 and 7), the calculated amplitude of the modes is almost uniform in the Py layer. To complete the analysis of the modes, we observe a highly dispersive mode which is present for negative wavevectors in both the parallel and antiparallel state for all of the investigated samples. This mode is localized in the area magnetized along the x -axis in both the NdCo and the Py layers and has a maximum amplitude at the top surface of NdCo (points 1 and 6). Such a spatial localization of intensity and its strongly dispersive character indicate that this mode originates from the Damon-Eshbach surface mode in the NdCo film. Its absence in the BLS spectra can be ascribed to the high damping in the NdCo layer, as discussed in detail in the [Supporting Information](#).

CONCLUSIONS

Detailed experimental and numerical investigations of the magnetization texture and SW dynamics in NdCo₇₅(64 nm)/Al(2.5, 5, 10)/Py(10) trilayers have been performed and their usefulness for magnonic applications was discussed. In this

system, the hard magnet with PMA develops a stable stripe-domain structure at remanence, which imprints the magnetization stripe texture onto a dipolar-coupled soft magnetic thin film. Two stable configurations, corresponding to the parallel and antiparallel alignment of the Py and NdCo magnetization component along the stripe domains axis, can be achieved at remanence by minor-loop switching at a small magnetic bias field of the order of 20 mT. BLS measurements have shown a marked influence of the imprinted magnetization texture on the dispersion relation of SWs in the Py film. A strongly asymmetric dispersion relation has been found in both configurations, though with opposite asymmetry. Moreover, in the sample with the thinnest Al layer, where the influence of the stray field produced by the NdCo film on the Py layer is more pronounced, the opening of a band gap at the boundary of the first BZ has been experimentally observed. The hybridization measured by BLS in the parallel and antiparallel state was identified as a complex process involving the Py film SW band folding from the second BZ. This demonstrates the formation of a magnonic band structure in the Py film and thus represents a magnonic crystal in the homogeneous Py film by imprinting the magnetization texture from the NdCo layer. It is noteworthy that the band-gap opening occurs only on one side of the first BZ due to the nonreciprocal SW band structure. Such results can find applications in reconfigurable and nonreciprocal magnonic devices based on complex magnetization textures.

EXPERIMENTAL SECTION

Sample Preparation. The NdCo/Al/Py trilayer samples were deposited by magnetron sputtering on thermally oxidized Si wafers. Between the Si/SiO₂ substrate and the NdCo_{7.5} layer, a 5 nm-thick Al film was deposited. The deposition rate of Co, Nd, Py, and Al was 0.72, 0.6, 1.14, and 0.44 Å/s, respectively. Py, Nd, and Al (Co) were deposited at an angle of incidence of 36° (0°) with respect of the substrate normal, under a 10⁻³ mbar Ar pressure.

Brillouin Light Scattering Spectroscopy. BLS experiments from thermally excited SWs were performed in the backscattering configuration by focusing a monochromatic laser beam of wavelength λ = 532 nm on the sample surface through a camera objective of numerical aperture NA = 0.24. The scattered light was frequency analyzed by a Sandercock-type (3 + 3)-tandem Fabry–Perot interferometer. The SW dispersion was measured at a fixed magnetic field H = 200 mT and at remanence by sweeping the wavevector in the range between 0 and 22.2 rad/μm.

Numerical Simulations. The SW dynamics are described by the Landau-Lifshitz-Gilbert equation:

$$\frac{\partial \mathbf{M}}{\partial t} = -\gamma \mu_0 \mathbf{M} \times \mathbf{H}_{\text{eff}} + \frac{\alpha}{M_S} \mathbf{M} \times \frac{\partial \mathbf{M}}{\partial t} \quad (1)$$

where $\mathbf{M} = (m_x, m_y, m_z)$ is the magnetization vector, γ is the gyromagnetic ratio, μ_0 is the magnetic permeability of vacuum, \mathbf{H}_{eff} is the effective magnetic field, α is the damping constant, and M_S is the saturation magnetization. The effective magnetic field \mathbf{H}_{eff} is described as follows:

$$\mathbf{H}_{\text{eff}} = H \hat{\mathbf{x}} + \frac{2A_{\text{ex}}}{\mu_0 M_S^2} \nabla^2 \mathbf{M} + \frac{2K_{\text{PMA}}}{\mu_0 M_S^2} m_z \hat{\mathbf{z}} + \frac{2K_{\text{IMA}}}{\mu_0 M_S^2} m_x \hat{\mathbf{x}} - \nabla \varphi \quad (2)$$

where H is the external magnetic field, A_{ex} is the exchange stiffness constant, K_{PMA} is the perpendicular magnetic anisotropy constant, K_{IMA} is the in-plane magnetic anisotropy constant, and φ is the scalar magnetostatic potential, which can be determined from the magnetostatic Maxwell equations in the form of Poisson-like equation:

$$\nabla^2 \varphi = \nabla \times \mathbf{M} \quad (3)$$

The finite-element method simulations were performed using COMSOL Multiphysics. A 2D model was used assuming an infinite uniform structure along the x -axis. The structure in the saturated state was analyzed with the 2D Landau-Lifshitz-Gilbert equation using the linear approximation of eq 1 assuming $m_y, m_z \ll m_x \approx M_S$.⁵¹ The dispersion relation was calculated by numerically solving the eigenproblem of eqs 1 and 3 for each wavevector separately.⁵³ The structure in the parallel and antiparallel states was analyzed using the full 3D Landau-Lifshitz-Gilbert equation. First, time-domain simulations were used to relax a single unit cell with the predefined domain structure [$m_x = M_S \cos(2\pi y/a)$, $m_y = M_S \sin(2\pi y/a)$ in the NdCo layer, $m_x = +(-)M_S$ in the Py layer in parallel (antiparallel) state] as a function of the lattice constant a to find the configuration of the minimum energy. In the second stage, eigenproblem was solved to calculate the dispersion relation, analogously to the saturated state.

The expected BLS intensity of the n th SW mode of the frequency f_n is calculated as

$$I_0(f_n) = \int_0^a \int_{z_{\text{Py,bottom}}}^{z_{\text{Py,top}}} m_z \exp(iky) \, dy \, dz \quad (4)$$

where $z_{\text{Py,bottom}}$ and $z_{\text{Py,top}}$ are the positions of the bottom and top interface at the Py layer. Then every value is turned into the BLS-like peak using the Lorentzian function:

$$I(f, f_n) = \frac{I_0}{1 + \frac{f - \text{Re}[f_n]}{\text{Im}[f_n]^2}} \quad (5)$$

At the end, the intensities from every mode obtained in the simulations are summed up to create a 2D array of the intensities at any given wavevector and frequency, all of which are then converted into colormaps. The intensity is calculated only in the Py layer to reproduce the effect of small penetration depth of the laser light in the BLS measurements. The SW amplitude associated with a particular mode with frequency f_i and wavenumber k_i is estimated as

$$A_{k_i, f_i} = \sqrt{|m_x|^2 + |m_y|^2 + |m_z|^2} \quad (6)$$

For the sake of validation, the results from frequency-domain finite-element method simulations were crosschecked with results from micromagnetic simulations in MuMax3. Overall, a good quantitative agreement between these two methods was obtained. However, frequency-domain finite-element method simulations were significantly faster and provided much clearer spectra.

Material Parameters. The magnetic parameters of Py (reported in Table 1) have been estimated from BLS measurements in the

Table 1. Magnetic Parameters of Py Layer in the Samples Investigated in the Paper

structure	M_{eff} (kA/m)	A_{ex} (pJ/m)	K_{IMA} (kJ/m ³)
NdCo(64)/Al(10)/Py(10)	465	7	3.5
NdCo(64)/Al(5)/Py(10)	525	9	3.5
NdCo(64)/Al(2.5)/Py(10)	590	10	1.2

saturated state. The effective magnetization $M_{\text{eff}} = M_S - 2K_{\text{PMA}}/\mu_0 M_S$ (resulting from the competition between the shape anisotropy energy and the perpendicular anisotropy field), the in-plane uniaxial anisotropy constant K_{IMA} , and the effective gyromagnetic ratio γ have been estimated from the measurements of the SW frequency as a function of both the intensity and direction of a saturating in-plane magnetic field, while the exchange constant A_{ex} has been estimated from the measurement of the dispersion relation. M_{eff} and A_{ex} (K_{IMA}) are found to decrease (increase) upon increasing the Al thickness. This behavior can be ascribed to the increase of the surface roughness when the thickness of the Al spacer increases. The gyromagnetic ratio γ , instead, is independent of the Al thickness and equals 1.85×10^{11} rad/s/T. The Gilbert damping was fixed to the value of $\alpha = 0.01$.

The magnetic parameters of NdCo_{7.5} were determined from both the simulation of the static magnetic configuration and the dispersion relations in the parallel and antiparallel states: $M_S = 1100$ kA/m, $A_{ex} = 10$ pJ/m, $K_{PMA} = 130$ kJ/m³, $K_{IMA} = 10$ kJ/m³, $\alpha = 0.1$, and $\gamma = 1.85 \times 10^{11}$ rad/s/T.

ASSOCIATED CONTENT

Supporting Information

The Supporting Information is available free of charge at <https://pubs.acs.org/doi/10.1021/acsnano.2c04256>.

Analysis of the effect of damping on spin-wave dynamics; explanation of wavevector shift in dispersion relations of different magnetization components (PDF)

AUTHOR INFORMATION

Corresponding Authors

Krzysztof Szulc – Institute of Spintronics and Quantum Information, Faculty of Physics, Adam Mickiewicz University, Poznań, 61-614 Poznań, Poland; orcid.org/0000-0003-1824-6642; Email: krzysztof.szulc@amu.edu.pl

Silvia Tacchi – Istituto Officina dei Materiali del CNR (CNR-IOM), Sede Secondaria di Perugia, c/o Dipartimento di Fisica e Geologia, Università di Perugia, I-06123 Perugia, Italy; Email: tacchi@iom.cnr.it

Authors

Aurelio Hierro-Rodríguez – Departamento de Física, Facultad de Ciencias, Universidad de Oviedo, 33007 Oviedo, Spain; Centro de Investigación en Nanomateriales y Nanotecnología (CINN), CSIC-Universidad de Oviedo, 33940 El Entrego, Spain; orcid.org/0000-0001-6600-7801

Javier Díaz – Departamento de Física, Facultad de Ciencias, Universidad de Oviedo, 33007 Oviedo, Spain; Centro de Investigación en Nanomateriales y Nanotecnología (CINN), CSIC-Universidad de Oviedo, 33940 El Entrego, Spain

Paweł Gruszecki – Institute of Spintronics and Quantum Information, Faculty of Physics, Adam Mickiewicz University, Poznań, 61-614 Poznań, Poland; orcid.org/0000-0003-3529-1744

Piotr Graczyk – Institute of Molecular Physics, Polish Academy of Sciences, 60-179 Poznań, Poland; orcid.org/0000-0003-1260-9860

Carlos Quirós – Departamento de Física, Facultad de Ciencias, Universidad de Oviedo, 33007 Oviedo, Spain; Centro de Investigación en Nanomateriales y Nanotecnología (CINN), CSIC-Universidad de Oviedo, 33940 El Entrego, Spain

Daniel Markó – Université Paris-Saclay, UVSQ, CNRS, GEMaC, 78000 Versailles, France; Present Address: Silicon Austria Labs GmbH, Magnetic Microsystem Technologies, Europastraße 12, 9524 Villach, Austria

José Ignacio Martín – Departamento de Física, Facultad de Ciencias, Universidad de Oviedo, 33007 Oviedo, Spain; Centro de Investigación en Nanomateriales y Nanotecnología (CINN), CSIC-Universidad de Oviedo, 33940 El Entrego, Spain

María Vélez – Departamento de Física, Facultad de Ciencias, Universidad de Oviedo, 33007 Oviedo, Spain; Centro de Investigación en Nanomateriales y Nanotecnología (CINN), CSIC-Universidad de Oviedo, 33940 El Entrego, Spain

David S. Schmool – Université Paris-Saclay, UVSQ, CNRS, GEMaC, 78000 Versailles, France

Giovanni Carlotti – Dipartimento di Fisica e Geologia, Università di Perugia, I-06123 Perugia, Italy

Maciej Krawczyk – Institute of Spintronics and Quantum Information, Faculty of Physics, Adam Mickiewicz University, Poznań, 61-614 Poznań, Poland; orcid.org/0000-0002-0870-717X

Luis Manuel Álvarez-Prado – Departamento de Física, Facultad de Ciencias, Universidad de Oviedo, 33007 Oviedo, Spain; Centro de Investigación en Nanomateriales y Nanotecnología (CINN), CSIC-Universidad de Oviedo, 33940 El Entrego, Spain

Complete contact information is available at <https://pubs.acs.org/doi/10.1021/acsnano.2c04256>

Author Contributions

[△]K.S. and S.T. contributed equally to this work.

Notes

The authors declare no competing financial interest.

ACKNOWLEDGMENTS

This study has received financial support from the National Science Center of Poland (Projects Nos. UMO-2018/30/Q/ST3/00416, UMO-2018/28/C/ST3/00052, UMO-2019/35/D/ST3/03729, and UMO-2021/41/N/ST3/04478), the Spanish Ministry of Science and Innovation (Project No. PID2019-104604RB/AEI/10.13039/501100011033), and the regional FICYT funding (Grant No. GRUPIN-AYUD/2021/51185) with the support of FEDER funds. The authors acknowledge the technical support provided by Servicios Científico-Técnicos de la Universidad de Oviedo. LMAP and ST acknowledge Italian CNR for financial support from Short Term Mobility Program. LMAP thanks F. Valdés-Bango for helping with samples growth and MFM imaging.

REFERENCES

- (1) Yu, H.; Xiao, J.; Schultheiss, H. Magnetic texture based magnonics. *Phys. Rep.* **2021**, *905*, 1–59.
- (2) Petti, D.; Tacchi, S.; Albisetti, E. Review on magnonics with engineered spin textures. *J. Phys. D: Appl. Phys.* **2022**, *55*, 293003.
- (3) Wagner, K.; Kákay, A.; Schultheiss, K.; Henschke, A.; Sebastian, T.; Schultheiss, H. Magnetic domain walls as reconfigurable spin-wave nanochannels. *Nat. Nanotechnol.* **2016**, *11*, 432–436.
- (4) Körber, L.; Wagner, K.; Kákay, A.; Schultheiss, H. Spin-Wave Reciprocity in the Presence of Néel Walls. *IEEE Magn. Lett.* **2017**, *8*, 1–4.
- (5) Xing, X.; Zhou, Y. Fiber optics for spin waves. *NPG Asia Mater.* **2016**, *8*, e245–e246.
- (6) Xing, X.; Pong, P. W. T.; Åkerman, J.; Zhou, Y. Paving Spin-Wave Fibers in Magnonic Nanocircuits Using Spin-Orbit Torque. *Phys. Rev. Appl.* **2017**, *7*, 054016.
- (7) Lan, J.; Yu, W.; Wu, R.; Xiao, J. Spin-Wave Diode. *Phys. Rev. X* **2015**, *5*, 041049.
- (8) Albisetti, E.; Petti, D.; Sala, G.; Silvani, R.; Tacchi, S.; Finizio, S.; Wintz, S.; Calò, A.; Zheng, X.; Raabe, J.; Riedo, E.; Bertacco, R. Nanoscale spin-wave circuits based on engineered reconfigurable spin-textures. *Commun. Phys.* **2018**, *1*, 56.
- (9) Garcia-Sanchez, F.; Borys, P.; Soucaille, R.; Adam, J.-P.; Stamps, R. L.; Kim, J.-V. Narrow Magnonic Waveguides Based on Domain Walls. *Phys. Rev. Lett.* **2015**, *114*, 247206.
- (10) Chen, J.; Hu, J.; Yu, H. Chiral Magnonics: Reprogrammable Nanoscale Spin Wave Networks Based on Chiral Domain Walls. *iScience* **2020**, *23*, 101153.
- (11) Sluka, V.; et al. Emission and propagation of 1D and 2D spin waves with nanoscale wavelengths in anisotropic spin textures. *Nat. Nanotechnol.* **2019**, *14*, 328–333.

- (12) Wang, Q.; Heinz, B.; Verba, R.; Kewenig, M.; Pirro, P.; Schneider, M.; Meyer, T.; Lägél, B.; Dubs, C.; Brächer, T.; Chumak, A. V. Spin Pinning and Spin-Wave Dispersion in Nanoscopic Ferromagnetic Waveguides. *Phys. Rev. Lett.* **2019**, *122*, 247202.
- (13) Heinz, B.; Brächer, T.; Schneider, M.; Wang, Q.; Lägél, B.; Friedel, A. M.; Breitbach, D.; Steinert, S.; Meyer, T.; Kewenig, M.; Dubs, C.; Pirro, P.; Chumak, A. V. Propagation of Spin-Wave Packets in Individual Nanosized Yttrium Iron Garnet Magnonic Conduits. *Nano Lett.* **2020**, *20*, 4220–4227.
- (14) Grundler, D. Nanomagnonics around the corner. *Nat. Nanotechnol.* **2016**, *11*, 407–408.
- (15) Haldar, A.; Kumar, D.; Adeyeye, A. O. A reconfigurable waveguide for energy-efficient transmission and local manipulation of information in a nanomagnetic device. *Nat. Nanotechnol.* **2016**, *11*, 437–443.
- (16) Haldar, A.; Tian, C.; Adeyeye, A. O. Isotropic transmission of magnon spin information without a magnetic field. *Sci. Adv.* **2017**, *3*, No. e1700638.
- (17) Liu, C.; et al. Current-controlled propagation of spin waves in antiparallel, coupled domains. *Nat. Nanotechnol.* **2019**, *14*, 691–697.
- (18) Banerjee, C.; Gruszecki, P.; Klos, J. W.; Hellwig, O.; Krawczyk, M.; Barman, A. Magnonic band structure in a Co/Pd stripe domain system investigated by Brillouin light scattering and micromagnetic simulations. *Phys. Rev. B* **2017**, *96*, 024421.
- (19) Hubert, A.; Schäfer, R. *Magnetic domains: the analysis of magnetic microstructures*; Springer Science & Business Media: Berlin, 2008.
- (20) Hellwig, O.; Denbeaux, G.; Kortright, J.; Fullerton, E. E. X-ray studies of aligned magnetic stripe domains in perpendicular multilayers. *Physica B* **2003**, *336*, 136–144. Proceedings of the Seventh International Conference on Surface X-ray and Neutron Scattering.
- (21) Fallarino, L.; Oelschlägel, A.; Arregi, J. A.; Bashkatov, A.; Samad, F.; Böhm, B.; Chesnel, K.; Hellwig, O. Control of domain structure and magnetization reversal in thick Co/Pt multilayers. *Phys. Rev. B* **2019**, *99*, 024431.
- (22) Fin, S.; Tomasello, R.; Bisero, D.; Marangolo, M.; Sacchi, M.; Popescu, H.; Eddrief, M.; Hepburn, C.; Finocchio, G.; Carpentieri, M.; Rettori, A.; Pini, M. G.; Tacchi, S. In-plane rotation of magnetic stripe domains in $\text{Fe}_{1-x}\text{Ga}_x$ thin films. *Phys. Rev. B* **2015**, *92*, 224411.
- (23) Garnier, L.-C.; Marangolo, M.; Eddrief, M.; Bisero, D.; Fin, S.; Casoli, F.; Pini, M. G.; Rettori, A.; Tacchi, S. Stripe domains reorientation in ferromagnetic films with perpendicular magnetic anisotropy. *J. Phys. Mater.* **2020**, *3*, 024001.
- (24) Coisson, M.; Barrera, G.; Celegato, F.; Tiberto, P. Rotatable magnetic anisotropy in $\text{Fe}_{78}\text{Si}_{19}\text{B}_3$ thin films displaying stripe domains. *Appl. Surf. Sci.* **2019**, *476*, 402–411.
- (25) de Abril, O.; Sánchez, M. d. C.; Aroca, C. New closed flux stripe domain model for weak perpendicular magnetic anisotropy films. *Appl. Phys. Lett.* **2006**, *89*, 172510.
- (26) Hierro-Rodríguez, A.; Cid, R.; Vélez, M.; Rodríguez-Rodríguez, G.; Martín, J. I.; Álvarez-Prado, L. M.; Alameda, J. M. Topological Defects and Misfit Strain in Magnetic Stripe Domains of Lateral Multilayers With Perpendicular Magnetic Anisotropy. *Phys. Rev. Lett.* **2012**, *109*, 117202.
- (27) Hierro-Rodríguez, A.; Rodríguez-Rodríguez, G.; Teixeira, J. M.; Kakazei, G. N.; Sousa, J. B.; Vélez, M.; Martín, J. I.; Álvarez-Prado, L. M.; Alameda, J. M. Fabrication and magnetic properties of nanostructured amorphous Nd–Co films with lateral modulation of magnetic stripe period. *J. Phys. D: Appl. Phys.* **2013**, *46*, 345001.
- (28) Gruszecki, P.; Banerjee, C.; Mruzkwicz, M.; Hellwig, O.; Barman, A.; Krawczyk, M. Chapter Two - The influence of the internal domain wall structure on spin wave band structure in periodic magnetic stripe domain patterns. In *Recent Advances in Topological Ferroids and their Dynamics*; Stamps, R. L., Schultheiß, H., Eds.; Solid State Physics; Academic Press, 2019; Vol. 70; pp 79–132.
- (29) Henry, Y.; Stoeffler, D.; Kim, J.-V.; Bailleul, M. Unidirectional spin-wave channeling along magnetic domain walls of Bloch type. *Phys. Rev. B* **2019**, *100*, 024416.
- (30) Sprenger, P.; Hofer, M. A.; Iacocca, E. Magnonic Band Structure Established by Chiral Spin-Density Waves in Thin-Film Ferromagnets. *IEEE Magn. Lett.* **2019**, *10*, 1–5.
- (31) Laliena, V.; Athanasopoulos, A.; Campo, J. Scattering of spin waves by a Bloch domain wall: Effect of the dipolar interaction. *Phys. Rev. B* **2022**, *105*, 214429.
- (32) Vukadinovic, N.; Vacus, O.; Labrune, M.; Acher, O.; Pain, D. Magnetic Excitations in a Weak-Stripe-Domain Structure: A 2D Dynamic Micromagnetic Approach. *Phys. Rev. Lett.* **2000**, *85*, 2817–2820.
- (33) Tacchi, S.; Fin, S.; Carlotti, G.; Gubbiotti, G.; Madami, M.; Barturen, M.; Marangolo, M.; Eddrief, M.; Bisero, D.; Rettori, A.; Pini, M. G. Rotatable magnetic anisotropy in a $\text{Fe}_{0.8}\text{Ga}_{0.2}$ thin film with stripe domains: Dynamics versus statics. *Phys. Rev. B* **2014**, *89*, 024411.
- (34) Camara, I. S.; Tacchi, S.; Garnier, L.-C.; Eddrief, M.; Fortuna, F.; Carlotti, G.; Marangolo, M. Magnetization dynamics of weak stripe domains in Fe–N thin films: a multi-technique complementary approach. *J. Phys.: Condens. Matter* **2017**, *29*, 465803.
- (35) Borys, P.; Garcia-Sanchez, F.; Kim, J.-V.; Stamps, R. L. Spin-Wave Eigenmodes of Dzyaloshinskii Domain Walls. *Adv. Electron. Mater.* **2016**, *2*, 1500202.
- (36) Soumah, L.; Beaulieu, N.; Qassym, L.; Carrétéro, C.; Jacquet, E.; Lebourgeois, R.; Youssef, J. B.; Bortolotti, P.; Cros, V.; Anane, A. Ultra-low damping insulating magnetic thin films get perpendicular. *Nat. Commun.* **2018**, *9*, 3355.
- (37) Ding, J.; Liu, C.; Zhang, Y.; Erugu, U.; Quan, Z.; Yu, R.; McCollum, E.; Mo, S.; Yang, S.; Ding, H.; Xu, X.; Tang, J.; Yang, X.; Wu, M. Nanometer-Thick Yttrium Iron Garnet Films with Perpendicular Anisotropy and Low Damping. *Phys. Rev. Appl.* **2020**, *14*, 014017.
- (38) Wu, C.; Tseng, C.; Fanchiang, Y.; Cheng, C.; Lin, K.; Yeh, S.; Yang, S.; Wu, C.; Liu, T.; Wu, M.; Hong, M.; Kwo, J. High-quality thulium iron garnet films with tunable perpendicular magnetic anisotropy by off-axis sputtering—correlation between magnetic properties and film strain. *Sci. Rep.* **2018**, *8*, 11087.
- (39) Wang, L.; Gao, L.; Jin, L.; Liao, Y.; Wen, T.; Tang, X.; Zhang, H.; Zhong, Z. Magnonic waveguide based on exchange-spring magnetic structure. *AIP Adv.* **2018**, *8*, 055103.
- (40) Markó, D.; Valdés-Bango, F.; Quirós, C.; Hierro-Rodríguez, A.; Vélez, M.; Martín, J. I.; Alameda, J. M.; Schmool, D. S.; Álvarez Prado, L. M. Tunable ferromagnetic resonance in coupled trilayers with crossed in-plane and perpendicular magnetic anisotropies. *Appl. Phys. Lett.* **2019**, *115*, 082401.
- (41) Álvarez Prado, L. M. Control of Dynamics in Weak PMA Magnets. *Magnetochemistry* **2021**, *7*, 43.
- (42) Blanco-Roldán, C.; Quirós, C.; Sorrentino, A.; Hierro-Rodríguez, A.; Álvarez-Prado, L. M.; Valcárcel, R.; Duch, M.; Torras, N.; Esteve, J.; Martín, J. I.; Vélez, M.; Alameda, J. M.; Pereiro, E.; Ferrer, S. Nanoscale imaging of buried topological defects with quantitative X-ray magnetic microscopy. *Nat. Commun.* **2015**, *6*, 8196.
- (43) Hierro-Rodríguez, A.; Quirós, C.; Sorrentino, A.; Blanco-Roldán, C.; Álvarez-Prado, L. M.; Martín, J. I.; Alameda, J. M.; Pereiro, E.; Vélez, M.; Ferrer, S. Observation of asymmetric distributions of magnetic singularities across magnetic multilayers. *Phys. Rev. B* **2017**, *95*, 014430.
- (44) Hierro-Rodríguez, A.; Quirós, C.; Sorrentino, A.; Valcárcel, R.; Estébanez, I.; Álvarez-Prado, L. M.; Martín, J. I.; Alameda, J. M.; Pereiro, E.; Vélez, M.; Ferrer, S. Deterministic propagation of vortex-antivortex pairs in magnetic trilayers. *Appl. Phys. Lett.* **2017**, *110*, 262402.
- (45) Quirós, C.; Hierro-Rodríguez, A.; Sorrentino, A.; Valcárcel, R.; Álvarez-Prado, L. M.; Martín, J. I.; Alameda, J. M.; Pereiro, E.; Vélez, M.; Ferrer, S. Cycloidal Domains in the Magnetization Reversal Process of $\text{Ni}_{80}\text{Fe}_{20}/\text{Nd}_{16}\text{Co}_{84}/\text{Gd}_{12}\text{Co}_{88}$ Trilayers. *Phys. Rev. Appl.* **2018**, *10*, 014008.

(46) Streubel, R.; Fischer, P.; Kopte, M.; Schmidt, O. G.; Makarov, D. Magnetization dynamics of imprinted non-collinear spin textures. *Appl. Phys. Lett.* **2015**, *107*, 112406.

(47) Grünberg, P. Magnetostatic spin-wave modes of a heterogeneous ferromagnetic double layer. *J. Appl. Phys.* **1981**, *52*, 6824–6829.

(48) Mruczkiewicz, M.; Graczyk, P.; Lupo, P.; Adeyeye, A.; Gubbiotti, G.; Krawczyk, M. Spin-wave nonreciprocity and magnonic band structure in a thin permalloy film induced by dynamical coupling with an array of Ni stripes. *Phys. Rev. B* **2017**, *96*, 104411.

(49) Gallardo, R.; Schneider, T.; Chaurasiya, A.; Oelschlägel, A.; Arekapudi, S.; Roldán-Molina, A.; Hübner, R.; Lenz, K.; Barman, A.; Fassbender, J.; Lindner, J.; Hellwig, O.; Landeros, P. Reconfigurable Spin-Wave Nonreciprocity Induced by Dipolar Interaction in a Coupled Ferromagnetic Bilayer. *Phys. Rev. Appl.* **2019**, *12*, 034012.

(50) Sobucki, K.; Śmigaj, W.; Rychły, J.; Krawczyk, M.; Gruszecki, P. Resonant subwavelength control of the phase of spin waves reflected from a Gires–Tournois interferometer. *Sci. Rep.* **2021**, *11*, 4428.

(51) Graczyk, P.; Zelent, M.; Krawczyk, M. Co- and contra-directional vertical coupling between ferromagnetic layers with grating for short-wavelength spin wave generation. *New J. Phys.* **2018**, *20*, 053021.

(52) Szulc, K.; Graczyk, P.; Mruczkiewicz, M.; Gubbiotti, G.; Krawczyk, M. Spin-Wave Diode and Circulator Based on Unidirectional Coupling. *Phys. Rev. Appl.* **2020**, *14*, 034063.

(53) Vaňatka, M.; Szulc, K.; Wojewoda, O.; Dubs, C.; Chumak, A. V.; Krawczyk, M.; Dobrovolskiy, O. V.; Klos, J. W.; Urbánek, M. Spin-Wave Dispersion Measurement by Variable-Gap Propagating Spin-Wave Spectroscopy. *Phys. Rev. Appl.* **2021**, *16*, 054033.

SUPPORTING INFORMATION

Reconfigurable Magnonic Crystals Based on Imprinted Magnetization Textures in Hard and Soft Dipolar-Coupled Bilayers

Krzysztof Szulc^{1*}, Silvia Tacchi^{2*†}, Aurelio Hierro-Rodríguez^{3,4}, Javier Díaz^{3,4}, Paweł Gruszecki¹, Piotr Graczyk⁵, Carlos Quirós^{3,4}, Daniel Markó^{6†}, José Ignacio Martín^{3,4}, María Vélez^{3,4}, David S. Schmool⁶, Giovanni Carlotti⁷, Maciej Krawczyk¹, Luis Manuel Álvarez-Prado^{3,4}

¹ *Institute of Spintronics and Quantum Information, Faculty of Physics, Adam Mickiewicz University, Poznań, Uniwersytetu Poznańskiego 2, 61-614 Poznań, Poland*

² *Istituto Officina dei Materiali del CNR (CNR-IOM), Sede Secondaria di Perugia, c/o Dipartimento di Fisica e Geologia, Università di Perugia, I-06123 Perugia, Italy*

³ *Departamento de Física, Facultad de Ciencias, Universidad de Oviedo, C/Federico Garcia Lorca nº 18, 33007 Oviedo, Spain*

⁴ *Centro de Investigación en Nanomateriales y Nanotecnología (CINN), CSIC-Universidad de Oviedo, 33940 El Entrego, Spain*

⁵ *Institute of Molecular Physics, Polish Academy of Sciences, M. Smoluchowskiego 17, 60-179 Poznań, Poland*

⁶ *Université Paris-Saclay, UVSQ, CNRS, GEMaC, 78000 Versailles, France*

⁷ *Dipartimento di Fisica e Geologia, Università di Perugia, I-06123 Perugia, Italy*

* *The authors contribute equally to this work*

† krzysztof.szulc@amu.edu.pl

‡ tacchi@iom.cnr.it

[†] *Current address : Silicon Austria Labs GmbH, Magnetic Microsystem Technologies, Europastraße 12, 9524 Villach, Austria*

Effect of damping in NdCo on spin-wave dynamics in Py

We have investigated the effect of damping in the NdCo layer on the dispersion relation in the Py layer for the parallel and antiparallel states at remanence. The simulations were performed for three values of $\alpha_{\text{NdCo}} = 0.01, 0.1, \text{ and } 0.2$. We restrict the analysis to the Al(2.5) sample, but the effects described below can be directly extended to larger Al thicknesses. The results are shown in Figure S1. Lower damping allows the observation of more modes in the dispersion relation. Every mode is approximated by the Lorentzian function described in Equation 5. The imaginary part of the frequency, which describes the full width at half maximum of the peak, depends on the value of the damping. The larger the damping, the broader the peak and, therefore, lower intensity of lines in Figure S1. As the peak of the highest intensity mode is almost independent of the NdCo damping (as it is concentrated in the Py layer), it produces an almost constant ambient intensity. If the damping is large enough, the modes concentrated in the NdCo layer are below this ambient intensity and disappear from the plots. Moreover, the damping has a large impact on the hybridizations between the modes. For $\alpha_{\text{NdCo}} = 0.2$, the mode of the highest intensity has almost no hybridizations except for the hybridization between its corresponding modes from neighboring Brillouin zones (Figure S1c) and hybridization with the low-frequency mode (Figure S1f). When the damping is lower, the hybridizations with the other modes appear and should be detectable in the experiment. Interestingly,

the hybridization in the antiparallel state of the Al(2.5) sample (Figure S1f), which is visible in the experiment, seems to involve also the mode originating from the oscillations of the domain structure in the NdCo layer. It also affects the amplitude of the mode (see Figure 6h plots 9 and 10). However, the hybridization between the Py modes from different Brillouin zones are the only visible hybridizations in the BLS spectra, indicating a large damping constant in the NdCo layer.

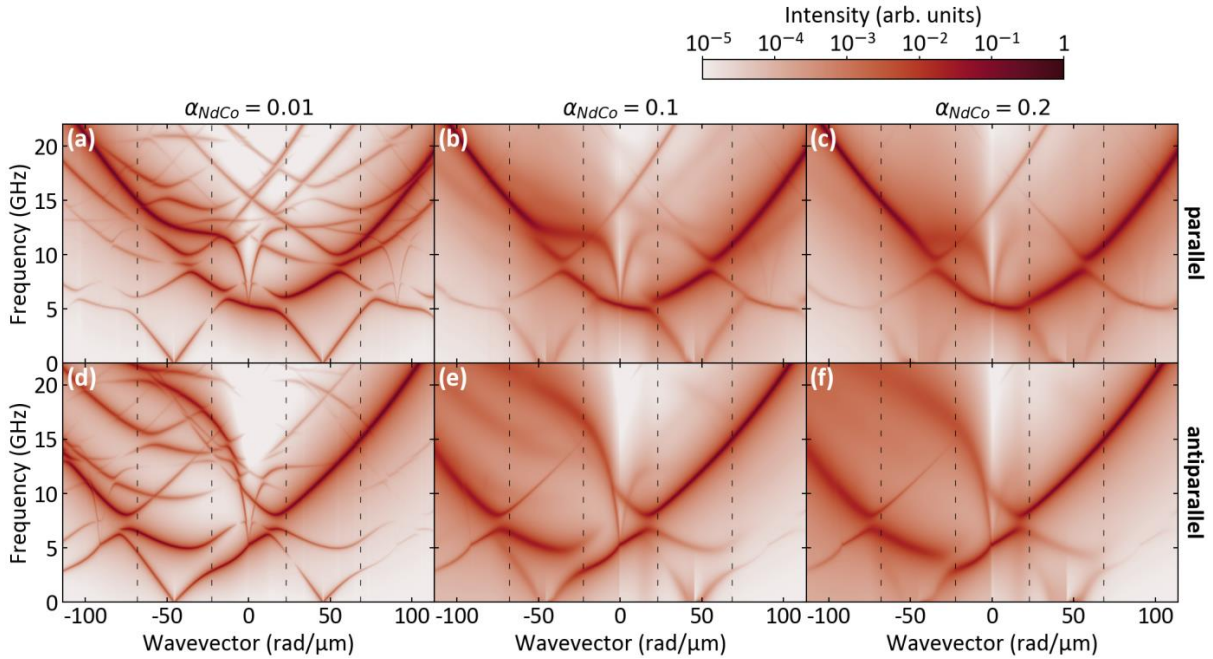


Figure S1. Influence of the damping in the NdCo layer on the dispersion relation of the Py layer in the Al(2.5) sample obtained from numerical simulations.

Double periodicity effect in the spin-wave dynamics in a stripe-domain structure

The dispersion relations for the three components of the dynamic magnetization are shown in Figure S2. The dispersion relations of the m_x and m_y components were calculated by replacing the m_z term in Equation 4 with the m_x and m_y , respectively. As can be seen, the dispersion for m_y and m_z are very similar and exhibit the same features as a function of the wavevector, while in the dispersion of the longitudinal component m_x all the bands are rigidly shifted by a reciprocal-space vector. This behavior has been also found in an investigation of Co/Pd multilayers¹, but its origin was not discussed. In the following, we provide a detailed explanation based on the analysis of the spin precession in adjacent stripe domains.

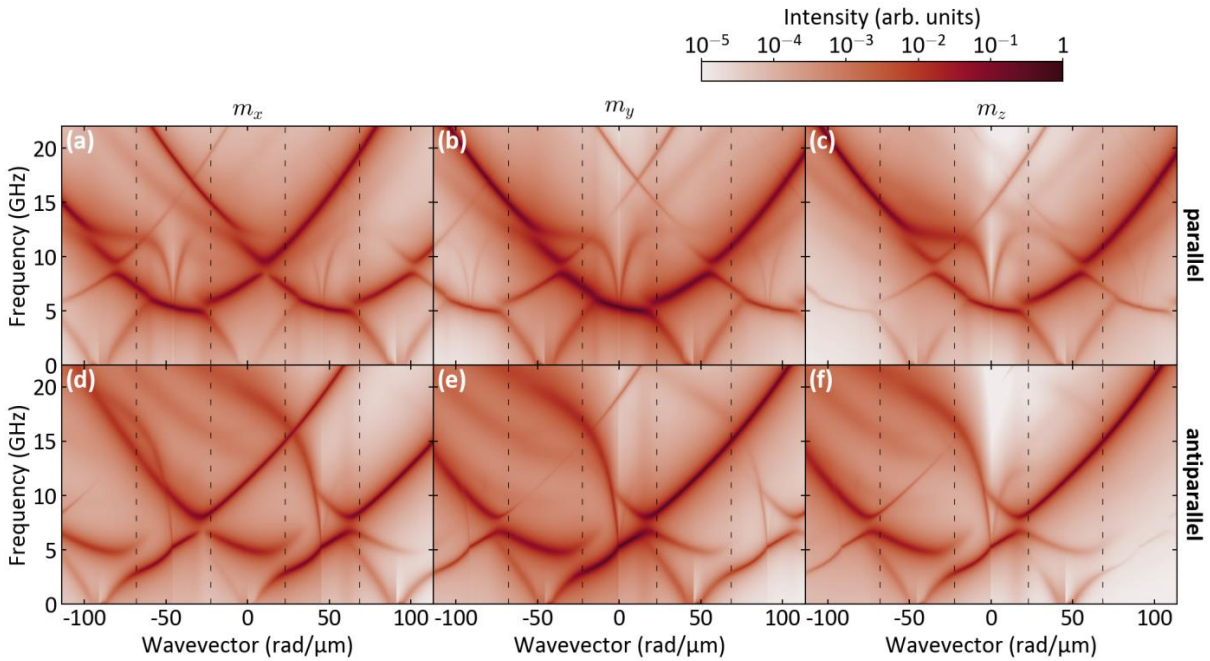


Figure S2. Contribution of the dynamic magnetization components— m_x (left column), m_y (middle column), and m_z [right column, see Figure 5c,f]—to the dispersion relation in the Al(2.5) sample in the parallel (a-c) and antiparallel (d-f) state.

Figure S3 shows a basic model of the stripe domain structure where the magnetization component perpendicular to the film plane is zero: the local magnetization is parallel to the x -axis in the center of the domain walls, while it is directed in the $\pm y$ -direction between the domain walls. This structure is analogous to the one imprinted onto the Py layer (see Figure 2), that gives the main contribution to the measured band structure as discussed in the main text, but the magnetization rotates by exactly 90° . Let us now analyze the spin dynamics of the uniform mode with $k = 0$ along the y -axis (perpendicular to the stripe domains) in a single period of the stripe domain pattern visible in top-left corner of Figure S3. The spin-precession direction is counter-clockwise as defined by the Landau-Lifshitz-Gilbert equation. At $t = 0$, all of the dynamic components are directed along the $+z$ -direction, since the mode is uniform and the static component lies in the xy -plane. At $t = T/4$, where T is the period of the spin wave, the dynamic component rotates by 90° .

¹ Banerjee, C.; Gruszecki, P.; Klos, J. W.; Hellwig, O.; Krawczyk, M.; Barman, A. Magnonic band structure in a Co/Pd stripe domain system investigated by Brillouin light scattering and micromagnetic simulations. *Phys. Rev. B* **2017**, *96*, 024421.

The spins aligned in the $+x$ -direction have their dynamic component directed in the $-y$ -direction, while the spins directed in the $\pm y$ -direction have their dynamic component directed in the $\pm x$ -direction. Similarly, at $t = 3T/4$, the spins directed in the $\pm y$ -direction have their dynamic component directed in the $\mp x$ -direction, while the spins aligned along the $+x$ -direction have their dynamic component directed in the $+y$ -direction. It implies that the m_y and m_z components oscillate in-phase (hence correspond to $k = 0$), whereas, the m_x component is shifted by 180° in adjacent domains and, therefore, behaves like a standing wave of wavenumber $k = 2\pi/a$.

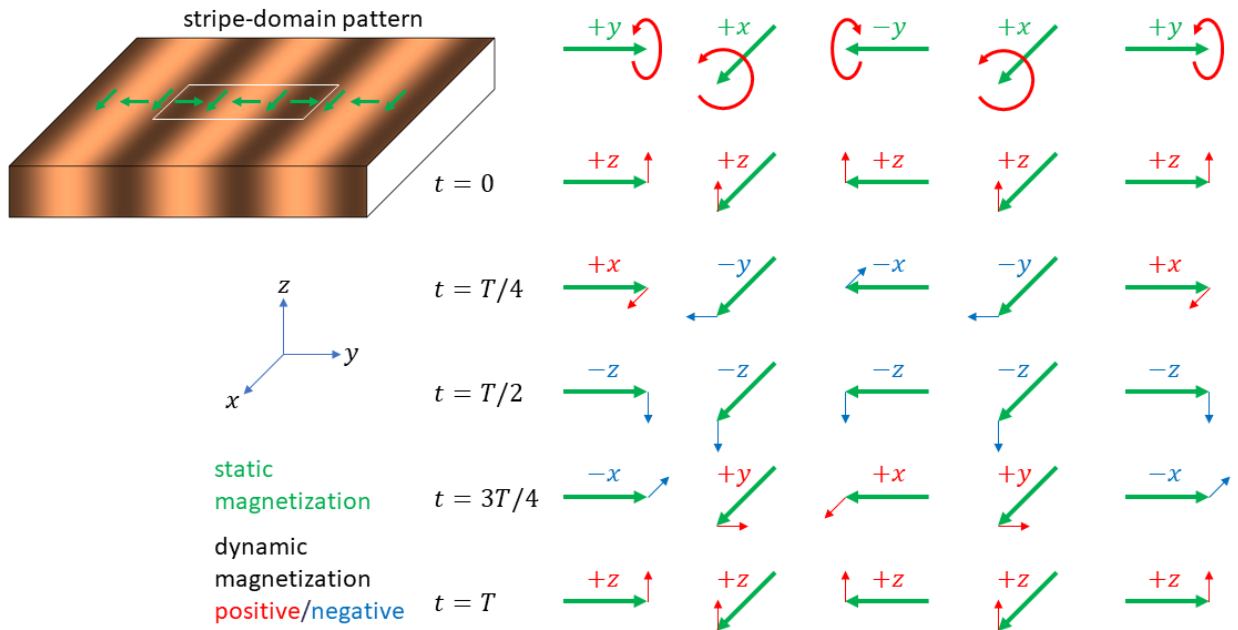


Figure S3. Magnetization dynamics of the fundamental mode at $k = 0$ in a direction perpendicular to the stripe domains (area marked by the white rectangle in the sketch in the top-left corner).

4.5 [P5] Reconfigurable spin-wave platform based on interplay between nanodots and waveguide in hybrid magnonic crystal

This work was the continuation of the work of M. Zelent *et al.* [210], in which they found that the skyrmion confined to the magnetic nanodot and placed over the magnetic layer is no longer circular—it becomes egg-shaped due to the dipolar interaction between the layer and the nanodot. The idea of the study was to take a nanodot, make a chain of them, and place it over a waveguide made of a low-damping material. In this way, we created a magnonic crystal. Moreover, we assumed that the configuration in the nanodots can be modified to be not only the skyrmion but also the single-domain state. The numerical simulations confirmed that both states in the nanodots can be stabilized in this hybrid system. We then investigated the spin-wave dynamics of the system. First of all, the dispersion relations of both systems have the markings of a magnonic crystal. Interestingly, the systems differ significantly in the band-gap sizes. Also, the system with skyrmions has many low-frequency modes (not present in the system with single-domain states) related to the dynamics of the skyrmion. We decided to study the system in more detail to quantitatively test the coupling between the waveguide and the nanodots. As a test parameter, we chose the spin-wave localization – the measure that compares the intensities of the spin-wave modes in both subsystems. It turned out to be a very useful parameter. We were able to separate the dispersion relation into ranges of isolated modes from the mode-mixing ranges and to pinpoint specific regions of strong coupling between the subsystems. This allowed us to identify hybridized and bound skyrmion modes.

Contribution of the Author

In this publication, I performed the numerical simulations, participated in the interpretation and discussion of the numerical results, wrote the Methods, Results and Discussion, and Conclusions sections, prepared the Supplementary Materials, prepared Figures 2-4, and was responsible for the manuscript submission and the correspondence with the journal.

Reconfigurable spin-wave platform based on interplay between nanodots and waveguide in hybrid magnonic crystal

Krzysztof Szulc,* Mateusz Zelent, and Maciej Krawczyk

*Institute of Spintronics and Quantum Information,
Faculty of Physics, Adam Mickiewicz University, Poznań,
Uniwersytetu Poznańskiego 2, 61-614 Poznań, Poland*

(Dated: April 17, 2024)

We present a hybrid magnonic crystal composed of a chain of nanodots with strong perpendicular magnetic anisotropy and Dzyaloshinskii–Moriya interaction, positioned above a permalloy waveguide. The study examines two different magnetization states in the nanodots: a single-domain state and an egg-shaped skyrmion state. Due to the dipolar coupling between the dot and the waveguide, a strongly bound hybrid magnetization texture is formed in the system. Our numerical results show complex spin-wave spectra, combining the effects of periodicity, magnetization texture, and hybridization of the propagating waves in the waveguide with the dot/skyrmion modes. The systems are characterized by different band gap sizes. For the skyrmion state, the azimuthal modes confined to the skyrmion domain wall lead to the formation of flat bands at low frequencies, while at higher frequencies we identify among them modes interacting with the propagating waves, which can introduce additional non-Bragg band gaps, as well as isolated modes leading to the formation of bound states. On the other hand, the system with a single-domain state in nanodots offers a wide range of frequencies where the spin waves are predominantly in the waveguide. Thus, the study shows that the proposed hybrid magnonic crystals have many distinct functionalities, highlighting their reconfigurable potential, magnon–magnon couplings, mode localization, and bound states overlapping with the propagating waves. This opens up potential applications in analog and quantum magnonics, spin-wave filtering, and the establishment of magnonic neural networks.

I. INTRODUCTION

Over the past decade, spin-wave (SW) computing has been extensively researched as a potential candidate to complement and surpass CMOS-based technologies [1, 2] for digital [3] or analog signal processing [4, 5] and neural network implementation [6, 7]. This is because SWs offer high-frequency operation, even at tens of GHz, miniaturization down to the nanoscale, well below 100 nm, and most importantly, ultralow power consumption, as low as 1 aJ per operation. Moreover, they can locally interact with magnetic solitons, i.e. domain walls in 1D and magnetic vortices or skyrmions in 2D, and thus can hybridize with, be excited by, and be controlled by soliton dynamics [8–10].

Magnetic skyrmions are topologically protected 2D magnetization textures, known for their stability and very small size, especially Néel skyrmions in thin ferromagnetic films, which are stabilized by Dzyaloshinskii–Moriya interaction (DMI) [11]. Their dynamics can be driven by external forces such as magnetic field, electric current, structural stress, thermal fluctuations, or laser pulses [12], which expands their possible applications also in magnonics, e.g., to control wave propagation [13], scatter SWs [14], form SW frequency combs [15], or to excite propagating SWs [16] in thin films. This makes them promising candidates for information storage and processing [17–20]. In particular, their potential has attracted considerable interest in non-Boolean logic and

unconventional computing devices [21–23]. However, due to the high damping of SWs in multilayers possessing DMI [24, 25], with a few exceptions those effects remain mainly numerical demonstrations [26].

In a skyrmion within confined geometry, three types of eigenmodes have been observed [27, 28]: gyroscopic, breathing, and azimuthal modes. The gyroscopic mode refers to the rotational motion of the skyrmion core [29]. The breathing mode involves the radial oscillation of the size of the skyrmion [30]. Azimuthal modes are SWs propagating along the skyrmion circumference [31–33]. Their quantization is described by an azimuthal wave number, with clockwise (CW) and counterclockwise (CCW) degeneracy lifted by the asymmetric exchange interaction. When the dots are arranged in a chain or array, bands of collective skyrmion excitations can be formed [34]. However, the dynamic dipolar coupling between the skyrmions is rather weak, especially between the azimuthal modes, and the non-zero bandwidths have been numerically demonstrated only for gyroscopic or breathing modes [31].

Hybrid structures are commonly used to obtain systems that combines two, usually mutually exclusive, material properties, such as ferromagnetism and superconductivity [35]. This is also true for magnonics and skyrmions. The former requires long propagation distances and thus low damping, while the latter requires DMI resulting from spin–orbit interactions and heavy neighboring metals, which is associated with increased damping. The bilayer structure composed of yttrium iron garnet and the Co/Pt multilayer with the skyrmion has been proposed as a point source to excite short SWs with

* krzysztof.szulc@amu.edu.pl

tens of nm wavelength [36].

We propose a hybrid structure consisting of a SW conduit made of a low-damping material (Py) and a chain of (Ir/Co/Pt) nanodots of 300 nm diameter, forming a hybrid magnonic crystal (HMC) that serves as a multifunctional platform for SW applications. Such an HMC structure has shown an extended range of DMI values, which facilitates Néel-type skyrmion stabilization at comparatively lower DMI values [37]. Using micromagnetic simulations, we show that this HMC exhibits several interesting properties arising from the coupling between the subsystems relevant to control SWs. These include flat magnonic bands both below and above the bottom of the SW spectrum in Py, and a reprogrammable magnonic band structure, where the width of the band gaps is modified by the magnetization texture in the dots at the remanence: skyrmion or single-domain state. The former property provides a system for the realization of bound states in the continuum in a magnonic domain [38], the latter for the SW filtering or Bose–Einstein condensation realization [39]. Moreover, the dynamic coupling between SWs propagating in the waveguide and SWs confined to the domain wall of the skyrmion results in band anticrossing, making this system suitable for exploiting the magnon–magnon coupling, and thus useful for quantum magnonics applications [40]. Taking into account the multifunctionality, the proposed HMCs represent a promising platform for magnonic artificial neural networks, as proposed in Ref. [41], or where the waveguide serves as synapses connected by propagating SWs, and interacting resonant neurons, i.e. nanodots on the waveguide with the rich spectra of SW modes [42]. The complex interactions between propagating SWs and nanodisks discussed in this paper open avenues for creating tunable artificial neurons.

II. METHODS

The system under investigation is presented in Fig. 1. It consists of the infinitely-long waveguide made of permalloy (Py, Ni₈₀Fe₂₀) with a width of 300 nm and a thickness of 4.5 nm and a chain of Co dots with a 300 nm diameter and 1.5 nm thickness. The dots are laying centrally above the waveguide with a relative separation of 50 nm, resulting in the periodic structure with a lattice constant of 350 nm. The waveguide and the dots are separated by a 3 nm-thick nonmagnetic layer.

The magnetization dynamics of the system are described by the Landau–Lifshitz–Gilbert equation:

$$\frac{\partial \mathbf{M}}{\partial t} = -|\gamma|\mu_0 \mathbf{M} \times \mathbf{H}_{\text{eff}} + \frac{\alpha}{M_S} \mathbf{M} \times \frac{\partial \mathbf{M}}{\partial t}, \quad (1)$$

where γ is the gyromagnetic ratio, μ_0 is the magnetic permeability of vacuum, \mathbf{H}_{eff} is the effective magnetic field, α is the damping constant, and M_S is the saturation magnetization. The effective magnetic field \mathbf{H}_{eff} is

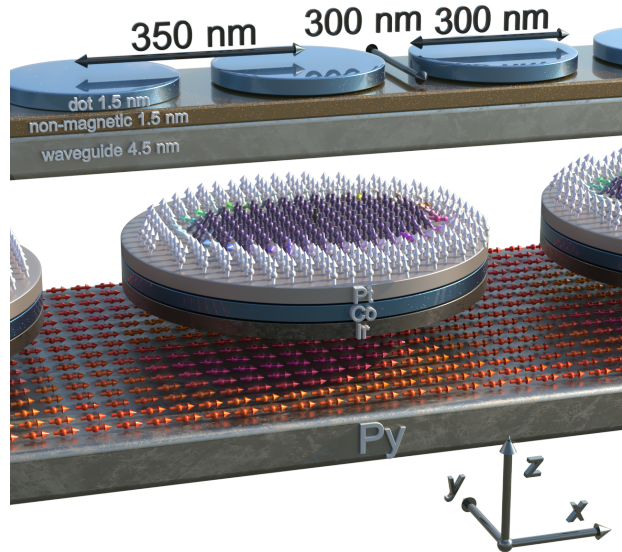


Figure 1. The visual representation of the system under consideration. The Ir/Co/Pt multilayer dot is separated from the 4.5 nm-thick Py strip by a 3 nm-thick nonmagnetic layer. In the dot, an egg-shaped Néel-type skyrmion is stabilized by the magnetostatic coupling to the skyrmion imprint on the in-plane magnetized strip. The arrows and their color (according to the HSL-cone color scale) indicate the direction of magnetization. Note that the figure is not to scale.

described as follows:

$$\mathbf{H}_{\text{eff}} = \mathbf{H}_0 + \frac{2A_{\text{ex}}}{\mu_0 M_S^2} \nabla^2 \mathbf{M} + \frac{2K_{\text{PMA}}}{\mu_0 M_S^2} M_z \hat{\mathbf{z}} - \nabla \varphi + \frac{2D}{\mu_0 M_S^2} \left(\frac{\partial M_z}{\partial x} \hat{\mathbf{x}} + \frac{\partial M_z}{\partial y} \hat{\mathbf{y}} - \left(\frac{\partial M_x}{\partial x} + \frac{\partial M_y}{\partial y} \right) \hat{\mathbf{z}} \right), \quad (2)$$

where \mathbf{H}_0 is the external magnetic field, A_{ex} is the exchange stiffness constant, K_{PMA} is the perpendicular magnetic anisotropy constant, D is the Dzyaloshinskii–Moriya constant, and φ is the magnetic scalar potential, which can be determined from the formula

$$\nabla^2 \varphi = \nabla \cdot \mathbf{M}, \quad (3)$$

which is derived from Maxwell equations in the magnetostatic approximation.

The system was studied using the finite-element method simulations in COMSOL Multiphysics [43]. The simulations were performed in the 3D model with the implementation of Eqs. (1) and (3). The static magnetization configuration was stabilized in the time-domain simulation with periodic boundary conditions placed at the ends of the unit cell perpendicular to the x -axis to introduce the periodicity into the system. For the proper calculation of the stray magnetic field, the condition $\varphi = 0$ is applied at a distance of 10 μm from the system. As

an initial magnetization configuration, the waveguide is uniformly magnetized along the x -axis while the dots are uniformly magnetized along the z -axis (for the study of a single-domain state configuration) or have a skyrmion inside (for the study of skyrmion state) [44]. The magnetic state relaxation lasts $1 \mu\text{s}$. The dispersion relation was calculated using the eigenfrequency solver. For this purpose, the Landau–Lifshitz–Gilbert equation is solved in its linearized form, where the total magnetization vector $\mathbf{M} = \mathbf{M}_0 + \mathbf{m}e^{i\omega t}$ is splitted to a static component $\mathbf{M}_0 = (M_{0x}, M_{0y}, M_{0z})$ and a dynamic component $\mathbf{m} = (m_x, m_y, m_z)$. The equation takes the form of an eigenvalue equation, where the complex eigenvalues give the frequencies, the dynamic magnetization \mathbf{m} and the dynamic magnetic scalar potential are the eigenvectors, and the wavevector is a sweep parameter. Here, the periodic boundary conditions are replaced by Bloch boundary conditions. The tetrahedral mesh is used with a maximum size of 5 nm in the dot and 7 nm in the waveguide. Outside the magnetic material, the mesh grows with ratio 1.4. On the sides where Bloch boundary condition is applied, we prepared identical triangular meshes.

The material parameters of Py are $M_S = 800 \text{ kA/m}$, $A_{\text{ex}} = 13 \text{ pJ/m}$, $D = 0$, $K_{\text{PMA}} = 0$, $\alpha = 0.005$. The magnetic dot is defined with an effective-medium approach [45–48] as a structure with DMI and PMA, where the three repetitions of the 0.5 nm-thick Ir/Co/Pt multilayer are simulated as a single Co layer with an effective thickness. The effective parameters of the dot are $M_S = 956 \text{ kA/m}$, $A_{\text{ex}} = 10 \text{ pJ/m}$, $D = -1.6 \text{ mJ/m}^2$, $K_{\text{PMA}} = 717 \text{ kJ/m}^3$, $\alpha = 0.02$. In all calculations, the external magnetic field $\mathbf{H}_0 = 0$.

III. RESULTS AND DISCUSSION

A. Static magnetization texture

First, let us consider the waveguide and nanodot subsystems separately, focusing on the static magnetic configuration of the system in the absence of an external magnetic field. In the multilayer nanodot, characterized by strong PMA and DMI, various magnetization states can be stabilized, including an out-of-plane single-domain state, a Néel-type skyrmion, a double-domain structure, and a worm-like domains [49]. In this paper, we are focusing on two of the above-mentioned configurations—a single-domain state (SD) and a skyrmion state (Sk). While the literature is well-versed in the static and dynamic behavior of these structures in isolation [33, 50], their static and dynamic properties become complex in a compact hybrid system [37].

Figure 2 presents the static magnetic configuration of a single unit cell of the HMC. Here, we consider hybrid systems with two different magnetization configurations—the waveguide (W) with a chain of dots with the single-domain out-of-plane magnetization state (W/SD) and the waveguide with a chain of dots with skyrmions

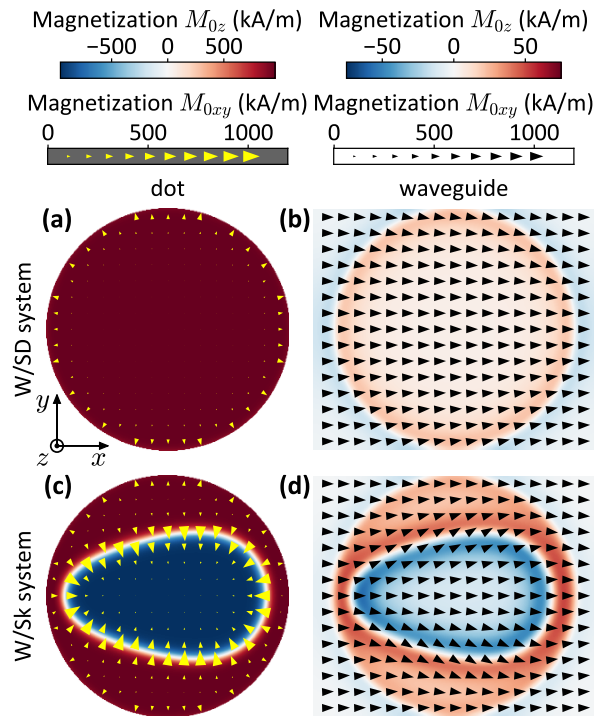


Figure 2. Configuration of the magnetization in the unit cell of the coupled system of waveguide with the chain of dots in (a,b) the single-domain state and (c,d) skyrmion state. The magnetization is shown in the xy -planes crossing (a,c) the center of the dot and (b,d) the center of the waveguide. The color map shows the M_{0z} component of the magnetization, and the in-plane component M_{0xy} is presented with the arrows.

(W/Sk). The magnetization texture is shown on the xy -planes crossing the center of the dot (a,c) and the center of the waveguide (b,d), respectively. In the HMC, the magnetization configuration differs from that of isolated subsystems. This change, induced by the dipolar coupling, is mainly caused by the competition between the strong PMA in the dots, which favors magnetization along the z -axis, and the shape anisotropy inherent in the waveguide, which induces a preference for magnetization along the x -axis.

In the W/SD system, the most pronounced effect of dipolar interaction between the subsystems manifests just beneath the edges of the dot, as illustrated in Fig. 2(b). Here, the peak deviation in magnetization reaches $\max |M_{0y}| = 216 \text{ kA/m}$ along the y -axis and $\max |M_{0z}| = 23 \text{ kA/m}$ along the z -axis. Notably, within the nanodot itself, the magnetization deviation of approximately 2% is present close to the dot edge.

The static magnetic texture in the W/Sk system undergoes more significant modification. Unlike the configurations observed in the individual subsystems, the skyrmion is not only imprinted in the waveguide, but also takes on an egg-like shape instead of being circu-

lar. This static effect has already been demonstrated in the system with a single dot and finite strip in Ref. [37]. Please note that the imprint intensity is stronger in the W/Sk system than in the W/SD system. The average net magnetization along the easy axis in the W/Sk system decreases by 20 kA/m in comparison with only 5 kA/m for W/SD system. Also, the maximum deviation reaches $\max |M_{0y}| = 475$ kA/m and $\max |M_{0z}| = 59$ kA/m.

B. Spin-wave dynamics

Following the analysis of the static magnetization configurations of the system, we performed numerical simulations of the SW dynamics. The dispersion relations of W/SD and W/Sk systems are depicted in Fig. 3(a) and Fig. 3(b), respectively, where the color map indicates the intensity I of the out-of-plane dynamic magnetization component m_z across the entire system. The intensity of each mode is quantified as follows:

$$I_{\text{mode}}(k, f_n(k)) = \left| \iiint_V m_z(f_n(k)) e^{ikx} dx dy dz \right|^2, \quad (4)$$

where V denotes the volume of magnetic material within a single unit cell and $f_n(k)$ is the frequency of the n th mode at wavevector k . Next, the intensities of all modes are converted into the Lorentzian function and then summed to give the total intensity I

$$I(k, f) = \sum_n \frac{I_{\text{mode}}(k, f_n(k))}{\text{Im}[f_n(k)] \left(1 + \left(\frac{f - \text{Re}[f_n(k)]}{\text{Im}[f_n(k)]} \right)^2 \right)} \quad (5)$$

at wavevector k and frequency f . This method of quantifying intensity makes these results comparable to the Brillouin light scattering measurement results [51]. For comparison, the dispersion relation of an isolated waveguide without a chain of dots is illustrated with dashed black lines. The comparison between the dispersion relation of the isolated waveguide and the frequencies of the SW modes in the isolated dot in the single-domain and skyrmion states is presented in Section S1 of the Supplementary Materials.

The dispersion relations of both systems contain complex mode dependencies, caused by the interaction between the dots and their imprints in the waveguide. The highest-intensity mode follows the fundamental mode of an isolated waveguide. The antisymmetric waveguide modes are barely visible in the plots due to the nature of the intensity calculation. Above the third waveguide mode, the intensity distribution is unclear and only the fundamental modes are recognizable. The reflected branches and band gaps are present as a result of the periodicity induced by the arrangement of the dots.

However, there are significant differences in the band-gap width of the Bragg gaps among the systems. The zoom-ins of the dispersions of W/SD and W/Sk systems are shown in Fig. 3(c) and Fig. 3(d), respectively, with

gray strips marking the positions of the band gaps. The widths of the first five band gaps are listed in Fig. 3(e). The W/SD system is characterized by larger low-order gaps, with the size exceeding 400 MHz. The size of higher-order gaps is much smaller, with gap 5 already being similar in size to the linewidth of the modes (which is 77 MHz), making it barely noticeable. In contrast, the W/Sk system is characterized by larger sizes of higher-order band gaps, i.e., third and higher. Interestingly, the first band gap is completely absent. Due to the backward wave character of the mode at low wavevectors, the edge of the first Brillouin zone lies close to the frequency minimum. As a result, the first and second bands share the same character. In the W/SD system, the stronger interaction between the modes pushes the first band much below the frequency of the isolated waveguide (see Fig. 3(a)). In the W/Sk system, this interaction is weaker, which causes the first band maximum to be at a higher frequency than the second band minimum, leading to the absence of the band gap, as visible in Fig. 3(d). These properties clearly demonstrate the reprogrammable nature of the proposed HMC system. By preserving the frequency positions of the band gaps, we can modify their width and even close or open the first band gap simply by changing the magnetization state in the dots.

Another difference is the presence of numerous flat bands in the dispersion of the W/Sk system, which lie below the waveguide modes and begin at frequencies below 1 GHz. These modes are directly connected to the dynamics of the skyrmion domain wall in the dots which starts at the level of hundreds of MHz (see, Fig. S1 in the Supplementary Materials). At higher frequencies, some of the skyrmion modes hybridize with the waveguide modes. Interestingly, one of these modes leads to the generation of an additional band gap with a width of 53 MHz, marked as gap 3a in Fig. 3(d). The modified spectra indicate that the presence of skyrmions in dots can directly affect the dynamics of SWs propagating in the waveguide. Obviously, such modes are not present in the W/SD system since the lowest resonant mode of the dot in a single-domain state is at the frequency of 9 GHz, which is above the third waveguide mode. These results show that the change of a magnetization configuration of the dots can induce additional flat bands in the SW spectrum and also magnon-magnon coupling, effects which are currently under intense investigation and also important from an application point of view. In the next section, we will explore these properties, focusing on understanding of the physical mechanisms involved.

C. Mode localization

In order to deepen the analysis of the SW dynamics in both systems, we calculated the localization of the modes and plotted it on the dispersion relation folded to the first Brillouin zone as shown in Fig. 4(b) and (c). We define

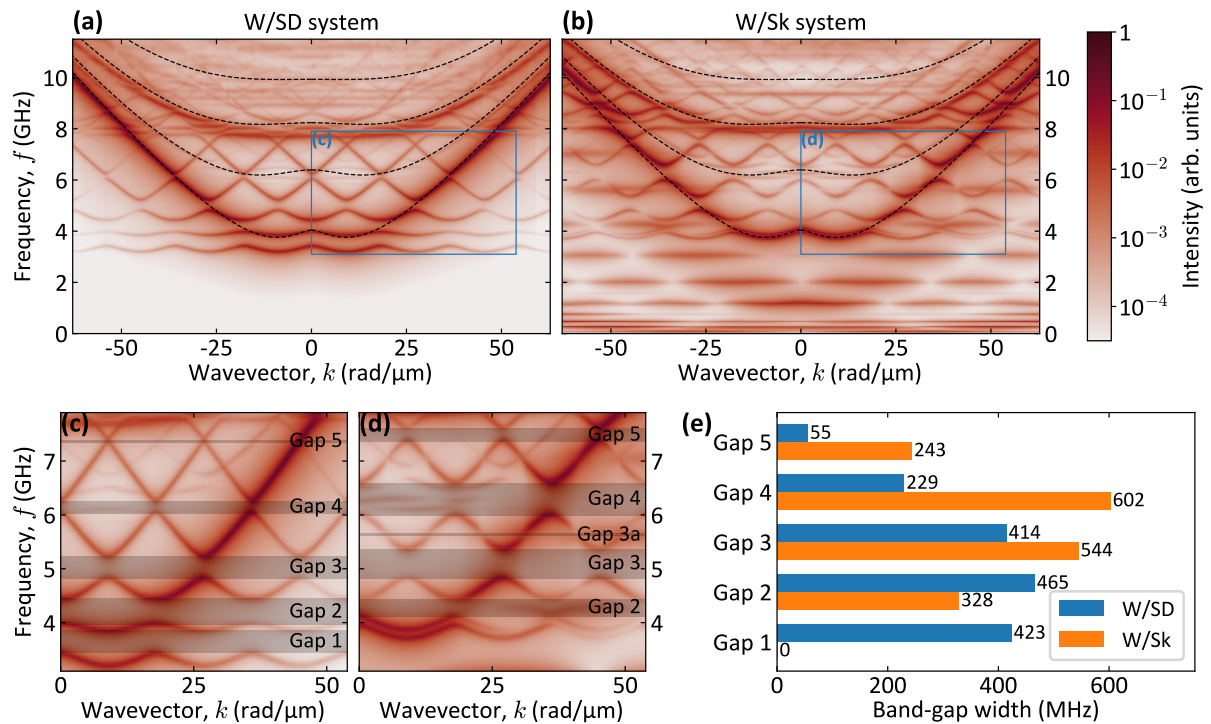


Figure 3. Dispersion relation of (a) the W/SD system and (b) the W/Sk system. Color maps show the intensity measured for the out-of-plane component of the magnetization m_z . Intensity is scaled logarithmically. Dashed black lines show the dispersion relation of waveguide itself without dots. Subfigures (c) and (d) are zoom-ins of the W/SD and W/Sk systems' dispersion relations as marked by blue rectangles in subfigures (a) and (b), respectively. Gray rectangles mark the Bragg gaps in the dispersion relation. (e) Bar chart collecting band-gap widths for both W/SD and W/Sk systems.

the mode localization as a measure of how much of the intensity of a given mode comes from a given subsystem (in this case – a waveguide). It is calculated as

$$L(k, f_n) = \frac{\mathcal{I}_w}{\mathcal{I}_w + \mathcal{I}_d}, \quad (6)$$

where \mathcal{I}_w and \mathcal{I}_d are the intensity of the mode in the waveguide and dot, respectively. Intensity is measured as

$$\mathcal{I}_{w(d)}(k, f_n) = \iiint_{V_{w(d)}} |\mathbf{m}(k, f_n)|^2 dx dy dz \quad (7)$$

where $V_{w(d)}$ is the volume of the waveguide (dot) in a unit cell. The mode fully localized in the dot has a value of $L = 0$ and is marked in Figs. 4(b,c) with light blue color, while the mode fully localized in the waveguide has a value of $L = 1$ and is marked with light brown color.

The mode localization for the W/SD system is shown in Fig. 4(b). The SW profiles of 5 selected modes (W/SD-1–W/SD-5) are presented in the first row of Fig. 4(e). Additionally, we plot the frequency as a function of localization in Fig. 4(a). In the range I, the lowest mode has a frequency above 3 GHz, and all modes up to 8.9 GHz are predominantly confined to the waveguide with minimal

amplitude in the dot. The lowest localization value in this region is $L = 0.89$. This result is consistent with the simulations of eigenstates of an isolated dot, where the lowest mode was observed at 9 GHz (see Section S1 in the Supplementary Materials). Therefore, any excitation in the dot below this frequency is only a forced oscillation. Most of the modes in this area resemble typical waveguide modes, e.g. mode W/SD-3. However, other modes, such as W/SD-1 and W/SD-2, are significantly distorted. Despite the Bragg gap being present only at the edge of the Brillouin zone, their branches are coupled throughout the entire range of the zone. This results in a non-uniform SW amplitude, even at zero k .

Above 8.9 GHz, the dispersion relation is densely populated with modes of mixed localization. In this frequency range, marked as range II, the modes have a mixed character, with a localization value in the range between 0.14 and 0.96, with the upper limit decreasing to 0.83 above 10.5 GHz. Among them, there are modes localized predominantly in the dot (e.g. mode W/SD-4), which originate from the resonant modes in the dot. However, there is always significant energy leakage to the waveguide. On the other hand, the propagating waveguide modes, such as mode W/SD-5, also have significant amplitude in the dot. The presence of the dot also strongly modifies the

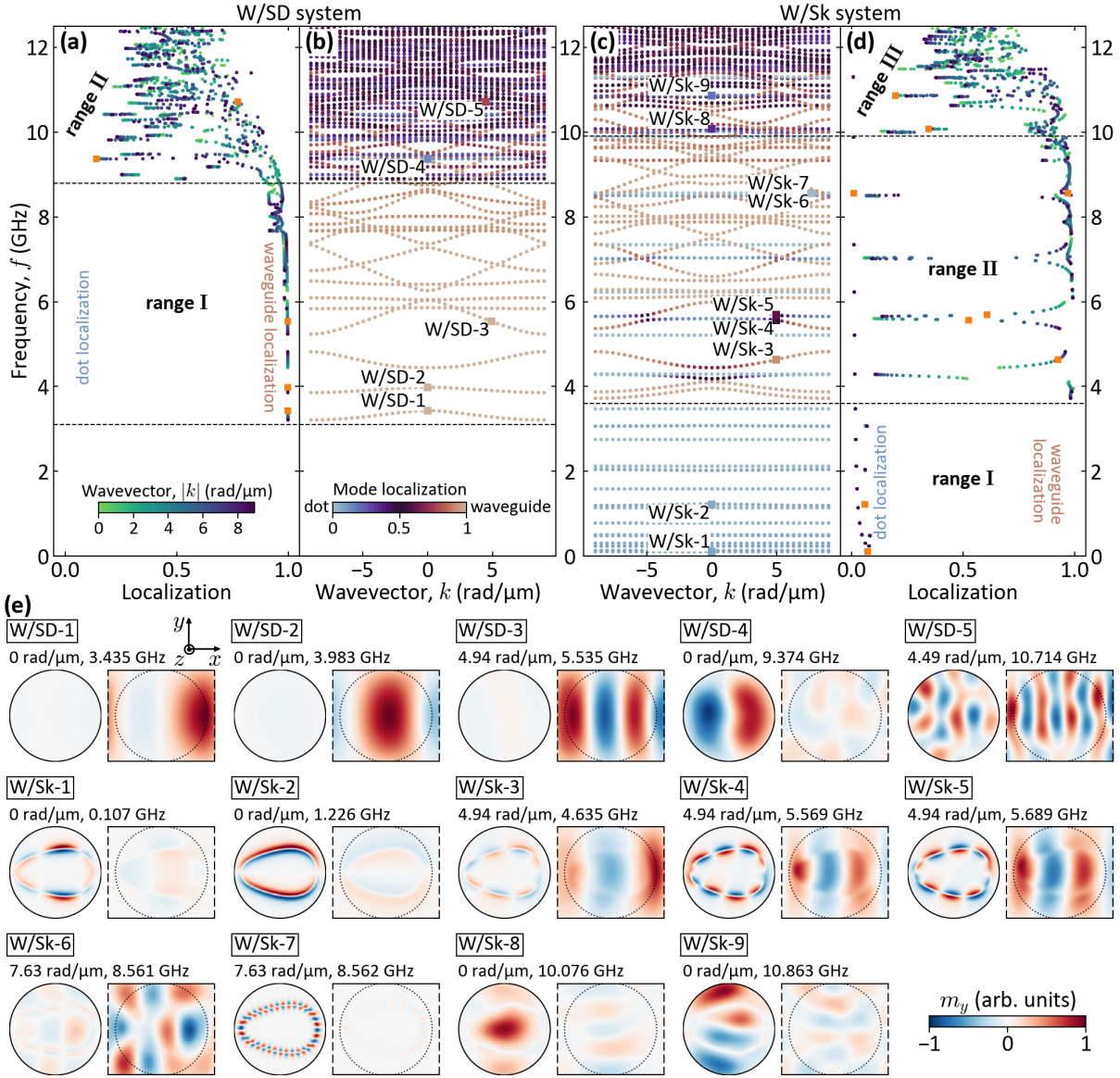


Figure 4. The dispersion relation in the first Brillouin zone presents the localization of modes in both (b) W/SD and (c) W/Sk systems. Each mode localization value is indicated by the color of the point on the dispersion. The corresponding plots with the localization value are shown in (a) for the W/SD system and in (d) for the W/Sk system. Here, the color of the point marks the absolute value of the wavevector. Dashed black vertical lines mark the limits of ranges. (e) SW mode profiles for 5 modes in the W/SD system and 9 modes in the W/Sk system. The modes are marked on the dispersion relations with a square point and a label. In each mode profile, the left color map displays the m_y magnetization component in the xy -plane at the center of the dot, while the right color map displays m_y in the xy -plane at the center of the waveguide. The intensity is normalized so that the maximum value of $|m_y|$ is 1 for each of the mode profiles. All profiles are labeled and their wavevector and frequency are given. The animated version of this figure is available in [52].

wavefront of the SW propagating in the waveguide (see mode W/SD-5). This effect can be used to excite propagating SWs in the waveguide by exciting the dots themselves, similar to the excitation of short-wavelength SWs with 2D diffraction couplers [53].

The W/Sk system exhibits different behavior, as pre-

sented in Fig. 4(c). The SW profiles of 9 selected modes are presented in two bottom rows of Fig. 4(e). Additionally, we plot the frequency as a function of localization in Fig. 4(d).

Range I spans the frequencies from 100 MHz to 3.5 GHz, which is below the frequency of the lowest

waveguide band. It contains 15 flat bands related to the modes localized in dots, which are clockwise and counterclockwise azimuthal modes of the skyrmion domain wall, similar to the skyrmion in an isolated dot (see Fig. S1 in Supplementary Materials) [33]. The lowest frequency mode, W/Sk-1, is a 3rd order counterclockwise mode. The skyrmion breathing mode, W/Sk-2, has a frequency of 1.226 GHz and is only the ninth lowest mode. The largest localization in this range is $L = 0.08$. The modes in this range have very small bandwidths ranging from 9 kHz to 34 MHz (breathing mode, W/Sk-2). This is because these modes can only interact through dipolar interactions or evanescent SWs, which are the only ones that can exist in the waveguide at such low frequencies. The simulation of the dot chain in the skyrmion state but without the waveguide (see Table 1 in Section S2 of the Supplementary Materials) shows that the bandwidths of most of the bands are significantly smaller in the absence of the waveguide, except for the breathing mode (of comparable bandwidth, 33 MHz) and the fourth counterclockwise mode, which is larger than in the system with the waveguide (further details on this comparison can be found in Section S2 of the Supplementary Materials). This suggests the coupling of the skyrmion modes from the range I through the evanescent waves in the waveguide. Such an effect is similar to the enhanced SW transmission in bi-component 1D MC at frequencies below the FMR frequency of one of the constituent materials [54]. However, here it is theoretically predicted for 1D HMC consisting of a homogeneous film and a chain of dots in the skyrmion state, the system easily extendable to a 2D array. The effects described above could be exploited for the design of frequency-selective magnonic devices, enabling precise control over signal modulation and processing at the nanoscale. The distinct localization and narrow bandwidths of these modes offer opportunities to create highly-efficient filters or oscillators that operate within a precisely-defined frequency range. Furthermore, these weakly dispersive bands can be used to exploit the flat-band physics recently demonstrated in 1D MCs with periodic modulation of a DMI [39, 55].

Starting from 3.5 GHz, similarly to W/SD system, modes localized in the waveguide start to appear but they coexist with skyrmion modes in this range (marked as range II). Interestingly, the skyrmion is always slightly excited even if the mode is strongly localized in the waveguide (see mode W/Sk-3 with localization 0.925). On the one hand, the clockwise skyrmion modes hybridize with the waveguide modes, resulting in mixed modes that are confined to both the waveguide and the dot. In Fig. 4(d), these modes form characteristic horizontally-aligned points with localization between 0.05 and about 0.55. As it was shown before, such a hybridization leads to the presence of an additional band gap marked as gap 3a in Fig. 3(d), whose modes are labeled W/Sk-4 and W/Sk-5. Thus, it is possible to excite propagating modes in the waveguide with a specific wavelength by excitation of specific skyrmion modes,

and study the recently intensively explored physics of the dynamically coupled systems, in particular magnon-magnon coupling [56–58]. Moreover, the resonant coupling offers a possibility for the realization of artificial neural networks [41, 42], where the propagating SWs act as synapses connecting neurons, playing through the nanodot in skyrmion or single-domain state. However, this requires the activation of neurons by propagating SWs. Such a nonlinear property can be achieved by slightly increasing the SW amplitude so that the static magnetic component decreases, resulting in a change of the resonance frequency (e.g. around the modes W/Sk-4 and W/Sk-5 or around 4 GHz, with a change of just about 10 MHz) [59–61] and, depending on the realization, activating or deactivating of the resonance effect.

On the other hand, counterclockwise skyrmion modes form a vertical line of points in Fig. 4(d) and have a strong localization in dots with L not exceeding 0.02. The interaction between counterclockwise modes and waveguide modes is negligible. Modes W/Sk-6 and W/Sk-7 differ in frequency only by 1 MHz but their localization values are 0.97 and 0.01, respectively. Moreover, the small amplitude in the dot for mode W/Sk-6 is not connected with the skyrmion mode W/Sk-7, confirming a lack of coupling between them. It points to the possibility of exploiting these modes, which are strongly localized in the dot or waveguide but are uncoupled, as bound states in the continuum. This effect that has been extensively studied in photonics but has yet to be explored in magnonics [38].

The last range, marked as range III, starts at 10 GHz, from where the dispersion is densely populated with modes having mixed localization. These modes include bulk dot modes, where the skyrmion core and the magnetization outside are excited (modes W/Sk-8 and W/Sk-9) and are coupled with the waveguide. However, counterclockwise skyrmion modes with very low localization and bandwidth below 10 kHz still exist in this range. Excluding them, the localization ranges from 0.13 to 0.96. Above 11.5 GHz, it ranges from 0.23 to 0.82. Range III starts at a higher frequency than the analogical range II in the W/SD system. This is due to the presence of skyrmion in the dot, which induces specific confinement of the resonant modes in the dot, leading to an increase in their frequency.

IV. CONCLUSIONS

We have studied a one-dimensional HMC consisting of an infinitely-long Py waveguide and a chain of nanodots with PMA and DMI (Ir/Co/Pt), in which we consider two different magnetic states: a skyrmion and a single-domain state. The static magnetization configuration in the HMC differs from that of its isolated subsystems. The configuration of the dot imprints the magnetization texture upon the waveguide, at the same time, the skyrmion shape becomes strongly distorted, taking on an egg-like

shape. This makes a SW dynamic in an HMC complex while increasing the skyrmion stability and offering multifunctional properties for advancing magnonics.

The dispersion relations of both systems exhibit characteristic features of magnonic crystals, such as folded branches and band gaps. However, there is a substantial difference in the sizes of the band gaps. Additionally, the W/Sk system has a large number of flat low-frequency skyrmion modes. These modes are azimuthal rotating modes, both clockwise and counterclockwise, localized in the skyrmion domain wall and are characterized by very narrow bandwidths ranging from single kHz to single MHz. Interestingly, the bandwidths are significantly larger compared to those of the dot chain without waveguide, indicating evanescent-wave coupling between the skyrmions in W/Sk system. The flat bands may also overlap with the waveguide modes at higher frequencies and, interestingly, depending on their sense of rotation, can hybridize with them, sometimes even leading to additional band gaps in the spectrum, or be uncoupled. In the same frequency range in the W/SD system, all modes are almost exclusively localized in the waveguide.

At frequencies above 9 GHz, the resonant modes of the dots begin to appear and strongly hybridize with the waveguide modes, causing the localization of the modes to become mixed. However, in the W/Sk system, some of

the modes (localized in the skyrmion domain wall) still can not interact with the waveguide at high frequencies, which promises the realization of the bound state in the continuum in magnonics.

The above-mentioned properties offer several useful functionalities for magnonics, including reconfigurability, filtering, magnon–magnon hybridizations, uncoupled SW modes in the band structure, as well as SW-skyrmion bands together with their evanescence coupling. These functionalities are suitable for the realization of magnonic artificial neural networks.

DATA AVAILABILITY

The raw data files that support this study are available via the Zenodo repository [52].

ACKNOWLEDGMENTS

K.S. and M.K. acknowledge the financial support from National Science Centre, Poland, grants no. UMO-2020/39/I/ST3/02413 and UMO-2021/41/N/ST3/04478. K.S. acknowledges the financial support from the Foundation for Polish Science.

-
- [1] A. V. Chumak, P. Kabos, M. Wu, C. Abert, C. Adelman, A. O. Adeyeye, J. Akerman, F. G. Aliev, A. Anane, A. Awad, C. H. Back, A. Barman, G. E. W. Bauer, M. Becherer, E. N. Beginin, V. A. S. V. Bitencourt, Y. M. Blanter, P. Bortolotti, I. Boventer, D. A. Bozhko, S. A. Bunyaev, J. J. Carmiggelt, R. R. Cheenikundil, F. Ciubotaru, S. Cotozana, G. Csaba, O. V. Dobrovolskiy, C. Dubs, M. Elyasi, K. G. Fripp, H. Fulara, I. A. Golovchanskiy, C. Gonzalez-Ballester, P. Graczyk, D. Grundler, P. Gruszecki, G. Gubbiotti, K. Guslienko, A. Haldar, S. Hamdioui, R. Hertel, B. Hillebrands, T. Hioki, A. Houshang, C.-M. Hu, H. Huebl, M. Huth, E. Iacocca, M. B. Jungfleisch, G. N. Kakazei, A. Khitun, R. Khymyn, T. Kikkawa, M. Klaui, O. Klein, J. W. Klos, S. Knauer, S. Koraltan, M. Kostylev, M. Krawczyk, I. N. Krivorotov, V. V. Kruglyak, D. Lachance-Quirion, S. Ladak, R. Lebrun, Y. Li, M. Lindner, R. Macedo, S. Mayr, G. A. Melkov, S. Mieszczak, Y. Nakamura, H. T. Nembach, A. A. Nikitin, S. A. Nikitov, V. Novosad, J. A. Otalora, Y. Otani, A. Papp, B. Pigeau, P. Pirro, W. Porod, F. Porrati, H. Qin, B. Rana, T. Reimann, F. Riante, O. Romero-Isart, A. Ross, A. V. Sadovnikov, A. R. Safin, E. Saitoh, G. Schmidt, H. Schultheiss, K. Schultheiss, A. A. Serga, S. Sharma, J. M. Shaw, D. Suess, O. Surzhenko, K. Szulc, T. Taniguchi, M. Urbanek, K. Usami, A. B. Ustinov, T. van der Sar, S. van Dijken, V. I. Vasyuchka, R. Verba, S. V. Kusminskiy, Q. Wang, M. Weides, M. Weiler, S. Wintz, S. P. Wolfski, and X. Zhang, *Advances in Magnetism Roadmap on Spin-Wave Computing*, *IEEE Trans. Magn.* **58**, 1 (2022).
- [2] Q. Wang, G. Csaba, R. Verba, A. V. Chumak, and P. Pirro, *Perspective on nanoscaled magnonic networks* (2023), arXiv:2311.06129 [physics.app-ph].
- [3] A. V. Chumak, A. A. Serga, and B. Hillebrands, Magnon transistor for all-magnon data processing, *Nat. Commun.* **5**, 4700 (2014).
- [4] S. Klingler, P. Pirro, T. Brächer, B. Leven, B. Hillebrands, and A. V. Chumak, Design of a spin-wave majority gate employing mode selection, *Appl. Phys. Lett.* **105**, 152410 (2014).
- [5] T. Fischer, M. Kewenig, D. A. Bozhko, A. A. Serga, I. I. Syvorotka, F. Ciubotaru, C. Adelman, B. Hillebrands, and A. V. Chumak, Experimental prototype of a spin-wave majority gate, *Appl. Phys. Lett.* **110**, 152401 (2017).
- [6] M.-K. Lee and M. Mochizuki, Reservoir computing with spin waves in a skyrmion crystal, *Phys. Rev. Appl.* **18**, 014074 (2022).
- [7] O. Lee, T. Wei, K. D. Stenning, J. C. Gartside, D. Prestwood, S. Seki, A. Aqeel, K. Karube, N. Kanazawa, Y. Taguchi, C. Back, Y. Tokura, W. R. Branford, and H. Kurebayashi, Task-adaptive physical reservoir computing, *Nat. Mater.* **23**, 79 (2024).
- [8] S. Wintz, V. Tiberkevich, M. Weigand, J. Raabe, J. Lindner, A. Erbe, A. Slavin, and J. Fassbender, Magnetic vortex cores as tunable spin-wave emitters, *Nat. Nanotechnol.* **11**, 948 (2016).
- [9] H. Yu, J. Xiao, and H. Schultheiss, Magnetic texture based magnonics, *Phys. Rep.* **905**, 1 (2021).
- [10] D. Petti, S. Tacchi, and E. Albisetti, Review on magnonics with engineered spin textures, *J. Phys. D: Appl. Phys.*

- 55, 293003 (2022).
- [11] A. Fert, V. Cros, and J. Sampaio, Skyrmions on the track, *Nat. Nanotechnol.* **8**, 152 (2013).
- [12] M. Lonsky and A. Hoffmann, Dynamic excitations of chiral magnetic textures, *APL Mater.* **8**, 100903 (2020).
- [13] K.-W. Moon, B. S. Chun, W. Kim, and C. Hwang, Control of spin-wave refraction using arrays of skyrmions, *Phys. Rev. Appl.* **6**, 064027 (2016).
- [14] J. Lan and J. Xiao, Skew scattering and side jump of spin wave across magnetic texture, *Phys. Rev. B* **103**, 054428 (2021).
- [15] Z. Wang, H. Y. Yuan, Y. Cao, Z.-X. Li, R. A. Duine, and P. Yan, Magnonic frequency comb through nonlinear magnon-skyrmion scattering, *Phys. Rev. Lett.* **127**, 037202 (2021).
- [16] S. A. Díaz, T. Hirose, D. Loss, and C. Psaroudaki, Spin wave radiation by a topological charge dipole, *Nano Lett.* **20**, 6556 (2020).
- [17] H. Vakili, J.-W. Xu, W. Zhou, M. N. Sakib, M. G. Morshed, T. Hartnett, Y. Quessab, K. Litzius, C. T. Ma, S. Ganguly, M. R. Stan, P. V. Balachandran, G. S. D. Beach, S. J. Poon, A. D. Kent, and A. W. Ghosh, Skyrmionics—Computing and memory technologies based on topological excitations in magnets, *J. Appl. Phys.* **130**, 070908 (2021).
- [18] K. Everschor-Sitte, J. Masell, R. M. Reeve, and M. Kläui, Perspective: Magnetic skyrmions—Overview of recent progress in an active research field, *J. Appl. Phys.* **124**, 240901 (2018).
- [19] A. Fert, N. Reyren, and V. Cros, Magnetic skyrmions: advances in physics and potential applications, *Nat. Rev. Mater.* **2**, 17031 (2017).
- [20] C. H. Marrows and K. Zeissler, Perspective on skyrmion spintronics, *Appl. Phys. Lett.* **119**, 250502 (2021).
- [21] D. Prychynenko, M. Sitte, K. Litzius, B. Krüger, G. Bourianoff, M. Kläui, J. Sinova, and K. Everschor-Sitte, Magnetic skyrmion as a nonlinear resistive element: A potential building block for reservoir computing, *Phys. Rev. Appl.* **9**, 014034 (2018).
- [22] K. M. Song, J.-S. Jeong, B. Pan, X. Zhang, J. Xia, S. Cha, T.-E. Park, K. Kim, S. Finizio, J. Raabe, J. Chang, Y. Zhou, W. Zhao, W. Kang, H. Ju, and S. Woo, Skyrmion-based artificial synapses for neuromorphic computing, *Nat. Electron.* **3**, 148 (2020).
- [23] M. S. N. Tey, X. Chen, A. Soumyanarayanan, and P. Ho, Chiral spin textures for next-generation memory and unconventional computing, *ACS Appl. Electron. Mater.* **4**, 5088 (2022).
- [24] A. Dhiman, M. Matczak, R. Gieniusz, I. Sveklo, Z. Kuran, U. Guzowska, F. Stobiecki, and A. Maziewski, Thickness dependence of interfacial Dzyaloshinskii-Moriya interaction, magnetic anisotropy and spin waves damping in Pt/Co/Ir and Ir/Co/Pt trilayers, *J. Magn. Magn. Mater.* **519**, 167485 (2021).
- [25] S. Azzawi, A. T. Hindmarch, and D. Atkinson, Magnetic damping phenomena in ferromagnetic thin-films and multilayers, *J. Phys. D: Appl. Phys.* **50**, 473001 (2017).
- [26] N. Tang, W. L. N. C. Liyanage, S. A. Montoya, S. Patel, L. J. Quigley, A. J. Grutter, M. R. Fitzsimmons, S. Sinha, J. A. Borchers, E. E. Fullerton, L. DeBeer-Schmitt, and D. A. Gilbert, Skyrmion-excited spin-wave fractal networks, *Adv. Mater.* **35**, 2300416 (2023).
- [27] C. Jin, S. Li, H. Zhang, R. Wang, J. Wang, R. Lian, P. Gong, and X. Shi, Spin-wave modes of elliptical skyrmions in magnetic nanodots, *New J. Phys.* **24**, 043005 (2022).
- [28] M. Zelent, P. Gruszecki, M. Moalic, O. Hellwig, A. Barman, and M. Krawczyk, Chapter One - Spin dynamics in patterned magnetic multilayers with perpendicular magnetic anisotropy (Academic Press, 2022) pp. 1–51.
- [29] K. Y. Guslienko and Z. V. Gareeva, Gyrotropic skyrmion modes in ultrathin magnetic circular dots, *IEEE Magn. Lett.* **8**, 1 (2017).
- [30] J.-V. Kim, F. Garcia-Sanchez, J. Sampaio, C. Moreau-Luchaire, V. Cros, and A. Fert, Breathing modes of confined skyrmions in ultrathin magnetic dots, *Phys. Rev. B* **90**, 064410 (2014).
- [31] M. Mruczkiewicz, P. Gruszecki, M. Zelent, and M. Krawczyk, Collective dynamical skyrmion excitations in a magnonic crystal, *Phys. Rev. B* **93**, 174429 (2016).
- [32] M. Garst, J. Waizner, and D. Grundler, Collective spin excitations of helices and magnetic skyrmions: review and perspectives of magnonics in non-centrosymmetric magnets, *J. Phys. D: Appl. Phys.* **50**, 293002 (2017).
- [33] M. Mruczkiewicz, P. Gruszecki, M. Krawczyk, and K. Y. Guslienko, Azimuthal spin-wave excitations in magnetic nanodots over the soliton background: Vortex, Bloch, and Néel-like skyrmions, *Phys. Rev. B* **97**, 064418 (2018).
- [34] Z. Chen and F. Ma, Skyrmion based magnonic crystals, *J. Appl. Phys.* **130**, 090901 (2021).
- [35] I. A. Golovchanskiy, N. N. Abramov, V. S. Stolyarov, P. S. Dzhumayev, O. V. Emelyanova, A. A. Golubov, V. V. Ryazanov, and A. V. Ustinov, Ferromagnet/superconductor hybrid magnonic metamaterials, *Adv. Sci.* **6**, 1900435 (2019).
- [36] J. Chen, J. Hu, and H. Yu, Chiral emission of exchange spin waves by magnetic skyrmions, *ACS Nano* **15**, 4372 (2021).
- [37] M. Zelent, M. Moalic, M. Mruczkiewicz, X. Li, Y. Zhou, and M. Krawczyk, Stabilization and racetrack application of asymmetric Néel skyrmions in hybrid nanostructures, *Sci. Rep.* **13**, 13572 (2023).
- [38] C. W. Hsu, B. Zhen, A. D. Stone, J. D. Joannopoulos, and M. Soljacic, Bound states in the continuum, *Nat. Rev. Mater.* **1**, 16048 (2016).
- [39] R. A. Gallardo, D. Cortés-Ortuño, T. Schneider, A. Roldán-Molina, F. Ma, R. E. Troncoso, K. Lenz, H. Fangohr, J. Lindner, and P. Landeros, Flat bands, indirect gaps, and unconventional spin-wave behavior induced by a periodic Dzyaloshinskii-Moriya interaction, *Phys. Rev. Lett.* **122**, 067204 (2019).
- [40] D. D. Awschalom, C. R. Du, R. He, F. J. Heremans, A. Hoffmann, J. Hou, H. Kurebayashi, Y. Li, L. Liu, V. Novosad, J. Sklenar, S. E. Sullivan, D. Sun, H. Tang, V. Tyberkevych, C. Trevillian, A. W. Tsen, L. R. Weiss, W. Zhang, X. Zhang, L. Zhao, and C. W. Zollitsch, Quantum engineering with hybrid magnonic systems and materials, *IEEE Trans. Quantum Eng.* **2**, 1 (2021).
- [41] Á. Papp, W. Porod, and G. Csaba, Nanoscale neural network using non-linear spin-wave interference, *Nat. Commun.* **12**, 6422 (2021).
- [42] K. G. Fripp, Y. Au, A. V. Shytov, and V. V. Kruglyak, Nonlinear chiral magnonic resonators: Toward magnonic neurons, *Appl. Phys. Lett.* **122**, 172403 (2023).
- [43] K. Szulc, S. Tacchi, A. Hierro-Rodríguez, J. Díaz, P. Gruszecki, P. Graczyk, C. Quirós, D. Markó,

- J. I. Martín, M. Vélez, D. S. Schmool, G. Carlotti, M. Krawczyk, and L. M. Álvarez Prado, Reconfigurable magnonic crystals based on imprinted magnetization textures in hard and soft dipolar-coupled bilayers, *ACS Nano* **16**, 14168 (2022).
- [44] K. Guslienko and Z. Gareeva, Magnetic skyrmion low frequency dynamics in thin circular dots, *J. Magn. Magn. Mater.* **442**, 176 (2017).
- [45] M. Zelent, J. Tóbiš, M. Krawczyk, K. Y. Guslienko, and M. Mruczkiewicz, Bi-stability of magnetic skyrmions in ultrathin multilayer nanodots induced by magnetostatic interaction, *Phys. Status Solidi RRL* **11**, 1700259 (2017).
- [46] I. Limes and G. S. D. Beach, Twisted domain walls and skyrmions in perpendicularly magnetized multilayers, *Phys. Rev. B* **98**, 104402 (2018).
- [47] S. Woo, K. Litzius, B. Krüger, M.-Y. Im, L. Caretta, K. Richter, M. Mann, A. Krone, R. M. Reeve, M. Weigand, P. Agrawal, I. Limes, M.-A. Mawass, P. Fischer, M. Kläui, and G. S. D. Beach, Observation of room-temperature magnetic skyrmions and their current-driven dynamics in ultrathin metallic ferromagnets, *Nat. Mater.* **15**, 501 (2016).
- [48] A. Suna, Perpendicular magnetic ground state of a multilayer film, *J. Appl. Phys.* **59**, 313 (1986).
- [49] I. V. Vetrova, M. Zelent, J. Šoltýs, V. A. Gubanov, A. V. Sadovnikov, T. Šcepka, J. Dérer, R. Stoklas, V. Cambel, and M. Mruczkiewicz, Investigation of self-nucleated skyrmion states in the ferromagnetic/nonmagnetic multilayer dot, *Appl. Phys. Lett.* **118**, 212409 (2021).
- [50] A. Riveros, F. Tejo, J. Escrig, K. Guslienko, and O. Chubykalo-Fesenko, Field-dependent energy barriers of magnetic Néel skyrmions in ultrathin circular nanodots, *Phys. Rev. Appl.* **16**, 014068 (2021).
- [51] G. Gubbiotti, L. L. Xiong, F. Montoncello, L. Giovannini, and A. O. Adeyeye, Spin wave dispersion and intensity correlation in width-modulated nanowire arrays: A Brillouin light scattering study, *J. Appl. Phys.* **124**, 083903 (2018).
- [52] K. Szulc, Dataset for "Reconfigurable spin-wave platform based on interplay between nanodots and waveguide in hybrid magnonic crystal" (2024), <https://doi.org/10.5281/zenodo.10964849>.
- [53] H. Yu, O. d'Allivy Kelly, V. Cros, R. Bernard, P. Bortolotti, A. Anane, F. Brandl, F. Heimbach, and D. Grundler, Approaching soft X-ray wavelengths in nanomagnet-based microwave technology, *Nat. Commun.* **7**, 11255 (2016).
- [54] H. Qin, G.-J. Both, S. J. Hämäläinen, L. Yao, and S. van Dijken, Low-loss YIG-based magnonic crystals with large tunable bandgaps, *Nat. Commun.* **9**, 5445 (2018).
- [55] S. Tacchi, J. Flores-Farías, D. Petti, F. Brevis, A. Cattani, G. Scaramuzzi, D. Girardi, D. Cortés-Ortuno, R. A. Gallardo, E. Albisetti, G. Carlotti, and P. Landeros, Experimental observation of flat bands in one-dimensional chiral magnonic crystals, *Nano Lett.* **23**, 6776 (2023).
- [56] K. Adhikari, S. Choudhury, S. Barman, Y. Otani, and A. Barman, Observation of magnon-magnon coupling with high cooperativity in Ni₈₀Fe₂₀ cross-shaped nanoring array, *Nanotechnology* **32**, 395706 (2021).
- [57] J. C. Gartside, A. Vanstone, T. Dion, K. D. Stenning, D. M. Arroo, H. Kurebayashi, and W. R. Branford, Reconfigurable magnonic mode-hybridisation and spectral control in a bicomponent artificial spin ice, *Nat. Commun.* **12**, 2488 (2021).
- [58] Y. Wang, Y. Zhang, C. Li, J. Wei, B. He, H. Xu, J. Xia, X. Luo, J. Li, J. Dong, W. He, Z. Yan, W. Yang, F. Ma, G. Chai, P. Yan, C. Wan, X. Han, and G. Yu, Ultrastrong to nearly deep-strong magnon-magnon coupling with a high degree of freedom in synthetic antiferromagnets, *Nat. Commun.* **15**, 2077 (2024).
- [59] P. Krivosik and C. E. Patton, Hamiltonian formulation of nonlinear spin-wave dynamics: Theory and applications, *Phys. Rev. B* **82**, 184428 (2010).
- [60] H. Merbouche, B. Divinskiy, K. O. Nikolaev, C. Kaspar, W. H. P. Pernice, D. Gouverne, R. Lebrun, V. Cros, J. Ben Youssef, P. Bortolotti, A. Anane, S. O. Demokritov, and V. E. Demidov, Giant nonlinear self-phase modulation of large-amplitude spin waves in microscopic YIG waveguides, *Sci. Rep.* **12**, 7246 (2022).
- [61] Q. Wang, R. Verba, B. Heinz, M. Schneider, O. Wojewoda, K. Davidkova, K. Levchenko, C. Dubs, N. J. Mauser, M. Urbánek, P. Pirro, and A. V. Chumak, Deeply nonlinear excitation of self-normalized short spin waves, *Sci. Adv.* **9**, eadg4609 (2023).

SUPPLEMENTARY MATERIALS

Reconfigurable spin-wave platform based on interplay between nanodots and waveguide in hybrid magnonic crystal

Krzysztof Szulc,* Mateusz Zelent, and Maciej Krawczyk
*Institute of Spintronics and Quantum Information,
 Faculty of Physics, Adam Mickiewicz University, Poznań,
 Uniwersytetu Poznańskiego 2, 61-614 Poznań, Poland*

We present a hybrid magnonic crystal composed of a chain of nanodots with strong perpendicular magnetic anisotropy and Dzyaloshinskii–Moriya interaction, positioned above a permalloy waveguide. The study examines two different magnetization states in the nanodots: a single-domain state and an egg-shaped skyrmion state. Due to the dipolar coupling between the dot and the waveguide, a strongly bound hybrid magnetization texture is formed in the system. Our numerical results show complex spin-wave spectra, combining the effects of periodicity, magnetization texture, and hybridization of the propagating waves in the waveguide with the dot/skyrmion modes. The systems are characterized by different band gap sizes. For the skyrmion state, the azimuthal modes confined to the skyrmion domain wall lead to the formation of flat bands at low frequencies, while at higher frequencies we identify among them modes interacting with the propagating waves, which can introduce additional non-Bragg band gaps, as well as isolated modes leading to the formation of bound states. On the other hand, the system with a single-domain state in nanodots offers a wide range of frequencies where the spin waves are predominantly in the waveguide. Thus, the study shows that the proposed hybrid magnonic crystals have many distinct functionalities, highlighting their reconfigurable potential, magnon–magnon couplings, mode localization, and bound states overlapping with the propagating waves. This opens up potential applications in analog and quantum magnonics, spin-wave filtering, and the establishment of magnonic neural networks.

S1. THE DYNAMICS OF ISOLATED SUBSYSTEMS

Figure S1(a) shows the comparison between the dynamics of the isolated subsystems. The dispersion relation of an isolated waveguide is shown with solid blue lines. The resonant modes of a dot are shown with horizontal dashed lines: orange line for an isolated dot in the single-domain state and green line for an isolated dot in the skyrmion state.

The lowest zero- k frequency of the waveguide is 4.04 GHz and it reaches a minimum of 3.76 GHz for $k = 9.0 \text{ rad}/\mu\text{m}$. Higher-order modes have their minima at 6.19 GHz, 8.17 GHz, 9.92 GHz, and 11.57 GHz, respectively. First four modes exhibit a backward-wave regime at small wavevectors, while higher modes can only propagate forward.

In case of the dot, its static configuration has a very large impact on the frequency of resonant modes. In a single-domain state, the lowest mode has a frequency of 8.89 GHz and it is a fundamental mode (SD-1). Modes with higher frequencies are clockwise (CW) [e.g. SD-2] and counterclockwise (CCW) [e.g. SD-3] azimuthal modes, as well as higher-order radial modes (e.g. SD-4).

The skyrmion state exhibits numerous low-frequency modes, which are all CW (e.g. Sk-1) and CCW (e.g. Sk-3) azimuthal modes in the skyrmion domain wall, except of one skyrmion breathing mode (Sk-2) (which can

be considered the 0th order azimuthal mode). The first mode not associated with the skyrmion domain wall is the fundamental mode of a skyrmion core (Sk-4) at the frequency 9.47 GHz. The higher-frequency modes include higher-order azimuthal and radial modes, which can be localized either in the skyrmion core (e.g. Sk-5), outside the skyrmion (e.g. Sk-7) or in both the core and outside (e.g. Sk-6). Interestingly, some of the skyrmion domain wall modes in this range can also be strongly excited outside the skyrmion (e.g. Sk-8).

S2. COMPARISON BETWEEN W/SK SYSTEM AND A DOT CHAIN

In order to investigate the contribution of the dipolar interaction between the dot and the waveguide to the bandwidth of the skyrmion domain wall modes, we studied a one-dimensional chain of dots in skyrmion state, which is a subsystem of the W/Sk system. Additionally, as a reference, we studied a single dot in a skyrmion state.

Table I shows the simulation data for the modes within the frequency range I of the W/Sk system, as depicted in Fig. 4(c,d) in the main manuscript. This range contains 15 modes, ranging from the 2nd CW to the 12th CCW mode. Modes at higher frequencies may be significantly impacted by interaction with waveguide modes and are therefore not included in Table I.

First of all, it is important to note that the static configurations of these systems are different. In a single dot, the skyrmion is round. In a dot chain, the dipolar interaction between the dots is very small so the skyrmion re-

* krzysztof.szulc@amu.edu.pl

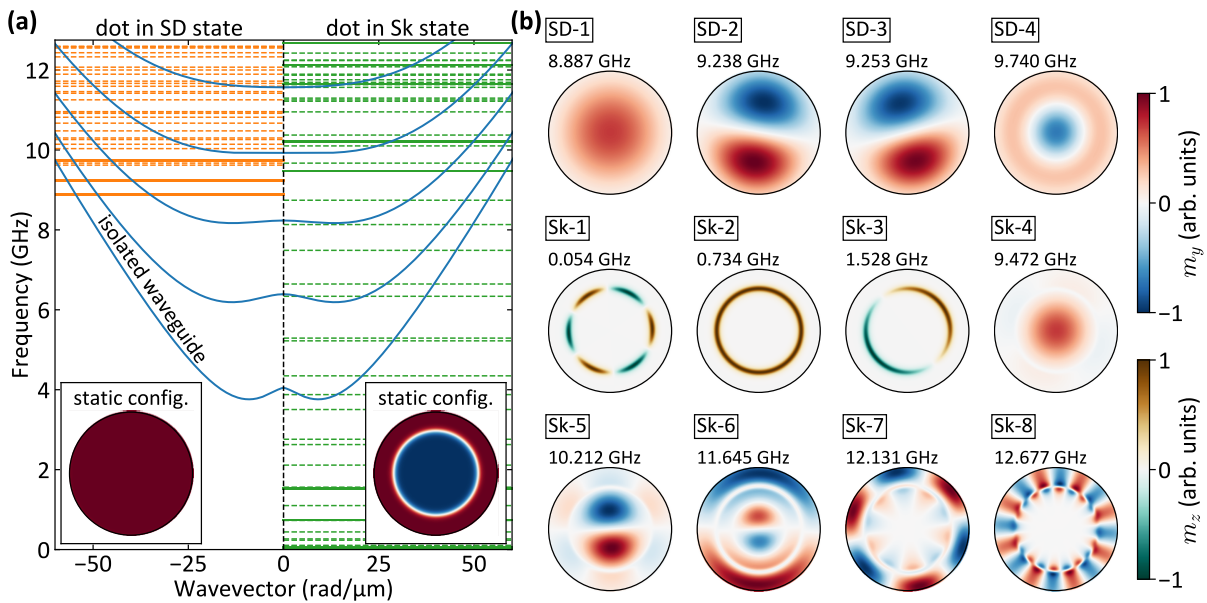


Figure S1. (a) Dispersion relation of an isolated waveguide (solid blue lines) and frequencies of the resonant modes of a dot in a single-domain state (horizontal dashed orange lines) and in a skyrmion state (horizontal dashed green lines). Solid orange and green lines correspond to the modes which profiles are shown in (b). Please note that the resonant modes are characterized solely by their frequencies and they are not connected with the wavevector presented on the horizontal axis. The division of the single-domain state and skyrmion modes on the negative and positive wavevector sides is made solely for the sake of presentation clarity. (b) Resonant mode profiles of the dot of four modes in the SD state and eight modes in the Sk state. Please note that all SD modes and Sk-4 – Sk-8 modes are presented with m_y component (top color bar), while modes Sk-1 – Sk-3 are presented with m_z component (bottom color bar). All modes are normalized to the maximum absolute value of the mode. The animated version of this figure is available in [52].

mains round. In the W/Sk system, the skyrmion changes its shape to an egg-like shape, as shown in Fig. 2(c) in the main manuscript. This change in shape significantly impacts the mode frequencies. As shown in Table I, the frequencies of modes in a single dot and an array of dots are very similar, differing by no more than 65 MHz. On the other hand, modes in the W/Sk system can differ from a single dot modes as much as 516 MHz for the 1st CW mode. However, for the higher-order CCW modes, this difference is strongly reduced.

When comparing the bandwidths of the same modes

in different systems, it is clear that the dipolar interaction between the dot and the waveguide significantly contributes to this value. The bandwidths of all modes, except of the 4th CCW mode, are larger in W/Sk system, indicating that the presence of the waveguide enhance the interaction between the skyrmions. This effect is particularly noticeable for higher-order CCW modes (5th order and higher), whose bandwidths are orders of magnitude larger in the W/Sk system. However, it is difficult to distinguish the contribution of modified static configuration of a skyrmion and dynamic dipolar interaction through the waveguide.

Table I. The comparison of the skyrmion domain wall modes in three different systems: single dot, dot chain, and W/Sk system as defined in the main manuscript. For a single dot, we present the value of the mode frequency, while for dot chain and W/Sk system, we show the lowest and the highest frequency of the band and the bandwidth. Please note that the frequencies are in MHz, while bandwidths are in kHz.

Mode	Single dot		Dot chain		W/Sk system		
	f (MHz)	f_{\min} (MHz)	f_{\max} (MHz)	Bandwidth (kHz)	f_{\min} (MHz)	f_{\max} (MHz)	Bandwidth (kHz)
CW 2	2628	2627	2628	1309.06	3065	3078	13085.05
CW 1	1528	1542	1549	7533.08	2023	2044	21187.33
breathing	734	747	780	33223.62	1192	1226	34143.46
CCW 1	266	290	296	5996.20	482	490	8453.12
CCW 2	91	106	107	354.05	238	239	1061.96
CCW 3	54	64	64	42.51	107	108	533.27
CCW 4	106	117	117	264.79	132	133	178.41
CCW 5	235	237	237	13.78	303	304	728.22
CCW 6	441	438	438	2.25	505	505	208.15
CCW 7	729	719	719	1.99	780	781	265.48
CCW 8	1101	1083	1083	0.96	1140	1140	26.74
CCW 9	1561	1534	1534	8.47	1586	1586	36.19
CCW 10	2113	2075	2075	0.10	2122	2122	9.06
CCW 11	2760	2710	2710	0.08	2750	2750	11.54
CCW 12	3504	3440	3440	0.01	3474	3474	54.62

4.6 Outlook

It is worth discussing the possibilities of continuing the studies presented in the Thesis. The devices presented in articles [P1] and [P2] have been demonstrated only in simulations. I believe it is possible to make their experimental demonstration. These systems can be measured using propagating spin-wave spectroscopy or micro-focused Brillouin light scattering spectroscopy. The latter can be particularly useful in this case, as it can measure spin waves with very large wavevectors [211]. Moreover, in collaboration with Olena Tartakivska, I studied the fundamentals of the rotating modes in the rectangular resonator. The manuscript is in preparation. Thanks to the invitation of Andrii Chumak, I prepared a subsection to the *Roadmap on Spin-Wave Computing* [129], where I presented the results of the articles [P1] and [P2]. The continuation of the article [P3] has taken a different path. In my project entitled *Three-dimensional magnonic structures for analog computing: interaction analysis and device development*, I study the coupled waveguides in the backward volume geometry. I found that for the system of two vertically-stacked waveguides, at a certain frequency they are not coupled and the spin wave is not transmitted between them. This property can be used to isolate the waveguides in the three-dimensional systems. The research from article [P4] has also found its continuation. We are currently studying the system with different spin-wave conduits in order to achieve stronger coupling with the layer with the stripe-domain pattern. In the case of article [P5], the study of the system can go in the direction of simulating of the spin-wave transmission through the system. Moreover, there is also the possibility of experimental demonstration of this device. A similar system with the array of nanodots in the vortex state above the thin film has been studied experimentally by the group of Prof. Sebastiaan van Dijken from Aalto University in Finland, and I am responsible for the fitting of the experimental results by the numerical simulations.

4.7 Other research

In addition to the five articles presented in the Thesis, I am the co-author of 6 research articles and 1 roadmap as listed in the note about the author at the end of the Thesis. The first publication [212] is about the magnetization reversal analysis in the periodic and quasiperiodic arrays of cuboids and it was finished before the beginning of the doctoral studies. In the next paper [208] I contributed to the experimental work of the group of M. Urbánek at CEITEC in Brno, Czech Republic. They prepared a new method to measure spin-wave propagation called variable-gap propagating spin-wave spectroscopy. They demonstrated the method on a single CoFeB layer which showed an unexpectedly strong hybridization of Damon–Eshbach mode with higher-order modes. This coupling enhancement was attributed to the partial pinning of the spin waves at the boundary. I was responsible for extending the COMSOL model to include the partial pinning conditions and performing of the numerical simulations that confirmed the critical role of pinning. This study led to a deeper investigation of the partial pinning of the spin waves, which further led to the publication of a paper in which the effects of the partial pinning are described in

detail using my numerical simulations and analytical formulas developed by J. Kharlan and P. Bondarenko [209]. In the study of M. Moalic *et al.* [213], I contributed to the explanation of the coupling between the bulk modes and rim modes in an antidot lattice with modified rims. I also started working in the field of solar cells, where I wrote a program in COMSOL to solve the problem of the electron and hole dynamics in the ps range in the thin film perovskite solar cells [214]. The numerical simulations helped to fit the crucial parameters of the solar cells to the experimental results of the broadband transient absorption. Another direction in which I am going in is superconductivity, especially to combine it with magnetism and magnonics. In the paper by J. Kharlan *et al.* [215], the confinement of a spin-wave mode in a magnetic field well created by the superconducting strip in the Meissner state was studied. I was responsible for the implementation of the London equation in COMSOL and its solution for the system investigated in this work. Moreover, this topic is continued and the spin-wave propagation is studied in the system with the periodic array of superconducting strips over the ferromagnetic film, system functioning as a magnonic crystal. The manuscript is currently in preparation.

There are other ongoing research projects in which I am involved. Except for the studies mentioned in Section 4.6, where I mentioned the continuation of papers [P2], [P3], [P4], and [P5], I am also working on the tasks of my PRELUDIUM project. One of the studies is mentioned as a continuation of [P3]. In another one, I found that it is possible to design a broadband directional coupler by aligning two waveguides not exactly one over another, but with a small offset between them. Another work is a continuation of the publication [209]. I found that using the partial pinning, it is possible to design a spin-wave diode using only a single ferromagnetic layer. In the study in collaboration with M. Gołębiewski, he performed the numerical simulations of the ferromagnetic thin-film gyroid structures and found that the ferromagnetic resonance mode is localized, which is not the case for the regular thin films. I helped in the interpretation of this phenomenon, which is a result of the interplay between the demagnetizing field in complex structures and the exchange interaction. The manuscript is currently in preparation.

Chapter 5

Summary

In the Thesis, I wanted to show how the spin-wave dynamics can be affected by the interaction between the layers, with an emphasis on contributing to the field of the spin-wave computing. The results were collected in five research articles, four of which have been published in peer-reviewed journals and one of which is currently under review.

In [P1], it was shown that it is possible to couple two ultrathin layers, one with Dzyaloshinskii–Moriya interaction and one without, and obtain the effect of unidirectional coupling of spin waves in a wide frequency range. This effect was used to design the broadband spin-wave diode and circulator. In [P2], two thin films were coupled with a long permalloy strip. Due to the rotating character of the resonant modes in the strip, such a system acts as a multifunctional device, performing at different frequencies different functions such as circulator, directional coupler, and reflector. In [P3], two ultrathin Co films with opposite sign of the DMI constant were separated by a W spacer of only 0.95 nm. Despite that, their coupling is negligible, resulting in non-interacting nanoscale spin-wave conduits. In [P4], the NdCo layer characterized by a stripe-domain structure was coupled with the soft, low-damping Py layer to create a hybrid system with a complex magnetization texture and good spin-wave properties. It was shown that this system functions as a reconfigurable magnonic crystal with non-reciprocal dispersion relation. In [P5], the chain of nanodots in the single-domain or skyrmion state was coupled to the waveguide to create a reconfigurable magnonic crystal. The results showed the significant differences between the spin-wave dynamics of these systems, such as different band-gap sizes, low-frequency modes present only in the skyrmion state, and different coupling mechanisms including hybridized and bound skyrmion modes in the skyrmion state and the range of pure waveguide modes in the single-domain state.

I believe that the results presented in the Thesis prove all the hypotheses stated in Preface. I also believe that these articles make a significant contribution to the field of magnonics, in particular to spin-wave computing. They have already found the interest of the scientific community, being cited a total of 75 times (as of 13 June 2024 according to Scopus). I believe that the field of spin-wave computing will continue to grow in the coming years, that the spin-wave circuit will finally be demonstrated, and that the spin-wave devices will be present in future computing units.

Bibliography

- [1] *International Roadmap for Devices and Systems*, URL: <https://irds.ieee.org/>.
- [2] J. M. D. Coey, *Magnetism and magnetic materials* (Cambridge University Press, 2010).
- [3] X. Liu, K. H. Lam, K. Zhu, et al., “Overview of spintronic sensors with internet of things for smart living”, *IEEE Transactions on Magnetics* **55**, 1–22 (2019).
- [4] B. Dieny, I. L. Prejbeanu, K. Garello, et al., “Opportunities and challenges for spintronics in the microelectronics industry”, *Nature Electronics* **3**, 446–459 (2020).
- [5] J. Åkerman, “Toward a universal memory”, *Science* **308**, 508–510 (2005).
- [6] C. Kittel, “Interaction of spin waves and ultrasonic waves in ferromagnetic crystals”, *Physical Review* **110**, 836–841 (1958).
- [7] R. L. Comstock and B. A. Auld, “Parametric coupling of the magnetization and strain in a ferrimagnet. I. Parametric excitation of magnetostatic and elastic modes”, *Journal of Applied Physics* **34**, 1461–1464 (1963).
- [8] Y. R. Shen and N. Bloembergen, “Interaction between light waves and spin waves”, *Physical Review* **143**, 372–384 (1966).
- [9] J. Slonczewski, “Current-driven excitation of magnetic multilayers”, *Journal of Magnetism and Magnetic Materials* **159**, L1–L7 (1996).
- [10] S. Zhang and Z. Li, “Roles of nonequilibrium conduction electrons on the magnetization dynamics of ferromagnets”, *Physical Review Letters* **93**, 127204 (2004).
- [11] S. Chikazumi, *Physics of Ferromagnetism*, 2nd ed. (Oxford University Press, Oxford, 1997).
- [12] F. Keffer, “Spin Waves”, in *Ferromagnetism*, edited by H. P. J. Wijn (Springer Berlin Heidelberg, Berlin, Heidelberg, 1966), pp. 1–273.
- [13] A. Hubert and R. Schäfer, *Magnetic Domains: The Analysis of Magnetic Microstructures* (Springer Berlin Heidelberg, Berlin, Heidelberg, 1998).
- [14] T. Böttcher, M. Ruhwedel, K. O. Levchenko, et al., “Fast long-wavelength exchange spin waves in partially compensated Ga:YIG”, *Applied Physics Letters* **120**, 102401 (2022).
- [15] R. Moskowitz and E. Della Torre, “Theoretical aspects of demagnetization tensors”, *IEEE Transactions on Magnetics* **2**, 739–744 (1966).
- [16] A. J. Newell, W. Williams, and D. J. Dunlop, “A generalization of the demagnetizing tensor for nonuniform magnetization”, *Journal of Geophysical Research: Solid Earth* **98**, 9551–9555 (1993).
- [17] D. D. Stancil and A. Prabhakar, *Spin Waves: Theory and Applications* (Springer, New York, 2009).
- [18] I. Dzyaloshinsky, “A thermodynamic theory of “weak” ferromagnetism of antiferromagnetics”, *Journal of Physics and Chemistry of Solids* **4**, 241–255 (1958).
- [19] T. Moriya, “Anisotropic superexchange interaction and weak ferromagnetism”, *Physical Review* **120**, 91–98 (1960).
- [20] P. Bak and M. H. Jensen, “Theory of helical magnetic structures and phase transitions in MnSi and FeGe”, *Journal of Physics C: Solid State Physics* **13**, L881 (1980).

- [21] O. Nakanishi, A. Yanase, A. Hasegawa, and M. Kataoka, “The origin of the helical spin density wave in MnSi”, *Solid State Communications* **35**, 995–998 (1980).
- [22] A. R. Fert, “Magnetic and transport properties of metallic multilayers”, in *Metallic multilayers*, Vol. 59, *Materials Science Forum* (1990), pp. 439–480.
- [23] A. Crépieux and C. Lacroix, “Dzyaloshinsky–Moriya interactions induced by symmetry breaking at a surface”, *Journal of Magnetism and Magnetic Materials* **182**, 341–349 (1998).
- [24] A. Kubetzka, M. Bode, O. Pietzsch, and R. Wiesendanger, “Spin-polarized scanning tunneling microscopy with antiferromagnetic probe tips”, *Physical Review Letters* **88**, 057201 (2002).
- [25] A. Thiaville, S. Rohart, É. Jué, V. Cros, and A. Fert, “Dynamics of Dzyaloshinskii domain walls in ultrathin magnetic films”, *Europhysics Letters* **100**, 57002 (2012).
- [26] L. D. Landau and E. M. Lifshitz, “On the theory of the dispersion of magnetic permeability in ferromagnetic bodies”, *Physikalische Zeitschrift der Sowjetunion* **8**, 153–169 (1935).
- [27] T. Gilbert, “A phenomenological theory of damping in ferromagnetic materials”, *IEEE Transactions on Magnetics* **40**, 3443–3449 (2004).
- [28] G. T. Rado and J. R. Weertman, “Spin-wave resonance in a ferromagnetic metal”, *Journal of Physics and Chemistry of Solids* **11**, 315–333 (1959).
- [29] W. S. Ament and G. T. Rado, “Electromagnetic effects of spin wave resonance in ferromagnetic metals”, *Physical Review* **97**, 1558–1566 (1955).
- [30] J. Bruyere, O. Massenet, R. Montmory, and L. Neel, “A coupling phenomenon between the magnetization of two ferromagnetic thin films separated by a thin metallic film—Application to magnetic memories”, *IEEE Transactions on Magnetics* **1**, 10–12 (1965).
- [31] O. Massenet, F. Biragnet, H. Juretschke, R. Montmory, and A. Yelon, “Origin of coupling in multilayered films”, *IEEE Transactions on Magnetics* **2**, 553–556 (1966).
- [32] E. Goto, N. Hayashi, N. Honma, R. Kuroda, and T. Miyashita, “Switching characteristics of composite magnetic thin films”, *Japanese Journal of Applied Physics* **4**, 712 (1965).
- [33] F. Hoffmann, A. Stankoff, and H. Pascard, “Evidence for an exchange coupling at the interface between two ferromagnetic films”, *Journal of Applied Physics* **41**, 1022–1023 (1970).
- [34] F. Hoffmann, “Dynamic pinning induced by nickel layers on permalloy films”, *physica status solidi (b)* **41**, 807–813 (1970).
- [35] P. Grünberg, R. Schreiber, Y. Pang, M. B. Brodsky, and H. Sowers, “Layered magnetic structures: Evidence for antiferromagnetic coupling of Fe layers across Cr interlayers”, *Physical Review Letters* **57**, 2442–2445 (1986).
- [36] C. Carbone and S. F. Alvarado, “Antiparallel coupling between Fe layers separated by a Cr interlayer: Dependence of the magnetization on the film thickness”, *Physical Review B* **36**, 2433–2435 (1987).
- [37] S. S. P. Parkin, N. More, and K. P. Roche, “Oscillations in exchange coupling and magnetoresistance in metallic superlattice structures: Co/Ru, Co/Cr, and Fe/Cr”, *Physical Review Letters* **64**, 2304–2307 (1990).
- [38] P. Bruno and C. Chappert, “Oscillatory coupling between ferromagnetic layers separated by a nonmagnetic metal spacer”, *Physical Review Letters* **67**, 1602–1605 (1991).
- [39] M. A. Ruderman and C. Kittel, “Indirect exchange coupling of nuclear magnetic moments by conduction electrons”, *Physical Review* **96**, 99–102 (1954).
- [40] T. Kasuya, “A theory of metallic ferro- and antiferromagnetism on Zener’s model”, *Progress of Theoretical Physics* **16**, 45–57 (1956).
- [41] K. Yosida, “Magnetic properties of Cu-Mn alloys”, *Physical Review* **106**, 893–898 (1957).
- [42] B. Hillebrands, “Spin-wave calculations for multilayered structures”, *Physical Review B* **41**, 530–540 (1990).

- [43] M. W. Muller, "Distribution of the magnetization in a ferromagnet", *Physical Review* **122**, 1485–1489 (1961).
- [44] W. F. Brown, "Rigorous calculation of the nucleation field in a ferromagnetic film or plate", *Physical Review* **124**, 1348–1353 (1961).
- [45] R. J. Spain, "Dense-banded domain structure in "rotatable anisotropy" permalloy films", *Applied Physics Letters* **3**, 208–209 (1963).
- [46] N. Saito, H. Fujiwara, and Y. Sugita, "A new type of magnetic domain in thin Ni-Fe films", *Journal of the Physical Society of Japan* **19**, 421–422 (1964).
- [47] I. Puchalska and R. Ferrier, "High-voltage electron microscope observation of stripe domains in permalloy films evaporated at oblique incidence", *Thin Solid Films* **1**, 437–445 (1968).
- [48] O. Hellwig, G. Denbeaux, J. Kortright, and E. E. Fullerton, "X-ray studies of aligned magnetic stripe domains in perpendicular multilayers", *Physica B* **336**, 136–144 (2003).
- [49] O. de Abril, M. d. C. Sánchez, and C. Aroca, "New closed flux stripe domain model for weak perpendicular magnetic anisotropy films", *Applied Physics Letters* **89**, 172510 (2006).
- [50] A. Hierro-Rodríguez, R. Cid, M. Vélez, et al., "Topological defects and misfit strain in magnetic stripe domains of lateral multilayers with perpendicular magnetic anisotropy", *Physical Review Letters* **109**, 117202 (2012).
- [51] A. Hierro-Rodríguez, G. Rodríguez-Rodríguez, J. M. Teixeira, et al., "Fabrication and magnetic properties of nanostructured amorphous Nd–Co films with lateral modulation of magnetic stripe period", *Journal of Physics D: Applied Physics* **46**, 345001 (2013).
- [52] S. Fin, R. Tomasello, D. Bisero, et al., "In-plane rotation of magnetic stripe domains in $\text{Fe}_{1-x}\text{Ga}_x$ thin films", *Physical Review B* **92**, 224411 (2015).
- [53] C. Banerjee, P. Gruszecki, J. W. Klos, et al., "Magnonic band structure in a Co/Pd stripe domain system investigated by Brillouin light scattering and micromagnetic simulations", *Physical Review B* **96**, 024421 (2017).
- [54] M. Coisson, G. Barrera, F. Celegato, and P. Tiberto, "Rotatable magnetic anisotropy in $\text{Fe}_{78}\text{Si}_9\text{B}_{13}$ thin films displaying stripe domains", *Applied Surface Science* **476**, 402–411 (2019).
- [55] L. Fallarino, A. Oelschlägel, J. A. Arregi, et al., "Control of domain structure and magnetization reversal in thick Co/Pt multilayers", *Physical Review B* **99**, 024431 (2019).
- [56] L.-C. Garnier, M. Marangolo, M. Eddrief, et al., "Stripe domains reorientation in ferromagnetic films with perpendicular magnetic anisotropy", *Journal of Physics: Materials* **3**, 024001 (2020).
- [57] A. Hubert, "Stray-field-free magnetization configurations", *physica status solidi (b)* **32**, 519–534 (1969).
- [58] T. Skyrme, "A unified field theory of mesons and baryons", *Nuclear Physics* **31**, 556–569 (1962).
- [59] N. S. Kiselev, A. N. Bogdanov, R. Schäfer, and U. K. Röβler, "Chiral skyrmions in thin magnetic films: new objects for magnetic storage technologies?", *Journal of Physics D: Applied Physics* **44**, 392001 (2011).
- [60] S. Rohart, J. Miltat, and A. Thiaville, "Path to collapse for an isolated Néel skyrmion", *Physical Review B* **93**, 214412 (2016).
- [61] V. Pokrovsky, "Properties of ordered, continuously degenerate systems", *Advances in Physics* **28**, 595–656 (1979).
- [62] A. N. Bogdanov and D. Yablonskii, "Thermodynamically stable "vortices" in magnetically ordered crystals. the mixed state of magnets", *Zh. Eksp. Teor. Fiz* **95**, 178–182 (1989).
- [63] A. Bogdanov and A. Hubert, "Thermodynamically stable magnetic vortex states in magnetic crystals", *Journal of Magnetism and Magnetic Materials* **138**, 255–269 (1994).
- [64] A. Bogdanov and A. Hubert, "The stability of vortex-like structures in uniaxial ferromagnets", *Journal of Magnetism and Magnetic Materials* **195**, 182–192 (1999).

- [65] A. N. Bogdanov and U. K. Rößler, “Chiral symmetry breaking in magnetic thin films and multilayers”, *Physical Review Letters* **87**, 037203 (2001).
- [66] S. Mühlbauer, B. Binz, F. Jonietz, et al., “Skyrmion lattice in a chiral magnet”, *Science* **323**, 915–919 (2009).
- [67] W. Münzer, A. Neubauer, T. Adams, et al., “Skyrmion lattice in the doped semiconductor $\text{Fe}_{1-x}\text{Co}_x\text{Si}$ ”, *Physical Review B* **81**, 041203 (2010).
- [68] X. Yu, Y. Onose, N. Kanazawa, et al., “Real-space observation of a two-dimensional skyrmion crystal”, *Nature* **465**, 901–904 (2010).
- [69] C. Moreau-Luchaire, C. Moutafis, N. Reyren, et al., “Additive interfacial chiral interaction in multilayers for stabilization of small individual skyrmions at room temperature”, *Nature Nanotechnology* **11**, 444–448 (2016).
- [70] O. Boulle, J. Vogel, H. Yang, et al., “Room-temperature chiral magnetic skyrmions in ultrathin magnetic nanostructures”, *Nature Nanotechnology* **11**, 449–454 (2016).
- [71] S. Woo, K. Litzius, B. Krüger, et al., “Observation of room-temperature magnetic skyrmions and their current-driven dynamics in ultrathin metallic ferromagnets”, *Nature Materials* **15**, 501–506 (2016).
- [72] S. Jaiswal, K. Litzius, I. Lemesch, et al., “Investigation of the Dzyaloshinskii-Moriya interaction and room temperature skyrmions in W/CoFeB/MgO thin films and microwires”, *Applied Physics Letters* **111**, 022409 (2017).
- [73] K. Y. Guslienko, “Skyrmion state stability in magnetic nanodots with perpendicular anisotropy”, *IEEE Magnetics Letters* **6**, 1–4 (2015).
- [74] K. Everschor-Sitte, J. Masell, R. M. Reeve, and M. Kläui, “Perspective: Magnetic skyrmions—Overview of recent progress in an active research field”, *Journal of Applied Physics* **124**, 240901 (2018).
- [75] X. Zhang, Y. Zhou, K. M. Song, et al., “Skyrmion-electronics: writing, deleting, reading and processing magnetic skyrmions toward spintronic applications”, *Journal of Physics: Condensed Matter* **32**, 143001 (2020).
- [76] N. Kent, N. Reynolds, D. Raftrey, et al., “Creation and observation of hopfions in magnetic multilayer systems”, *Nature Communications* **12**, 1562 (2021).
- [77] A. G. Gurevich and G. A. Melkov, *Magnetization Oscillations and Waves* (CRC Press, 1996).
- [78] B. Kalinikos, “Excitation of propagating spin waves in ferromagnetic films”, English, *IEE Proceedings H (Microwaves, Optics and Antennas)* **127**, 4–10 (1980).
- [79] M. Hurben and C. Patton, “Theory of magnetostatic waves for in-plane magnetized isotropic films”, *Journal of Magnetism and Magnetic Materials* **139**, 263–291 (1995).
- [80] R. Damon and J. Eshbach, “Magnetostatic modes of a ferromagnet slab”, *Journal of Physics and Chemistry of Solids* **19**, 308–320 (1961).
- [81] R. E. De Wames and T. Wolfram, “Dipole-Exchange Spin Waves in Ferromagnetic Films”, *Journal of Applied Physics* **41**, 987–993 (1970).
- [82] T. Wolfram, “Magnetostatic surface waves in layered magnetic structures”, *Journal of Applied Physics* **41**, 4748–4749 (2003).
- [83] R. Arias and D. L. Mills, “Theory of spin excitations and the microwave response of cylindrical ferromagnetic nanowires”, *Physical Review B* **63**, 134439 (2001).
- [84] J. Rychlý, V. S. Tkachenko, J. W. Kłos, A. Kuchko, and M. Krawczyk, “Spin wave modes in a cylindrical nanowire in crossover dipolar-exchange regime”, *Journal of Physics D: Applied Physics* **52**, 075003 (2018).
- [85] B. A. Kalinikos and A. N. Slavin, “Theory of dipole-exchange spin wave spectrum for ferromagnetic films with mixed exchange boundary conditions”, *Journal of Physics C: Solid State Physics* **19**, 7013 (1986).

- [86] B. A. Kalinikos, M. P. Kostylev, N. V. Kozhus, and A. N. Slavin, “The dipole-exchange spin wave spectrum for anisotropic ferromagnetic films with mixed exchange boundary conditions”, *Journal of Physics: Condensed Matter* **2**, 9861 (1990).
- [87] R. E. Arias, “Spin-wave modes of ferromagnetic films”, *Physical Review B* **94**, 134408 (2016).
- [88] P. Grünberg, “Magnetostatic spinwave modes of a ferromagnetic double layer”, *Journal of Applied Physics* **51**, 4338–4341 (1980).
- [89] T. McKinnon, B. Heinrich, and E. Girt, “Spacer layer thickness and temperature dependence of interlayer exchange coupling in Co/Ru/Co trilayer structures”, *Physical Review B* **104**, 024422 (2021).
- [90] H. Pfeiffer, “Characteristics of magnetostatic surface waves for a system of two magnetic films”, *physica status solidi (a)* **18**, K53–K56 (1973).
- [91] P. Grünberg, “Magnetostatic spin-wave modes of a heterogeneous ferromagnetic double layer”, *Journal of Applied Physics* **52**, 6824–6829 (1981).
- [92] P. Grünberg and K. Mika, “Magnetostatic spin-wave modes of a ferromagnetic multilayer”, *Physical Review B* **27**, 2955–2963 (1983).
- [93] R. E. Camley, T. S. Rahman, and D. L. Mills, “Magnetic excitations in layered media: Spin waves and the light-scattering spectrum”, *Physical Review B* **27**, 261–277 (1983).
- [94] P. Grünberg, “Some ways to modify the spin-wave mode spectra of magnetic multilayers (invited)”, *Journal of Applied Physics* **57**, 3673–3677 (1985).
- [95] R. E. Camley and M. G. Cottam, “Magnetostatic theory of collective excitations in ferromagnetic and antiferromagnetic superlattices with magnetization perpendicular to the surface”, *Physical Review B* **35**, 189–196 (1987).
- [96] L. Dobrzynski, B. Djafari-Rouhani, and H. Puzkarski, “Theory of bulk and surface magnons in Heisenberg ferromagnetic superlattices”, *Physical Review B* **33**, 3251–3256 (1986).
- [97] E. Albuquerque, P. Fulco, E. Sarmiento, and D. Tilley, “Spin waves in a magnetic superlattice”, *Solid State Communications* **58**, 41–44 (1986).
- [98] J. Barnaś, “Spin waves in superlattices. II. Magnetostatic modes in the Voigt configuration”, *Journal of Physics C: Solid State Physics* **21**, 4097 (1988).
- [99] M. Vohl, J. Barnaś, and P. Grünberg, “Effect of interlayer exchange coupling on spin-wave spectra in magnetic double layers: Theory and experiment”, *Physical Review B* **39**, 12003–12012 (1989).
- [100] H. Bouloussa, Y. Roussigné, M. Belmeguenai, et al., “Spin-wave calculations for magnetic stacks with interface Dzyaloshinskii-Moriya interaction”, *Physical Review B* **98**, 024428 (2018).
- [101] C. Elachi, “Waves in active and passive periodic structures: A review”, *Proceedings of the IEEE* **64**, 1666–1698 (1976).
- [102] E. Yablonovitch, “Inhibited spontaneous emission in solid-state physics and electronics”, *Physical Review Letters* **58**, 2059–2062 (1987).
- [103] S. John, “Strong localization of photons in certain disordered dielectric superlattices”, *Physical Review Letters* **58**, 2486–2489 (1987).
- [104] M. Krawczyk and D. Grundler, “Review and prospects of magnonic crystals and devices with reprogrammable band structure”, *Journal of Physics: Condensed Matter* **26**, 123202 (2014).
- [105] C. Elachi, “Magnetic wave propagation in a periodic medium”, *IEEE Transactions on Magnetics* **11**, 36–39 (1975).
- [106] C. G. Sykes, J. D. Adam, and J. H. Collins, “Magnetostatic wave propagation in a periodic structure”, *Applied Physics Letters* **29**, 388–391 (1976).
- [107] J. Barnaś, “Exchange modes in ferromagnetic superlattices”, *Physical Review B* **45**, 10427–10437 (1992).

- [108] J. Barnas, “Spin waves in superlattices. IV. The exchange-dominated region”, *Journal of Physics: Condensed Matter* **4**, 4849 (1992).
- [109] H. Puzskarski and M. Krawczyk, “On the multiplicity of the surface boundary condition in composite materials”, *Physics Letters A* **282**, 106–112 (2001).
- [110] S. Nikitov, P. Tailhades, and C. Tsai, “Spin waves in periodic magnetic structures—magnonic crystals”, *Journal of Magnetism and Magnetic Materials* **236**, 320–330 (2001).
- [111] Y. V. Gulyaev and S. Nikitov, “Magnonic crystals and spin waves in periodic structures”, in *Doklady physics*, Vol. 46, 10 (Moscow, Russia: Maik nauka/Interperiodica Publishing; Woodbury, NY, 2001), pp. 687–689.
- [112] V. Kruglyak and A. Kuchko, “Spectrum of spin waves propagating in a periodic magnetic structure”, *Physica B: Condensed Matter* **339**, 130–133 (2003).
- [113] H. Puzskarski and M. Krawczyk, “Magnonic crystals — the magnetic counterpart of photonic crystals”, in *Interfacial effects and novel properties of nanomaterials*, Vol. 94, *Solid State Phenomena* (2003), pp. 125–134.
- [114] M. Krawczyk and H. Puzskarski, “Plane-wave theory of three-dimensional magnonic crystals”, *Physical Review B* **77**, 054437 (2008).
- [115] G. Gubbiotti, S. Tacchi, G. Carlotti, et al., “Magnetostatic interaction in arrays of nanometric permalloy wires: A magneto-optic Kerr effect and a Brillouin light scattering study”, *Physical Review B* **72**, 224413 (2005).
- [116] G. Gubbiotti, S. Tacchi, G. Carlotti, et al., “Collective spin modes in monodimensional magnonic crystals consisting of dipolarly coupled nanowires”, *Applied Physics Letters* **90**, 092503 (2007).
- [117] Z. K. Wang, V. L. Zhang, H. S. Lim, et al., “Observation of frequency band gaps in a one-dimensional nanostructured magnonic crystal”, *Applied Physics Letters* **94**, 083112 (2009).
- [118] S. Tacchi, F. Montoncello, M. Madami, et al., “Band diagram of spin waves in a two-dimensional magnonic crystal”, *Physical Review Letters* **107**, 127204 (2011).
- [119] S. Tacchi, G. Duerr, J. W. Klos, et al., “Forbidden band gaps in the spin-wave spectrum of a two-dimensional bicomponent magnonic crystal”, *Physical Review Letters* **109**, 137202 (2012).
- [120] X. Zhou, G.-L. Chua, N. Singh, and A. O. Adeyeye, “Large area artificial spin ice and anti-spin ice Ni₈₀Fe₂₀ structures: Static and dynamic behavior”, *Advanced Functional Materials* **26**, 1437–1444 (2016).
- [121] V. S. Bhat, F. Heimbach, I. Stasinopoulos, and D. Grundler, “Angular-dependent magnetization dynamics of kagome artificial spin ice incorporating topological defects”, *Physical Review B* **96**, 014426 (2017).
- [122] J. Topp, D. Heitmann, M. P. Kostylev, and D. Grundler, “Making a reconfigurable artificial crystal by ordering bistable magnetic nanowires”, *Physical Review Letters* **104**, 207205 (2010).
- [123] S. Tacchi, M. Madami, G. Gubbiotti, et al., “Analysis of collective spin-wave modes at different points within the hysteresis loop of a one-dimensional magnonic crystal comprising alternative-width nanostripes”, *Physical Review B* **82**, 184408 (2010).
- [124] O. Dobrovolskiy, R. Sachser, T. Brächer, et al., “Magnon–fluxon interaction in a ferromagnet/superconductor heterostructure”, *Nature Physics* **15**, 477–482 (2019).
- [125] F. Lisiecki, J. Rychły, P. Kuświk, et al., “Reprogrammability and scalability of magnonic Fibonacci quasicrystals”, *Physical Review Applied* **11**, 054003 (2019).
- [126] N. Träger, P. Gruszecki, F. Lisiecki, et al., “Real-space observation of magnon interaction with driven space-time crystals”, *Physical Review Letters* **126**, 057201 (2021).
- [127] A. Mahmoud, F. Ciubotaru, F. Vanderveken, et al., “Introduction to spin wave computing”, *Journal of Applied Physics* **128**, 161101 (2020).

- [128] A. Barman, G. Gubbiotti, S. Ladak, et al., “The 2021 Magnonics Roadmap”, *Journal of Physics: Condensed Matter* **33**, 413001 (2021).
- [129] A. V. Chumak, P. Kabos, M. Wu, et al., “Advances in Magnetics Roadmap on Spin-Wave Computing”, *IEEE Transactions on Magnetics* **58**, 1–72 (2022).
- [130] A. Khitun and K. L. Wang, “Nano scale computational architectures with spin wave bus”, *Superlattices and Microstructures* **38**, 184–200 (2005).
- [131] A. Khitun, D. E. Nikonov, M. Bao, K. Galatsis, and K. L. Wang, “Efficiency of spin-wave bus for information transmission”, *IEEE Transactions on Electron Devices* **54**, 3418–3421 (2007).
- [132] A. Khitun, D. E. Nikonov, M. Bao, K. Galatsis, and K. L. Wang, “Feasibility study of logic circuits with a spin wave bus”, *Nanotechnology* **18**, 465202 (2007).
- [133] A. Khitun, “Magnonic holographic devices for special type data processing”, *Journal of Applied Physics* **113**, 164503 (2013).
- [134] S. Dutta, S.-C. Chang, N. Kani, et al., “Non-volatile clocked spin wave interconnect for beyond-CMOS nanomagnet pipelines”, *Scientific Reports* **5**, 9861 (2015).
- [135] F. Gertz, A. V. Kozhevnikov, Y. A. Filimonov, D. E. Nikonov, and A. Khitun, “Magnonic holographic memory: from proposal to device”, *IEEE Journal on Exploratory Solid-State Computational Devices and Circuits* **1**, 67–75 (2015).
- [136] M. Balinsky and A. Khitun, “Magnonic combinatorial memory”, *npj Spintronics* **2**, 2 (2024).
- [137] G. Csaba, A. Papp, and W. Porod, “Spin-wave based realization of optical computing primitives”, *Journal of Applied Physics* **115**, 17C741 (2014).
- [138] Y. Khivintsev, M. Ranjbar, D. Gutierrez, et al., “Prime factorization using magnonic holographic devices”, *Journal of Applied Physics* **120**, 123901 (2016).
- [139] D. Lachance-Quirion, S. P. Wolski, Y. Tabuchi, et al., “Entanglement-based single-shot detection of a single magnon with a superconducting qubit”, *Science* **367**, 425–428 (2020).
- [140] S. O. Demokritov, V. E. Demidov, O. Dzyapko, et al., “Bose–Einstein condensation of quasi-equilibrium magnons at room temperature under pumping”, *Nature* **443**, 430–433 (2006).
- [141] T. Kikkawa, K. Shen, B. Flebus, et al., “Magnon polarons in the spin Seebeck effect”, *Physical Review Letters* **117**, 207203 (2016).
- [142] H. Y. Yuan, S. Zheng, Z. Ficek, Q. Y. He, and M.-H. Yung, “Enhancement of magnon-magnon entanglement inside a cavity”, *Physical Review B* **101**, 014419 (2020).
- [143] I. A. Golovchanskiy, N. N. Abramov, V. S. Stolyarov, et al., “Ultrastrong photon-to-magnon coupling in multilayered heterostructures involving superconducting coherence via ferromagnetic layers”, *Science Advances* **7**, eabe8638 (2021).
- [144] D. Lachance-Quirion, Y. Tabuchi, A. Gloppe, K. Usami, and Y. Nakamura, “Hybrid quantum systems based on magnonics”, *Applied Physics Express* **12**, 070101 (2019).
- [145] N. Locatelli, V. Cros, and J. Grollier, “Spin-torque building blocks”, *Nature Materials* **13**, 11–20 (2014).
- [146] M. Rahman, S. Khasanvis, J. Shi, and C. A. Moritz, “Wave interference functions for neuromorphic computing”, *IEEE Transactions on Nanotechnology* **14**, 742–750 (2015).
- [147] T. Brächer and P. Pirro, “An analog magnon adder for all-magnonic neurons”, *Journal of Applied Physics* **124**, 152119 (2018).
- [148] H. Arai and H. Imamura, “Neural-network computation using spin-wave-coupled spin-torque oscillators”, *Physical Review Applied* **10**, 024040 (2018).
- [149] Á. Papp, W. Porod, and G. Csaba, “Nanoscale neural network using non-linear spin-wave interference”, *Nature Communications* **12**, 6422 (2021).

- [150] S. Watt, M. Kostylev, and A. B. Ustinov, “Enhancing computational performance of a spin-wave reservoir computer with input synchronization”, *Journal of Applied Physics* **129**, 044902 (2021).
- [151] S. Watt, M. Kostylev, A. B. Ustinov, and B. A. Kalinikos, “Implementing a magnonic reservoir computer model based on time-delay multiplexing”, *Physical Review Applied* **15**, 064060 (2021).
- [152] A. Papp, G. Csaba, and W. Porod, “Characterization of nonlinear spin-wave interference by reservoir-computing metrics”, *Applied Physics Letters* **119**, 112403 (2021).
- [153] B. Heinz, T. Brächer, M. Schneider, et al., “Propagation of spin-wave packets in individual nanosized yttrium iron garnet magnonic conduits”, *Nano Letters* **20**, 4220–4227 (2020).
- [154] T. Sebastian, Y. Ohdaira, T. Kubota, et al., “Low-damping spin-wave propagation in a microstructured $\text{Co}_2\text{Mn}_0.6\text{Fe}_0.4\text{Si}$ Heusler waveguide”, *Applied Physics Letters* **100**, 112402 (2012).
- [155] V. E. Demidov, S. O. Demokritov, K. Rott, P. Krzysteczko, and G. Reiss, “Mode interference and periodic self-focusing of spin waves in permalloy microstripes”, *Physical Review B* **77**, 064406 (2008).
- [156] A. Haldar, C. Tian, and A. O. Adeyeye, “Isotropic transmission of magnon spin information without a magnetic field”, *Science Advances* **3**, e1700638 (2017).
- [157] F. Garcia-Sanchez, P. Borys, R. Soucaille, et al., “Narrow magnonic waveguides based on domain walls”, *Physical Review Letters* **114**, 247206 (2015).
- [158] K. Wagner, A. Kákay, K. Schultheiss, et al., “Magnetic domain walls as reconfigurable spin-wave nanochannels”, *Nature Nanotechnology* **11**, 432–436 (2016).
- [159] K. Vogt, H. Schultheiss, S. Jain, et al., “Spin waves turning a corner”, *Applied Physics Letters* **101**, 042410 (2012).
- [160] V. S. Tkachenko, A. N. Kuchko, M. Dvornik, and V. V. Kruglyak, “Propagation and scattering of spin waves in curved magnonic waveguides”, *Applied Physics Letters* **101**, 152402 (2012).
- [161] E. N. Beginin, A. V. Sadovnikov, A. Y. Sharaevskaya, A. I. Stognij, and S. A. Nikitov, “Spin wave steering in three-dimensional magnonic networks”, *Applied Physics Letters* **112**, 122404 (2018).
- [162] C. S. Davies, A. Francis, A. V. Sadovnikov, et al., “Towards graded-index magnonics: Steering spin waves in magnonic networks”, *Physical Review B* **92**, 020408 (2015).
- [163] M. Vogel, R. Aßmann, P. Pirro, et al., “Control of spin-wave propagation using magnetisation gradients”, *Scientific Reports* **8**, 11099 (2018).
- [164] S. Mieszczak, O. Busel, P. Gruszecki, et al., “Anomalous refraction of spin waves as a way to guide signals in curved magnonic multimode waveguides”, *Physical Review Applied* **13**, 054038 (2020).
- [165] E. Albisetti, D. Petti, G. Sala, et al., “Nanoscale spin-wave circuits based on engineered reconfigurable spin-textures”, *Communications Physics* **1**, 56 (2018).
- [166] B. Divinskiy, V. E. Demidov, S. Urazhdin, et al., “Excitation and amplification of spin waves by spin-orbit torque”, *Advanced Materials* **30**, 1802837 (2018).
- [167] T. Brächer, P. Pirro, and B. Hillebrands, “Parallel pumping for magnon spintronics: Amplification and manipulation of magnon spin currents on the micron-scale”, *Physics Reports* **699**, 1–34 (2017).
- [168] B. Rana and Y. Otani, “Towards magnonic devices based on voltage-controlled magnetic anisotropy”, *Communications Physics* **2**, 90 (2019).
- [169] A. Khitun, D. E. Nikonov, and K. L. Wang, “Magnetoelectric spin wave amplifier for spin wave logic circuits”, *Journal of Applied Physics* **106**, 123909 (2009).
- [170] A. Khitun and K. L. Wang, “Non-volatile magnonic logic circuits engineering”, *Journal of Applied Physics* **110**, 034306 (2011).
- [171] A. V. Chumak, A. A. Serga, and B. Hillebrands, “Magnon transistor for all-magnon data processing”, *Nature Communications* **5**, 4700 (2014).

- [172] A. V. Chumak, A. A. Serga, and B. Hillebrands, “Magnonic crystals for data processing”, *Journal of Physics D: Applied Physics* **50**, 244001 (2017).
- [173] K.-S. Lee and S.-K. Kim, “Conceptual design of spin wave logic gates based on a Mach–Zehnder-type spin wave interferometer for universal logic functions”, *Journal of Applied Physics* **104**, 053909 (2008).
- [174] T. Schneider, A. A. Serga, B. Leven, et al., “Realization of spin-wave logic gates”, *Applied Physics Letters* **92**, 022505 (2008).
- [175] B. Rana and Y. Otani, “Voltage-controlled reconfigurable spin-wave nanochannels and logic devices”, *Physical Review Applied* **9**, 014033 (2018).
- [176] M. P. Kostylev, A. A. Serga, T. Schneider, B. Leven, and B. Hillebrands, “Spin-wave logical gates”, *Applied Physics Letters* **87**, 153501 (2005).
- [177] S. Klingler, P. Pirro, T. Brächer, et al., “Design of a spin-wave majority gate employing mode selection”, *Applied Physics Letters* **105**, 152410 (2014).
- [178] N. Kanazawa, T. Goto, K. Sekiguchi, et al., “The role of Snell’s law for a magnonic majority gate”, *Scientific Reports* **7**, 7898 (2017).
- [179] T. Fischer, M. Kewenig, D. A. Bozhko, et al., “Experimental prototype of a spin-wave majority gate”, *Applied Physics Letters* **110**, 152401 (2017).
- [180] G. Talmelli, T. Devolder, N. Träger, et al., “Reconfigurable submicrometer spin-wave majority gate with electrical transducers”, *Science Advances* **6**, eabb4042 (2020).
- [181] S. V. Vasiliev, V. V. Kruglyak, M. L. Sokolovskii, and A. N. Kuchko, “Spin wave interferometer employing a local nonuniformity of the effective magnetic field”, *Journal of Applied Physics* **101**, 113919 (2007).
- [182] V. E. Demidov, S. Urazhdin, and S. O. Demokritov, “Control of spin-wave phase and wavelength by electric current on the microscopic scale”, *Applied Physics Letters* **95**, 262509 (2009).
- [183] Q. Wang, M. Kewenig, M. Schneider, et al., “A magnonic directional coupler for integrated magnonic half-adders”, *Nature Electronics* **3**, 765–774 (2020).
- [184] U. Garlando, Q. Wang, O. V. Dobrovolskiy, A. V. Chumak, and F. Riente, “Numerical model for 32-bit magnonic ripple carry adder”, *IEEE Transactions on Emerging Topics in Computing* **11**, 679–688 (2023).
- [185] A. V. Sadovnikov, E. N. Beginin, S. E. Sheshukova, et al., “Directional multimode coupler for planar magnonics: Side-coupled magnetic stripes”, *Applied Physics Letters* **107**, 202405 (2015).
- [186] A. V. Sadovnikov, E. N. Beginin, M. A. Morozova, et al., “Nonlinear spin wave coupling in adjacent magnonic crystals”, *Applied Physics Letters* **109**, 042407 (2016).
- [187] Q. Wang, P. Pirro, R. Verba, et al., “Reconfigurable nanoscale spin-wave directional coupler”, *Science Advances* **4**, e1701517 (2018).
- [188] Y. Au, M. Dvornik, O. Dmytriev, and V. V. Kruglyak, “Nanoscale spin wave valve and phase shifter”, *Applied Physics Letters* **100**, 172408 (2012).
- [189] J. Lan, W. Yu, R. Wu, and J. Xiao, “Spin-wave diode”, *Physical Review X* **5**, 041049 (2015).
- [190] M. Grassi, M. Geilen, D. Louis, et al., “Slow-wave-based nanomagnonic diode”, *Physical Review Applied* **14**, 024047 (2020).
- [191] J. Zou, S. Bosco, E. Thingstad, J. Klinovaja, and D. Loss, “Dissipative spin-wave diode and nonreciprocal magnonic amplifier”, *Physical Review Letters* **132**, 036701 (2024).
- [192] Q. Wang, A. V. Chumak, and P. Pirro, “Inverse-design magnonic devices”, *Nature Communications* **12**, 2636 (2021).
- [193] F. Heussner, M. Nabinger, T. Fischer, et al., “Frequency-division multiplexing in magnonic logic networks based on caustic-like spin-wave beams”, *physica status solidi (RRL) – Rapid Research Letters* **12**, 1800409 (2018).

- [194] F. Heussner, G. Talmelli, M. Geilen, et al., “Experimental realization of a passive gigahertz frequency-division demultiplexer for magnonic logic networks”, *physica status solidi (RRL) – Rapid Research Letters* **14**, 1900695 (2020).
- [195] A. Khitun, M. Bao, and K. L. Wang, “Magnonic logic circuits”, *Journal of Physics D: Applied Physics* **43**, 264005 (2010).
- [196] A. Vansteenkiste, J. Leliaert, M. Dvornik, et al., “The design and verification of MuMax3”, *AIP Advances* **4**, 107133 (2014).
- [197] *OOMMF Project at NIST*, URL: <https://math.nist.gov/oommf>.
- [198] R. Hertel, S. Christophersen, and S. Börm, “Large-scale magnetostatic field calculation in finite element micromagnetics with H2-matrices”, *Journal of Magnetism and Magnetic Materials* **477**, 118–123 (2019).
- [199] M.-A. Bisotti, M. Beg, W. Wang, et al., *FinMag: Finite-element micromagnetic simulation tool*, URL: <https://github.com/fangohr/finmag>.
- [200] L. Körber, G. Quasebarth, A. Otto, and A. Kákay, “Finite-element dynamic-matrix approach for spin-wave dispersions in magnonic waveguides with arbitrary cross section”, *AIP Advances* **11**, 095006 (2021).
- [201] L. Körber, G. Quasebarth, A. Hempel, et al., “TetraX: Finite-Element Micromagnetic-Modeling Package”, 10.14278/rodare.1418 (2022).
- [202] R. Chang, S. Li, M. V. Lubarda, B. Livshitz, and V. Lomakin, “FastMag: Fast micromagnetic simulator for complex magnetic structures”, *Journal of Applied Physics* **109**, 07D358 (2011).
- [203] C. Abert, L. Exl, F. Bruckner, A. Drews, and D. Suess, “magnum.fe: A micromagnetic finite-element simulation code based on FEniCS”, *Journal of Magnetism and Magnetic Materials* **345**, 29–35 (2013).
- [204] J. Zhang, W. Yu, X. Chen, and J. Xiao, “A frequency-domain micromagnetic simulation module based on COMSOL Multiphysics”, *AIP Advances* **13**, 055108 (2023).
- [205] *About COMSOL*, URL: <https://www.comsol.com/company>.
- [206] M. Mruczkiewicz and M. Krawczyk, “Nonreciprocal dispersion of spin waves in ferromagnetic thin films covered with a finite-conductivity metal”, *Journal of Applied Physics* **115**, 113909 (2014).
- [207] J. Rychły and J. W. Kłos, “Spin wave surface states in 1D planar magnonic crystals”, *Journal of Physics D: Applied Physics* **50**, 164004 (2017).
- [208] M. Vaňatka, K. Szulc, O. Wojewoda, et al., “Spin-wave dispersion measurement by variable-gap propagating spin-wave spectroscopy”, *Physical Review Applied* **16**, 054033 (2021).
- [209] K. Szulc, J. Kharlan, P. Bondarenko, E. V. Tartakovskaya, and M. Krawczyk, “Impact of surface anisotropy on the spin-wave dynamics in a thin ferromagnetic film”, *Physical Review B* **109**, 054430 (2024).
- [210] M. Zelent, M. Moalic, M. Mruczkiewicz, et al., “Stabilization and racetrack application of asymmetric Néel skyrmions in hybrid nanostructures”, *Scientific Reports* **13**, 13572 (2023).
- [211] O. Wojewoda, F. Ligmajer, M. Hrtoň, et al., “Observing high-k magnons with Mie-resonance-enhanced Brillouin light scattering”, *Communications Physics* **6**, 94 (2023).
- [212] K. Szulc, F. Lisiecki, A. Makarov, et al., “Remagnetization in arrays of ferromagnetic nanostripes with periodic and quasiperiodic order”, *Physical Review B* **99**, 064412 (2019).
- [213] M. Moalic, M. Zelent, K. Szulc, and M. Krawczyk, “The role of non-uniform magnetization texture for magnon–magnon coupling in an antidot lattice”, *Scientific Reports* **14**, 11501 (2024).
- [214] K. Szulc, K. Pydzińska-Białek, and M. Ziółek, “Modeling of charge injection, recombination, and diffusion in complete perovskite solar cells on short time scales”, *Materials* **16**, 7110 (2023).
- [215] J. Kharlan, K. Sobucki, K. Szulc, S. Memarzadeh, and J. W. Kłos, “Spin-wave confinement in a hybrid superconductor-ferrimagnet nanostructure”, *Physical Review Applied* **21**, 064007 (2024).

About the Author

The Author's education was fully connected with Adam Mickiewicz University, Poznań. The Author started his scientific career in 2016 after joining Department of Physics of Nanomaterials, where he prepared his bachelor thesis entitled *Demagnetizing field analysis in periodic and quasiperiodic one-dimensional magnonic structures* and master thesis entitled *Analytical model development and analysis of remagnetization in arrays of ferromagnetic nanostripes with periodic and quasiperiodic order* under the supervision of Prof. Maciej Krawczyk. Later he changed his main research topic to magnonics. He is the co-author of 10 research articles and 1 roadmap, wrote 5 reviews, and actively participated in 24 national and international conferences.

Career timeline

2019–2024	PhD student – Physical sciences Adam Mickiewicz University, Poznań Doctoral School of Exact Sciences
2017–2019	Master student – Physics Adam Mickiewicz University, Poznań Faculty of Physics
2014–2017	Bachelor student – Physics Adam Mickiewicz University, Poznań Faculty of Physics

Publications

1. **K. Szulc**, F. Lisiecki, A. Makarov, M. Zelent, P. Kuświk, H. Głowiński, J. W. Kłos, M. Münzenberg, R. Gieniusz, J. Dubowik, F. Stobiecki, M. Krawczyk
Remagnetization in arrays of ferromagnetic nanostripes with periodic and quasiperiodic order
Physical Review B 99, 064412 (2019)

2. **K. Szulc**, P. Graczyk, M. Mruczkiewicz, G. Gubbiotti, M. Krawczyk
Spin-wave diode and circulator based on unidirectional coupling
Physical Review Applied 14, 034063 (2020)
3. **K. Szulc**, S. Mendisch, M. Mruczkiewicz, F. Casoli, M. Becherer, G. Gubbiotti
Nonreciprocal spin-wave dynamics in Pt/Co/W/Co/Pt multilayers
Physical Review B 103, 134404 (2021)
4. P. Roberjot, **K. Szulc**, J. W. Kłos, M. Krawczyk
Multifunctional operation of the double-layer ferromagnetic structure coupled by a rectangular nanoresonator
Applied Physics Letters 118, 182406 (2021)
5. M. Vaňatka, **K. Szulc**, O. Wojewoda, C. Dubs, A. V. Chumak, M. Krawczyk, O. V. Dobrovolskiy, J. W. Kłos, M. Urbánek
Spin-wave dispersion measurement by variable-gap propagating spin-wave spectroscopy
Physical Review Applied 16, 054033 (2021)
6. A. V. Chumak, P. Kabos, M. Wu, C. Abert, C. Adelman, A. O. Adeyeye, J. Åkerman, F. G. Aliev, A. Anane, A. Awad, C. H. Back, A. Barman, G. E. W. Bauer, M. Becherer, E. N. Beginin, V. A. S. V. Bittencourt, Y. M. Blanter, P. Bortolotti, I. Boventer, D. A. Bozhko, S. A. Bunyae, J. J. Carmiggelt, R. R. Cheenikundil, F. Ciubotaru, S. Cotofana, G. Csaba, O. V. Dobrovolskiy, C. Dubs, M. Elyasi, K. G. Fripp, H. Fulara, I. A. Golovchanskiy, C. Gonzalez-Ballester, P. Graczyk, D. Grundler, P. Gruszecki, G. Gubbiotti, K. Guslienko, A. Haldar, S. Hamdioui, R. Hertel, B. Hillebrands, T. Hioki, A. Houshang, C.-M. Hu, H. Huebl, M. Huth, E. Iacocca, M. B. Jungfleisch, G. N. Kakazei, A. Khitun, R. Khymyn, T. Kikkawa, M. Kläui, O. Klein, J. W. Kłos, S. Knauer, S. Koraltan, M. Kostylev, M. Krawczyk, I. N. Krivorotov, V. V. Kruglyak, D. Lachance-Quirion, S. Ladak, R. Lebrun, Y. Li, M. Lindner, R. Macêdo, S. Mayr, G. A. Melkov, S. Mieszczak, Y. Nakamura, H. T. Nembach, A. A. Nikitin, S. A. Nikitov, V. Novosad, J. A. Otálora, Y. Otani, A. Papp, B. Pigeau, P. Pirro, W. Porod, F. Porrati, H. Qin, B. Rana, T. Reimann, F. Riente, O. Romero-Isart, A. Ross, A. V. Sadovnikov, A. R. Safin, E. Saitoh, G. Schmidt, H. Schultheiss, K. Schultheiss, A. A. Serga, S. Sharma, J. M. Shaw, D. Suess, O. Surzhenko, **K. Szulc**, T. Taniguchi, M. Urbánek, K. Usami, A. B. Ustinov, T. van der Sar, S. van Dijken, V. I. Vasyuchka, R. Verba, S. Viola Kusminskiy, Q. Wang, M. Weides, M. Weiler, S. Wintz, S. P. Wolski, and X. Zhang
Advances in Magnetism Roadmap on Spin-Wave Computing
IEEE Transactions on Magnetism 58, 1-72 (2022)
(Co-author of Section VI-A together with J. W. Kłos, M. Krawczyk, and P. Graczyk)
7. **K. Szulc**, S. Tacchi, A. Hierro-Rodríguez, J. Díaz, P. Gruszecki, P. Graczyk, C. Quirós, D. Markó, J. I. Martín, M. Vélez, D. S. Schmool, G. Carlotti, M. Krawczyk, L. M. Álvarez-

Prado

Reconfigurable magnonic crystals based on imprinted magnetization textures in hard and soft dipolar-coupled bilayers

ACS Nano 16, 14168-14177 (2022)

8. **K. Szulc**, K. Pydzińska-Białek, M. Ziótek
Modeling of charge injection, recombination, and diffusion in complete perovskite solar cells on short time scales
Materials 16, 7110 (2023)
9. **K. Szulc**, J. Kharlan, P. Bondarenko, E. V. Tartakovskaya, M. Krawczyk
Impact of surface anisotropy on the spin-wave dynamics in a thin ferromagnetic film
Physical Review B 109, 054430 (2024)
10. M. Moalic, M. Zelent, **K. Szulc**, M. Krawczyk
The role of non-uniform magnetization texture for magnon–magnon coupling in an antidot lattice
Scientific Reports 14, 11501 (2024)
11. J. Kharlan, K. Sobucki, **K. Szulc**, S. Memarzadeh, J. W. Kłos
Spin-wave confinement in a hybrid superconductor-ferrimagnet nanostructure
Physical Review Applied 21, 064007 (2024)

Manuscripts under review

1. **K. Szulc**, M. Zelent, M. Krawczyk
Reconfigurable spin-wave platform based on interplay between nanodots and waveguide in hybrid magnonic crystal
arXiv:2404.10493 [cond-mat.mes-hall] (2024)

Reviews

1. **Journal of Physics D: Applied Physics** – 2 reviews
2. **ACS Applied Nano Materials** – 1 review
3. **ACS Applied Electronic Materials** – 1 review
4. **Advanced Electronic Materials** – 1 co-review

Conference presentations

Oral presentations

1. **QuTechNOMM 2018**, Poznań, 28.11–06.12.2018
2. **QuTechNOMM 2019**, Poznań, 15.10–18.11.2019
3. **InterMag 2021**, 26–30.04.2021 (online)
4. **Sol-SkyMag 2021**, 21–24.06.2021 (online)
5. **Physics of Magnetism 2021**, 28.06–02.07.2021 (online)
6. **7th International Conference on Magnonics**, Oxnard, USA, 31.07–04.08.2022
7. **Sol-SkyMag 2023**, San Sebastian, Spain, 19–23.06.2023
8. **Physics of Magnetism 2023**, Poznań, 26–30.06.2023
9. **MagIC+ 2023**, Będlewo, 24–28.07.2023
10. **JEMS2023**, Madrid, Spain, 27.08–01.09.2023
11. **InterMag 2024**, Rio de Janeiro, Brasil, 05–10.05.2024

Poster presentations

1. **MagIC 2017**, Trzebaw, 02–07.07.2017
2. **NanoTech Poland 2018**, Poznań, 07–09.06.2018
3. **JEMS2018**, Mainz, Germany, 03–07.09.2018
4. **3rd International Advanced School on Magnonics**, Kyiv, Ukraine, 17–21.09.2018
5. **24th Soft Magnetic Materials Conference**, Poznań, 04–07.09.2019
6. **Polish Scientific Network 2019**, Poznań, 19–21.09.2019
7. **45. Zjazd Fizyków Polskich PTF**, Kraków, 13–18.09.2019
8. **Italian School on Magnetism 2020**, Rome, Italy, 03–07.02.2020
9. **JEMS2020**, 07–11.12.2020 (online)
10. **Nanoengineered Superconductors - NES21**, 10–12.05.2021 (online)
11. **4th International Advanced School on Magnonics**, Porto, Portugal, 18–22.07.2022
12. **2022 Trends in MAGnetism**, Venice, Italy, 04–09.09.2022
13. **International meeting on superconducting quantum materials and nanodevices**, Budva, Montenegro, 17–21.04.2023

Awards, grants, and scholarships

1. **National Science Center, Poland grant PRELUDIUM 20**
Three-dimensional magnonic structures for analog computing: interaction analysis and device development
2. **Scholarship for young, talented researchers from Foundation for Polish Science – program START 2022**
3. **Best oral presentation – 1st place**
Physics of Magnetism 2023
4. **1st degree Rector Award for scientific achievements in 2022**
Group award together with Prof. Maciej Krawczyk and Dr. Paweł Gruszecki
5. **Rector research scholarship in 2022**

Scientific visits

1. **Martin-Luther Universität Halle-Wittenberg**, Halle, Germany, 14–18.02.2022, group of Prof. Jamal Berakdar
2. **Universität Wien**, Vienna, Austria, 15.01–14.02.2023, group of Dr. Andrii Chumak and Dr. Oleksandr Dobrovolskiy
3. **Central European Institute of Technology (CEITEC)**, Brno, Czechia, 16–20.02.2023, group of Dr. Michal Urbanek

Student supervision

1. **Pierre Roberjot**, 2020-2021, co-supervisor